UNIVERSITY OF MINNESOTA

This is to certify that I have examined this bound copy of a doctoral thesis by

Eric William Grashorn

and have found that it is complete and satisfactory in all respects and that any and all revisions
required by the final examining committee have been made.

———————————————   ———————————————
Marvin L. Marshak   Alec T. Habig
(Faculty Co-Adviser)   (Faculty Co-Adviser)

———————————————
Date

GRADUATE SCHOOL

Astroparticle Physics with the MINOS Far Detector

A THESIS

SUBMITTED TO THE FACULTY OF THE GRADUATE SCHOOL

OF THE UNIVERSITY OF MINNESOTA

BY

Eric William Grashorn

IN PARTIAL FULFILLMENT OF THE REQUIREMENTS

FOR THE DEGREE OF

Doctor Of Philosophy

June, 2008

Astroparticle Physics with the MINOS Far Detector

by Eric William Grashorn

ABSTRACT

Since August 2003, the MINOS Far Detector collected over 67 million underground muons at Soudan MN, USA. As the temperature of the atmosphere changes, the interaction height of incident cosmic rays changes, which affects the production of muons that are seen underground. A four percent peak-to-peak seasonal fluctuation was seen over a period of four years, which was highly correlated to the measured temperature variations of the upper atmosphere over the same period. The coefficient relating changes in the muon rate to changes changes in atmospheric temperature, α_T, was found to be: $\alpha_T = 0.877 \pm 0.010$ (stat.) ± 0.017 (syst.). A new model was developed to describe the observed effect, and is the first to include the contribution from kaons. This model predicts $\alpha_T = 0.865 \pm 0.015$. The first measurements of charge separated seasonal variations were reported: $\alpha_T(\mu^+) = 0.782 \pm 0.056$ (stat.) ± 0.02 (syst.), $\alpha_T(\mu^-) = 0.788 \pm 0.066$ (stat.) ± 0.02 (syst.). The observed difference between the pion-only temperature coefficient and the kaon-inclusive temperature coefficient allowed a measurement of the atmospheric K/π ratio = 0.21 ± 0.08.

A high significance observation of two muon signals, the shadow of the sun and moon, have been seen. The shadow of the moon was observed at the $5\,\sigma$ level, and the shadow of the sun was observed at the $4.3\,\sigma$ level. The angular resolution of the detector was found to be $0.62°$ using dimuons, and the two dimensional shadowing distribution was used to quantify the absolute pointing of the detector $0.15 \pm 0.10°$.

A cosmic ray point source search was performed, and no statistically significant source was found. In the absence of a source, 95% flux limits were placed on cosmic ray sources. The minimum flux limit was $2.7 \times 10^{-16}\,\mathrm{cm}^{-2}\mathrm{s}^{-1}$, which is comparable to the previous best limit set by MACRO [1, 2]. Using the 239 Gamma Ray Bursts (GRBs) of the first Swift catalog a search for space-time coincidence between neutrino induced muons and GRBs was performed. In the absence of a statistically significant coincidence, 90% flux limits were placed on neutrino production in GRBs. Assuming a Waxman-Bahcall neutrino spectrum [3], the average 90% flux limit was found to be $1.7 \times 10^{-8}\,\mathrm{GeVcm}^{-2}\mathrm{s}^{-1}$. This new limit is slightly better than the MACRO [4] and AMANDA [5] limits as well as the theoretical limit set by cosmic rays [6, 7], but does not constrain the model.

Acknowledgements

Thanks to God, for everything.

Thanks to Alec, for your continual advice elbows deep in these analyses, for focusing my scattered thoughts and indulging my ideas, even when you knew they wouldn't work. Thanks to Marvin, for your encouragement and wisdom, for the kind of advice that can only be offered after advising 1,000 other PhDs (approximately).

Thanks to all the great people in MINOS who have given so much time to ponder an analysis, critique a paper draft or argue breathlessly during a meeting, especially Giles Barr, Stuart Mufson and Maury Goodman. Thanks to Ben Speakman for continually enduring my ignorance with a Cheshire cat grin. Thanks to the Minnesota contingent who have given so much "hands on" help: Sue Kasahara, Kregg Arms, Sujeewa Kumaratunga, Dipu Rahman, Matt Strait and everyone else. Most of this couldn't have been done without your help. Seriously. Thanks to Jason Koskinen for giving me my start and continuing to fuel the conversation with wine. Thanks to Seth Cooper for answering my computing questions, for arguing on principle, and for playing a wicked bass. Thanks to Brian Bock for useful suggestions, witty banter, and esoteric knowledge.

Oceans of thanks go to my lovely wife Anna, for supporting me, enduring me and loving me.

Thanks to Mom and Dad for believing in me and being impressed with me as only parents can. Thanks to Laura, Elizabeth, Ryan, Shawn, Ethan and Jason. Don't fear that your dreams are too grand, fear rather that you don't dream great enough, "...like an ignorant child who wants to go on making mud pies in a slum because he cannot imagine what is meant by the offer of a holiday at the sea" [8]. Thanks to Mike, Tanner, Matt, Tom for the continual reminder that there is more to ponder in this life than just physics. Thanks to Sujeewa, Matt, Ben, Jeremy and Dipu for keeping the office lively, the coffee brewing and the blunt objects airborne.

Thanks to the old friends who still keep in touch: Ben, Brock, Jon, Wolfy, Randy, Erin, April,

Josh. Thanks to my family for the many facets of their support, especially Julie and Fritz and Peter. Thanks to Tom, Kathy, Becky, Sean and Brian for taking me in.

And, finally, thanks to the imagination and creativity that causes us to wonder.

Dedication

To my grandfathers, Eugene Grashorn and Andy Gregor.

I stand amid the roar
Of a surf-tormented shore,
And I hold within my hand
Grains of the golden sand-
How few! yet how they creep
Through my fingers to the deep,
While I weep- while I weep!
O God! can I not grasp
Them with a tighter clasp?
O God! can I not save
One from the pitiless wave?
Is all that we see or seem
But a dream within a dream?

Edgar Allan Poe – *A Dream within a Dream*

Contents

List of Tables

List of Figures

Chapter 1

Introduction

For every question that a scientist answers, it seems two more are asked. The discovery of the Big Bang makes one wonder what caused it and what existed before this event; the discovery of Dinosaurs begs the questions why aren't there such massive creatures on earth these days and how did they disappear. The discovery of cosmic rays in the 1930's begged many questions as well. From where do they originate? Why are there so many, everywhere? "Coming out of space and incident on the high atmosphere, there is a thin rain of charged particles known as the primary cosmic radiation" [9]. These particles, ranging from barely relativistic electrons to ultra-relativistic iron nuclei, hold an entire universe of information to be gleaned by the careful experimenter. There are also more exotic particles eager to divulge secrets to anyone who will listen; most abundant is the ghost-like, flavor changing neutrino that streams undeviated from a stellar death. Particle detectors are as far removed from the cartoon telescopes used by comic-book astronomer stereotypes as the origin of the particles they study are from the medium of conventional astronomy, but they are producing tantalizing, tangible results. There are detectors that get a trip outside of the Earth's atmosphere to get a pure cosmic signal, detectors tied together with complex timing systems to pick up individual drops of extended air showers, and deep underground detectors that minimize noise with rock overburden to filter unwanted particles.

1.1   The Brief Historical Context

Shortly before the turn of the Twentieth Century, the development of the Cathode Ray Tube gave rise to a flourish of research in the phenomena phosphorescence and fluorescence. While investigating these wonders at the University of Würzburg, Wilhelm Conrad Roentgen noticed that he could see the outline of his bones when he placed his hand between the CRT and fluorescent screen. The 1901 Nobel Prize for Physics, the first ever, was awarded to Roentgen for the discovery of X-rays and ushered in a new era of physics, one in which radiation would dominate. Further understanding of electromagnetic phenomena via the use of electroscopes led to the curious observation that no matter the quantity of insulation, charge still would leak from these devices. Some researchers took their electroscopes to the tops of tall buildings, and the inconclusive results suggested that erratic radioactivity levels in the diverse building materials caused these variations. An electroscope was carried to the top of the Eiffel Tower in 1910 by Father Thomas Wulf with the hypothesis that the radiation from the ground would be absorbed by the increasing volume of air, resulting in a greater charge retention. The charge retention was actually *lower* than he had expected, which lead to the suggestion that there was radiation coming down through the atmosphere, a radical claim for the time. To test this hypothesis, experiments using balloons were devised to reach greater heights and see if there really could be radiation raining down from the sky. In 1911, Austrian Victor Hess flew in a balloon with his electroscope, and noted that by the time he reached 5 km above sea level, radiation levels had increased dramatically. With his empirical findings in hand, Hess claimed the cause must be "an extra-terrestrial source of penetrating radiation" [9]. Hess received the 1936 Nobel prize for his discovery [10]. Hess and the German Werner Kohlhörster made many measurements over the ensuing years, with Kohlhörster flying balloons to altitudes of 9 km, while drawing the ire of physicists who were slow to believe the claim that radiation could actually originate in space. American Robert Millikan began his own investigations with the intent to disprove the findings of his European counterparts.

Millikan studied this radiation phenomenon using detectors in balloons over San Antonio, TX. His findings did not agree with his European colleagues, and he asserted that there was no evidence of radiation of extra-terrestrial genesis. As it turns out, both parties were correct for "we now know that Millikan's findings of low intensities, though correct, were produced by the Earth's magnetic field, which is very different over Texas and Europe" [9]. He was still mystified by the origin of this cosmic radiation, and developed an experimental method that is still used today. He

lowered detectors into deep mountain lakes, because he realized that the particles attenuate much more in water than they do in air, given that the total thickness of the atmosphere corresponds to only 10 meters of water [10]. He thought this would help him to better understand the absorption length of cosmic rays, but it actually added to the confusion, since they have very different absorption lengths in air than water. Through repeated experimentation, Millikan eventually came to recognize that this radiation did originate in the cosmos, and he even suggested they be called cosmic rays, a moniker that stuck. His suggestion was tied to the fact that he believed this radiation was from gamma rays bombarding the atmosphere. His idea was shown to be erroneous, and another American, Arthur Compton, was correct in stating that this energetic stream came from charged particles. In spite of that fact, the name cosmic ray lives on to describe the thin rain of primary cosmic radiation.

About this same time, Wolfgang Pauli pondered a similarly troubling puzzle. Experimental investigation of beta decay (where a neutron decays into a proton and an electron), a decay that often occurs during nuclear fission, revealed that the energy of the neutron was not the same as the energy of the electron and proton combined. This apparent violation of one of the most widely held symmetries of the universe, the conservation of energy, had profound ramifications for science as a whole. Certain that some unknown mechanism was at work (and that energy was truly conserved), Pauli postulated that this "missing energy" was carried away by a new, "undetectable" particle. This particle had no mass (like the photon) and no charge (like the neutron), which meant that it was impossible to observe. Fortunately, experimentalists have never shied away from observing the impossible. In 1956 Fred Reines and Clyde Cowan reported the first detection of the neutrino [11], the name given to this mysterious, chargeless, light particle by the Italian physicist Enrico Fermi. Neutrino means "little, neutral one" in Italian. Reines and Cowan used a reactor at the Savannah River Nuclear Plant in Aiken, South Carolina, USA as their neutrino source, and the study of neutrinos as byproducts of nuclear interactions prompted Raymond Davis, Jr. and John Bahcall to search for neutrinos coming from the sun as a test of solar models. They succeeded in 1968, showing the first evidence for extraterrestrial neutrinos [12, 13]. Since their discovery, neutrinos have proved mysterious enough to inspire an entire sub-field of high energy physics, complete with departments in national laboratories and dedicated international conferences.

While Davis and Bahcall were physicists engaged in pure science in the 1960's, the cold war prompted the expansion of physics departments to provide the manpower to develop high-tech

weaponry and monitoring systems. After the signing of the 1963 Partial Test Ban treaty, which forbade nuclear tests in the atmosphere, outer space and under water, the United States launched the first pair of Vela (Spanish for *vigil*) satellites. These satellites had X-ray, neutron and gamma-ray detectors and could detect a nuclear explosion coming from the earth, either in the atmosphere or underground. A number of explosions were observed, but to the surprise of many, these were coming from *outer space.* In 1973, three Los Alamos scientists, Ray Klebesadel, Ian Strong and Roy Olson, made the first report of cosmic Gamma-Ray Bursts [14]. These incredibly energetic, short duration (one to tens of seconds) outbursts of highly energetic photons have been shown to have X-ray and optical components and originate in distant galaxies. The combination of their enormous power output, transient nature and uncertain origin make Gamma-Ray Bursts viable candidates for astrophysical particle sources [15, 3, 16, 17, 18, 19, 20, 21, 22].

While they have been studied for nearly 100 years, there are still many mysteries surrounding astrophysical particles. The field is in its infancy, with only two widely accepted extraterrestrial sources[1] the sun [12, 13] and Supernova 1987A [33, 34]. Both of these are (were; a supernova is a one-time event) neutrino sources within our galactic neighborhood. Neutrinos could offer a probe complementary to electromagnetic radiation into the structure of cosmic bodies. Additionally, neutrinos can be used to detect dark matter when it interacts in the sun [35, 36, 37, 38], to provide confirmation of the Greisen-Zatsepin-Kuz'min (GZK) [39, 40] effect of cosmic ray annihilation with the Cosmic Microwave Background radiation (CMB) and advance warning of a supernova (so astronomers can direct their telescopes) [41]. Cosmic rays, despite their innocuous composition (hydrogen, other lighter elements and iron) offer these questions: How could an atom be accelerated to the energy of a 100 mile per hour tennis ball? Why does the spectrum change around the so called "knee", (10^{15} eV, an electron Volt (eV) is the amount of energy contained in one fundamental charge, the charge of an electron, accelerated by a potential difference of one Volt. This corresponds to 1.602×10^{-19} J) , then change again around the so called "ankle", 10^{18} eV? Is there an end to the cosmic ray spectrum (the GZK effect)? Since there is a net galactic magnetic field, any charged particle with energy less than 10^{19} eV that enters the galaxy would be deflected from its original trajectory; it should not point back to its source. A source discovery

[1] There are reports that the X-ray binary system Cygnus X-3 is a source of cosmic rays [23, 24, 25, 26, 27, 28], and there are other reports that Cygnus X-3 is *not* a source of cosmic rays [2, 29, 30, 1, 31, 32]. Owing to the contentious political climate surrounding this astronomical object, I choose to neither confirm nor deny that this is a source of astrophysical particles.

could mean either that the source is nearby, which runs counter to our understanding of a uniform cosmic ray sky, or that this is the signal from some exotic stable, neutral particle. Finding a source could help to unravel these mysteries. In addition to interest in their own right, the study of cosmic rays and neutrinos produced by Gamma-Ray Bursts could add greatly to the understanding of these mysterious objects.

1.2 The MINOS Experiment

The Main Injector Neutrino Oscillation Search (MINOS) is a long-baseline neutrino oscillation experiment. It consists of three major components: A muon neutrino (ν_μ) beam, Neutrinos at the Main Injector (NuMI), provided by the Main Injector at Fermi National Accelerator Laboratory in Batavia, IL, the Near Detector about 1 km from the neutrino beam target, to detect the initial neutrino flux; and the Far Detector in Soudan, MN, to observe the final neutrino flux. The 735 km journey through Wisconsin, the western tip of Lake Superior, and the Iron Range of northern Minnesota, will give the muon neutrinos the opportunity to oscillate to one of the other types of neutrino, electron or tau. The ν_μ flux (number per unit time over the entire beam) at the Far Detector is predicted to be about half of that seen at the Near Detector, and a clearer image of neutrino oscillations will be produced. The aforementioned neutrino beam began operation in January, 2005, while the Far Detector was already running with both supermodules in operation by July, 2003, and the collaborators, in an effort to be good stewards of the $60 million taxpayers invested in their dream, did not let their detector lie idle. With its flat rock overburden, half-mile of rock shielding, and nearly six kiloton total mass, the MINOS Far Detector is conveniently situated to double as a muon telescope and atmospheric neutrino observatory. Studies of cosmic ray muons, while interesting in their own and the basis of the following analyses, provide useful calibration of the detector, a process to refine calibration constants, and an opportunity for the highly skilled technicians working full time on site to streamline maintenance and repair procedures. Atmospheric neutrinos provide a source of neutrinos with which studies of neutrino oscillations can be performed, a perfect complement to the neutrinos that originate in the beam. The MINOS collaboration is an international effort, with major funding coming from the U.S. Department of Energy, the U.S. National Science Foundation, Great Britain's Science and Technology Facilities Council, and the State and University of Minnesota. MINOS institutions cover five countries over
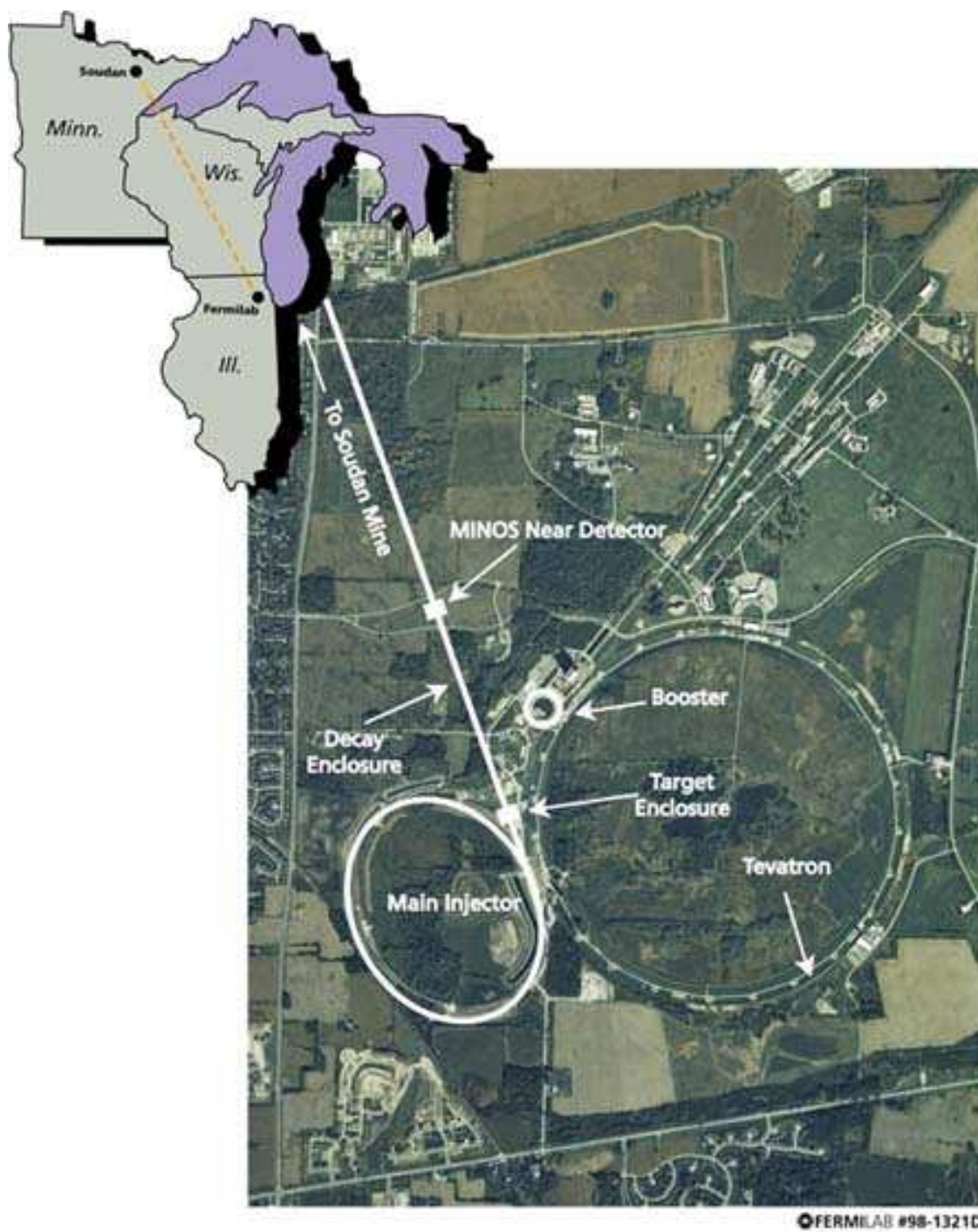
Figure 1.1: The path of the neutrino beam from Batavia, IL; to Soudan, MN, by way of Wisconsin. Also, the Main Injector and Tevatron on the Fermilab campus are shown in an aerial photograph.
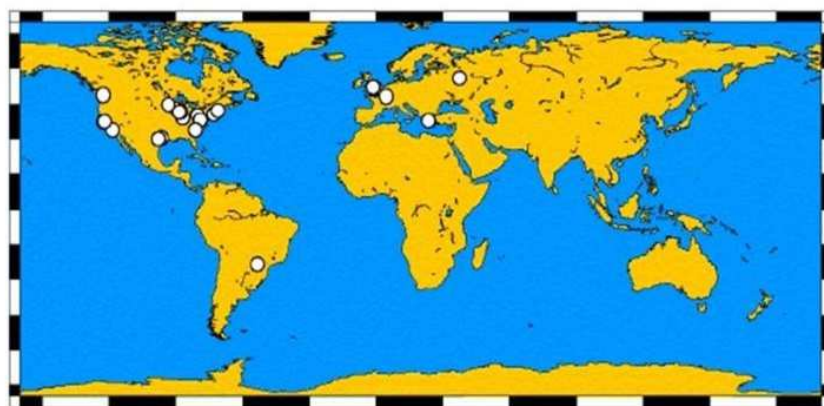
Figure 1.2: The far reaching, diverse representation of the MINOS collaboration.

three continents, and has representation in both hemispheres.

1.3 Physics Beyond the Design with the MINOS Far Detector

Terrestrial detections of cosmic rays are indirect in nature. That is to say that the primary cosmic ray itself is not detected, but rather the products that are created by the cosmic ray's interaction with particles in the atmosphere creating extensive air showers, which are seen as energy deposition in a detector. There are two classes of cosmic ray interactions: hadronic and electromagnetic. Electromagnetic interactions produce electrons, positrons and photons, while hadronic interactions tend to produce pions and kaons which decay to muons. Both gamma rays and cosmic rays can produce an electromagnetic shower, but only cosmic rays will interact hadronically, and this can be seen in the detection of muons. While electromagnetic showers dissipate upon reaching the earth, muons can penetrate kilometers of rock before expending all of their energy.

MINOS has a unique place in the discussion of a cosmic ray source. While it is not designed for the study of cosmic rays (see Ch. 3 on page 36), it is optimized for muon detection. The shadow of the moon has been observed with a degree of precision, so the pointing capacity of the detector has been determined (see Ch. 7 on page 128). Additionally, it has been running for nearly five years, which has allowed the collection of sufficient muons to observe seasonal variations in the muon flux (Ch. 5 on page 78), observe the cosmic ray shadow of the sun and the moon (Ch. 7 on page 128) and make a statement on the topic of astrophysical cosmic ray sources (Ch. 8 on page 149). It possesses a magnetic field that will allow charge sign determination, a first for an underground detector. This makes a direct observation CPT violation in the leptonic sector possible, and it also allows a glimpse into the possibility of a μ^+ source having different properties than a μ^- source.

1.4 Personal Contributions

Graduate students working on an experiment expect to spend time analyzing data, but they do not always have a hand in construction. I was fortunate enough to begin working on MINOS as the Near Detector construction was about to commence. I spent the summer of 2004 at Fermilab, assisting in the assembly of the Near Detector hardware and the initial calibration of the detector. Much of the time was spent with my hands on the detector, attaching optical cables to the detector

plane (Ch. 3 on page 36) that had previously been set in place. Once the scintillator module cables (Sec. 3.2 on page 38) and light injection fibers (Sec. 3.5 on page 49) were in place, the plane was scanned for light leaks before it was buried by the next plane. I had a hand in writing software to analyze the photomultiplier tube (Sec. 3.4 on page 45) output to see that the readout was up to specification. In addition to these hardware activities, I wrote a true cosmic ray airshower *Monte Carlo* (Sec. 4.3.2 on page 59). This is an upgrade from the underground parameterization that has been used, because it included multiple muons and information about the cosmic ray primary and meson secondaries.

Chapter 2

Astroparticle Phenomenology

Primary cosmic rays are energetic particles of extraterrestrial origin that interact with atoms in the upper atmosphere to produce showers of mesons (predominantly π and K). These mesons either interact again and again or decay into electrons, neutrinos and the long lived, penetrating muons that are the cosmic ray signal in the MINOS Far Detector. The primaries can be as light as an electron (though cosmic electrons are not seen by MINOS because they cannot penetrate the rock overburden), as heavy as a uranium nucleus [42] (though most cosmic rays are protons) and can have energies as high as 10^{20} eV! (While at approximately 10 J this is many orders of magnitude smaller than common plastic explosives, let alone an atomic bomb, consider a single atom, weighing at most 10^{-25} kg, in possession of that much energy. This is the same as the amount of energy stored in a professionally served tennis ball! It staggers the imagination.) It is not possible to trace a cosmic ray back to its source the way one traces photons back to a star since cosmic rays are charged particles moving through a non-uniform galactic magnetic field. Neutral particles do point back to their origin, but offer their own set of observational difficulties. Neutrons have a very short lifetime, a 1 GeV neutron will only travel 1.8 AU (Astronomical Unit, the distance from the Sun to the Earth, 1.5×10^9 km) before it decays. Most acceleration mechanisms require far more than 10 minutes to accelerate particles to ultra-relativistic energies ($v \sim c = 3 \times 10^5$ km/s, the speed of light in vacuum). Neutrinos are also neutral and very long lived, but they interact very infrequently. It takes a light-year (the amount of distance light travels in a year, 9.5×10^{12} km) of lead to reliably stop one neutrino! Despite such a low interaction probability, the incredibly

high flux that could be produced by astronomical objects (about 10^{10} neutrinos from nuclear reactions on the sun pass through a thumbnail every second) makes their detection possible by a large, patient detector.

2.1 Cosmic Rays

Little is known about Ultra-High Energy cosmic ray production, as no source has yet been found. Cosmic rays are predominantly ionized hydrogen (protons), since hydrogen makes up the majority of the visible matter in the universe as a consequence of the big bang. Helium, carbon and oxygen are the end result of nuclear fusion processes in many stars, and they compose another large fraction of the observed cosmic rays. Iron is the most massive element that can be created in stellar fusion processes and thus a major contribution to the composition of cosmic rays. Cosmic rays of intermediate mass elements are also seen, but in far smaller abundance, as a result of stellar evolution and stellar deaths. Main sequence stars with masses up to $7M_\odot$ (one solar mass, $M_\odot = 1.99 \times 10^{33}$ g) will never have core temperatures high enough to continue the fusion chain. As the temperature of their core rises it contracts and evolves into a white dwarf, which accelerates and ejects its outer shell, creating winds of various elements. Stars up to $0.5M_\odot$ create helium winds, $0.5 - 5M_\odot$ create carbon winds, and $0.5 - 5M_\odot$ create oxygen winds. Stars greater than $7M_\odot$ can attain core temperatures great enough to fuse magnesium into iron, where the fusion chain stops. The core temperature continues to rise, which leads to a gravitational collapse or supernova. This provides the iron content seen in cosmic ray primaries, and nucleosynthesis in supernova also create small quantities of heavier cosmic rays that have been observed. Despite our understanding of stellar nucleosynthesis, the chemical abundances of cosmic rays is inconsistent with the known chemical abundances in the galaxy [43].

The greatest question in cosmic ray physics is whether the particles are accelerated near point objects or by large scale acceleration processes. It is likely that both play an important role. Particles of GeV energies are created in solar flares, and *in situ* spacecraft have measured particles accelerated to MeV energies by the solar wind. These sorts of mechanisms do not provide enough power to accelerate particles to energies above 10^{16} eV, however, which is why this is such an interesting question.

2.1.1 Acceleration

The problem of cosmic ray acceleration consists of two questions: what provides the power to the accelerator, and what is the mechanism by which the cosmic rays are accelerated. There is a lot of speculation and no direct evidence to the first question, and a growing body of literature describing an answer to the second.

While the exact nature of the accelerator's power mechanism is not known, power requirement arguments restrict the possibilities to a few classes of objects. Active Galactic Nuclei (AGN) are some of the most luminous objects in the universe, radiating over many if not all of the electromagnetic spectrum. This luminosity is thought to be caused by the radiation of material falling into a super-massive black hole at the center of the galaxy. A recent result by the Pierre Auger Observatory [44] (see Sec. 2.3.1 on page 28) suggests a correlation between their 27 highest energy cosmic rays and the location of nearby AGN [45, 46]. This does not prove that AGN are cosmic ray progenitors, though it is an interesting result. Gamma Ray Bursts (GRB), short duration outbursts of extremely energetic photons, are thought to originate from hypernovae, the gravitational collapse of an enormous star with an energy one hundred times greater than an average supernova. GRB could provide enough energy to accelerate a particle above 10^{16} eV and will be discussed in detail in Sec. 2.2 on page 25. There are other radio-loud objects (quasars and BL Lacertae objects) as well as topological defects (monopoles, cosmic strings) that could power a cosmic ray accelerator, though these are a bit more exotic [47].

Shock acceleration is a mechanism by which "kinetic energy of moving magnetized plasma (is transferred) to individual charged particles, thereby increasing the energy per particle to many times its original value and achieving the non-thermal energy distribution characteristic of particle acceleration [43]." This "moving magnetized plasma" could be a diffuse gas cloud or a supernova blast wave, and the mechanism was first described by Fermi [48]. There are two kinds of Fermi acceleration, first and second order. They are distinguished by the fact that the amount of energy astrophysical shocks transfer to individual particles is proportional to the velocity of the shock, while the amount of energy diffuse gas clouds transfer to particles is proportional to the square of the velocity of the cloud. In both cases energy is transferred by the collisionless interaction of the particle with irregularities in the magnetic field of the plasma. Interaction with a diffuse gas cloud can be seen in Fig 2.1 on the following page. The interaction of an energetic particle with an astrophysical shock front is shown in Fig 2.2 on page 14.
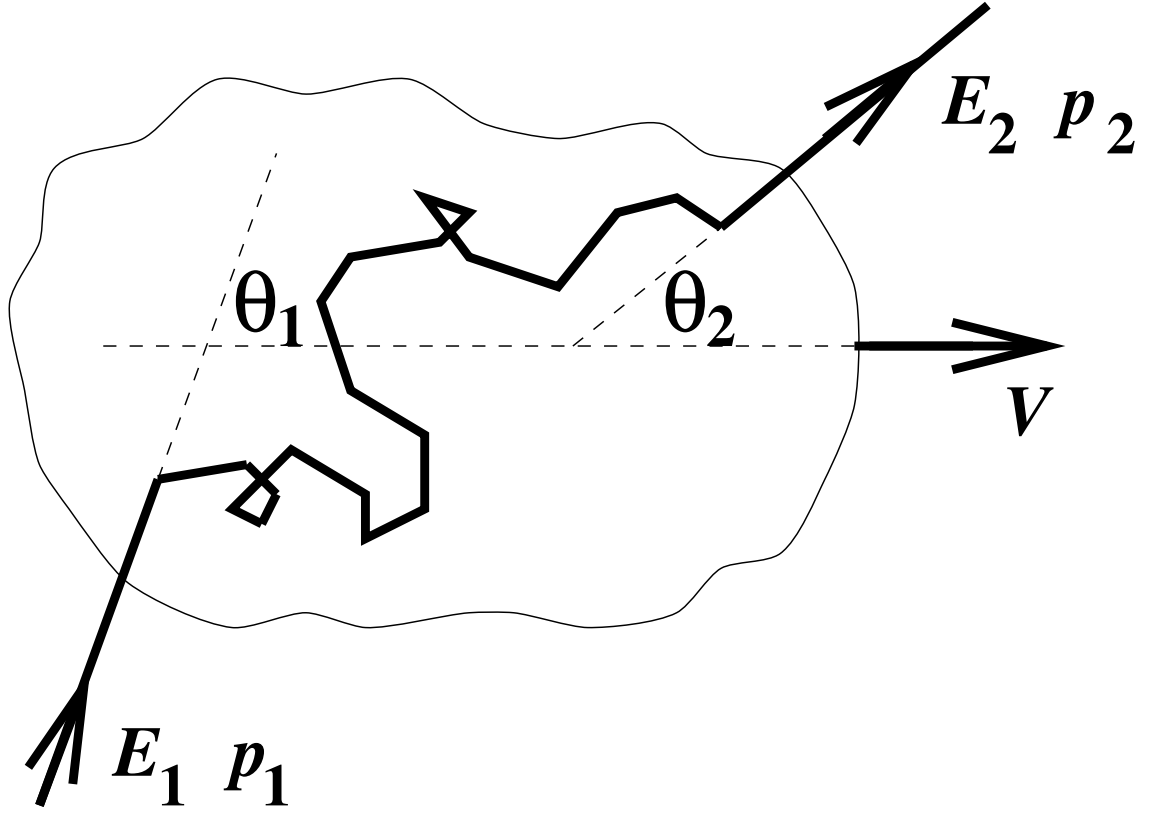
Figure 2.1: The interaction of a cosmic ray with the magnetic irregularities of an ionized gas cloud, moving with velocity V. This figure was taken from [47].

Second-order shock acceleration was Fermi's original theory [48]. Relative to the moving cloud, there is no change in energy because the interaction between the particle and the cloud is collisionless (elastic) and the cloud is much more massive than the particle. The interaction of the cosmic ray with irregularities in the cloud causes random changes in the direction in which the particle is moving. The particle takes a random walk path through the cloud, and once the particle has gained sufficient energy to emerge from the cloud, its original direction of motion is lost. One entry and exit from a cloud is referred to as an encounter, and the particle experiences a net energy gain. The overall amount of energy an ultrarelativistic particle gains in the encounter
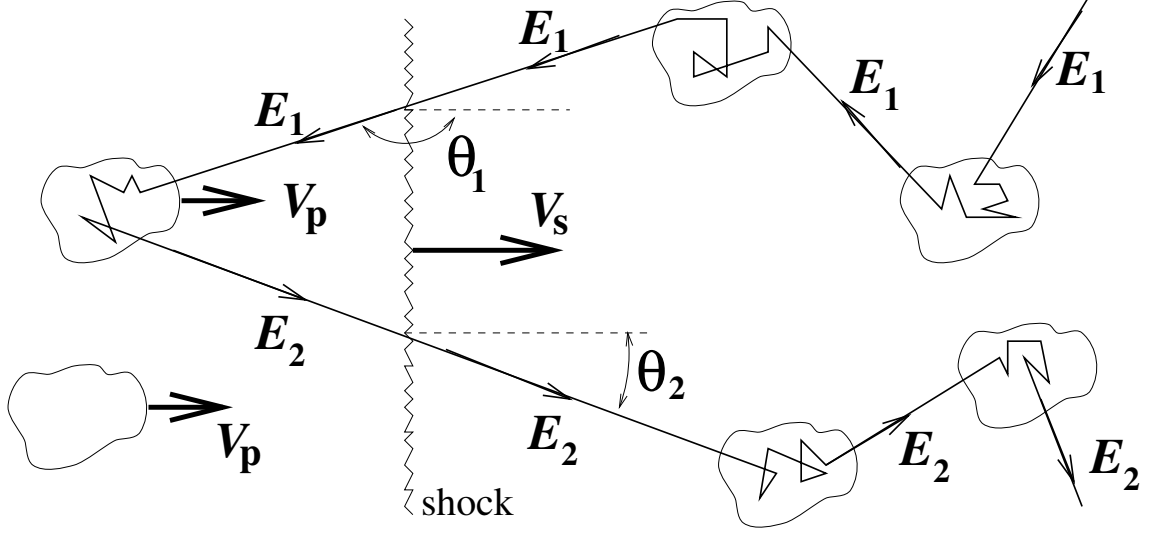
Figure 2.2: The interaction of a cosmic ray with the magnetic irregularities of an astrophysical shock front, moving with velocity V_S. This figure was taken from [47].

can be written [47]:

$$\frac{\langle \Delta E \rangle}{E} = \frac{1 + \beta^2/3}{1 - \beta^2} \simeq \frac{4}{3}\beta^2, \tag{2.1}$$

where $\beta \equiv V/c$, V is the velocity of the plasma ($V \sim 15\,\mathrm{km/s}$ for interstellar gas clouds) and c is the speed of light. This expression only holds for non-relativistic cloud velocities ($v_p \ll c$). Since the expression is of second order in β, in the case where β is very small, the amount of energy transferred per encounter will be much smaller still. If the collision is head on (the particle's direction of motion is opposite the plasma's direction of motion), there is a net increase in the energy of the particle. In the case of an overtaking collision or one where the particle goes out the back side of the cloud, the particle loses energy. This process is called second order not only because the amount of energy transferred during an encounter is proportional to the plasma's velocity, but because the particle can either lose or gain energy during a particular encounter. After a number of encounters, however, there is an overall gain in energy [43].

First order Fermi acceleration is caused by multiple interactions between an energetic particle and a plane shock front. This discussion is taken from [47]. A shock front can be caused by an explosion that sends matter streaming out into space, such as a supernova. The velocity of this material ($\sim 10^4\,\mathrm{km/s}$) is much greater than the speed of sound in the ISM ($\sim 10\,\mathrm{km/s}$), which

forms the shock wave. The shock wave propagates with velocity V_S, and the material of the ISM (along with associated magnetic fields) that piles up in front of the shock wave now moves with velocity V_P. Relative to the shock, gas flows into the shock with velocity V_S (and density ρ_1), while gas flows out of the shock with velocity $u_2 = V_S - V_P$ (density ρ_2).   The velocity

(a) Upstream frame   **(b) Shock frame**
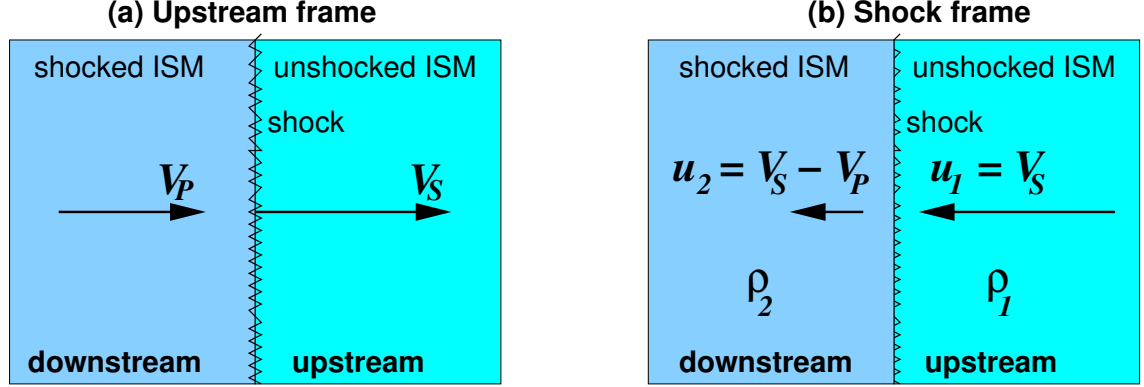
Figure 2.3: An astrophysical shock with velocity V_S moving through the ISM, shown in the upstream frame (a) and the downstream frame (b). This figure was taken from [47].

of the shock depends on the velocity of the ejecta V_P and the ratio of the specific heat of the gas involved, g. The compression ratio can be written:

$$R = \frac{\rho_2}{\rho_1} = \frac{u_1}{u_2} = \frac{g+1}{g-1} \tag{2.2}$$

thus $V_S = Ru_2$, $V_P = (u_1 - u_2) = (R-1)u_2$ and

$$\frac{V_S}{V_P} \simeq \frac{R}{R-1}. \tag{2.3}$$

For strong, non-relativistic shocks, the surrounding gas will be ionized, thus monatomic ($g = 5/3$), and so R=4. [47]

A particle gains energy by crossing the shock front opposite direction of the motion of the shock. The particle interacts with the magnetic field downstream of the shock, and again, a random walk path eventually takes the particle back across the shock. One back and forth path across the shock is referred to as an encounter. The net energy gain in the encounter can be written for ultrarelativistic particles as [47]:

$$\frac{\langle \Delta E \rangle}{E} \simeq \frac{4}{3}\beta \simeq \frac{4}{3}\frac{(R-1)}{R}\frac{V_S}{c}. \tag{2.4}$$

Recalling that the shock front is moving with a non-relativistic velocity ($V_S \ll c$), first order Fermi acceleration can transfer much more energy per encounter than can second order Fermi acceleration. Also, because the shock front is an infinite plane, the only particle encounters are head on, so the particle always experiences a net gain in energy. Protheroe and Clay [47] show that for first order Fermi acceleration, the cosmic ray spectrum is:

$$\frac{dN}{dE} \propto E^{-\gamma} \tag{2.5}$$

where the spectral index, γ, is given by

$$\gamma = \left(1 - \frac{\ln\left[1 - \text{Prob.(escape)}\right]}{\ln\left(1 + \Delta E/E\right)} \right) \simeq \frac{R+2}{R-1}. \tag{2.6}$$

Thus, for a strong shock of R=4, the expected energy spectrum is E^{-2}.

Experimental evidence for non-thermal (synchrotron) x-ray emission around SNR 1006 suggests shock acceleration of cosmic ray electrons [49]. Evidence for the shock acceleration of protons has been shown in [50], which is strong evidence that shocks accelerate the bulk of cosmic rays, with energies up to 10^{16} eV.

2.1.2 Propagation

For the bulk of cosmic rays, most of which originate within the Milky Way, acceleration and propagation are nearly indistinguishable processes that occur continuously. Since boron is not an end result of stellar evolution, it is unlikely that cosmic rays composed of boron were created by a cosmic ray accelerator. Rather, boron is a likely spallation product of carbon interacting with the ISM, which has about 10^{-3} g/cm^2 of matter through the disk of the galaxy. The measured boron to carbon ratio decreases with energy, which suggests that higher energy primaries spend less time in the galactic disk. The ratio of boron to carbon at 1 GeV suggests that cosmic rays traverse $5 - 10$ g/cm^2 equivalent of hydrogen between production and detection [43].

The Milky Way Galaxy has a net magnetic field of approximately 3 micro-gauss [43]. The interaction of particles with electromagnetic fields is described by the Lorentz force equation [51]:

$$\frac{d\overrightarrow{p}}{dt} = \frac{e}{c}\left[\overrightarrow{E} + \overrightarrow{v} \times \overrightarrow{B}\right]. \tag{2.7}$$

For the case of relativistic particles ($v \sim c$), the factor $\gamma_{sr} \equiv \frac{1}{\sqrt{1+v^2/c^2}}$ is wrapped up in the momentum of the particle,

$$\overrightarrow{p} = \gamma_{sr} m \overrightarrow{v}. \tag{2.8}$$

Since energy is constant in time, γ_{sr} and the magnitude of the velocity are also constant. It is shown in [51] that in the absence of an electric field (as is the case of charged particles in the galaxy), Eq. 2.7 on the facing page can be rewritten as:

$$p_\perp c = aBe, \tag{2.9}$$

where a is the gyroradius and e is the charge of the particle. The radius of the galaxy is approximately 25 kpc [52] (kiloparsecs, 3.26×10^3 light years (ly) or 3.086×10^{19} m), and the galactic magnetic field is about $3\,\mu G$. This means that any proton with energy of $\sim 6 \times 10^{19}$ eV has a gyroradius greater than the radius of the galaxy, and such a particle could be of extragalactic origin. For ultra high energy cosmic rays with $E_0 > 4 \times 10^{19}$ eV, total deflection by the galactic magnetic field is about $4 - 6°$; with $E_0 > 10^{20}$ eV, deflection is only $1 - 2°$ [53]. With curvature this small, it would not be hard to resolve a source given direction and distance. It's worth noting that at least one such cosmic ray has been observed by the Fly's Eye group in Utah [54], and no likely source was observed along its path of propagation [55].

The relative emptiness of the galaxy, which leaves cosmic rays free to arc gracefully in the galactic magnetic field, is punctuated by numerous gas clouds with densities thousands of times greater than the ISM, on scales of 1 to 10 pc [43]. These are probable sites for acceleration via the Fermi mechanism described in Sec. 2.1.1 on page 12. An average particle will reside in the galactic disk for about 10^7 years until it could have obtained sufficient energy to escape the galactic magnetic field [43]. This has lead to two similar models of cosmic ray propagation. The leaky box model proposes that a particle continues to acquire energy by interacting with gas clouds and irregularities in the galactic magnetic field until it escapes the net magnetic field of the galaxy. This model considers diffusion to be constant, which results in an isotropic distribution of cosmic rays in the galaxy. This model predicts a source spectrum

$$\frac{dN}{dE} \propto E^{-\gamma}, \tag{2.10}$$

with $\gamma \simeq 2.1$ [43]. The nested leaky box model proposes that there are regions near sources that where particles diffuse for a short time, such as a supernova in a dense cloud. An observer inside a source region would measure the same spectral index as for the simple leaky box model, because of energy dependent loss of particles. An observer on earth, outside the source region, would observe a source spectrum of index $\gamma \simeq 2.7$.

2.1.3 Air Showers

When cosmic rays interact with the upper atmosphere, a chain reaction is induced that sends a shower of particles raining down toward the surface of the earth. The primary products of these hadronic showers are π and K mesons, which interact with atmospheric molecules to produce more pions and kaons, as well as electrons, positrons and photons. This effect is multiplied many times in a fraction of a second, until the energetic shrapnel of this hadronic explosion is absorbed by the ground. Detailed study of cosmic ray primaries is possible as a result of these aptly named extensive air showers (EAS), which can cover square kilometers of area. The flux of high energy cosmic rays is low, and were the primary particle to pass through the atmosphere unnoticed, its footprint would be nearly infinitesimal relative to the area of an EAS; detectors would be searching for the figurative needle in the haystack. (This is one of the reasons that pinning down a neutrino point source has been so difficult. Despite their large terrestrial flux, a neutrino is stealthy and only interacts weakly, so one needs to be directly in its path to even have a chance of detection.) The frequency of interactions increases rapidly with the change in density of the propagation medium as a particle travels from air to land, and particles that interact as readily as pions and kaons will deposit all of their remaining energy in the rock and water on the surface of the earth. Along with hadronic showers come electromagnetic showers in the upper atmosphere. These are given birth by ultra high energy gamma rays incident on the atmosphere producing cascades of electrons and photons. The end result that is seen by surface detectors is similar despite the divergent nature of their origin.

Both pions and kaons are extremely short lived, and were they to not interact on their descent through the atmosphere to produce an EAS, they would decay within two hundred microseconds [9]. The most prevalent decay channels and branching ratios are [57]

$$
\begin{aligned}
\pi^{\pm} &\rightarrow \mu^{\pm} + \nu_{\mu}(\bar{\nu}_{\mu}) &&(\sim 100\%) \\
\pi^{0} &\rightarrow 2\gamma &&(\sim 98.8\%) \\
K^{\pm} &\rightarrow \mu^{\pm} + \nu_{\mu}(\bar{\nu}_{\mu}) &&(\sim 63.5\%)
\end{aligned}
$$

where γ here refers to a photon, rather than the spectral index as it has been used before. Muon decay is a prominent source of neutrinos. At low energies (or after a very long amount of time), muons will decay as

$$\mu^{\pm} \rightarrow e^{\pm} + \nu_{e}(\bar{\nu}_{e}) + \bar{\nu}_{e}(\nu_{e}). \tag{2.11}$$
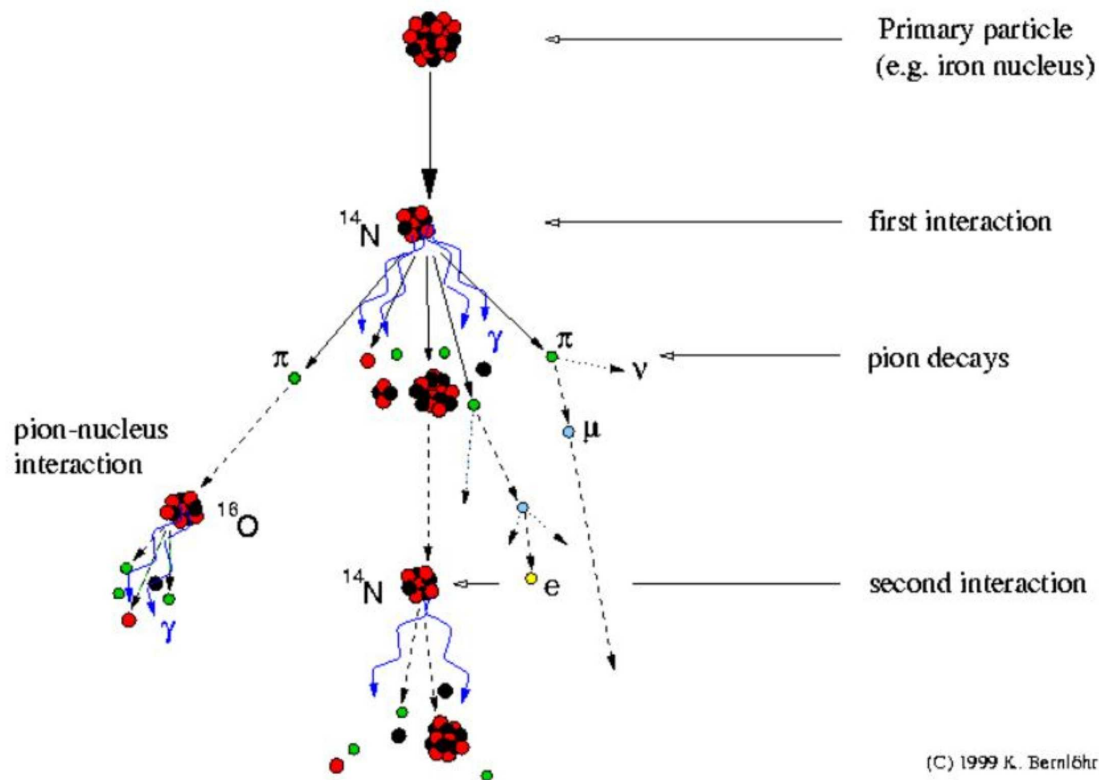
Figure 2.4: A diagram of an Extensive Air Shower showing all of the possible components: electromagnetic, hadronic and muonic, as well as neutrinos [56].

At high energies, where $E_\nu \gg \epsilon_\mu \simeq 1\,\mathrm{GeV}$, however, muon decay is not the dominate mode of neutrino production. The primary source for neutrinos is the semileptonic, three body decay of a kaon to a muon, electron, and electron neutrino [57].

The muons produced in the decay of pions and kaons are of great interest. Unlike the other particles produced in a hadronic shower, muons do not deposit their energy in the atmosphere as they rarely interact with molecules, and they are 40,000 times less likely than electrons to produce the photons necessary for an EAS [9]. Only gradually will a muon transfer some of its energy to the electrons in an atmospheric molecule, allowing it to retain most of its original high energy at the ground. This means that muons will readily penetrate the earth, where they will deposit more of their energy per distance as a result of the greater probability of interactions with electrons in the rock atoms. Still, high energy muons can travel thousands of meters in the earth, giving

rise to a nearly background-free way to study high energy cosmic rays; with an underground detector. Almost all of the muons that are seen on earth are of cosmic origin [57] (originate from the hadronic interaction of cosmic ray primaries). This is a very important note as a detector has no knowledge of the origin of a particle. The detection of muons is therefore a possible channel to understanding cosmic rays.

2.1.4 Energy Spectrum

The flux of cosmic rays on the earth's surface is a function of energy, and the higher the particle energy, the less frequent the appearance. This is a consequence of the power law energy spectrum. A particle with energy of the order 10^{20} eV has over a million times the energy of the most energetic protons sent through Fermilab's Tevatron, accelerating particles to energies just below 1 TeV. It is not surprising, then, that cosmic rays *were* the high energy particles that HEP physicists studied, before they figured out how to use electromagnets to accelerate particles to extreme energies. While the expected flux of 10 GeV cosmic rays on the surface of the earth is about $1 \, \mathrm{particle/cm^2/s}$, the appearance of 10^{20} eV cosmic rays is about 1 particle per century per kilometer squared! [9] Needless to say, a large detector or a patient, long lived scientist is required to make any significant study of such particles. Energies this high do not come from well-understood particle acceleration means; there is no galactic synchrotron shooting particles out at random with high energies. This is an area of Cosmic Ray Physics that is not yet well understood, and one of the motivations for such study.

There is an upper energy threshold for cosmic ray transmission through the galaxy. The Greisen-Zatsepin-Kuz'min (GZK) [39, 40] cutoff is the limit where the cosmic rays actually interact with the relic radiation from the Big Bang, the Cosmic Microwave Background radiation (CMB). Though space is generally transparent to cosmic rays, particles at the maximum of the energy spectrum can scatter the CMB photons and lose energy, seemingly disappearing. Empty space becomes opaque to the highest energy particles. Despite $E_{\mathrm{GZK}} \sim 5 \times 10^{19}$ eV, there have been reports of particles with energy greater than this cutoff. Possible explanations are that they are coming from nearby and haven't yet been annihilated by the CMB, or that there are other mechanisms for their propagation and acceleration through the galaxy. If the particles are coming from a nearby source, such an energetic source should be observable in other wavelengths. So far, no such source has come to light.

2.1.5   Muon Intensity Underground

The intensity of muons underground is directly related to the production of mesons in the upper atmosphere by hadronic interactions between cosmic rays and the nuclei of air molecules. It is assumed that meson production falls off exponentially as e^{-X/Λ_N} where Λ_N is the absorption mean free path of the meson producing cosmic rays and X is the slant depth of atmospheric material traversed. It is also assumed that the mesons retain the same direction as their progenitors, that the cosmic ray sky is isotropic in solid angle at the top of the atmosphere, and ionization is neglected. These assumptions are particularly valid for the large energies of the mesons that produce muons seen in the MINOS Far Detector. In this approximation, Λ_N is constant. Two meson absorption processes will be considered: further hadronic interactions, dX/Λ_M, where dX is the amount of atmosphere traversed and M is either a π or K meson (charm and heavier meson production doesn't become important until $\sim 10^5$ TeV), and $M \rightarrow \mu\nu_\mu$ decay,

$$dN_M(M \rightarrow \mu\nu_\mu) = \frac{m_M c}{p'} \frac{dX}{\rho c \tau_0} \tag{2.12}$$

where ρ = air density, τ_0 = mean M lifetime (at rest) [59]. For an isothermal, exponentially vanishing atmosphere, H(T) = RT/Mg, the atmospheric scale height. The density ρ is then related to X by $\rho = X\cos\theta/H(T)$. The constant ϵ_M, the critical energy that separates the atmospheric interaction from meson decay regimes, is:

$$\epsilon_M = \frac{m_M c^2 H(T)}{c\tau_M} \tag{2.13}$$

Since most interactions take place in the first few interaction lengths [43], and to first order $H(T) \approx H_0 = 6.5\,\mathrm{km}$, $\epsilon_\pi = 0.115\,\mathrm{TeV}$, $\epsilon_K = 0.850\,\mathrm{TeV}$. The differential meson intensity as it relates to these processes, $\mathcal{M}(E, X, \cos\theta)$ can be written as a function of X [59, 43]:

$$\frac{d\mathcal{M}}{dX} = \frac{Z_{NM}}{\lambda_N} N_0(E) e^{-X/\Lambda_N} - \mathcal{M}(E, X, \cos\theta) \left[\frac{1}{\Lambda_M} + \frac{\epsilon_M}{EX\cos\theta}\right] \tag{2.14}$$

for relativistic M, and where $N_0(E)$ is the differential M production spectrum which has the form $E_M^{-(\gamma+1)}$, λ_N is the nucleon interaction length, and Z_{NM} is the spectrum-weighted inclusive cross section moment. This differential equation is straightforward to solve using the integrating factor

$$\beta(X) = e^{\int \frac{1}{\Lambda_M} + \frac{\epsilon_M}{EX\cos\theta}}$$

and rewriting 2.14 on the facing page:

$$\frac{d\mathcal{M}}{dX} + \mathcal{M}(E, X, \cos\theta)\beta(X) = \frac{Z_{NM}}{\lambda_N} N_0(E)e^{-X/\Lambda_N}.$$

The solution to this differential equation is

$$\mathcal{M}(E, X, \cos\theta) = \frac{1}{\beta(X)} \int \frac{Z_{NM}}{\lambda_N} N_0(E)e^{-X/\Lambda_N} \beta(X). \tag{2.15}$$

Integrating both sides gives [59, 43]:

$$\begin{aligned}
\mathcal{M}(E, X, \cos\theta) &= \frac{Z_{NM}}{\lambda_N} N_0(E)e^{-X/\Lambda_M} X^{-\epsilon_M/E\cos\theta} \int_0^X X'^{\epsilon_M/E\cos\theta} e^{X'/\Lambda'} dX' \\
&= \frac{Z_{NM}}{\lambda_N} N_0(E)e^{-X/\Lambda_M} X \times \left\{ \frac{1}{\epsilon_M/E\cos\theta + 1} - \frac{X/\Lambda'}{\epsilon_M/E\cos\theta + 2} \right. \\
&\qquad\qquad \left. + \frac{1}{2!}\frac{(X/\Lambda')^2}{\epsilon_M/E\cos\theta + 3} - ... \right\},
\end{aligned} \tag{2.16}$$

where $1/\Lambda' \equiv 1/\Lambda_N - 1/\Lambda_M$.

Now that an expression for the production and propagation of mesons through the atmosphere has been found, a function describing the production of muons must be found. Muons are the penetrating component of cosmic ray air showers, and at energies of order TeV, have enough energy and live long enough to traverse thousands of meters water equivalent of earth to underground detectors. High energy muons are produced by the decay of short lived mesons in the upper atmosphere, and point back to the parent cosmic ray. Muons are produced from mesons via the two body decay process $M \to \mu\nu$. The rest frame momentum for this decay is $p_r = (1 - m_\mu^2/m_M^2)m_M/2$, since the neutrino has vanishingly small mass. The differential flux per unit cross section is proportional to the differential flux per energy, which can be written:

$$\frac{dn}{dE} = \frac{Bm_M}{2p_r E_L}, \tag{2.17}$$

where B is the branching ratio and E_L is the momentum of the decaying particle in the lab frame. The important muon producing branching ratia are given in Eq. 2.11 on page 18. The muon production spectrum for meson M parents is given by Gaisser [43]:

$$\mathcal{P}_\mu(E, X, \cos\theta) = \sum_{mesons} \int_{E_{min}}^{E_{max}} \frac{dn(E, E')}{dE} \frac{\epsilon_M}{EX\cos\theta} \mathcal{M}(E', X, \cos\theta) dE' \tag{2.18}$$

Inserting Eq. 2.17 on the facing page into the muon production spectrum (Eq. 2.18 on the preceding page), gives:

$$\mathcal{P}_\mu(E, X, \cos\theta) = \frac{\epsilon_M}{X\cos\theta(1 - r_M)} \int_{E_\mu}^{E_\mu/r_M} \frac{dE}{E} \frac{\mathcal{M}(E, X, \cos\theta)}{E} \tag{2.19}$$

where $r_M = m_\mu^2/m_M^2$. Since muons are sampled at one particular depth, the production spectrum needs to be integrated over the whole atmosphere to find the energy spectrum of interest. The differential muon energy spectrum is [43]:

$$\frac{dI_\mu}{dE_\mu} = \int_0^\infty \mathcal{P}_\mu(E, X)dX \simeq A \times E^{-(\gamma+1)} \left(A_{\pi\mu} \frac{1}{1 + 1.1E_\mu\cos\theta/\epsilon_\pi} + 0.635 A_{K\mu} \frac{1}{1 + 1.1E_\mu\cos\theta/\epsilon_K} \right) \tag{2.20}$$

where

$$A_{M\mu} \equiv Z_{NM} \frac{1 - r_M^{\gamma+1}}{(1 - r_M)(\gamma + 1)} \tag{2.21}$$

and $\gamma = 1.7$ is the muon spectral index [60]. Using numeric values from [43], Eq. 2.20 can be written:

$$\frac{dI_\mu}{dE_\mu} \simeq \frac{0.14 \times E^{-(\gamma+1)}}{cm^2 sr GeV} \left(\frac{1}{1 + 1.1E_\mu\cos\theta/\epsilon_\pi} + \frac{\eta}{1 + 1.1E_\mu\cos\theta/\epsilon_K} \right) \tag{2.22}$$

where [61]:

$$\eta \equiv \frac{Z_{NK}}{Z_{N\pi}} \frac{1 - r_\pi}{1 - r_K} \frac{1 - r_K^{\gamma+1}}{1 - r_\pi^{\gamma+1}} = 0.054 \tag{2.23}$$

Ultimately, the integral of the production spectrum is most useful to this particular application, which can be written in the form [59]:

$$I_\mu(E) = \int_{E_{th}}^\infty dE_\mu \frac{dI_\mu}{dE_\mu}. \tag{2.24}$$

This is the total number of muons with energy greater than the threshold required to reach the MINOS Far Detector. The threshold surface energy required for a muon to survive to slant depth $D(\theta, \phi)$ (mwe) (meters water equivalent, the depth of the detector multiplied by the average rock density. This is a measure of the normalized amount of material a particle must encounter to reach the detector from the surface) increases exponentially as a function of D and parameters a(E) and b(E) [43]. Since a and b depend on energy, an iterative procedure is used to find the threshold energy [60]:

$$E_{th} = E_{th}^{n+1}(\theta, \phi) \simeq (E^n + \frac{a}{b})e^{bD(\theta,\phi)} - \frac{a}{b} \tag{2.25}$$

where the energy-dependent parameters $a = 0.00195 + 1.09 \times 10^{-4} \ln(E)$ and $b = 1.381 \times 10^{-6} + 3.96 \times 10^{-6} \ln(E)$ [60], at column depth $D(\theta, \phi)$. At the minimum depth of the Far Detector, 2.1 kmwe, this equation gives $E_{th} = 0.7\,\text{TeV}$. Since this is an investigation of variations in intensity with respect to temperature, it is natural to integrate Eq. 2.24 on the preceding page using the differential muon intensity from Eq. 2.20 on the facing page. A fair approximation, analogous to Ref. [59], can be written:

$$I_\mu \simeq B \times E_{th}^{-\gamma} \left(\frac{1}{\gamma + (\gamma + 1)1.1 E_{th} \cos\theta/\epsilon_\pi} + \frac{0.054}{\gamma + (\gamma + 1)1.1 E_\mu \cos\theta/\epsilon_K} \right). \qquad (2.26)$$

2.1.6 Particle Astronomy

The first indication of a cosmic ray point source by an underground detector came in 1958 [62]. Sekido *et al.* used Geiger Müller counters as a cosmic ray telescope on altitude/azimuth mounts on the surface of the earth. They chose low zenith angles for their observations since the particles would travel through the most atmosphere at those angles, giving a reduction in overall flux. This reduction is almost almost insignificant, however, as discussed in section 1.1 on page 2. They observed an excess of cosmic rays coming from the direction of Orion, but this result was never confirmed. In 1965, Bukata and Standil reported a narrow anisotropy of muons in an underground detector coincident with cosmic ray primaries [63]. Their results were contradicted by Barrows *et al.* with an underground detector in Utah. The Utah detector utilized cylindrical spark counters triggered by underwater photomultiplier tubes that detected Cherenkov radiation. A pointing resolution of 1° was achieved, though because of limited statistics they used 5° by 6° angular bins for their all sky survey. Despite this precision, no anisotropies were reported.

Subsequent reports of a cosmic ray signal came from X-ray binaries Cyg X-3, Her X-1 and 1E2259+59, and were by ultra-high energy air shower arrays. The Kiel [64] result was substantiated by Haverah Park's [65] report of a signal modulation in Cyg X-3, and the CYGNUS collaboration [26] indicated a signal coming from Her X-1. These experiments suggested a source of gamma rays, which would not be too surprising since they are uncharged and therefore unaffected by the galactic magnetic field. The underground experiments Soudan [25, 24] and Nusex [23] also reported a signal coming from Cyg X-3, which suggested it produced long lived particles that interact hadronically and were unaffected by the galactic magnetic field. This result did not come without some disagreement, however. Numerous experiments have searched in vain for this elusive signal. The water Cherenkov detectors IMB [29] in the United States and Kamioka [30]

in Japan did not identify a cosmic ray signal, while the Frejus flash chamber/Geiger tube experiment [31], the radio-chemical chlorine experiment at the Homestake mine [32] and streamer tube/scintillator detector MACRO [1, 2] also reported no signal.

2.2 Gamma Ray Bursts

A gamma ray burst (GRB) is an enormous gamma ray outburst that briefly floods the sky with incredibly energetic photons. The gamma ray sky is relatively quiet, so GRBs outshine all other gamma ray sources combined, including the sun. Until 1997, no other electromagnetic wavelength component was associated with these outbursts, so no astrophysical progenitor could be identified. Thus, the description remained their name, Gamma Ray Burst.

GRBs were first detected in 1967 and originally suspected to be the product of an advanced extraterrestrial civilization [66]. This idea was quickly abandoned. GRBs are now known to be distributed isotropically throughout the sky, which suggests extra-galactic origin. The burst durations range from 10^{-3} s to 10^3 s, with afterglows in x-ray and optical wavelengths that can last up to a day after the initial gamma ray outburst. The afterglow observations are made when a GRB trigger is confirmed from a wide field of view instrument and optical and x-ray telescopes focus on the region of sky where the GRB was seen. Astronomers divide GRBs into two classes, long ($t_b > 2$ s) and short ($t_b < 2$ s) [66]. The study of afterglows has given rise to two models for GRB creation, distinct for each type of GRB, and has also made redshift determination (distance) possible. The class of long GRBs is much more common, therefore well studied. They are likely the outcome of a massive core collapse supernova. The short GRBs could be the result of the collision of massive compact objects, such as binary neutron stars systems or neutron star - black hole systems, that lose angular momentum from gravitational wave emission.

The distance of GRBs from earth is particularly important. Redshifts from z = 0.0085 to z>6 have been measured [67]. Since the universe is expanding, the detection of redshifted light from distant objects is the same as detecting the distance the object is from the detection. The distance is given by [68]:

$$d \simeq \frac{c}{H_0} \frac{(z+1)^2 - 1}{(z+1)^2 + 1} \tag{2.27}$$

and the Hubble Constant $H_0 \simeq 70$ km/s/Mpc [69]. Thus, GRBs range from 24-1400 Mpc. For z>6 GRBs, the actual gamma ray production happened 4.6 billion years ago! That is some of

the oldest light ever detected, thus GRBs may prove an important cosmological tool [66]. These distances are far greater than the size of our galaxy, and are known as cosmological distances, where the curved nature of spacetime could be important.

The great distance of GRBs imply an enormous amount of electromagnetic energy, as much as 10^3 times greater than an average supernova ($\sim 10^{51}$ erg). In addition, the GRB energy is emitted over a few minutes, while supernova energy is emitted over weeks or months. The total *fluence* (emitted energy integrated over the duration of the burst, $\mathrm{erg/cm}^2$) from a GRB is enormous if emitted isotropically. New spectral evidence suggests that the burst may be collimated into a jet, which reduces the energy requirement to about 10^{51} erg, similar to supernova energy output.

The leading model for the observed radiation from a GRB is the relativistic fireball. In this model, a compact source of a few solar masses of matter with radius about 10^7 cm [70] collapses, and the gravitational energy is converted to free energy over milisecond time scales. This energy expands rapidly outward, with a luminosity of about 10^{53} ergs of the free energy emitted in $\sim 20\,\mathrm{MeV}$ neutrinos and gravitational waves. $10^{50} - 10^{52}$ ergs of the energy remain trapped in an electron, gamma ray and baryon fireball. The fireball expands at relativistic or near relativistic speeds, and contains the non-thermal gamma ray energy that is observed. The gamma-ray spectrum is non-thermal, peaks around $100\,\mathrm{keV}$ and constitutes the bulk of the detected energy. Gamma rays above $100\,\mathrm{GeV}$ have also been observed in a few cases. The electromagnetic blast wave preceded by an outburst of neutrinos is similar to what happens in a supernova, with the difference that the energy is released over months, while in the case of a GRB, the energy is released over seconds or minutes [66].

2.2.1   The GRB as an Astroparticle Source

The relativistic fireball that expands rapidly outward from the central engine of the GRB could have luminosity $L \sim 10^{52}\,\mathrm{erg/s}$ and mass loss rate M. The fireball could have a Lorentz factor $\Gamma \sim L/Mc^2$ [70]. This creates an enormous shock wave when it encounters the ISM, which can then Fermi accelerate protons as discussed in Sec. 2.1.1 on page 12. The extremely high Γ suggests that the there is sufficient energy in the fireball to accelerate protons to $10^{20}\,\mathrm{eV}$ [3]. Additionally, the observed spectrum and observed flux of cosmic rays above $10^{20}\,\mathrm{eV}$ is consistent with the prediction of GRB progenation [20].

As the fireball wind expands and cools, protons and neutrons will decouple and then collide.

These inelastic collision produce pions, which decay (Eq. 2.11 on page 18, Eq. 2.11 on page 18) into $\sim 10\,\mathrm{GeV}$ $\nu_\mu(\bar{\nu}_\mu)$ and muons, which decay into $\sim 5\,\mathrm{GeV}$ $\nu_e(\bar{\nu}_e)$ [15]. The neutrons that do not interact with protons will decay into $\sim 100\,\mathrm{MeV}$ $\bar{\nu}_e$.

There is a large flux of protons that are accelerated to 10^{15} eV in the expanding fireball, which leads to pion production when these protons interact with the 10^6 eV photons carrying the bulk of the fireball energy [3]. About half of the proton energy that is lost goes to π^+. These charged pions decay to produce 10^{14} eV neutrinos.

2.3 Recent Experiments

2.3.1 Air Shower Detectors

There are two signals commonly used to directly detect cosmic ray air showers. The interaction of cosmic ray primaries with atmospheric nuclei causes fluorescence in blue and near ultra-violet wavelengths. This fluorescence can be seen by high elevation wide field of view telescopes operating on moonless nights. The energetic particles created by the airshowers can also be collected by detectors arranged on the surface of the Earth over a large area. Coincidences between detectors give indication of an airshower, and the area over which the particles are distributed give an indication of how much energy the parent particle contained.

Akeno Giant Air Shower Array (AGASA)

The Akeno Giant Air Shower Array (AGASA) [71] was a $100\,\mathrm{km}^2$ detector array constructed in Akeno, Japan, 120 km west of Tokyo. AGASA consisted of 111 $2.2\,\mathrm{m}^2$ scintillation detectors and 27 muon detectors of various sizes, spaced about 1 km. Surface arrays are an economical way to create a large area detector, but their energy scale is calibrated against simulations (*Monte Carlo*) at energies many orders of magnitude greater than anything that is measured in a laboratory on Earth. Thus, the energy scale could be incorrect by as much as 30% [44]. The spacing of the detectors and size of the array were chosen to maximize the detection of cosmic rays above 10^{17} eV, the very top of the cosmic ray energy spectrum. Construction began in 1987, and the array was completed in 1992. While a point source was not detected, some indication of a 4% excess of cosmic rays coming from the galactic center [72] and cosmic rays above the GZK cutoff were observed [73].

High Resolution Fly's Eye

The High Resolution Fly's Eye (HiRes) [74] experiment was a fluorescence detector constructed in the United States Army Dugway Proving Grounds in the West Desert of Utah, USA. It was constructed in 1993 and based on the technology of the Fly's Eye fluorescence detector [54] located nearby. The apparatus consists of a number of individual telescopes that are operated as one detector to provide full-sky coverage. Because of atmospheric limitations (daylight, the moon, clouds) the duty cycle of fluorescence detectors is only 10%. There are 22 telescopes with 256 photomultiplier tubes (PMTs) at one site, and 42 telescopes at a second site 12.6 km away, and the apparatus is sensitive to cosmic rays with energy above 10^{18} eV. The two sites can be operated independently or in coincidence (stereo mode). The stereo mode gives a more precise geometric reconstruction. A point source was not detected, but a measurement of the cosmic ray spectrum above 10^{18} eV was made [75], and the anisotropy measurement of AGASA was not confirmed [76], though with weak statistical significance.

Pierre Auger Observatory

The Pierre Auger Observatory [44] is the next generation Ultra High Energy cosmic ray detector, building on the experience of HiRes and AGASA. The observatory is located near Malargüe, Mendoza, Argentina and started operation in January, 2004, while partially constructed. The detector was completed in early 2008. It consists of an array of surface detectors (like AGASA) and a number of fluorescence detectors (like HiRes). The surface array covers an area of $3000\,\mathrm{km}^2$ with surface array of 1600 $10\,\mathrm{m}^2$ water Cherenkov tanks and twenty-four fluorescence detectors (there are four locations, with six detectors each) . An unambiguous point source signal has *not* been found, but a correlation between the arrival position of the highest energy cosmic rays $E > 10^{18}$ eV with the position of active galactic nuclei has been seen [45].

2.3.2 Underground Detectors

There are fifty times fewer muons produced by electromagnetic showers than by hadronic showers of comparable energy [77], and even the highest energy electrons penetrate no more than one meter of earth. The only component of a hadronic shower that will survive to reach an underground detector is the muon, so placing a detector under more than a meter of earth assures the investigator

that the signal being seen is of hadronic origin. Since there are no terrestrial sources of muons, underground detectors interpret downward going muons that pass through the detector as cosmic ray induced. Thus, underground detectors can observe cosmic rays by detecting the muons they produce in atmospheric air showers. Underground detectors are also sensitive to muons induced by neutrino interactions in the detector or in the rock surrounding the detector. There is too much rock underneath a detector for cosmic ray induced muons to penetrates, so any muon detected from such a direction must have been induced by a neutrino.

IceCube

IceCube is the second generation neutrino telescope in Antarctica [78], constructed around the Antarctic Muon and Neutrino Detector Array (AMANDA) near the South Pole. It consists of 80 strings of photomultiplier tubes arranged in a $1\,\text{km}^2$ hexagon. The strings are drilled into the ice and then frozen. They are instrumented at depths from 1,400 km to 2,400 km, which gives total detector volume of $1\,\text{km}^3$. It is sensitive to neutrinos and cosmic ray muons with energies above $10^{11}\,\text{eV}$. Construction began in 2004, and the detector is expected to be completed in early 2010. So far, no indication of a neutrino point source has been found. IceCube will also be sensitive to tau neutrinos, neutrinos induced by cosmic ray annihilation with the CMB (so called "GZK" neutrinos) and possibly dark matter [79]. AMANDA searched for coincidence between neutrinos and gamma-ray bursts and found no signal [5].

Monopole, Astrophysics and Cosmic Ray Observatory (MACRO)

The Monopole, Astrophysics and Cosmic Ray Observatory (MACRO) was located in the underground Laboratori Nazionali del Gran Sasso (LNGS), Abruzzo, Italy [80]. The detector began operation of one supermodule in February, 1989, and the construction of the final configuration was completed in 1995. It was built to search for magnetic monopoles, sources of cosmic rays and other exotic phenomena. It was constructed under a mountain with a minimum depth of 3000 mwe (meters water equivalent) and detected muons with liquid scintillation counters, streamer tubes and track-etch plastics. MACRO was sensitive to muons with energy greater than $1.2 \times 10^{12}\,\text{eV}$ and neutrinos with energy greater than $10^9\,\text{eV}$. The detector operated at the same time as the EAS-Top airshower array, and coincidences between the detectors provided new information about cosmic ray composition for primaries of energy $10^{13}\,\text{eV}$ to $10^{16}\,\text{eV}$. No cosmic ray or neutrino point

sources were discovered, (nor were any magnetic monopoles seen), but MACRO did make measurements of atmospheric neutrino oscillation parameters [81] and put limits on antimatter content in airshowers [82].

Soudan2

Soudan 2 is the second-generation nucleon decay experiment in the Soudan Underground Mine in northern Minnesota, USA [83]. It was a 1 kton iron tracking calorimeter that used drift tubes in a hexagonal array. Data taking began in April, 1989, when one quarter of the detector had been constructed; the detector reached its final configuration in 1993. The detector is located at a depth of 2090 mwe under a flat overburden, and observed muons with minimum energy 7×10^{11} eV and neutrinos with energy greater than 10^8 eV. No cosmic ray or neutrino source was found (nor was nucleon decay discovered), but neutrino oscillation parameters were measured [84] and the cosmic ray composition was measured for primaries of energy 10^{13} eV to 10^{16} eV [85].

Super-Kamiokande

Super-Kamiokande is the second generation ring imaging water Cherenkov nucleon decay detector in Kamioka Mozumi mine in Japan [86]. It consists of 50 kton of ultra-purified water in stainless steel tank that is divided into an inner detector, viewed by 11200 PMTs, and an outer detector, viewed by 1800 PMTs, that acts as an active veto. Construction was completed in 1996, and the detector was then fully operational. The detector is located in a mountain under 2700 mwe of rock and observes both electron-type and muon-type neutrinos with energy greater than 10^7 eV. No neutrino source has yet been found (nor has nucleon decay been seen), but neutrino oscillations were confirmed [87]. A search for coincidence between neutrinos and gamma-ray bursts yielded a null result [88].

2.3.3 Next Generation Ultra-High Energy Neutrino Detectors

The current limits placed on astrophysical neutrino sources suggests that detectors must grow by orders of magnitude. If IceCube, with a cubic kilometer volume, sees nothing, it will be difficult to find a way to make a larger volume water detector. Already, pioneers in the field are exploring new technology. The phenomenon of Cherenkov radiation has many remarkable consequences.

In addition to the emission of ultra violet light, radio and acoustic signals are also caused by an energetic particle traveling faster than the speed that light travels through the medium. This is known as the Askaryan effect, confirmed experimentally in 2000 [89]. A number of experiments are exploiting this effect to detect the highest energy neutrinos.

The Radio Ice Cherenkov Experiment (RICE) consists of radio antennae incorporated into the AMANDA PMT strings [90]. The Askaryan Under-ice Radio Array (AURA) is the next generation RICE detector, currently being deployed with the IceCube PMT strings [91]. Both detectors sample frequencies in the range 200 MHz to 1 GHz, and AURA builds on the experience of RICE. No results have been published for either experiment. The coherent radio impulse that is a consequence of the Askaryan effect has an acoustic counterpart as well, which boasts an even narrower peak than the radio impulse. This has given rise to the prototype South Pole Acoustic Test Setup (SPATS), which consists of acoustic detectors deployed with some of the IceCube strings [92]. Thus, many of the IceCube strings have three detectors on board: the IceCube optical modules, AURA radio detectors, and SPATS acoustic detectors. No results have been reported by any of these experiments.

The ANtarctic Impulsive Transient Antenna (ANITA) is an Antarctic balloon experiment with radio payload that detects the coherent radio pulse from ultra-high energy neutrino interactions in the ice [93]. ANITA has completed two flights: ANITA-lite, an 18 day test flight in the austral summer of 2003-2004, and the first ANITA flight, 2006-2007. The final ANITA flight is planned for the austral summer of 2008-2009. No neutrino source has yet been observed, but limits have been placed on the ultra-high energy neutrino flux from the ANITA-lite flight [94].

2.3.4 Gamma-Ray Burst Detectors

Since the first report of gamma-ray bursts in using the Vela satellites in 1973, a number of satellites have been launched for the purpose of detecting and studying these incredibly energetic astronomical objects. The field of ground based gamma-ray astronomy began in 1989 with the Whipple Observatory High Resolution Camera observation of the Crab Nebula. Despite great advances in ground-based gamma ray detection, all detections of gamma-ray bursts have come from satellites with wide field of view telescopes. Ground-based telescopes require a finite amount of time to collect enough light to detect a gamma-ray source and cannot respond quickly enough to a gamma-ray burst trigger, which lasts for a few seconds and could happen anywhere on the sky.

The naming convention for GRBs is to use the date that they were detected, YYMMDD. No one knows what will happen in 2073, when the dates overlap.

Compton Gamma Ray Observatory

At 17 tons, the Compton Gamma Ray Observatory (CGRO) was the heaviest astrophysical payload ever flown when it was launched on April 5, 1991, from the space shuttle Atlantis. Its mission ended on June 4, 2000. CGRO had sensitivity to electromagnetic radiation from 30 keV to 30 GeV via four instruments: Burst And Transient Source Experiment (BATSE), the Oriented Scintillation Spectrometer Experiment (OSSE), the Imaging Compton Telescope (COMPTEL), and the Energetic Gamma Ray Experiment Telescope (EGRET). The BATSE instrument recorded 300 bursts a year with its 4π steradian field of view. The BATSE survey showed an isotropic distribution of GRB throughout the universe, which suggests that they are at cosmological distances [95].

Satellite per Astronomia X

Satellite per Astronomia X (X-Ray Astronomy Satellite, BeppoSAX), was a collaborative Italian-Dutch satellite. It was launched on April 30, 1996, and its mission ended on April 30, 2002 because of rapid orbital decay. It was sensitive to electromagnetic radiation from 0.1 keV to 300 keV with four x-ray telescopes, High Pressure Gas Scintillator Proportional Counter (HPGSPC), Phoswich Detection System (PDS), and Wide Field Camera. The Wide Field Camera had a 0.12 sr field of view. BeppoSAX was able to detect fading x-ray afterglow of GRB, which allowed follow up observations by ground based optical telescopes. These observations allowed for the first measurements of GRB distances, confirming the BATSE survey result that they were indeed at cosmological distances [96].

High Energy Transient Explorer

The High Energy Transient Explorer (HETE-2) is a collaboration between institutions in the USA, France, Japan and Italy, headed by the Center for Space Research at MIT [97]. It was launched on October 9, 2000 on a two year mission, but it continues to observe and filled the gap left by the demise of CGRO and BeppoSAX. The satellite carried three instruments capable of observing photons from 0.1 keV to 300 keV: Soft X-ray Camera (SXC), Wide Field X-ray Monitor (WXM)

and French Gamma-ray Telescope (FREGATE), with 3 sr field of view. All instruments point away from the sun. HETE-2 provided the first unambiguous GRB association with a supernova, GRB 030329 with SN2003dh [98].

Swift

Swift is a collaboration between NASA, the UK and Italy. It was launched on November 20, 2004 from Cape Canaveral (USA) and continues to observe gamma ray bursts [99]. Swift is a multiwavelegth observatory carrying three instruments: the Burst Alert Telescope (BAT; Gamma Ray), the X-ray Telescope (XRT) and the Ultraviolet/Optical Telescope (UVOT). Its name comes from the fast response of the spacecraft to a trigger from the BAT. Within minutes, the trigger location is transmitted to the ground and the spacecraft slews to focus its afterglow observation instruments. It is sensitive to photons from 0.1 keV to 300 keV, as well as optical and ultra-violet (170-650 nm). The BAT instrument has a 1.4 sr field of view, which allows it to catalog about 100 GRBs per year. Because of its rapid response, Swift was the first observatory able to record the afterglows of short GRBs and also detected the first astronomical object with redshift z>6 [100].

Gamma-ray Large Area Space Telescope

The Gamma-ray Large Area Space Telescope (GLAST) was launched on on June 11, 2008, and is billed as the next generation CGRO [101]. The satellite consists of two instruments, the Large Area Telescope (LAT) and GLAST Burst monitor (GBM) give it a greater energy range, 1 keV to 300 GeV, comparable field of view, and similar sensitivity to GRB (less than $0.5\,\mathrm{cm}^{-2}\mathrm{s}^{-1}$).

Terrestrial Gamma Ray Detectors

There are a number of terrestrial gamma ray telescopes, including the High Energy Stereoscopic System (HESS) in Namibia, Africa [102] , Very Energetic Radiation Imaging Telescope Array System (VERITAS) at the Whipple Observatory in Arizona, USA [103], Major Atmospheric Gamma-ray Imaging Cherenkov (MAGIC) on La Palma in the Canary Islands [104] and Collaboration of Australia and Nippon (Japan) for a GAmma Ray Observatory in the Outback (CANGAROO) in Woomera, Australia [105]. These telescopes build on the method of atmospheric Cherenkov radiation detection pioneered by the Whipple observatory. Since these observatories

must focus the light from the object that they want to observe, they do not usually detect GRBs since it is unlikely that they will be focused on that particular part of the sky where a GRB occurs. In addition, the threshold gamma-ray energy for these telescopes is about 1 TeV, and most GRB energy is emitted around 500 keV. A new experiment, High Altitude Water Cherenkov (HAWC) has been proposed that would observe the entire northern sky continuously [106], building on the technology of the Milagro experiment [107].
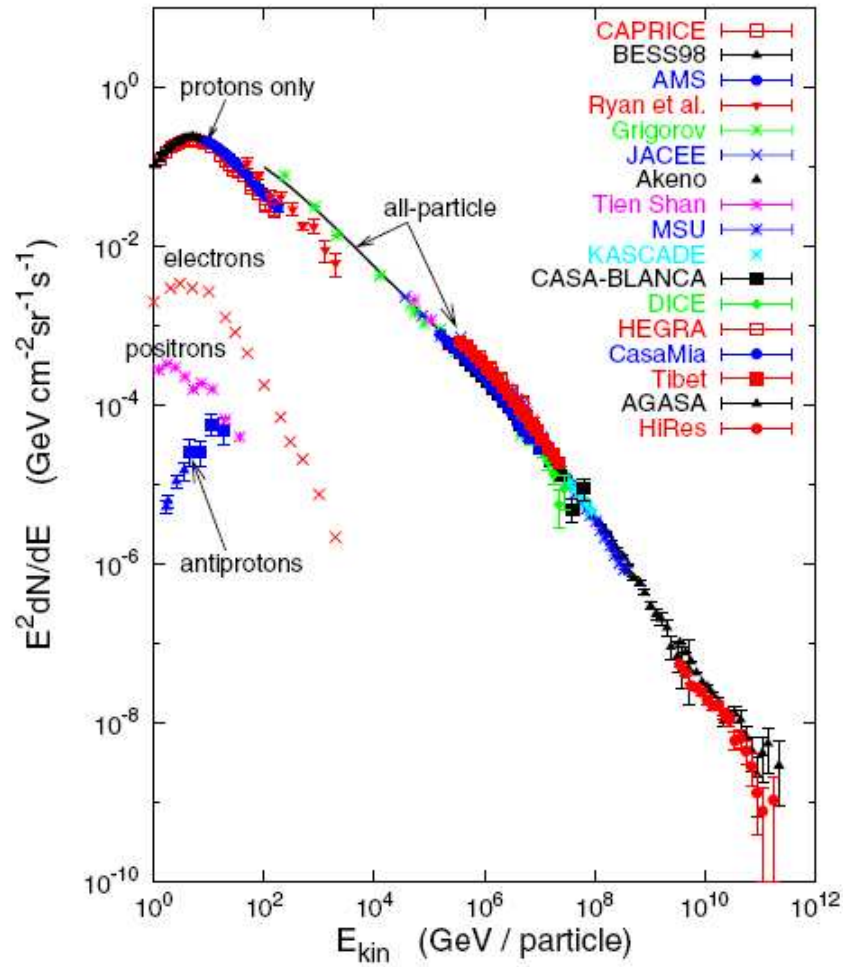
Figure 2.5: The world data for the cosmic ray energy spectrum. This figure is from [58].

Chapter 3

Detector

The MINOS Far Detector is a large scintillator and steel tracking calorimeter situated on the edge of the Superior National Forest in the Soudan Underground Mine State Park, Soudan, MN, USA, $47°$ 49' 13.3" N, $92°$ 14' 28.5" W. It is on the 27th level of the former U. S. Steel Corporation Iron Mine, at a depth of 713 m below the surface. The significant features about the location are the distance from the beam neutrino source, 735 km, and sufficient depth to provide shielding from extra terrestrial radiation. The detector is in a freshly excavated cavern adjacent to the hall that contained the Soudan 2 experiment. The primary purpose of MINOS is the detection of neutrinos from a distant beam, and since the beam spreads as it is transmitted and neutrinos only interact via the weak force, it is a difficult task. A large, well understood detector is necessary to perform such a task, and the MINOS Far Detector is both of these. The major sub-systems of the detector are: steel, active scintillator, magnet and electronics. A neutrino enters the detector where it interacts with the steel and produces a charged particle. This daughter particle then enters the scintillator module and produces photons. These photons are transmitted via a fiber optic cable to a photomultiplier tube (PMT), which turns the small light signal into an electrical signal that is recorded by the Data Acquisition System (DAQ).

3.1 Steel

The detector is composed of octagonal steel planes 2.54 cm thick with a diameter of 8 m, and a 30 cm central bore through which the magnet coil to passes. There is a 5.94 cm gap between

each plane to allow for the thickness of the scintillator modules and an air gap. The total mass of the 486 identical planes is 5.4 kt. The steel planes are oriented vertically and stacked face to face horizontally, like a loaf of bread. They are suspended in the air by an extension (ear) coming off of the octagonal plane structure, like hanging file folders on a rail in a desk drawer. The steel planes are arranged in two distinct groups, called supermodules (SM), with a gap of 1.5 m separating SM1 from SM2. This spacing between supermodules allows for the installation of the magnet coils.
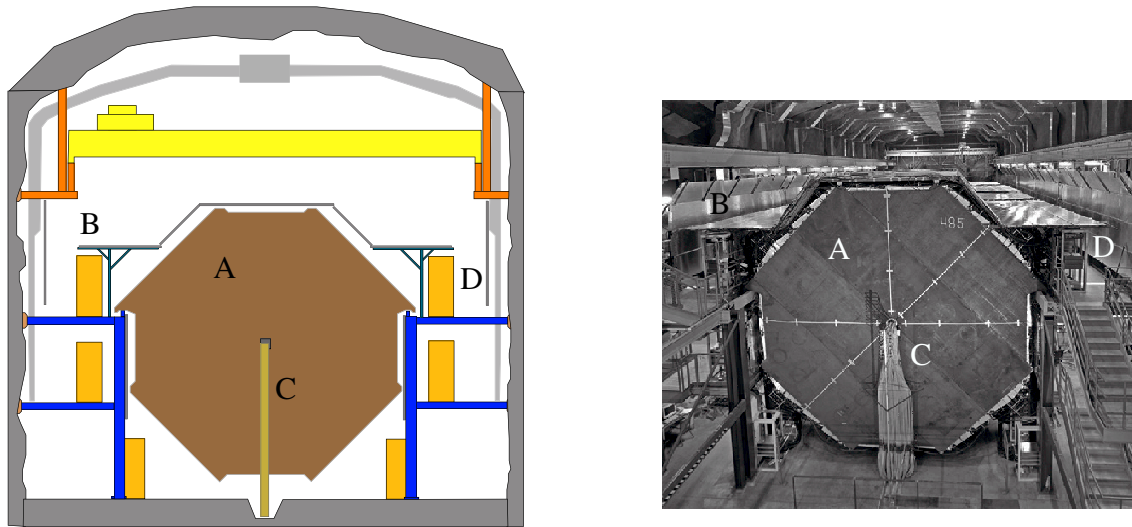
Figure 3.1: The front view of the far detector, showing the octagonal plane structure (A), the veto shield on the top (B), the magnet coils coming out of the center (C), and the electronics rack (D).

Neutrinos are observed indirectly by the detector, and their existence is inferred by a particle production chain, similar in concept but very different in mechanism from the detection of cosmic rays. Quasi-elastic scattering (QES), Deep Inelastic Scattering (DIS), and resonant scattering are the processes by which a neutrino interacts with an iron nucleus to produce daughter particles that are observable by the MINOS detector. The interaction $\nu_\mu + p \rightarrow \mu^- + n$ produces the desired ν_μ detection, and the other common interaction is $\nu_e + p \rightarrow e^- + n$. It is fairly easy to discriminate these events since the neutron and positron deliver their energy to the steel rapidly, while the μ^- of the first interaction produces a long track, depositing less energy per plane than the other particles.

While the steel is largely unnecessary for the detection of cosmic ray muons, the detection of a

neutrino and the structural integrity of the scintillator modules depends on it. Exacting alignment of the planes is necessary in a precision particle physics experiment, and the steel insures that the scintillator modules will not shift or sag in the course of their duty. A ferromagnetic material is required to produce a strong magnetic field that will bend the path of a charged particle to allow charge sign determination. The steel is an integral component of this magnetized detector, unique in its ability to determine the charge sign of sampled particles.

3.2 Active Scintillator

The active detector component is the scintillator, strips of extruded polystyrene 1 cm thick and 4.1 cm wide. The polystyrene is enhanced with the fluors PPO (1%) and POPOP(0.030%) These strips are formed with a center groove to hold the wavelength-shifting (WLS) fiber and are co-extruded with an outer layer of TiO_2 for internal reflectivity [108]. Panels of either 20 or 28 strips are joined to make an array of 192 strips for each octagonal detector plane. The modules are produced in a number of distinct groups for ease of fabrication and detector readout. The scintillating strips were adhered to aluminum covers 0.5 mm thick [109] to complete the module assembly.

As a charged particle traverses the detector modules, it deposits energy in both the steel and the scintillator. The energy that is deposited in the scintillator is re-emitted in the form of UV photons. These photons are internally reflected off the walls of the strip until some of the photons are absorbed by the WLS Y-11 fluor that traverses the strip. The absorption spectrum of the WLS Y-11 is centered on 420 nm (violet), and only overlaps slightly with its emission spectrum centered beyond 470 nm, in the green band of visible light. Shifting the wavelength of the incident light is an effective method to minimize self absorption. The WLS fibers end at the terminus of the scintillator module, where they connect to an array of clear optical fibers to complete the path of the photons from the scintillant to the PMT.

The planes of the detector are organized in a rectangular coordinate system, nominally referred to as U and V. The strips on each plane are arranged at an angle of 45° with the horizontal, the U planes a 90° rotation from the V planes. The choice of (U,V) facilitates connections to both ends of the scintillator strips. This provides a set of mutually orthogonal coordinates with which to measure a particle's location in the detector. The orientation of the orthogonal axis can be seen

MINOS SCINTILLATOR STRIP

UP TO 8m

REFLECTIVE SEAL

TiO2 LOADED POLYSTYRENE CAP

CLEAR POLYSTYRENE
SCINTILLATOR

WLS FIBER

10mm

41mm
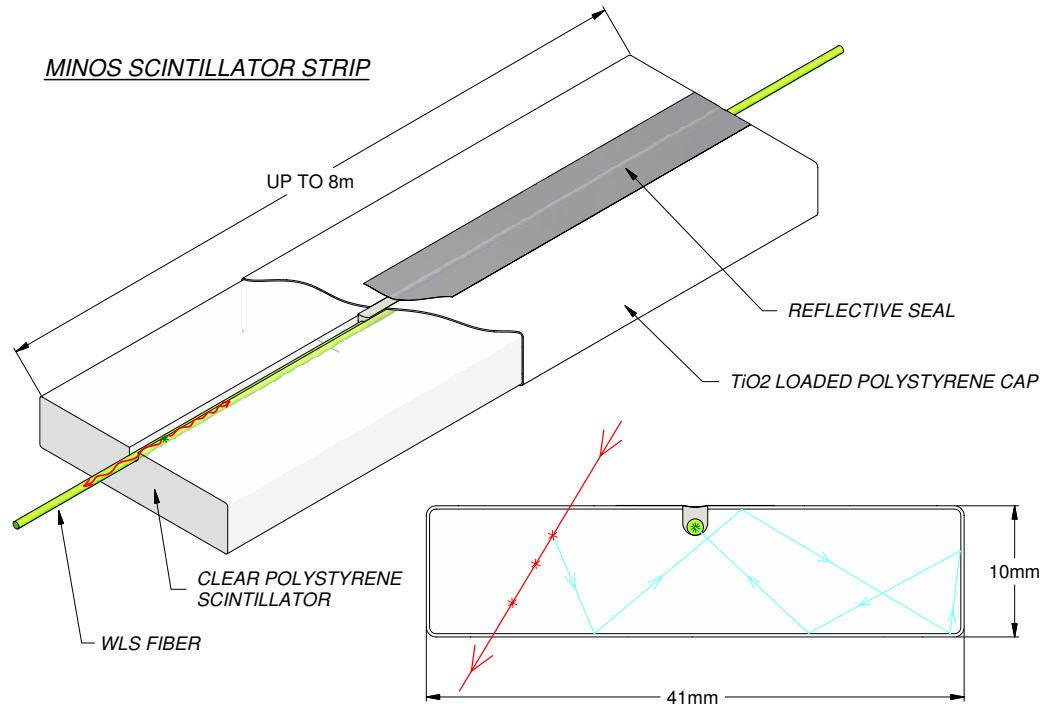
Figure 3.2: Diagram of a scintillator strip.

in figure 3.5 on page 42.   "Vertical" and "horizontal" positions are determined by a particle hit in a combination of two or more planes, at least one U and one V, and depth is found by simply counting how many planes the particle traversed.

3.3   Magnetic Field

MINOS is the first neutrino experiment able to discriminate neutrinos from antineutrinos, and this capacity is derived from the magnetic field. The Far Detector has a toroidal magnetic field produced by a 15,000 A-turns current, generated by an 80 A current run through 192 turns of stranded copper wire housed inside a 25 cm diameter, water-cooled, copper jacket, formed into a coil running the length of each supermodule. The average magnitude of the magnetic field is 1.5 T at a radius of 2 m [110]. The magnetic field began operation in a nominal "field forward"
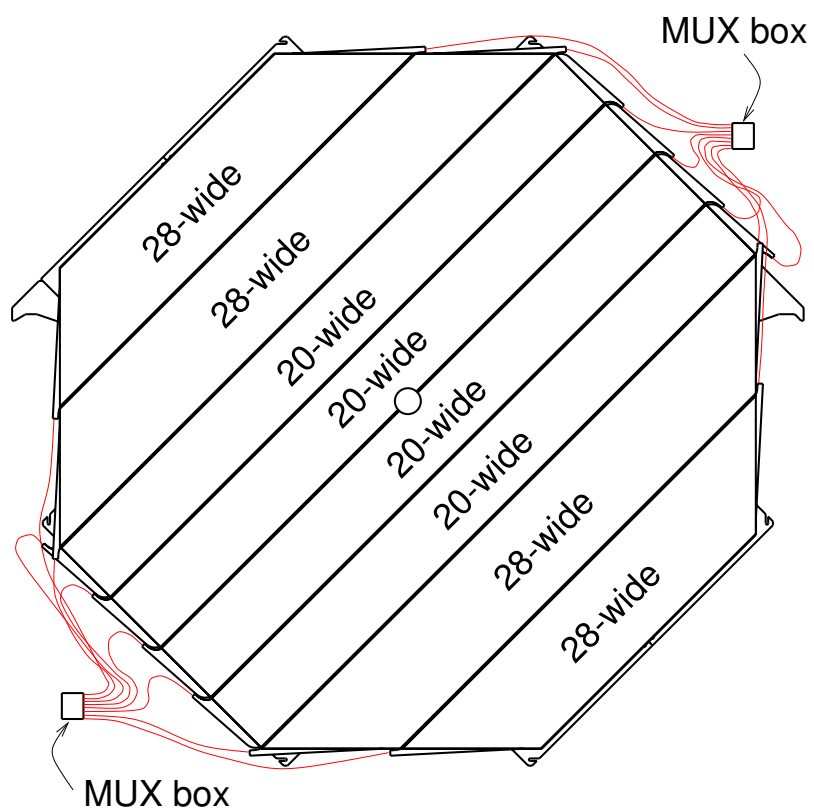
Figure 3.3: A schematic showing the module layout as well as the connections to the MUX boxes, the front end electronics component that contains the PMT assembly.
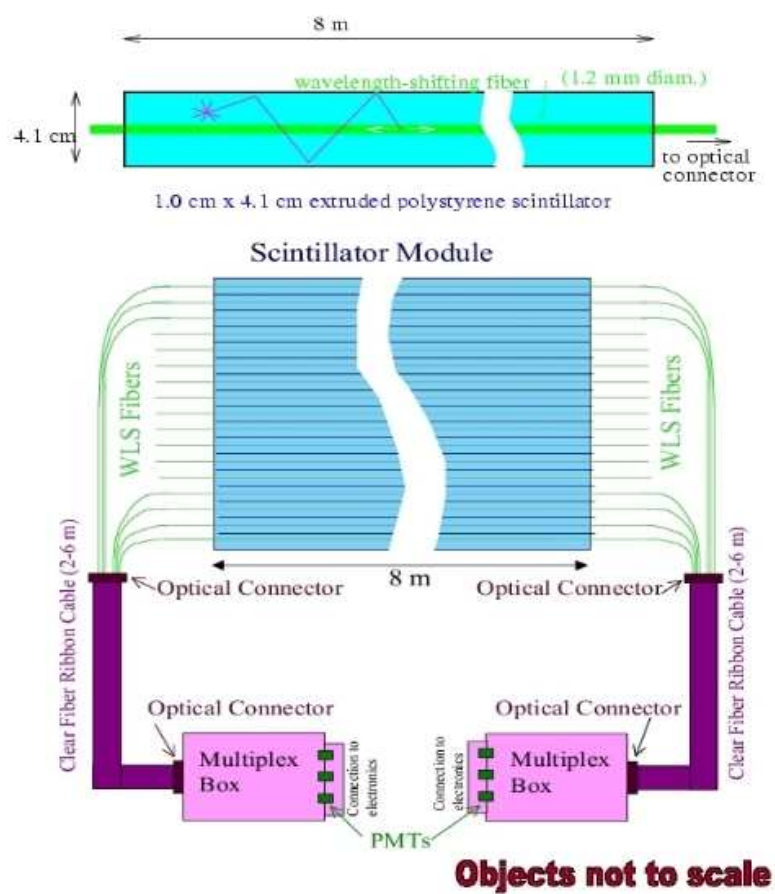
Figure 3.4: A drawing showing the module design and scintillator layout.

Top steel plane layer

Bottom steel plane layer

Scintillator plane

Orientations alternate 90º in
successive planes
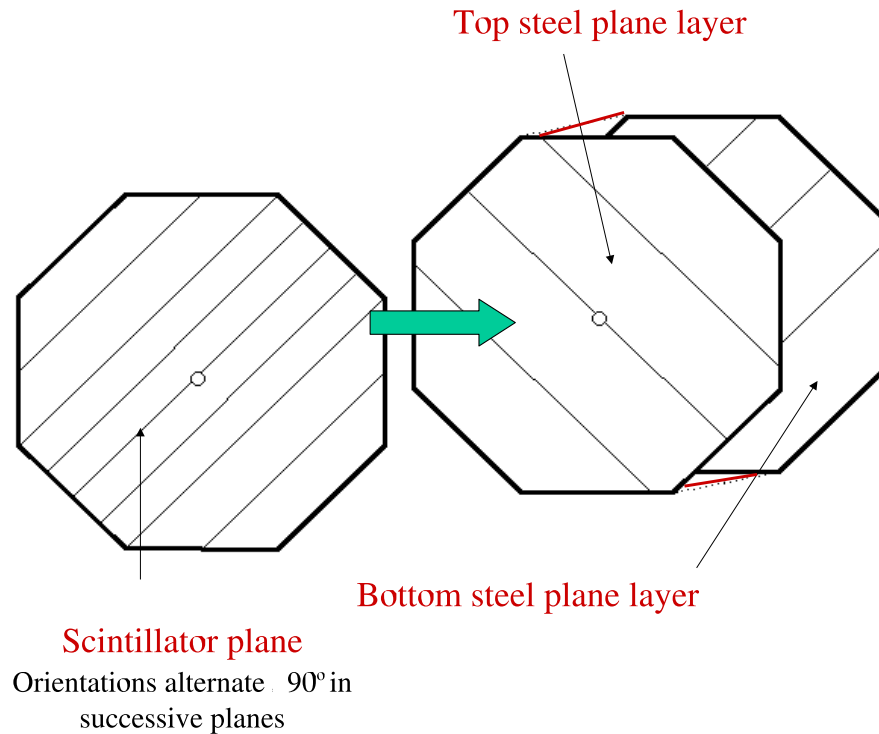
Figure 3.5: The relative orientation of U and V planes.

direction to focus μ^-, thus increasing the detector acceptance.,The current can easily be reversed for the reverse polarity of the field. This is a vital capability that allows the study of detector spatial irregularities and slight magnetic field asymmetries. Data can be taken with a particular field configuration and compared with reversed field data, with the ideal case resulting in particle tracks with a mirror image of the tracks from the original. Once the detector is well understood, this will provide an important cross check for charge determination efficiency.

The desired neutrino signal is detected as charged particles interacting with the detector components, while the neutrino is itself a neutral particle. The beauty of using a magnetized detector for such studies is that interaction of an energetic charged particle with a magnetic field is well understood, so the direction of curvature of the particle's motion compared to the direction of the magnetic field allows a determination of charge sign, while the radius of curvature is used to
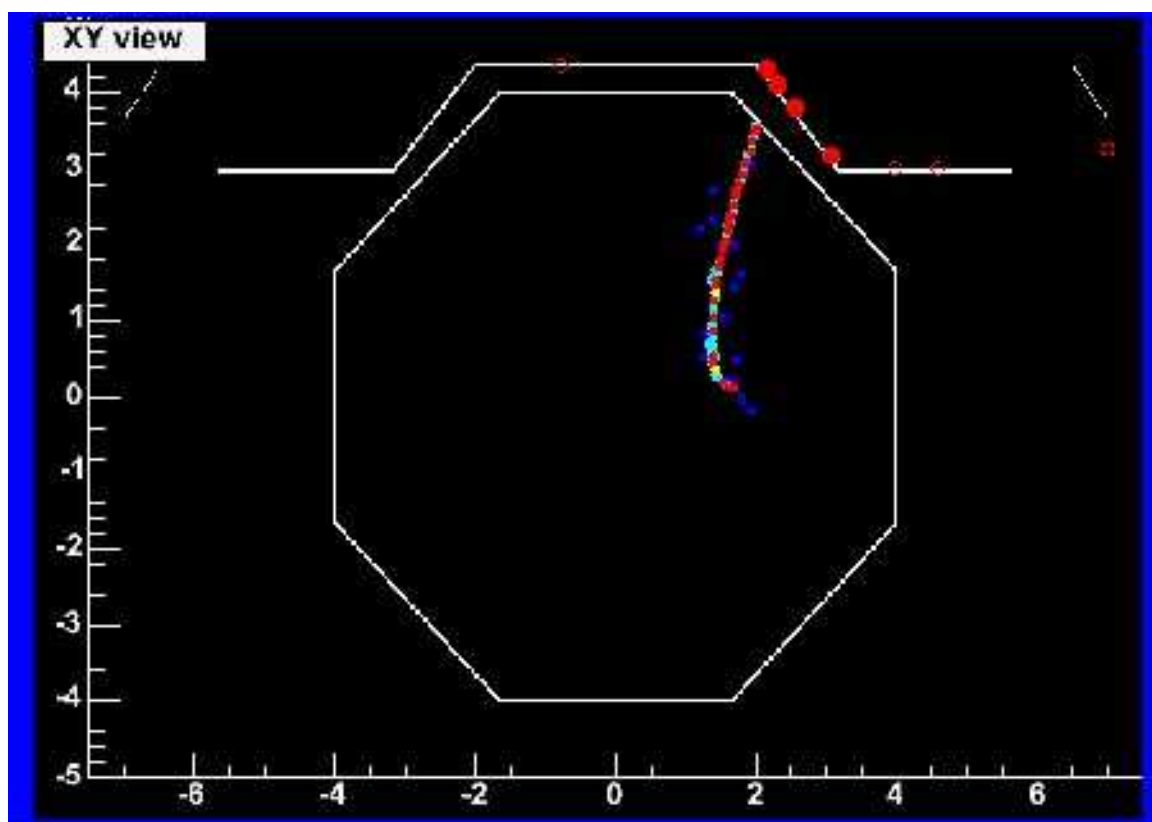
Figure 3.6: The effect of the magnetic field on a charged particle inside of the detector.
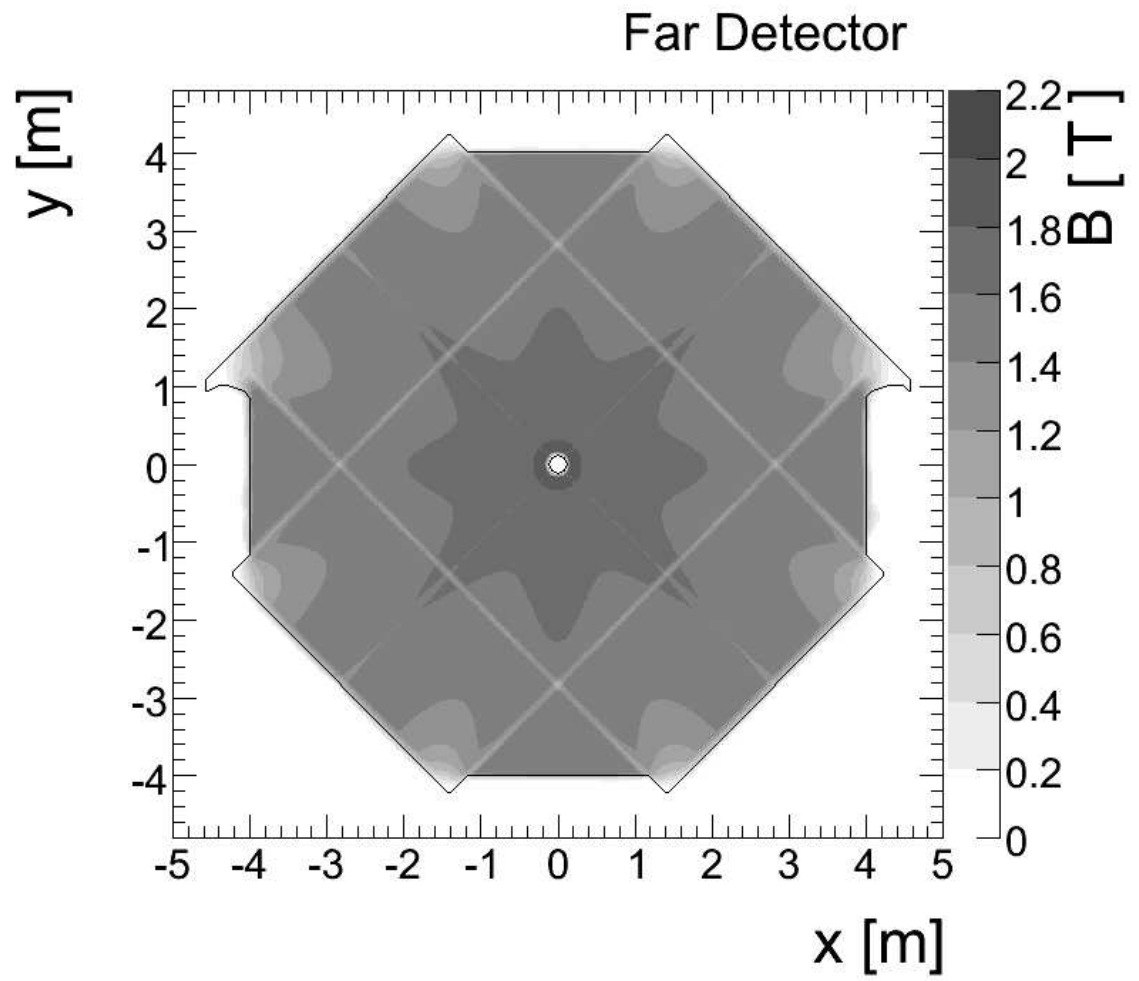
Figure 3.7: The magnetic field in the far detector.

deduce momentum. This illustrates the pioneering status of MINOS as the first deep underground detector to be able to separate μ^+ from μ^- directly, and by extension, ν_μ from $\bar{\nu}_\mu$. This feature allows the possibility of the first direct measurement of charge, parity and time (CPT) violation in the leptonic sector. Conservation of charge, parity and time is a central prediction of the standard model, and the violation of CPT would spell profound impetus for physics beyond the standard model. This effect would manifest itself in MINOS in $\bar{\nu}_\mu \rightarrow \nu_\mu$ oscillations or as different oscillation parameters for ν_μ and $\bar{\nu}_\mu$, meaning that the oscillation probability is different for $\nu_\mu \rightarrow \nu_\tau$ than for $\bar{\nu}_\mu \rightarrow \bar{\nu}_\tau$. The capacity to determine the momentum of muons in the detector is unprecedented for deep underground neutrino detectors. This ability heightens the MINOS detector's value in the study of atmospheric neutrinos, and adds another parameter by which to probe the properties of these ghost-like particles.

3.4   Electronics

There are a number of electronics subsystems that the light signal encounters after traveling to the PMT via the WLS fiber. The first step in the electronic journey is the encounter with the PMT that converts light to an electrical signal via the photoelectric effect. The process of converting light into electricity makes a PMT "basically an inverse light bulb" [111]. The photon is absorbed in the PMT by a photoemissive cathode, where the photon excites the material, which then emits electrons. These first few electrons are accelerated with a large electric potential toward a dynode, where more electrons are created. These electrons are again accelerated in the same manner, and the cascading effect continues until the now amplified signal reaches the anode of the PMT, where the signal is then ready to be used. The PMTs particular to the Far Detector are the multi-anode Hamamatsu R5900U-00-M16 (M16) with 16 photosensing channels (pixels) per photomultiplier [112]. The PMT utilizes a high voltage to turn an incoming signal, with a 0.3 photoelectron (pe, 1.602×10^{-19} C) threshold, to a charge of ~ 50 fC, with an average gain of 10^6 [110].   These PMTs were chosen to reduce the number of PMTs used in the detector. Using one PMT per 16 pixels greatly reduces the number of detecting components. A further reduction is made possible by the fact that eight fibers are attached to one pixel, and there is a de-multiplexing algorithm that is used (section 3.4.1 on page 49) to determine which strip was actually hit.

The PMTs are located on and read by the 32 channel ASIC VA32_HDR11 ("Viking chip")
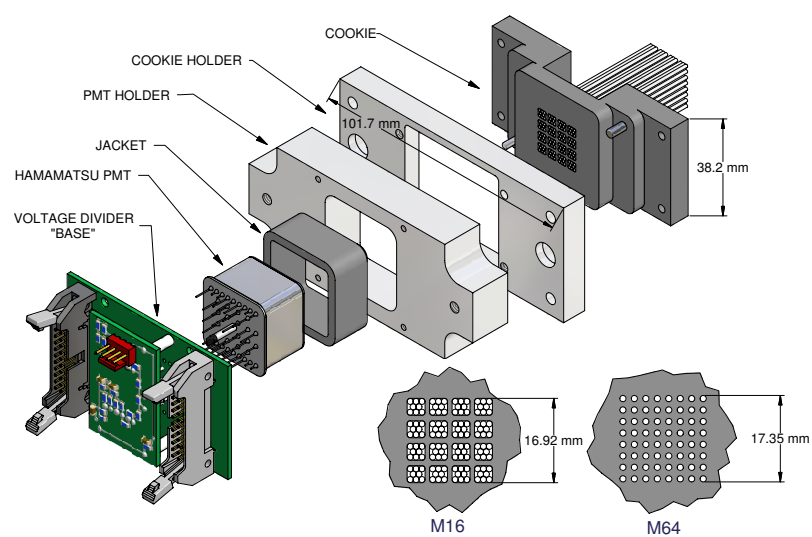
Figure 3.8: The Hamamatsu M16 PMT

CMOS chip. The VA chip is read by the VA Front end board (VFB). The VFB houses three VA chips, with their respective PMTs. The signal from the VFB is sent to the VARC Mezzanine Module (VMM), which amplifies and digitizes the VA output [113]. The signal is then sent to the VA Readout Controller (VARC), which is located in a VME crate separate from the VFB. The VARC keeps track of the trigger time with an internal 53 MHz clock and controls the VA devices. Each VMM interfaces with two VFBs, and each VARC can contain 6 VMM, which means that each VARC can control up to 32 PMTs [113].

Once the light signal has been converted to a digital signal, it is transmitted to a local FIFO and stored. The memory is then read by the DAQ, where it is recorded as data. A Read-Out Processor (ROP) in each VME crate records the digitized data. There are 16 ROPs at the Far Detector. The ROPs are chained together with a PCI Vertical Interconnection (PVIC) and read by Branch Readout Processors (BRPs). BRPs 1-4 read three ROPs each, while BRPs 5 and 6 read two ROPs each. The timing for both the front-end and DAQ electronics is recorded from a GPS receiver underground that connects to an antenna on the surface. The resolution of each receiver is better than 200 ns. Once all ROPs have been read, an entire time frame of data from the whole detector is sent to a Trigger Processor (TP), with an average rate of 5 MB/s. There are a number of triggering algorithms executed by the TP at the Far Detector [109].

1. Remote Spill Trigger: The near detector GPS system is used to generate time-stamps of the spill signals. These are transmitted to the far detector over the internet where they are stored and served to the TPs. All hit information recorded during a time window around each spill is extracted and written out as a spill-event.

2. Fake Remote Spill Trigger: Fake spill times are generated randomly between spills to provide random sampling of detector activity.

3. Plane Trigger: M detector planes in any set of N contiguous planes must contain at least 1 hit. Nominally M =4, N =5.

4. Energy Trigger: M contiguous planes of the detector have a summed raw pulse height greater than E and a total of at least N hits in those planes. Nominally M =4, E=1500 ADC counts, N =6.

5. Activity Trigger: There must be activity in any N planes of the detector. Nominally N =20.

Typically the Plane Trigger is used, and it is superseded by the Spill Trigger at the appropriate moments. The average trigger rate is 4 Hz, which results in a data rate of 10 kB/s. The data is cached on computers at the Soudan site until it can be transferred to Fermilab, where events are reconstructed for use in physics analysis and detector sub-system calibration.
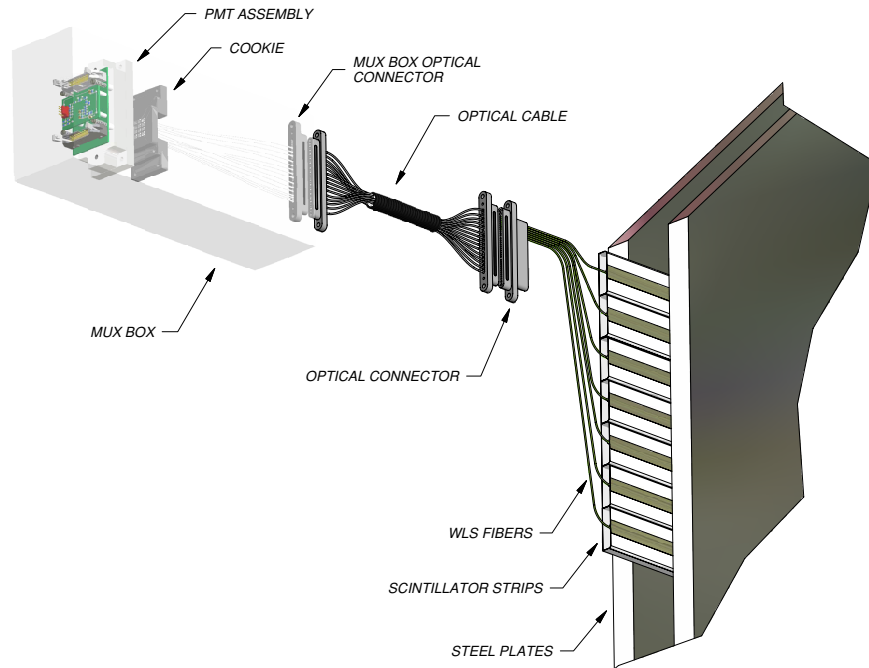
Figure 3.9: Cut-away of the connection of the PMT to a module

The front-end electronics exist in racks stacked on two levels, running the length of the detector on both the east and the west walls. Each scintillator strip has two sets of readout electronics associated with it, to measure the light output at each end of the strip. The multiplexing pattern is different for each side, so double sided readout helps break the eightfold degeneracy in the demultiplexing of events. This also has the distinct advantage of getting a strong signal, no matter where the event occurred in the plane. Even the best WLS fiber will attenuate substantially while sending such a small signal a distance of 8 m, so the duplicate electronics are necessary for the reliability of the signal detection. The signals on each end are compared and verified, and then combined into a single signal.

3.4.1 De-multiplexing

One of the important facets of the electronics system is the de-multiplexing (demuxing) algorithm. This is the way that a single pixel can deconvolve the signal from each individual strip that it reads. The algorithm is able to determine the likelihood of a particular strip being the cause of the event in the pixel, and is therefore able to pinpoint the location of the hit. This procedure is not flawless, and a large amount of time was invested in calibrating this algorithm. As a result of the inherent experimental imperfections that are associated with this routine, there has been introduced a Figure of Merit (FOM) to determine how "well" the demuxing algorithm performed for a particular event. Nominally, the FOM identifies the number of misidentified, or unhit ("stray") planes, and compares them with the properly identified (properly hit) planes in a view, for a particular event. A threshold has been set to determine what percentage of hit planes constitutes an acceptable demuxing, and a cut can then be applied to glean properly reconstructed events.

3.5 Calibration Systems

Accurately determining energy deposition in the MINOS Far Detector requires a calibration system more sensitive than the measurements it is trying to make. A threshold of only 0.3 pe in the photodetection system enables many possible fluctuations that can manifest themselves as a false signal, extra noise, or simply a detector malfunction. The extreme gain and nonlinear response of a PMT makes it a delicate device to subdue, and the fact that fiber attenuation and scintillator properties can cause light detection characteristics that change with age make calibration of special importance with the MINOS detector. Scintillator modules were determined to be light tight before being shipped to Soudan, and they were tested again once they were attached to the steel plane. A final light tightness test was performed after the plane was hung, but before the plane was considered complete and buried by the next one. There are few things that can go wrong over time with WLS fiber and scintillating material secured inside a protective steel shell. The electronics and PMTs, however, have a large number of failure modes. It is vital to be able to diagnose and resolve electronics failures before they manifest themselves as detector failures. This aim is achieved through the main components of the calibration system: Light Injection (LI) and Charge Injection (CI), and the Veto Shield. A run as defined for the MINOS experiment is a period of recording data for a specific purpose. There are two general classifications of runs, ones that take

data specifically for calibration, and ones that record data for use in physics analysis. Of course, physics data can be used for calibration efforts, but calibration runs introduce unnatural effects that could be misconstrued as anomalous physics. Both the LI and CI systems require special runs for peak calibration efficiency, and they are of a special class of runs that are interspersed with the normal physics runs for neutrino and muon data collection. There can be many calibration runs in between physics runs, and the runs are sequenced identically. This shows up in the data as a gap in the distribution of a plot of events versus run number. It is neither a flaw nor feature, just something for an experimenter to be mindful of, that runs void of significant cosmic ray data are not necessarily indicative of a detector malfunction. While not a system, *per se*, cosmic ray muons provide an additional calibration of detector alignment as well as a "standard candle" for energy calibration.

3.5.1 Light Injection

The LI system is a novel way to simulate the illumination of the PMT in a normal particle inter-action in a controlled, well understood way. The LI systems consists of a pulser box filled with light emitting diodes (LEDs) connected to clear optical fibers that are inserted into the detector snout assembly, the junction of the WLS fibers embedded in the scintillator with the fibers that transmit the absorbed light to the PMT. These LEDs can be pulsed (emit a burst of light for a brief period) at regular intervals, or at the discretion of the operator of the detector, and can operate during a normal physics run. Pulse height can be precisely controlled, as can pulse width, ranging from $10 - 40 \, \mu$s. The precision of the calibration system is a result of the fact that the electrical components are well understood, and that there are no mechanical parts as in filter wheel calibration systems that can wear and change in unpredictable ways. The pulse heights are monitored by PIN diodes to account for the small ways the LED output changes over time, and there is no pulse to pulse jitter [114]. Each LI pulser box assembly contains multiple LEDs, and each LED can illuminate 640 fibers with as much as 200 pe.

The LI system was designed to be used when the detector is not anticipating beam data, since the PMTs are saturated in the process and cannot be used for data taking. A light injection run is in a class of "special" runs, and what data is taken is reported as LI data, to distinguish it from physics data. Indeed, it is a simple matter to differentiate LI data from particle data as entire pulser boxes illuminate at a time, making it look like herds of glowing basketballs are flying through the

detector. Blue LEDs are used in the pulser box, and the light from a single LED is distributed amongst many channels. Given the large number of varied path lengths the pulse could encounter because of necessary fiber length variations, it is impossible to pass an equal amount of light through each channel. Instead of calibrating with a known quantity of light, a PIN diode, a stable solid state device, is used to monitor the output of the LED and the light produced is plotted against the PMT response. The PIN scale is known to be a linear function of light intensity, and this can account for nonlinear behavior of the optical readout devices and provide a precise calibration of optical components.

3.5.2   Charge Injection

It may seem redundant to calibrate the electronics separately from the optical system of the Far Detector. After all, these optical instruments are electronic devices, they are merely specialized to produce a voltage given a particular light input. This calibration *is* entirely necessary, though the reason is subtle. In the CI system a known charge is put into the front end electronics and digitized, producing a response that is recorded over time and developed into a function that allows ADC counts to be quantified. This is necessary for the calibration of the PMTs, and the LI system would be useless without it. The PIN diode is read out by the self-same electronics that reads out the PMT; their response in this system is dependent one to the other, and no calibration is possible. Using the CI system, however, provides an absolute calibration of the electronics such that the response of the PMT can be compared to the the actual output of the LI LED, and a real calibration can be determined.

A digital potentiometer is used to dispense a known quantity of charge into the electronics. The potentiometer is well understood, and behaves in a way that is linear to better than 1% over the range of the ADC [114]. The ADC will produce a small signal even when there is no information passed to it from the PMT; this constitutes the major component of the electronics noise. Another component of the electronics calibration is the subtraction of pedestals, or electronic noise, from the data. Pedestals are recorded by measuring ADC counts even when there is no event in the particular channel. In the end, calibration accuracy is consistent with the experiment wide effort to reduce systematic errors to less than 2%.

3.6   Veto Shield

Its physical structure might make it the most interesting looking feature of the MINOS detector (see Fig. 3.10), and its purpose may very well be the most important; the veto shield is one of those rare moments in High Energy Particle Physics when the perfect marriage of form and function yields the ideal detector. The veto shield is constructed with the same scintillator material used in the detector, and differs from the detector planes only in its orientation and the fact that it does not have the same steel backbone. The veto shield lies perpendicular to the detector planes, and uses their stability for support.   While the design of the veto shield was to eliminate cosmic
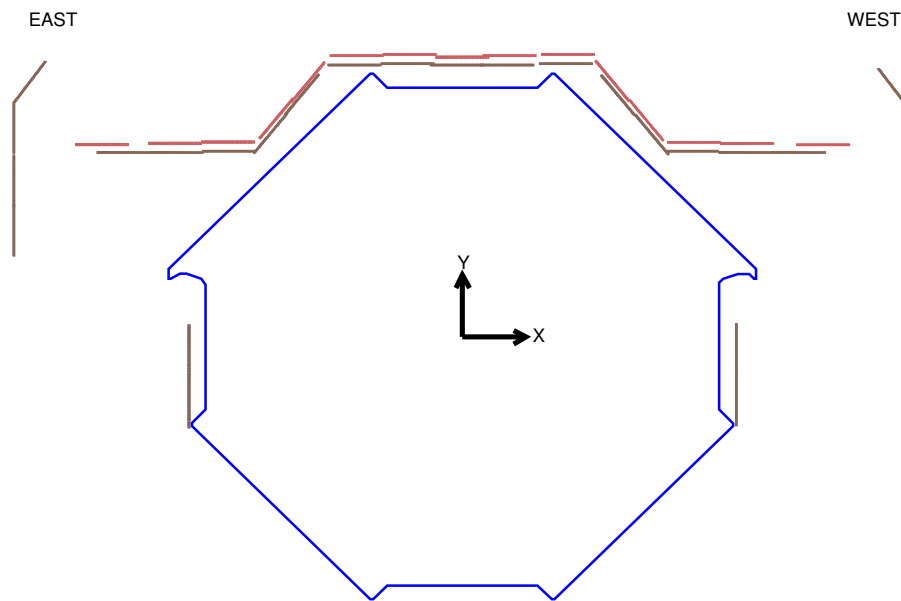
Figure 3.10: Schematic of the components of the veto shield

ray events from a set of beam neutrino data, it also adds a purity cut for the scientific study of cosmic rays. Any muon that passes through the veto shield will have entered the detector through the smallest amount of rock overburden; these are the lowest energy muons the Far Detector will accept. This is not inherently a bad thing, the problem is one of resolution and background.

The study of atmospheric neutrinos involves the analysis of fully and partially contained downward going events in the detector, as well as upward going and horizontal events. Downward going events originate in the atmosphere above the detector, and pass through the smallest amount of rock to get to the detector. A fully contained event, as its name suggests, would spend its entire existence inside the detector. These events are induced by neutrinos of low energy, such that they enter the detector unseen from above, interact with the steel to produce a low energy muon that loses all of its energy before it can exit. A partially contained event would be caused by a neutrino of higher energy, but still of atmospheric origin, that enters undetected, interacts with the steel and produces a muon of sufficient energy to exit the detector. It is entirely likely that muons could enter the detector from virtually overhead, between two detector planes, then continue through a sufficient number of cuts to be considered a candidate for a contained event. The veto shield can positively identify a downgoing muon that entered between detector planes, and cast it out of a data set consisting of contained events. The veto shield will detect sufficient downward going cosmic muons to reduce the background by about 10^5 times [115], as cosmic ray muons are the dominant contamination for atmospheric neutrino analysis.

Chapter 4

Cosmic Data Underground

As discussed in Ch. 2 on page 10, an underground detector is particularly suited to the study of muons, the penetrating component of cosmic rays. Such a detector is virtually singular in its acceptance of cosmic ray induced particles, indeed only neutrinos and exotic particles could also descend the depths. Cosmic ray induced muons outnumber neutrino induced muons by a factor of 10^5, so the contribution from neutrinos is negligible to a cosmic ray analysis.

4.1 The Data

The Far Detector began operation in September 2002, when the first supermodule (SM1) came on line. The second supermodule (SM2) was completed in July 2003, and at this point the entire detector was operational. The data set in this analysis includes only that which was taken with both supermodules magnetized, referred to as the SM1+SM2 set. This spans the period from 1 August, 2003 until 31 December, 2007, for a total of 1614 days of detector running. Over this span of time, the detector was live for 70% of the time, including scheduled downtimes for repairs as well as unscheduled power outages cause by perfect northern Minnesota storms. This represents a nearly 50% increase in exposure time over the previous MINOS cosmic ray analysis [60], a measurement of the cosmic ray induced μ^+/μ^- ratio. Far detector events can be divided into three distinct groups, fully contained, partially contained and through going.

Fully contained events are low energy neutrino induced muons that stop in the detector. They

have an average energy of 1 GeV and include low energy atmospheric ν_μ and ν_e. The discrimination of a ν_e event from noise or a malformed track is difficult because of the granularity of the detector (see Fig.4.1), thus the detector has a very low efficiency for the detection of ν_e [116]. This is an extension of the capabilities of the detector, as it was designed for the detection of ν_μ from a beam at Fermilab.
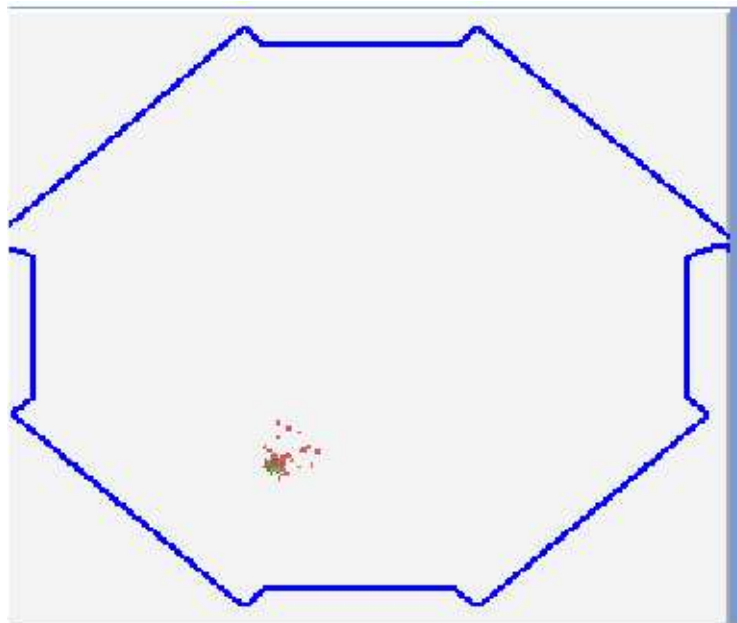
Figure 4.1: A typical snarl, showing a short lived, low resolution electromagnetic event in the Far Detector. Electrons deposit their energy over such a short distance in the steel that their signature looks like a smudge.

Partially contained events include downward and upward going neutrino induced muons (contained vertex) that originate in the detector and contain sufficient energy to traverse the detector, and stopping cosmic ray muons that have low enough energy that they deposit all of it in the detector. Contained vertex events make up the bulk of the atmospheric neutrino charged current (CC, muon type neutrinos that interact via the exchange of a charged ($W^\pm$) boson) sample and have an average energy of 10 GeV [117]. A contained vertex neutrino induced muon track can be seen in Fig. 4.2. Stopping muons provide a signal for *in situ* absolute energy calibration of the detector and deposit an average of 10 GeV in the detector. They make up less than 1% of the total cosmic ray muon sample.
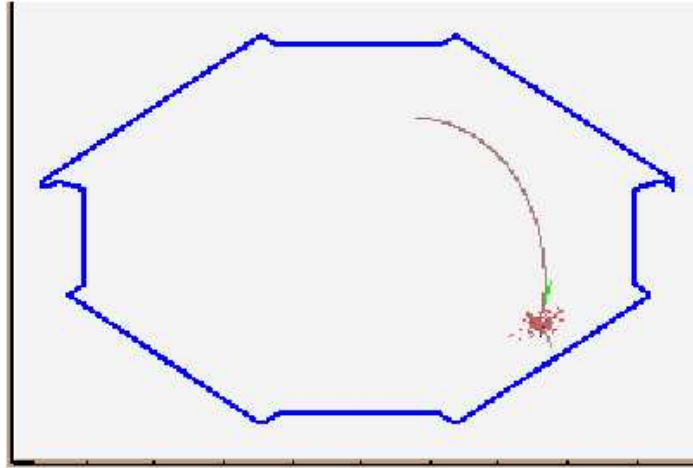
Figure 4.2: A typical track showing some hadronic debris from the interaction of a neutrino with the steel, then a nice long muon arc. The curvature is the result of the magnetic field and allows the determination of charge sign.

Downward through going muons are cosmic ray induced and pass through the detector, depositing little of their total energy. They make up the majority of the cosmic ray muon data set, and because they contain such great energy, many of them do not curve in the magnetic field of the detector, thus the energy measurement is unreliable. A very small fraction of these events are induced by atmospheric neutrinos interacting in the rock surrounding the detector, but these are impossible to discriminate from the cosmic ray induced muons, which outnumber these neutrinos by a factor of 10^5. Upward going muons are induced by neutrinos interacting in the rock below the detector. Since the Far Detector has nanosecond timing resolution, it is possible to discriminate the muons that originate in the rock below the detector from those that originate above, which greatly increases the neutrino data sample [118].

4.2 Reconstruction

The process of interpreting physical meaning from a collection of light in the detector is called reconstruction. For the Far Detector, this involves:

- **Data Cleaning** - distinguishing signal (particle information) from noise (anything not caused by a particle: electronics malfunction, environmental effect, etc.)

- **Calibration** - the art of mapping ADC counts to physical quantities and parameterizing errors.

- **Alignment** - interpreting U,V and Z coordinates as three dimensional location in space (X,Y,Z).

- **Track Finding** - combining spatial coordinates from all hits to determine the actual path of the particle through the detector

- **Physics** - determining physical characteristics about the now reconstructed track (particle type, charge sign, energy)

The energy response of each module was measured using a collimated radioactive source (5 mCi cesium). The calibration is checked against data and simulations, and improved corrections are included with every software release. Two surveys were carried out as the detector was constructed with sub-mm precision. The alignment of each plane was also determined with a strip-to-strip method that used muon data. The track finding algorithm uses a Kalman filter to determine the most likely path the particle could have taken, given the collection of hit coordinates. Once calibration has been performed, alignment has been taken into account, and a track has been found, the physical characteristics of the particle can be determined.

4.3 *Monte Carlo* Simulations

The collection of particle data is straightforward, but the interpretation of said data is a difficult, complex question. The difficulty lies in identifying the particle, understanding how a particular particle interacts with the detector, understanding the behavior of the set of particles in the detector, and understanding the physical processes that give rise to the class of particles. There is a wealth of information that has been accumulated about cosmic rays, muon production, muon interaction with materials, particle energy deposition in scintillator, and PMT response to deposited energy, and it can be applied to simulate expected detector response. Simply applying analytic mathematics to detector components does not adequately simulate the physics of particle detection that happens on an event by event basis. Rather, the input is generated at random from known probability distributions, subjected to known physical processes. This process is referred to as a *Monte Carlo* method, a "rolling of the dice", with the turn of phrase coined by mathematician

Stanislaw Ulam after the famous casino district in the French Riviera [116]. In this way, individual events, with known inputs and expected outcomes, are generated in random way, just like the data. Unlike the data, however, the input is known and the outcome expected. This way, one can see what happens when a particular type of event occurs. Such a method was employed by Peter Jackson *et al.* while making of the Battle of Helm's Deep in The Two Towers [119]. Armies from both sides were designed with their respective abilities and the number from each side were put into the simulation which produced an outcome. The simulation had to be run many times to produce the "correct" outcome (that good prevailed over evil).

4.3.1 GMINOS

GMINOS is the general MINOS *Monte Carlo* generator, which includes

1. Particle generator: beam or cosmic-ray

2. Particle vertex: detector or rock

3. Simulated detector response to the particle

This can be modified by the end user to create a number of different particle types in the detector.

Particle Generator

In the case of cosmic ray muon input, a parameterization of the differential muon flux (Eq. 2.20) at the detector location is used. A distinct method is used for the calculation of the neutrino flux from cosmic ray interactions, developed by Barr *et al.* [120]. For beam input flux (not used in this analysis), a Geant3-based [121] beam *Monte Carlo* was created by Hylen *et al.*, GNuMI [122].

Particle Vertex

In the case of a cosmic ray muon, vertices were generated in the rock surrounding the detector with a Geant3 [121] simulation of the energy loss mechanisms: ionization, bremsstrahlung, and photo-nuclear effects. For a neutrino, the interaction with a material is generated by NEUGEN [123].

Detector Simulation

Once the particle type is chosen from the flux and the vertex is determined, the resulting particle, typically a muon, is propagated through a simulated detector. There are three parts to the detector simulation. The propagation and energy loss of the particle as it traverses the detector is determined by Geant3. The deposition of energy in the scintillator strips and propagation of the resulting light is determined by *PhotonTransport*, while the PMT response and VA electronics response is simulated by *DetSim* [116].

The combination of these software packages results in a simulation of the expected input particles, and how the detector will respond to such an input. Once the simulated signal has been "digitized", the simulated detector information is reconstructed using the same software that is used on the data (Sec. 4.2). Thus, the detector performance can be measured and event selections can be determined.

4.3.2 Airshower *Monte Carlo*

While GMINOS does a good job of simulating the detector's response to charged particles, input neutrinos and the gross features of the cosmic ray muon flux, two things are missing that are important to a cosmic ray analysis: information about the muon progenitor and information about the propagation of the muon through the rock above the detector. To remedy this, a full cosmic ray airshower simulation was created. This simulation consists of three parts:

1. Cosmic ray primary flux input

2. Airshower creation and propagation

3. Muon propagation through rock

This simulation provides information about the cosmic ray primary, the creation and decay of secondary mesons which leads to muon production.

Primary Input Spectrum

The composition of cosmic ray primaries is well known (see Sec. 2.1), and the flux of muons underground only very weakly depends on the chemical species of the original cosmic ray. A

data-driven primary input routine was written by S. Kasahara [124], which divides the primary composition into five groups by mass.

1. Protons: charge +1e, mass 1 amu, 95.0% of the total flux

2. He: charge +2e, mass 4 amu, 4.7% of the total flux

3. CNO: charge +7e, mass 14 amu, 0.3% of the total flux

4. Mg: charge +12e, mass 24 amu (represents Ne - S), 0.01% of the total flux

5. Fe: charge +26e, mass 56 amu 0.002% of the total flux

The composition of a particular primary is chosen out of this distribution at random and used to generate muons.

Airshower Simulation

The COsmic Ray SImulation for KAskade (CORSIKA) [125] package is widely used to simulate cosmic ray airshowers, and was employed here. CORSIKA takes an input primary, selects and energy out of the known cosmic ray spectrum, then propagates the cosmic ray and resulting spallation products (airshower) to the surface of the earth. CORSIKA offers the choice of seven different high energy hadronic interaction models, and the two most widely used models are the Quark Gluon String model (QGSJet) [126] and Sibyll [127]. Both models were used for this simulation, following the tradition in cosmic ray physics.

The tracking of particle cascades through the atmosphere requires considerable processing time, and higher energy cosmic rays produce larger cascades, thus more particles to track through the atmosphere. Since muons are the the only airshower component that is visible in the Far Detector, and the threshold surface energy for a muon to survive to the Far Detector is 700 GeV (see Sec. 4.6), any particle with energy less than 700 GeV was not tracked through the rest of the simulation. The primary energy range is set by the user, and since the cosmic ray energy spectrum is a power law, the bulk of the flux will be near the minimum. The minimum energy proton to produce a muon that will survive to the far detector is 700 GeV, assuming that the neutrino that is created in pion decay has negligible energy. Since most of the primaries will be injected with energies near the minimum and the threshold muon energy only applies to vertical muons, while

the majority of muons will come from higher zenith angles and require more energy to penetrate to the far detector (see Sec. 4.6), the minimum primary energy was set to 2.2 TeV. It was found that less than 1% of the muons observed in the far detector could have been produced by such primaries, which is acceptable for the analyses that follow.

Muon Propagation Through Rock

CORSIKA produced a file with muon energies and trajectories at the surface of the Soudan site, and those muons were propagated through the rock overburden by Geant4 [121]. Geant4 simulated the important muon energy loss mechanisms: ionization, bremsstrahlung, photo-nuclear interactions, and Coulomb scattering and tracked the particle along its resulting path until it reached the detector. The amount of rock a muon would have to traverse to reach the detector, given its initial trajectory and position, were found using the rock map discussed in Sec. 4.6. This map was empirically determined using muon flux data normalized to the world average underground muon intensity for standard rock.

To ensure computing time was not wasted, checks were performed on the muon before it was propagated through the rock. First, the location was specified such that a muon with the given trajectory would intersect the detector. Then, the minimum momentum required to traverse the particular amount rock was calculated, and if the muon did not posses at least 80% of the required momentum, it was discarded. All remaining muons were propagated to the detector hall, where the momentum and trajectory of the muon were recorded.

4.4 Selection Cuts

All of the software to reconstruct events has been developed by MINOS collaborators over the last eight years. The data in this analysis were reconstructed with Minossoft release R1.24 and R1.24.3. All of the plots were generated with CERN's ROOT V5.12/00 [128], and at times utilizing LOON, MINOS' customized version of ROOT with additional, experiment specific libraries and routines. The majority of the computing was done on the neutrino cluster at the University of Minnesota. Additional computing utilized facilities at FNAL and the CLEO Farm at the University of Minnesota.

The muon data for this analysis were accumulated over a four and a half year span, beginning

on 1 August, 2003, at which time the detector was fully operational, ending on 31 December, 2007. Beginning with 67.99 million cosmic ray tracks, a series of cuts were performed to ensure a clean data sample. Entire runs were excluded based on the following criteria [60]:

1. Require physics data, runs must be more than 5 minutes long

2. Detector must be reading all channels

3. Runs must contain "good physics data", which includes correct trigger bits, complete read-out, and minimal dead chips

4. Remove runs with anomalous rates: $0\,\mathrm{Hz} < R_\mu < 1\,\mathrm{Hz}$

5. Remove runs that the atmospheric neutrino analysis has flagged as having far too many contained events [117, 118]

Events were excluded if taken during periods when the detector was not functioning within normal parameters, mainly due to electronics repairs, the magnetic field being out of tolerance, calibration, etc [60]. In addition to these data quality cuts, upward going (neutrino induced) muons were also excluded [118]. Since the MINOS experiment is designed to measure beam neutrino oscillations, there is a different trigger used when the neutrino beam pulses to maximize the detection of beam-produced neutrinos. This trigger is based on the timing of the beam pulse and it opens the detector to record all hits during a $100\,\mu$s window. The muon data that is recorded $\pm 50\,\mu$s of a beam pulse is excluded since it could be of terrestrial, not cosmic origin. This cut eliminates a very small number (2186) of well understood background events. A total of 59.24 million events survived the cuts for the μ^+, μ^- combined sample.

Cut	Fraction Remaining
Total Triggers	67.9943×10^6
1. Reconstructed Tracks	0.8887
2. Good Run List	0.8754
3. Light Injection Removal	0.8713
4. Spill Removal	0.8712

Table 4.1: Percentage of events that survive each cut

4.5   Time Distribution of Muons

With the exception of routine maintenance, weather-induced power outages and shutdowns to re-pair malfunctioning electronics, the Far Detector has been running continuously with a constant detector configuration. Many of the maintenance and electronics repairs took place at the beginning of operations, when new problems offered new challenges that required more time to fix. The result is stable data accumulation coupled with a slight increase in the number of muons recorded as the experiment progressed. The number of muons recorded per month can be seen in Fig. 4.3, along with the fractional uptime of the detector.   The distribution of rate per run can be
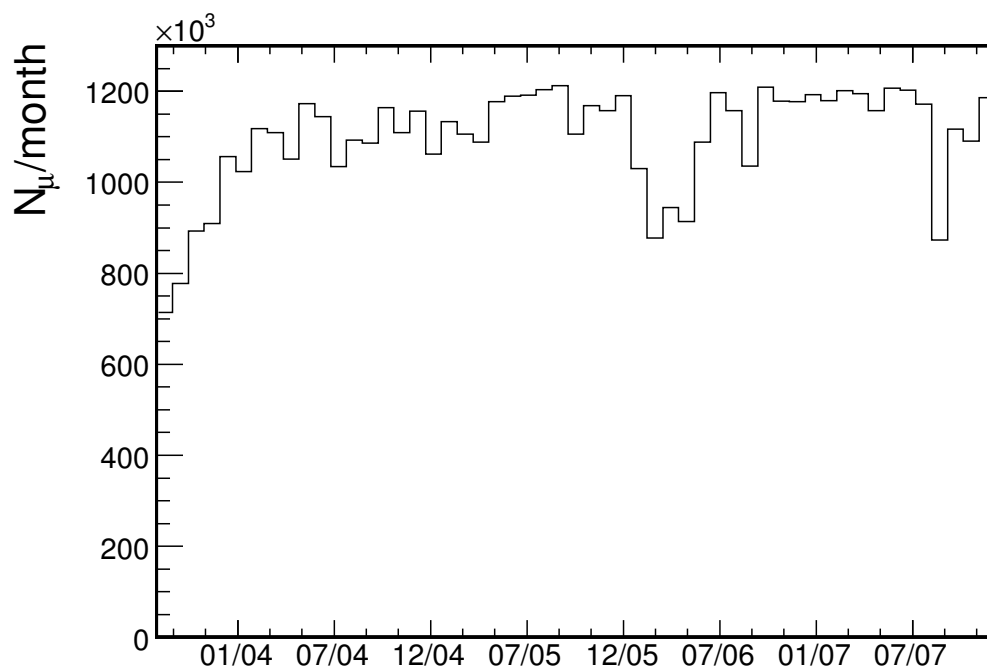
Figure 4.3: The number of muons accumulated per month of detector running, along with the fractional livetime of the detector. Note overall increase in monthly muon recording, corresponding with the increasing uptime of the detector.

seen in Fig. 4.4.

Events that are known to arrive at random can be described by the M-order gamma function
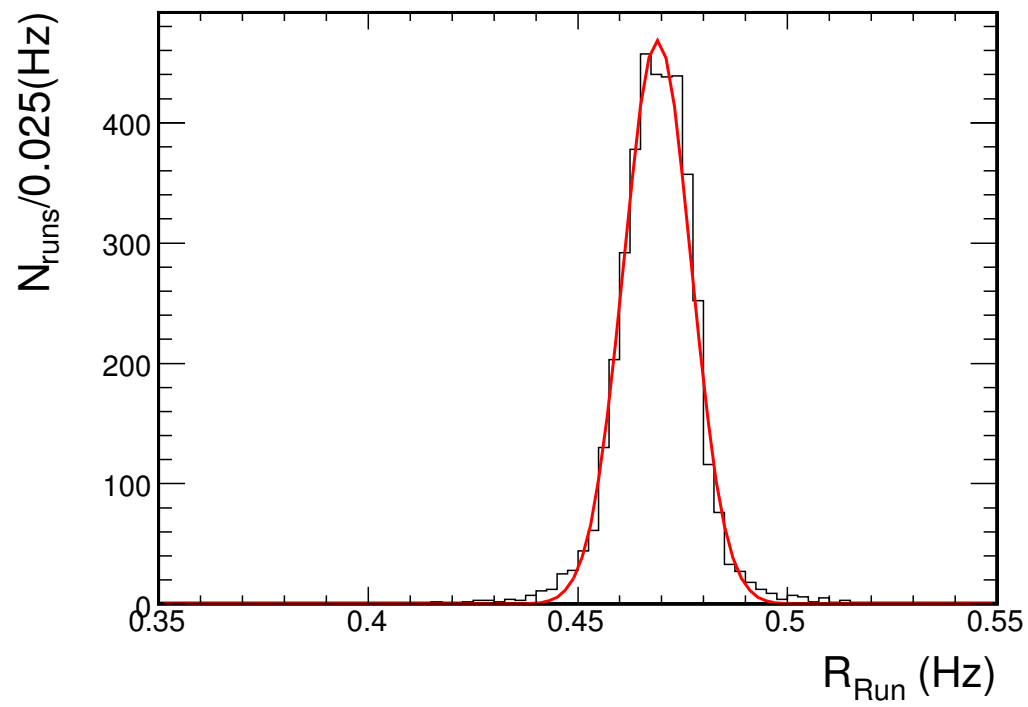
Figure 4.4: A histogram of the distribution of rate per run. The distribution is well described by a Gaussian with $\chi^2/ndf = 145/48$, $\mu = 0.469 \pm 0.000\,\mathrm{Hz}$ and $\sigma = 0.00805 \pm 0.00011\,\mathrm{Hz}$.

[129]:

$$G(t; \lambda, M) = N\lambda \frac{(\lambda t)^{M-1} e^{-\lambda t}}{(M-1)!}, \tag{4.1}$$

with N as the normalization factor and $1/\lambda$ as the average time between events. The order M is for a particular series of events; M=1 for $(t_1 - t_0)$, M=2 for $(t_2 - t_0)$, and so on. The first order gamma function becomes a simple exponential:

$$G(t; \lambda, M = 1) = N\lambda e^{-\lambda t}, \tag{4.2}$$

This is the expected arrival time difference between consecutive events, and it can be used to predict future or simulated events. This function was shown to describe the muon arrivals in MACRO [130].   The time between consecutive underground muon arrivals has been shown
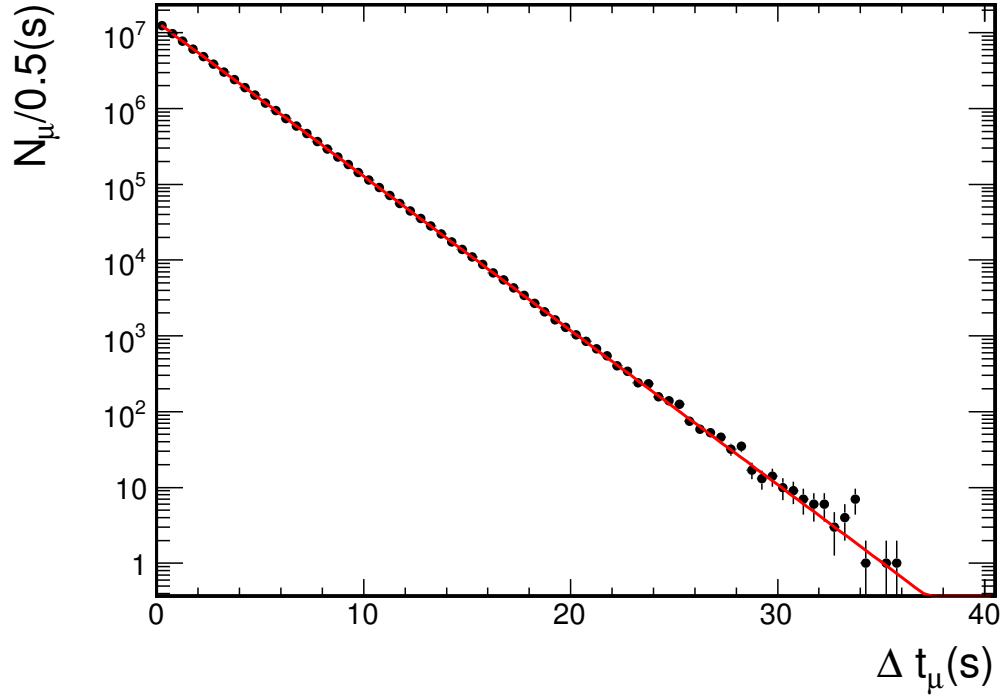
Figure 4.5: The time between consecutive cosmic ray muon arrivals. A fit to a Poisson distribution [131] gives $\chi^2/ndf = 52/69$; $\langle R_\mu \rangle = 0.4688 \pm 0.0001$ Hz (from slope). The Poissonian nature of the muon arrival times demonstrates the absence of short-timescale systematic effects on the data.

to follow a gamma function (Poisson of order one) for MACRO [131]. A histogram of the time

between consecutive muon arrivals (Δt_n) in the MINOS data is shown in Fig. 4.5, along with a Poisson expectation. The fit result from Fig. 4.5 was used to find the mean rate $\langle R_\mu \rangle$ 0.4688 $\pm$ 0.0001 Hz. The fact that the data is so well described by the Poisson distribution demonstrates the absence of short-timescale systematic effects on the data. The livetime for each run was calculated by adding the time between consecutive muon arrivals, $\sum_{n=1}^{n(\mu)} \Delta t_n$. Any $\Delta t_n > 38$ s was assumed to be an instrumental downtime and excluded from the calculation.

To further analyze the time between muon arrivals, a study was performed of the time elapsed between the arrival of the first muon (t_0) and the subsequent four muons (t_2, t_3, t_4, t_5): ($t_2 - t_0$),($t_2 - t_0$),($t_4 - t_0$)($t_5 - t_0$). The second, third, fourth and fifth order gamma functions were fit to time differences ($t_2 - t_0$), ($t_3 - t_0$) ($t_4 - t_0$) and ($t_5 - t_0$), respectively. The correlation of the measured time distributions with these functions is displayed in figures 4.6 and 4.7. The list of λ values for each order of the gamma can be seen in table 4.2.

Table 4.2: The λ values for each order of the gamma function.

M	λ (Hz)
1	0.4688 $\pm$0.0001
2	0.46768 $\pm$0.00004
3	0.46870 $\pm$0.00003
4	0.46873 $\pm$0.00003
5	0.46874 $\pm$0.00003

4.6 Spatial Distribution of Muons

A muon that stops in the detector will deposit less less than 20 GeV, but attaining a 20 GeV energy deposition requires that the muon pass the length of the detector, which is oriented horizontally. Since a very large zenith angle is required to be able traverse the entire detector end to end and the distribution of muons falls off rapidly with decreasing zenith (see Fig. 4.9), very few muons will stop in the detector. Determining the energy of the muon by the energy deposited is therefore quite difficult for the majority of muons. The magnetic field extends the momentum determining capability of the Far Detector by bending the trajectory of the particle, which allows momentum determination up to 250 GeV. Unfortunately, many of the muons will enter the detector at a small angle relative to the magnetic field, which is toroidal about the z axis (the axis that points to
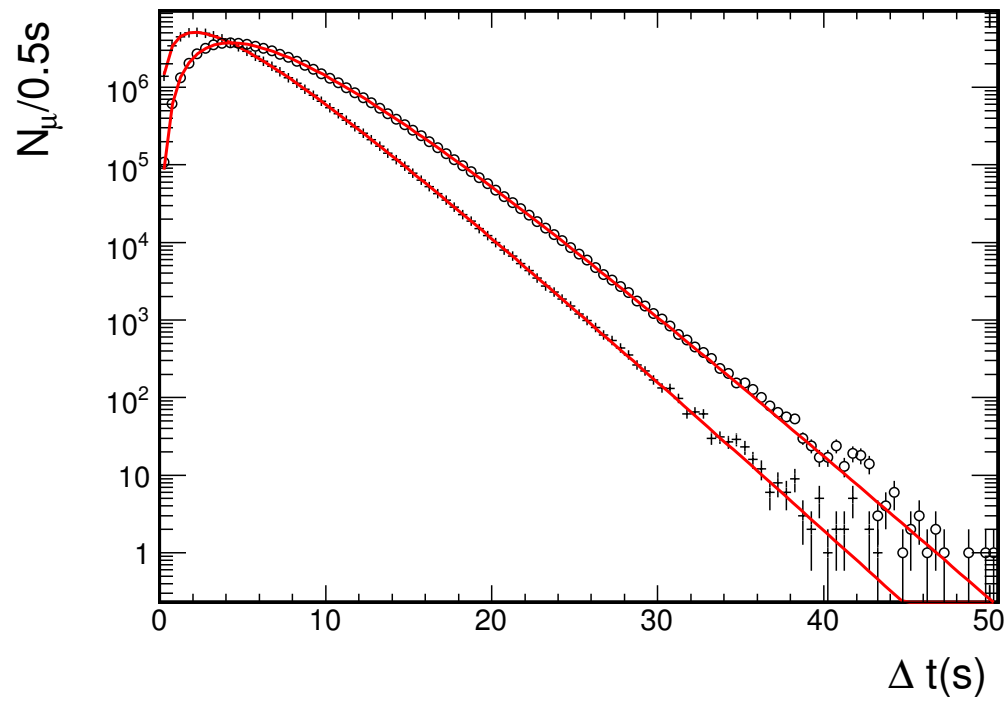
Figure 4.6: Histogram of $(t_2 - t_0)$(crosses) and $(t_3 - t_0)$(circles), fit with a second order (M=2) and third order (M=3) gamma functions.
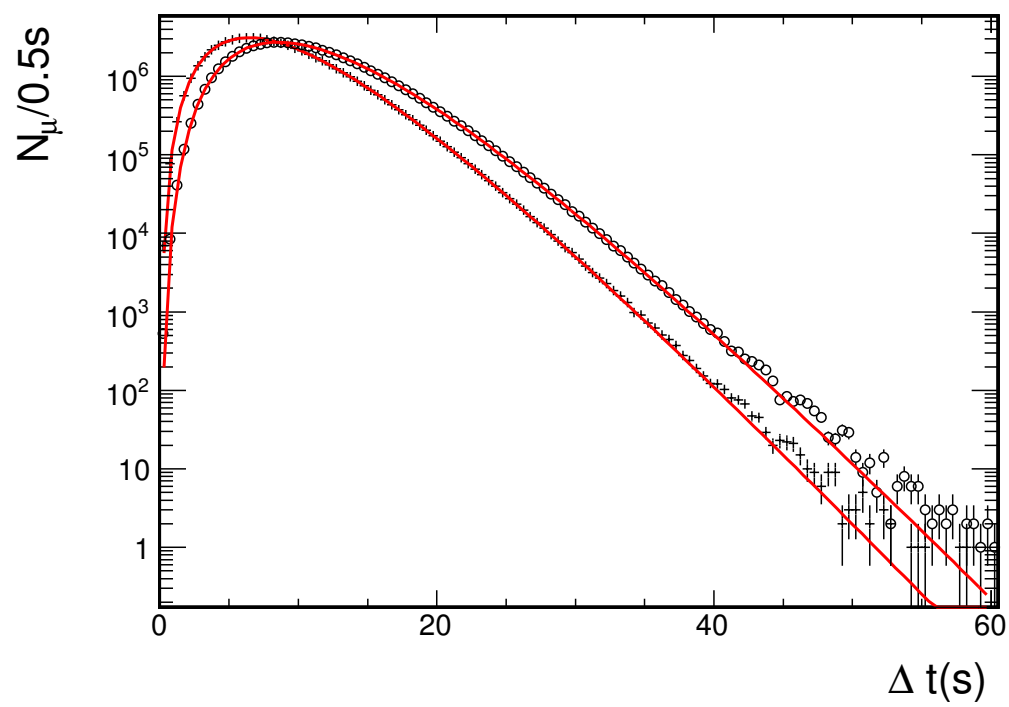
Figure 4.7: Histogram of $(t_4 - t_0)$(crosses) and $(t_5 - t_0)$(circles), fit with a fourth order (M=4) and fifth order (M=5) gamma functions.

Fermilab).

Perhaps more interesting to a study of cosmic rays is the momentum of the muon at the surface. While it is rather difficult to precisely project the muon back to the surface and determine its momentum, with a few assumptions it is possible to estimate the momentum to within about 10%. The arrival trajectory of the muon is well known, the amount of rock traversed for a given trajectory can be found, and the amount of energy required to traverse a column of rock is well known (Eq. 2.25). The amount of rock a muon must traverse for a given arrival trajectory $(\phi, \cos\theta)$ is found by measuring the intensity for the trajectory and normalizing to the Crouch world average [132]. The the rock overburden of the Far Detector is 700 m of what is known locally as Lake Vermillion Greenstone. The density of the Lake Vermillion Greenstone, though far from uniform and interspersed with pockets of iron ore, is $2.8\,\mathrm{g/cm^3}$ on average, which gives a column depth of 2100 mwe [124] for particles coming down from directly above the detector. While this is rather shallow in comparison to other underground muon telescopes, there are other features that make MINOS a useful and unique detector. MINOS has a nearly flat rock overburden, so its slant depth varies smoothly as a function of zenith angle, which distinguishes it from experiments such as Super K and MACRO, which were built in mountains and had diverse slant depths for a given zenith angle. Thus, the surface muon energy can be found by integrating Eq. 2.25 from the detector to the surface. The surface energy spectrum can be seen in Fig. 4.8.

MINOS was designed to detect particles moving horizontally through the earth, not coming from the sky (see Ch. 3), so its sensitivity increases with decreasing zenith angle, and thus increasing rock overburden. The number of events falls off as a function of increasing slant depth, so this feature of the Far Detector is of little advantage to the study of cosmic particles when taken to extremes. This can be seen in figure 4.9 as $\cos(\theta)$ decreases (approaching the horizontal). The dip as $\cos(\theta)$ goes to one (approaching the vertical) is the effect of decreasing detector acceptance for particles coming straight down (parallel to the planes). The maximum detector acceptance is for particles traveling horizontally through the detector since it was designed to detect particles sent through Wisconsin from Fermilab. Even more telling of the detector geometry is the view of events in azimuth, figure 4.10. The south cardinal direction at $\phi = 180^o$, with north at $\phi = 360^\circ (0^\circ)$.

The preferred coordinate system when studying astronomical objects is one that is stationary
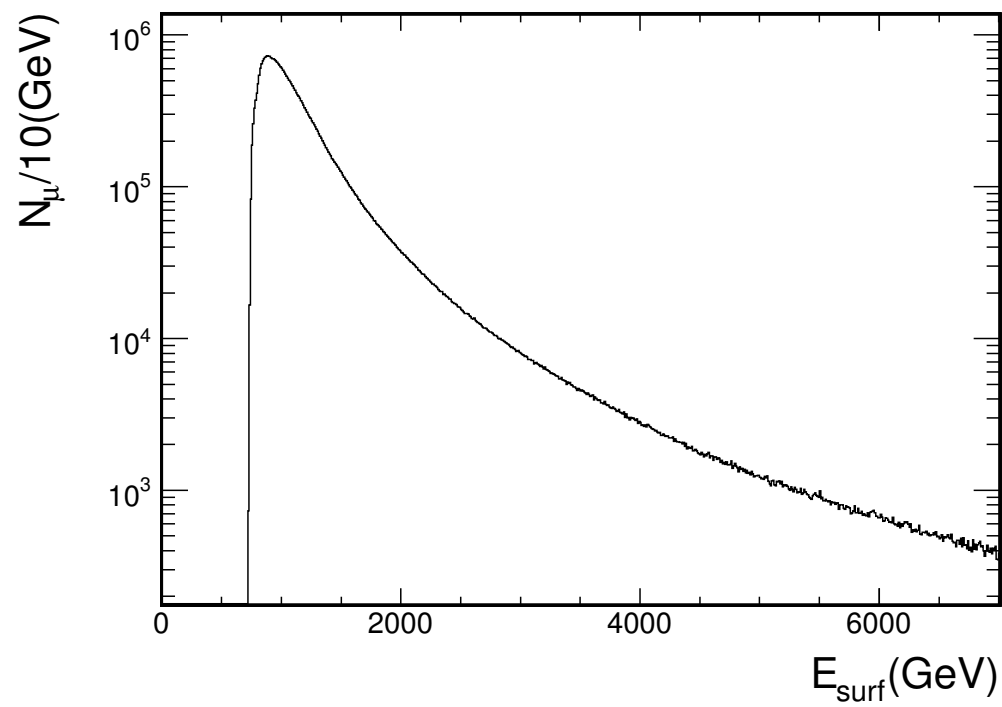
Figure 4.8: The surface energy spectrum for muons that survive to the far detector. The mean of the distribution gives $\langle E \rangle = 0.9 \, \text{TeV}$.
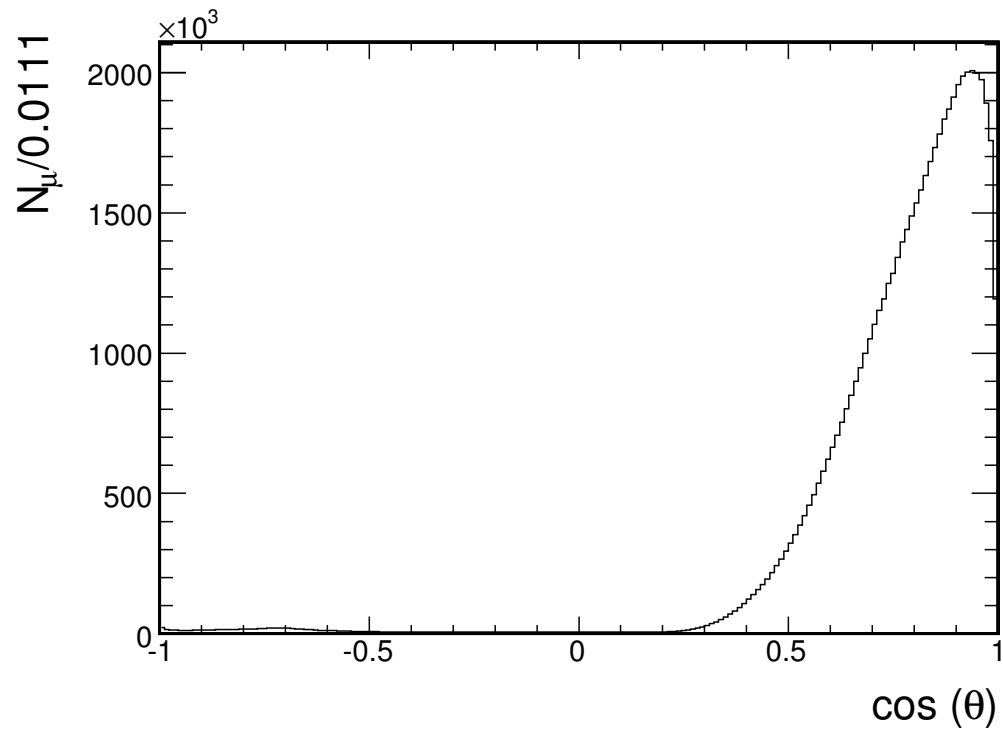
Figure 4.9: The zenith distribution of downward going muons in bins of equal solid angle ($\cos\theta$). The distribution falls off drastically as $\cos(\theta) \to 1$, because of detector geometry, and gradually as $\cos(\theta) \to 0$, because of increasing slant depth.
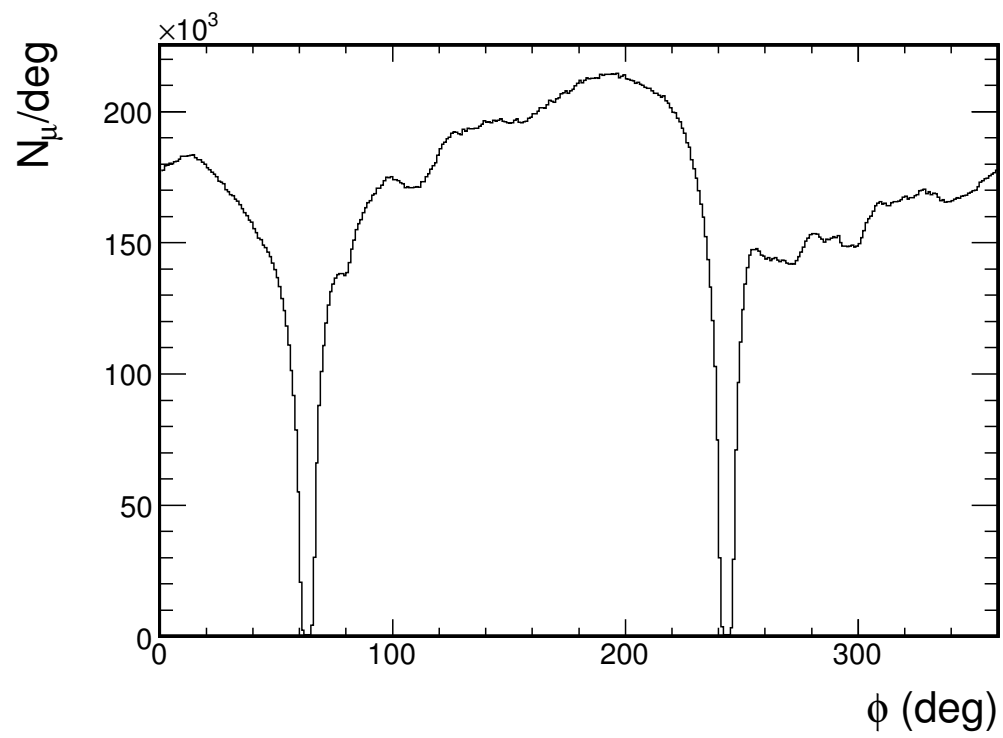
Figure 4.10: Event distribution in terms of azimuth, defined as $\phi = 0°$ to the north, $\phi = 90°$ to the east.

relative to the object being studied. Celestial coordinates are almost the inverse of horizon coordinates, with a point on the sky as the basis as opposed to a point on earth. Celestial coordinates use an imaginary grid projected on the sky, centered on the Earth's equatorial plane.   Azimuthal
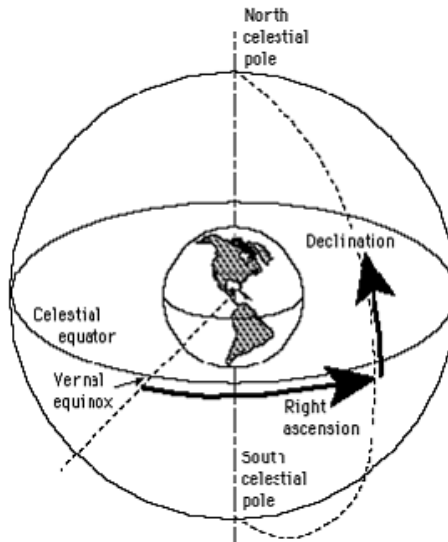
Figure 4.11: Celestial coordinates, superimposed on the celestial sphere

angle is right ascension (RA, α), and it ranges from 0° to 360°. RA is measured eastward from the Vernal equinox. Astronomers tend to use hours instead of degrees, to be consistent with the lines of longitude on Earth, but in this analysis, degrees will be used for computational ease. The angle out of the equatorial plane is declination (δ), ranging from $\pm 90^o$. An astronomical object precesses with respect to an observer on earth (reaches its zenith earlier on successive days) by four minutes (1°) since it takes 365.25 days for earth to cover the 360° sidereal year.   The effect of the difference between sidereal year and an Earth year is seen in the variation (dip) in the RA distribution of muons, as in figure 4.12. The detector was down for maintenance on the same day every week in the beginning of running. That downtime became a fraction of a day as maintenance became routine, so the downtimes would drift through the various sidereal times, and thus right ascensions, giving the distribution a smooth dip instead of a sharp dropoff. Also, these downtimes were longer at first, leaving a more distinct mark on the RA distribution of muons. This distribution illustrates the increasing percentage of livetime for the detector.   The declination distribution of muons in the Far Detector does not have a uniform exposure, as shown
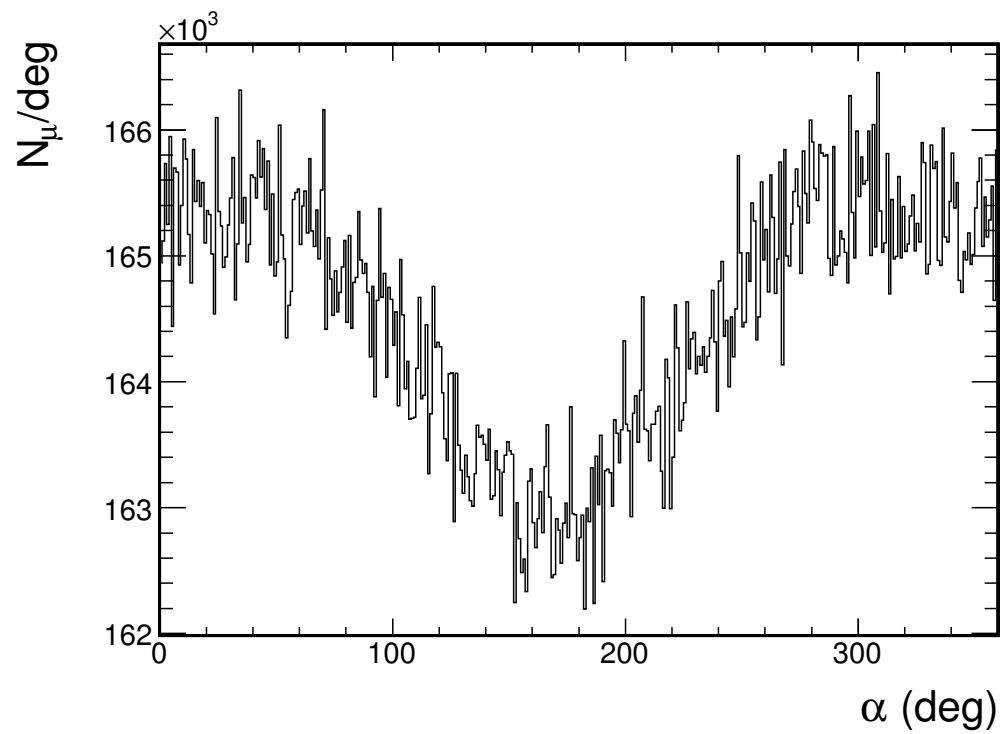
Figure 4.12: The RA distribution of muons in the Far Detector. The dip in the distribution is a feature of detector livetime, since RA is a function of time. Note that the vertical scale is hundreds of thousands of muons, so the dip has an overall magnitude of $\sim 1\%$.
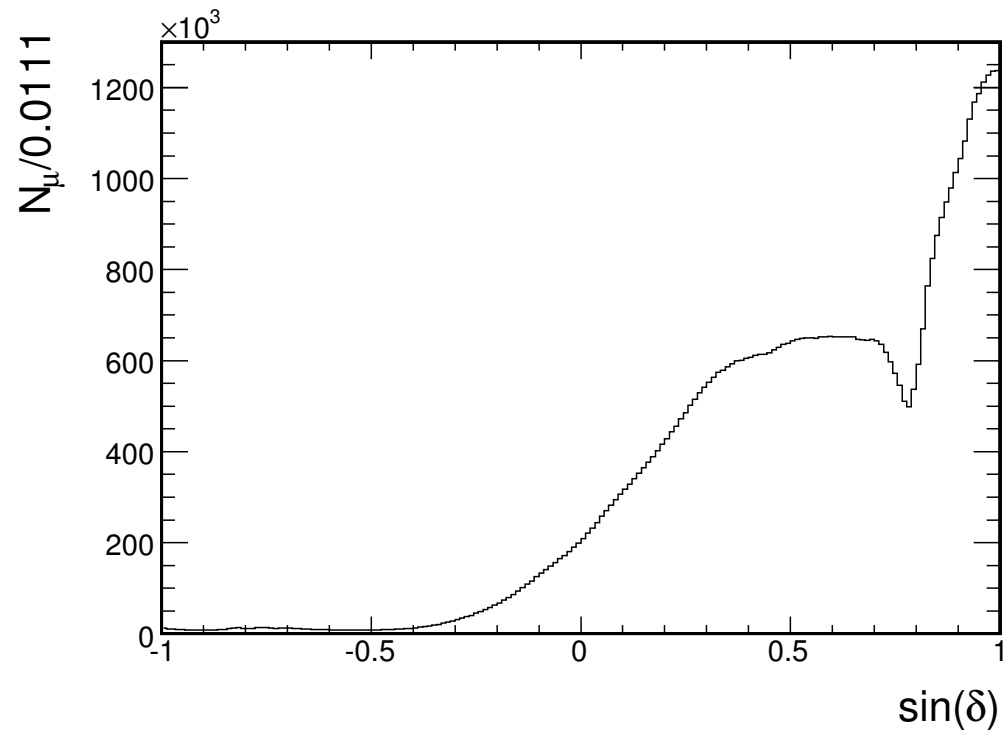
Figure 4.13: Declination distribution of muons in the Far Detector. The sharp dip at $\sim 45^o$ is the effect of detector orientation and acceptance, while the overall decreasing trends on both sides of the distribution show the effects of increasing slant depth.

in figure 4.13. Since the detector lies on its side, the range centered on declination 45° is underexposed. Also, the rock overburden restricts the search to northern hemisphere objects. This means that the all sky survey for cosmic ray point sources will be confined to two major regions of δ in the northern hemisphere, but unrestricted by RA.

4.7   The Study of Astrophysical Particles in the Far Detector

Using the ideas developed in chapter 2, we can gain an understanding of the astrophysical particles seen in the Far Detector. For cosmic ray muons coming from directly overhead, the minimum energy required to penetrate the rock overburden of the Far Detector is 700 GeV. While this is on the low end of the cosmic ray energy scale, it allows a larger statistical sample than would greater depth since cosmic ray primary flux as a function of energy falls off as $E^{-2.7}$. Taking the zenith angle to its limit increases the slant depth to the diameter of the earth. Though it is a gross approximation, if the rock that composed the entire earth was of similar density to the rock above the Far Detector, the slant depth would be on the order of 3×10^8 mwe It would require a muon of higher energy than ever detected to travel even 1% of this slant depth. Despite this fact, there are muons that are detected as coming from the other side of the earth, and they are of great importance. These muons are induced by neutrinos interacting with the rock below the detector. This is a viable way to detect neutrinos, put the detector in a place that no other particle could penetrate. Though downward going events may be neutrino induced, if an event can be determined to have originated from below the detector, it is surely neutrino induced. This fact is of great importance to the search for a correlation between particles in the far detector and Gamma Ray Bursts.

The highest energy cosmic ray primaries are of the most interest to a point source search, as they have minimal deflection by the galactic magnetic field and might actually give rise to muon astronomy by conventional means (see chapter 2), rather than new and exotic physics. Their extremely low flux makes them difficult to study with an underground detector, however. While surface experiments have the luxury of placing detectors across kilometers of rolling prairie to see one or two particles from an EAS, underground detectors are confined to contiguous configurations limited by cavern size, material transport cost and assembly feasibility. The entire surface area of the Far Detector visible to muons, neglecting known acceptance issues, is a mere 500 m^2. Were

the detector on the surface, it would see one event with energy of the order 10^{20} eV every 40 *years*. Underground, because of the power law falloff in energy spectrum as a function of slant depth, it would take 90 years for such an event to be detected. MINOS will be unable to make a statement about the behavior of these enigmatic particles, given that it will not detect any. Therefore, were a cosmic ray point source to be detected by the Far Detector from lower energy cosmic rays, it would signal the existence of some exotic new physics.

Chapter 5

Seasonal Effect

When cosmic rays interact in the stratosphere, mesons are produced in the primary hadronic shower. These mesons either interact again and produce lower energy hadronic cascades, or decay into high energy muons which might be observed deep underground. While the temperature of the troposphere varies considerably within the day, the temperature of the stratosphere remains nearly constant, only changing slowly over longer timescales such as seasons. Increases in temperature of the stratosphere cause decreases in density, reducing the chance of meson interaction, resulting in a larger fraction decaying to produce muons. In addition, the height of the primary cosmic ray interaction increases with increasing temperature. This results in a higher muon rate observed deep underground [59, 133, 134]. The effect increases as higher energy muons are sampled, because higher energy mesons with increased lifetimes (due to time dilation) are involved. The rate of low energy muons at the surface is also affected by the temperature because the varying production altitude changes the chances of the muon decaying before reaching earth, an effect not relevant for detectors deep underground which only see much higher energy particles.

The Far Detector has a 5.4 kton fiducial mass and a 6.91×10^6 cm^{2}sr [135] acceptance. Its depth, large acceptance and flat overburden make it possible to observe cosmic-ray induced muons of minimum surface energy 0.7 TeV and thus detect the small seasonal fluctuations in the flux of deep underground muons. The seasonal effect increases as muon energy increases, and the large acceptance of the Far Detector allows a significant accumulation of statistics with which to perform this analysis. The Far Detector is the deepest underground detector with a magnetic field, which allows the separation of particles by charge. This allows the first measurement of

seasonal variations for μ^+ separate from μ^-, as well as a measurement of a seasonal variation in the cosmic ray charge ratio. A new model was developed to describe the observed effect, and is the first to include the contribution from kaons. Collaboration with atmospheric physicists has made available atmospheric temperature data from the European Centre for Medium-Range Weather Forecasts (ECMWF) at the Soudan site [136]. This temperature data set has higher precision than any other used for the seasonal variation analysis. The muon data used in this analysis were collected over four years, from August 1, 2003 to July 31, 2007; this period was chosen because it includes four complete annual cycles and numbers 55.18 million muons.

5.1 Motivation

5.1.1 Muon Intensity Underground

The intensity of muons underground is directly related to the production of mesons in the upper atmosphere by hadronic interactions between cosmic rays and the nuclei of air molecules. It is assumed that meson production falls off exponentially as e^{-X/Λ_N} where Λ_N is the absorption mean free path of the meson producing cosmic rays and X is the slant depth of atmospheric material traversed. It is also assumed that the mesons retain the same direction as their progenitors, that the cosmic ray sky is isotropic in solid angle at the top of the atmosphere, and we neglect ionization. These are particularly valid for the large energies of the mesons that produce muons seen in the MINOS Far Detector. In this approximation, Λ_N is constant. We will consider two meson absorption processes: further hadronic interactions, dX/Λ_M, where dX is the amount of atmosphere traversed and M is either a π or K meson (charm and heavier meson production doesn't become important until $\sim 10^5$ TeV), and $M \rightarrow \mu\nu_\mu$ decay,

5.1.2 Temperature Effect on Muon Intensity

The temperature changes that occur in the atmosphere are not uniform, instead occurring at multiple levels, and neither muon nor meson production occurs at one particular level. It would be very difficult to record the temperature distribution of the atmosphere and try to determine where in this distribution a particular muon was created. The perturbations that variations in temperature cause in μ intensity are small, however, and as a result properly chosen atmospheric weights can be used to approximate the effective temperature of the atmosphere as a whole, T_{eff}. Define

$\eta(X) \equiv (T(X) - T_{\text{eff}})/T_{\text{eff}}$, and $\epsilon_M = \epsilon_M^0(1 + \eta)$, where ϵ_M^0 is the constant value of ϵ_M when $T = T_{\text{eff}}$. This is the temperature that would cause the observed μ intensity if the atmosphere actually were isothermal. To quantify the temperature effect on intensity, the temperature dependence of Eq. 2.13 on page 21 needs to be considered. The meson production term in Eq. 2.14 on page 21 can then be expanded:

$$\frac{d\mathcal{M}}{dX} = \frac{Z_{NM}}{\Lambda_N} N_0 e^{-X/\lambda_N} - \mathcal{M}(E, X, \cos\theta) \left[\frac{1}{\Lambda_M} + \frac{\epsilon_M^0(1+\eta)}{EX\cos\theta} \right]. \tag{5.1}$$

The analytic solution to this differential equation is difficult to find since $\eta(X')$ is an arbitrary function of X'. A solution to first order in $\eta(X')$ can be found by expanding the exponential in a power series, and then following the procedure outlined above, beginning with Eq. 2.15 on page 21. The solution can be written as $\mathcal{M}(E, X, \cos\theta) = \mathcal{M}^0 - \mathcal{M}^1$, where $\mathcal{M}^0(E, X)$ is the solution where $\epsilon = \epsilon^0$, which occurs at temperature $T = T_{\text{eff}}$ is given by:

$$
\begin{aligned}
\mathcal{M}^1(E, X, \theta) &= \frac{Z_{NM}}{\lambda_N} N_0(E) e^{-X/\Lambda_M} \left(\frac{X}{\Lambda_M} \right)^{-\epsilon_M^0/E\cos\theta} \frac{\epsilon_M^0}{E\cos\theta} \\
&\quad \int_0^X dX' \frac{\eta\Lambda_M}{X'} \left(\frac{X'}{\Lambda_M} \right)^{\epsilon_M^0/E\cos\theta+1} \left\{ \frac{1}{\epsilon_M/E\cos\theta + 1} - \frac{X'/\Lambda_M'}{\epsilon_M/E\cos\theta + 2} \right. \\
&\quad \left. + \frac{1}{2!} \frac{(X'/\Lambda_M')^2}{\epsilon_M/E\cos\theta + 3} - ... \right\}, \tag{5.2}
\end{aligned}
$$

If $E\cos\theta \gg \epsilon_M^0$, then the integrand is very small and $\eta(X') = \eta(X)$. This is the case when interactions dominate, as time dilation effects allow these very high energy pions to travel a great distance before decaying. If $E\cos\theta \ll \epsilon_M^0$, then the pions will not travel as far before decaying and the integrand is large only when X' is near X, and again, $\eta(X')$ can be taken out of the integral [59].

Writing the solution of $\mathcal{M}$ where $T = T_{\text{eff}}$ as $\mathcal{M}^0$ and letting $\epsilon_M = \epsilon_M^0(1+\eta)$, an expression for the change in muon production induced by temperature variations can be found. Define $\Delta\mathcal{M} \equiv \mathcal{M} - \mathcal{M}^0$, then

$$
\begin{aligned}
\Delta\mathcal{M} &= \frac{Z_{NM}}{\lambda_N} N_0(E) e^{-X/\Lambda_M} \frac{\epsilon_M^0 \eta X}{E\cos\theta} \times \left[\left\{ \frac{1}{(\epsilon_M(X)/E\cos\theta + 1)^2} \right. \right. \\
&\quad \left. - \frac{X/\Lambda_M'}{(\epsilon_M(X)/E\cos\theta + 2)^2} + \frac{1}{2!} \frac{(X/\Lambda_M')^2}{(\epsilon_M(X)/E\cos\theta + 3)^2} - ... \right\} \\
&\quad - \left\{ \frac{1}{\epsilon_M^0/E\cos\theta + 1)^2} - \frac{X/\Lambda_M'}{(\epsilon_M^0/E\cos\theta + 2)^2} + \frac{1}{2!} \frac{(X/\Lambda_M')^2}{(\epsilon_M^0/E\cos\theta + 3)^2} - ... \right\} \right]
\end{aligned} \tag{5.3}
$$

To first order in η, this expression reduces to:

$$\Delta\mathcal{M} = \frac{Z_{NM}}{\lambda_N} N_0(E) e^{-X/\Lambda_M} \frac{\epsilon_M^0 \eta X}{E\cos\theta} \times \left\{ \frac{1}{(\epsilon_M^0/E\cos\theta+1)^2} - \frac{2X/\Lambda_M'}{(\epsilon_M^0/E\cos\theta+2)^2} \right. \qquad (5.4)$$
$$\left. + \frac{1}{2!} \frac{3(X/\Lambda_M')^2}{(\epsilon_M^0/E\cos\theta+3)^2} - ... \right\}$$

Using Eq. 2.19 on page 23 and Eq. 2.20 on page 23, an expression for the change in differential muon intensity can be found:

$$\Delta\frac{dI_\mu}{dE_\mu} = \int_0^\infty dX \frac{\epsilon_M^0}{X\cos\theta(1-r_M)} \int_{E_\mu}^{E_\mu/r_M} \frac{dE}{E^2} \frac{Z_{NM}}{\lambda_N} N_0(E) e^{-X/\Lambda_M} \frac{\epsilon_M^0 \eta X}{E\cos\theta} \times$$
$$\left\{ \frac{1}{(\epsilon_M/E\cos\theta+1)^2} - \frac{2X/\Lambda_M'}{(\epsilon_M/E\cos\theta+2)^2} + \frac{1}{2!}\frac{3(X/\Lambda_M')^2}{(\epsilon_M/E\cos\theta+3)^2} - ... \right\}, \quad (5.5)$$

which can be written:

$$\Delta\frac{dI_\mu}{dE_\mu} = \frac{Z_{NM}}{\lambda_N} \left(\frac{\epsilon_M^0}{E_\mu\cos\theta}\right)^2 \frac{E_\mu^{-(\gamma+1)}}{(1-r_M)} \int_0^\infty dX e^{-X/\Lambda_M} \eta I_M(z), \qquad (5.6)$$

where

$$I_M(z) = \int_1^{1/r_M} \frac{dz}{z^{-(\gamma+2)}} \times \left\{ \frac{1}{(\epsilon_M^0/E_\mu\cos\theta+z)^2} - \frac{2X/\Lambda_M'}{(\epsilon_M^0/E_\mu\cos\theta+2z)^2} \right.$$
$$\left. + \frac{1}{2!}\frac{3(X/\Lambda_M')^2}{(\epsilon_M^0/E_\mu\cos\theta+3z)^2} - ... \right\}, \qquad (5.7)$$

Now, a solution to this integral can be found for $E_\mu \gg \epsilon_\pi (I^H)$ and for $E_\mu \ll \epsilon_\pi (I^L)$:

$$\begin{aligned}
I_M^H(E_\mu) &= \frac{1}{\gamma+3}\left[1-(r_M)^{\gamma+3}\right]\left\{1 - \frac{2X/\Lambda_M'}{2^2} + \frac{1}{2!}\frac{3(X/\Lambda_M')^2}{3^2} - ...\right\} \\
&= \frac{1}{\gamma+3}\left[1-(r_M)^{\gamma+3}\right]\sum_{n=0}^\infty \frac{(-X/\Lambda_M')^n}{n!(n+1)} \\
&= \frac{1}{\gamma+3}\left[1-(r_M)^{\gamma+3}\right](1-e^{-X/\Lambda_M'})\frac{\Lambda_M'}{X} \\
I_M^L(E_\mu) &= \frac{1}{\gamma+1}\left[1-(r_M)^{\gamma+1}\right]\left(\frac{E_\mu\cos\theta}{\epsilon_M}\right)^2\left\{1 - 2X/\Lambda_M' + \frac{1}{2!}3(X/\Lambda_M')^2 - ...\right\} \\
&= \frac{1}{\gamma+1}\left[1-(r_M)^{\gamma+1}\right]\left(\frac{E_\mu\cos\theta}{\epsilon_M}\right)^2\sum_{n=0}^\infty \frac{(-X/\Lambda_M')^n(n+1)}{n!} \\
&= \frac{1}{\gamma+1}\left[1-(r_M)^{\gamma+1}\right]\left(\frac{E_\mu\cos\theta}{\epsilon_M}\right)^2(1-X/\Lambda_M')e^{-X/\Lambda_M'} \qquad (5.8)
\end{aligned}$$

These expressions can be combined in a form that is valid for all energies (Eq. 2.20 on page 23):

$$\Delta\frac{dI_\mu}{dE_\mu} \simeq \frac{E_\mu^{-(\gamma+1)}}{1-Z_{NN}}\int_0^\infty dX(1-X/\Lambda'_M)^2 e^{-X/\Lambda_M}\eta(X)\frac{A_M^1}{1+B_M^1 K(X)\left(E_\mu\cos\theta/\epsilon_M^0\right)^2}, \quad (5.9)$$

where

$$A_M^1 \equiv \frac{Z_{N,\mathcal{M}}}{(1-r_\pi)}\frac{1-(r_M)^{\gamma+1}}{\gamma+1}$$

$$B_M^1 \equiv \frac{(\gamma+3)}{(\gamma+1)}\frac{1-(r_M)^{\gamma+1}}{1-(r_M)^{\gamma+3}}$$

$$K(X) \equiv \frac{(1-X/\Lambda'_M)^2}{(1-e^{-X/\Lambda'_M})\Lambda'_M/X}$$

The exact solution for $I_M^L(E_\mu)$ has been replaced with an approximation that preserves the physical behavior of the system at low energies. These low energy mesons are relatively insensitive to changes in temperature because they decay before they have a chance to interact. So, this equation describes the expected behavior that mesons at very low energies will decay fairly high in the atmosphere. It should be noted that these mesons will not contribute any muons to an underground detector, because the muons they produce will be below the threshold energy.

There is a slight dip in this distribution as X approaches Λ'_M, which results from the approximation made to join the high and low energy solutions for the approximation to Eq. 5.6 on the preceding page. The low energy solution will go to zero when $X = \Lambda'_M$ and below zero when $E_{th} \ll \epsilon_M$. The reason for this is that these low energy muons have such little energy that they decay in flight, producing a deficit in muons correlated to temperature changes (the "negative temperature coefficient" related in older literature [59, 137, 138]). This effect is not seen by detectors deeper than 50 mwe, such as MINOS. The fact that there is a dip and subsequent rise for $X > 480\,\text{g/cm}^2$ does not affect an analysis for a detector deeper than 50 mwe since the weight is integrated over the entire atmosphere in discrete steps of dX and properly normalized, and this atmospheric depth is unimportant for the production of muons.

Remembering that $\eta(X) \equiv (T(X) - T_{\text{eff}})/T_{\text{eff}}$, the relationship between atmospheric temperature fluctuations and intensity variations can be written as:

$$\Delta I_\mu \equiv \int_{E_{th}}^\infty \Delta\frac{dI_\mu}{dE_\mu}dE_\mu = \int_0^\infty dX\alpha(X)\frac{\Delta T(X)}{T_{\text{eff}}}e^{X/\Lambda_M} \qquad (5.10)$$

where the temperature coefficient $\alpha(X)$ can be written:

$$\alpha(X) = \int_{E_{th}}^{\infty} dE_\mu \frac{A_M^1 E_\mu^{-(\gamma+1)}}{1 + B_M^1 \left(E_\mu \cos\theta/\epsilon_M\right)^2} \tag{5.11}$$

Recalling that M applies independently to K and π mesons and that the total muon intensity is the sum of the contribution by K and π (Eq. 2.26 on page 24), the temperature induced change in muon intensity can be written as:

$$\Delta I_\mu \equiv \int_0^{\infty} dX \alpha(X) \frac{\Delta T(X)}{T_{\text{eff}}} e^{X/\Lambda_\pi} + \int_0^{\infty} dX \alpha(X) \frac{\Delta T(X)}{T_{\text{eff}}} e^{X/\Lambda_K} \tag{5.12}$$

Thus far, T_{eff} has been treated as an arbitrary constant. T_{eff} cannot be arbitrary, however, since it determines the weighting of the various atmospheric levels such that the isothermal atmosphere approximation can be made. Knowing that $\eta(X) \equiv (T(X) - T_{\text{eff}})/T_{\text{eff}}$, et T_{eff} be defined such that when $T(X) = T_{\text{eff}}$, $\Delta I_\mu = 0$, which gives:

$$T_{\text{eff}} = \frac{\int_0^{\infty} dX T(X) \alpha^\pi(X) + \int_0^{\infty} dX T(X) \alpha^K(X)}{\int_0^{\infty} dX \alpha^\pi(X) + \int_0^{\infty} dX \alpha^K(X)} \tag{5.13}$$

Since the temperature was measured at discrete levels, the actual integration was done numerically over the atmospheric levels ΔX_n:

$$T_{\text{eff}} \simeq \frac{\sum_{n=0}^{N} \Delta X_n T(X_n) \left(W_n^\pi + W_n^K\right)}{\sum_{n=0}^{N} \Delta X_n \left(W_n^\pi + W_n^K\right)} \tag{5.14}$$

where

$$W_n^\pi \equiv \frac{A_\pi^1 e^{-X_n/\Lambda_\pi} (1 - X_n/\Lambda_M')^2}{\gamma + (\gamma+1) B_\pi^1 K(X_n) \left(E_{th} \cos\theta/\epsilon_\pi\right)^2}$$

$$W_n^K \equiv \frac{A_K^1 e^{-X_n/\Lambda_K} (1 - X_n/\Lambda_M')^2}{\gamma + (\gamma+1) B_K^1 K(X_n) \left(E_{th} \cos\theta/\epsilon_K\right)^2}$$

$$K(X) \equiv \frac{(1 - X/\Lambda_M')^2}{(1 - e^{-X/\Lambda_M'})\Lambda_M'/X}$$

and $1/\Lambda_M' \equiv 1/\Lambda_N - 1/\Lambda_M$. Using the appropriate values for the constants $A_\pi^1 = 1$, $A_K^1 = 0.054$, $B_\pi^1 = 1.47$, $B_K^1 = 1.74$ (Eq. 5.9 on the preceding page), $\Lambda_N = 120\,\text{g/cm}^2$, $\Lambda_\pi = 160\,\text{g/cm}^2$ and $\Lambda_K = 180\,\text{g/cm}^2$ [43] as well as the experimental value for the threshold energy, $E_{th} \cos\theta =$

$0.7\,\mathrm{TeV}$, a numerical value of the effective temperature can be found. Note that the expression to calculate T_{eff} in the pion scaling limit, ignoring the kaon contribution, can be written

$$T_{\mathrm{eff}} \simeq \frac{\sum_{n=0}^{N} \Delta X_n T(X_n) 1/X_n \left(e^{-X_n/\Lambda_\pi} - e^{-X_n/\Lambda_N}\right)}{\sum_{n=0}^{N} \Delta X_n 1/X_n \left(e^{-X_n/\Lambda_\pi} - e^{-X_n/\Lambda_N}\right)}. \tag{5.15}$$

This recovers the MACRO [133] calculation for effective temperature.

With this definition of effective temperature, an "effective temperature coefficient" can be defined:

$$\alpha_T = \frac{1}{I_\mu^0} \int_0^\infty dX \int_{E_{th}}^\infty dE_\mu \frac{A_M^1 E_\mu^{-(\gamma+1)}}{1 + B_M^1 \left(E_\mu \cos\theta/\epsilon_M\right)^2}, \tag{5.16}$$

where I_μ^0 is the intensity for a given temperature T. Now that the atmospheric temperature has been parameterized and the effective temperature coefficient defined, the relationship between atmospheric temperature fluctuations and intensity variations can be found:

$$\frac{\Delta I_\mu}{I_\mu^0} = \int_0^\infty dX \alpha(X) \frac{\Delta T(X)}{T_{\mathrm{eff}}} = \alpha_T \frac{\Delta T_{\mathrm{eff}}}{T_{\mathrm{eff}}} \tag{5.17}$$

The theoretical prediction of α_T for properly weighted atmospheric temperature distribution can be written (Eq. 5.17) as:

$$\alpha_T = \frac{T}{I_\mu^0} \frac{\partial I_\mu}{\partial T}. \tag{5.18}$$

Barrett [59] shows that for a muon spectrum such as Eq. 2.20 on page 23, the theoretical α_T can be written in the more useful form:

$$\alpha_T = -\frac{E_{th}}{I_\mu^0} \frac{\partial I_\mu}{\partial E_{th}} - \gamma \tag{5.19}$$

This can be calculated using the intensity found in Eq. 2.26 on page 24 and a little algebra:

$$\alpha_T = \frac{1}{D_\pi} \frac{1/\epsilon_K + A_K(D_\pi/D_K)^2/\epsilon_\pi}{1/\epsilon_K + A_K(D_\pi/D_K)/\epsilon_\pi} \tag{5.20}$$

where

$$D_\pi \equiv \frac{\gamma}{\gamma+1} \frac{\epsilon_\pi}{1.1 E_{th} \cos\theta} + 1,$$

$$D_K \equiv \frac{\gamma}{\gamma+1} \frac{\epsilon_K}{1.1 E_{th} \cos\theta} + 1$$

and $A_K = 0.054$, the same coefficient as for the kaon contribution to the intensity. Note that this can be reduced to MACRO's previously published expression for $\langle \alpha_T \rangle_\pi$ [133], which was only valid for pion induced muons, by setting $A_K = 0$ (no kaon contribution).

ΔI_μ is the deviation from the overall average muon intensity, I_μ^0 is the muon intensity evaluated at a given temperature T, and $\alpha(X)$ is the coefficient relating changes in temperature to changes in intensity as a function of slant depth X, the path length through the atmosphere.

The atmosphere consists of many different levels that vary continuously in temperature and pressure, and meson production does not always occur at the same pressure level. A viable way to study the effect of temperature on muon rate is to approximate the atmosphere as an isothermal body. Of course, the atmosphere is *not* and isothermal body, as seen in the solid line in Fig. 5.1 on the next page. The surface of the earth is at approximately 1000 hPa, and the density of the atmosphere falls off exponentially beyond 1 hPa. The weighting of the atmosphere is done with carefully chosen levels such that the essential hadronic interaction physics is included and can be treated with a characteristic temperature [59, 133]. T_{eff} is defined as the effective temperature the atmosphere would have were it an isothermal meson producing entity, weighted exponentially with increasing height because high energy muons tend to be produced higher in the atmosphere.

The critical energy values are of particular relevance to this effect since the relationship between meson energy and meson critical energy mediate interaction or decay probability. A meson with energy greater than its critical energy is more likely to interact than decay, and the probability of interaction increases with energy. The weight for each pressure level $(W_n^\pi + W_n^K)$ is shown in Fig. 5.1 on the following page, normalized to one. This distribution reflects the dominant atmospheric features that produce muons visible to a detector under 2100 mwe of earth. The most probable height for a cosmic ray proton to interact is at the very top of the atmosphere, and the most probable meson that produces a high energy muon is one that is produced high in the atmosphere. High energy mesons that are produced lower in the atmosphere have a greater probability of interacting a second time, and thus greater probability of producing muons that are *not* seen by MINOS. These effects are reflected in this distribution that properly weights the various atmospheric temperature levels such that the isothermal approximation can be applied.

The intensity for a detector counting discrete particles can be written as:

$$R_\mu = \int I_\mu(\Omega)\epsilon(\Omega)A_{\text{tot}}(\Omega)\mathrm{d}\Omega, \qquad (5.21)$$

where $R_\mu = N_\mu/t$, the number of muons observed over a particular time period t, A_{tot} is the total
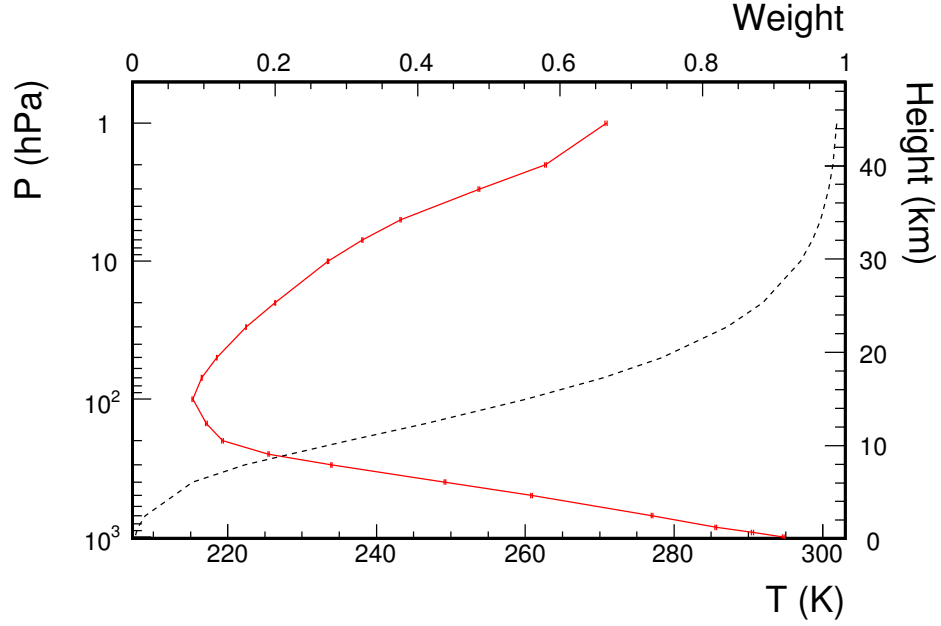
Figure 5.1: The four year average summer temperature at various atmospheric depths (solid line). The range is from $1000\,\mathrm{hPa}$ ($1\,\mathrm{hPa} = 1.019\,\mathrm{g/cm^2}$), near Earth's surface, to $1\,\mathrm{hPa}$ (nearly $50\,\mathrm{km}$) , near the top of the stratosphere. The dashed line is the weight as a function of pressure level used to find T_{eff}. The weights are determined by Eq. 5.14 on page 83.

effective area of the detector, ϵ is the efficiency, and the expression is integrated over the solid angle Ω. The detector configuration has remained constant over the entire data collection period, so A_{tot} is constant. The detector is triggered by a particle that makes at least four hits in five contiguous planes. The result is a well-reconstructed track of length at least 0.3 m, which corresponds to a minimum muon energy within the detector of 100 MeV [139]. This eliminates any low energy or non-muon backgrounds. Atmospheric neutrino interactions in the detector are so rare that they provide a negligible contribution to the intensity, (though their intensity should also be affected by the change in atmospheric temperature). Detector instability could cause fluctuations that obscure intensity variations by reducing the efficiency term in the muon intensity. However, the detector reconstruction includes redundancy so that inefficiencies in any one plane do not reduce the efficiency to find the track. The planes use the stable medium of plastic scintillator as their active detector, and the regular calibration of the light detection systems assures detector stability [109]. Thus, the geometric acceptance is constant over time and Eq. 5.17 on page 84 and Eq. 5.21 lead

to:

$$\frac{\Delta I_\mu}{I_\mu} = \frac{\Delta R_\mu/\epsilon(\Omega)A_{\text{tot}}(\Omega)}{\langle R_\mu\rangle/\epsilon(\Omega)A_{\text{tot}}(\Omega)} = \frac{\Delta R_\mu}{\langle R_\mu\rangle} \qquad (5.22)$$

where ΔR_μ is the deviation from the mean muon rate for the particular time period.

Now that the atmospheric temperature has been parameterized, α_T defined, and an expression for the experimental intensity determined, the relationship between atmospheric temperature fluctuations and intensity variations can be written:

$$\int_0^\infty dX \alpha(X)\frac{\Delta T(X)}{T(X)} = \alpha_T \frac{\Delta T_{\text{eff}}}{\langle T_{\text{eff}}\rangle} = \frac{\Delta R_\mu}{\langle R_\mu\rangle}. \qquad (5.23)$$

Eq. 5.23 is the expression that will be used to experimentally determine the effective temperature coefficient, α_T. As the muon energy increases, muon intensity becomes proportional to the meson critical energy. The critical energy, in turn, depends linearly on atmospheric temperature. Thus, for high energy muons, the effective temperature coefficient approaches one. This dimensionless parameter α_T then is the fraction of mesons that are sensitive to atmospheric temperature variations.

5.1.3   The Data

The muon data for this analysis were accumulated over a four year span, beginning on 1 August, 2003, at which time the detector was fully operational. Beginning with 55.18 million cosmic ray tracks, a series of cuts were performed to ensure a clean data sample. Entire runs were excluded based on the criteria described in [60]:

1. Require physics data, runs must be more than 5 minutes long

2. Detector must be reading all channels

3. Runs must contain "good physics data", which includes correct trigger bits, complete readout, and minimal dead chips

4. Remove runs with anomalous rates: $0\,\text{Hz} < \text{cosmic ray rate} < 1\,\text{Hz}$

5. Remove runs that the atmospheric neutrino analysis has flagged as having far too many contained events [117, 118]
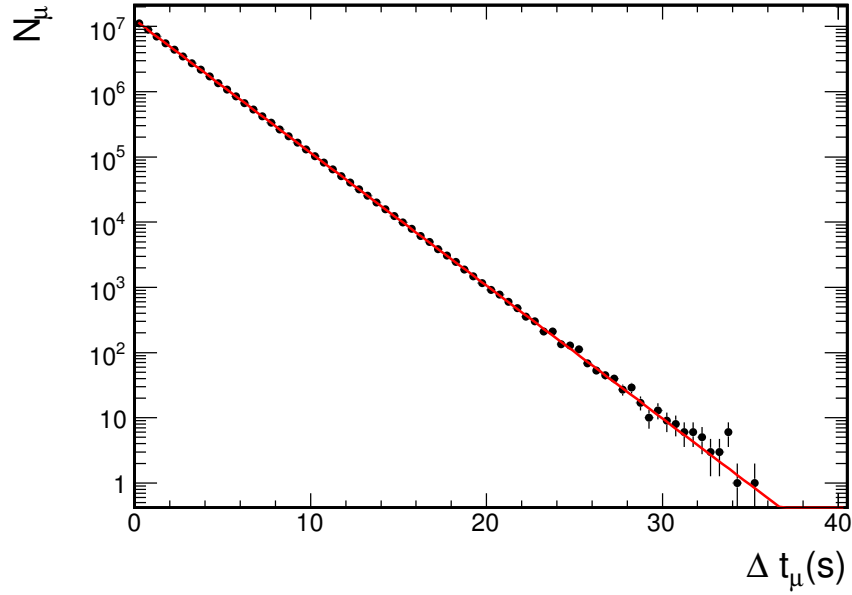
Figure 5.2: The time between consecutive cosmic ray muon arrivals. A fit to a Poisson distribution [131] gives $\chi^2/ndf = 45.59/68$; $\langle R_\mu \rangle = 0.4690 \pm 0.0001$ (from slope). The Poissonian nature of the muon arrival times demonstrates the absence of short-timescale systematic effects on the data.

Events were excluded if taken during periods when the detector was not functioning within normal parameters, mainly due to electronics repairs, the magnetic field being out of tolerance, calibration, etc [60]. Since the MINOS experiment is designed to measure beam neutrino oscillations, there is a different trigger used when the neutrino beam pulses to maximize the detection of beam-produced neutrinos. This trigger is based on the timing of the beam pulse and it opens the detector to record all hits during a $100\,\mu$s window. The muon data that is recorded $\pm50\,\mu$s of a beam pulse is excluded since it could be of terrestrial, not cosmic origin. This cut eliminates a very small number (2186) of well understood background events. A total of 53.12 million events survived the cuts for the μ^+, μ^- combined sample. Upon examination of the data, it was found that on three days there were fluctuations that deviated greatly from similar days. The great stability of the detector over the 1461 days of data made these days stand out, and the experiment logbook confirmed that exceptional events occurred (*e.g.* September 25-26, 2003, when new timing system firmware caused channel failures) and the data from these days were excluded from analysis. After all cuts were applied, 96.3% of the data remained.

The time between consecutive underground muon arrivals has been shown to follow a gamma function (Poisson of order one) for MACRO [131] as well as MINOS (Sec. 4.5). A histogram of the time between consecutive muon arrivals in the MINOS data is shown in Fig. 5.2 on the preceding page, along with a Poisson expectation. The fit result from Fig. 5.2 on the facing page was used to find the mean rate $\langle R_\mu \rangle$ 0.4690 Hz $\pm$ 0.0001. The fact that the data is so well described by the Poisson distribution demonstrates the absence of short-timescale systematic effects on the data. To find the rate for each day, the number of muons counted was divided by the livetime in seconds for that day.

The consistency and availability of European Centre for Medium-Range Weather Forecasts (ECMWF) atmospheric temperature data at the Soudan site [136] over the period of time in which the muon data was recorded ensures a high statistics temperature sample. T_{eff} was found using the ECMWF global atmospheric model [136]. The model uses a number of different observation methods (land surface sounding, satellite sounding, upper air sounding) at various locations around the globe, then interpolates for a particular location. For this analysis, The ECMWF model produced atmospheric temperatures at 16 discrete pressure levels: 1000, 925, 850, 700, 500, 400, 300, 250, 200, 150, 100, 70, 50, 30, 20 and 10 hPa (1 hPa = $1.019 \, \mathrm{g/cm}^2$), at four times, 0000 h, 0600 h, 1200 h and 1800 h each day. T_{eff} was calculated four times each day using these temperature values and Eq. 5.14 on page 83, then averaged. The daily statistical error on T_{eff} was estimated by calculating $\sigma^2 = \langle T_{\mathrm{eff}}^2 \rangle - \langle T_{\mathrm{eff}} \rangle^2$.

The experimentally determined parameter, α_T (Eq. 5.23 on page 87), is a dimensionless value that depends on the daily deviation from $\langle R_\mu \rangle$ and $\langle T_{\mathrm{eff}} \rangle$. The deviation from the mean rate was calculated as $\Delta R_\mu = (R_{\mathrm{day}} - \langle R_\mu \rangle)/ \langle R_\mu \rangle$. A histogram of the deviation from the mean rate per day over the entire set of data is shown in Fig. 5.3 on the next page. The errors in the daily rate were calculated from the square root of the number of events divided by the livetime. A typical day at $\langle R_\mu \rangle = 0.4690$ Hz yields ~40,000 muons, resulting in error bars of order 0.5%. The expected variation with season is clearly shown, with maxima in August and minima in February. These maxima peak at rates that are within 0.5% of each other.

For the four year period $\langle T_{\mathrm{eff}} \rangle = 221.44$ K. The deviation from $\langle T_{\mathrm{eff}} \rangle$ was calculated as $\Delta T_{\mathrm{eff}} = (T_{\mathrm{eff,day}} - \langle T_{\mathrm{eff}} \rangle)/ \langle T_{\mathrm{eff}} \rangle$. The distribution of ΔT_{eff} over the data period can be seen in Fig. 5.4 on the following page, with strong periodic seasonal correlation with the data. There is also striking correspondence between Fig. 5.3 and Fig. 5.4 for short term maxima and minima
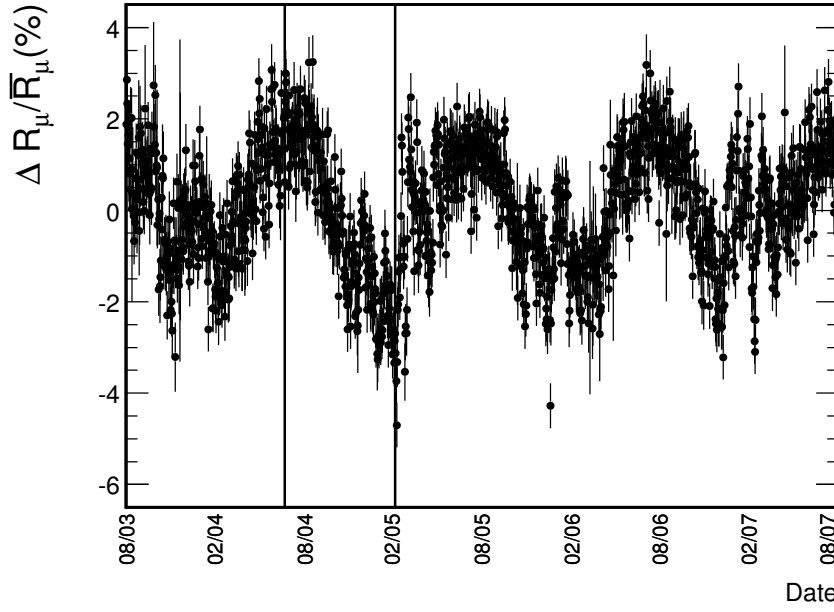
Figure 5.3: The daily deviation from the mean rate of cosmic ray muon arrivals from 8/03-8/07, shown here with statistical error bars. The periodic fluctuations have the expected maxima in August, minima in February. The vertical bars indicate the period of time when the detector ran in nominal reverse field mode.
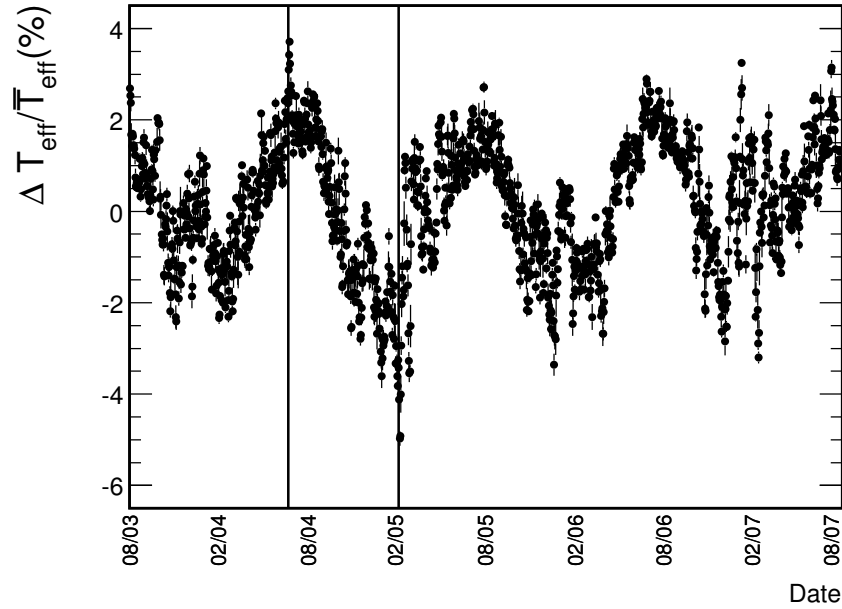
Figure 5.4: The daily deviation from $\langle T_{\mathrm{eff}} \rangle$ over a period of four years, beginning when the Far Detector was complete, 08/03-08/07. The vertical bars indicate the period of time when the detector ran in nominal reverse field mode.

over a few days' span.

A plot of $\Delta R_\mu(\Delta T_{\text{eff}})$ was produced (Fig. 5.5) for each day's ΔR_μ and ΔT_{eff} data to quantify the daily correlation between rate and temperature. To find the value for α_T, a linear regression was performed using ROOT's MINUIT [140] fitting package. This package performs a linear regression accounting for error bars on both the x and y axis using a numerical minimization method. The result of this fit is a correlation coefficient (R-value) of 0.906, and a slope of $\alpha_T = 0.877 \pm 0.010$. As a cross check, a routine that performed a fit with errors in two dimensions from Numerical Recipes in C++ [129] was used. It produced a result identical to MINUIT.
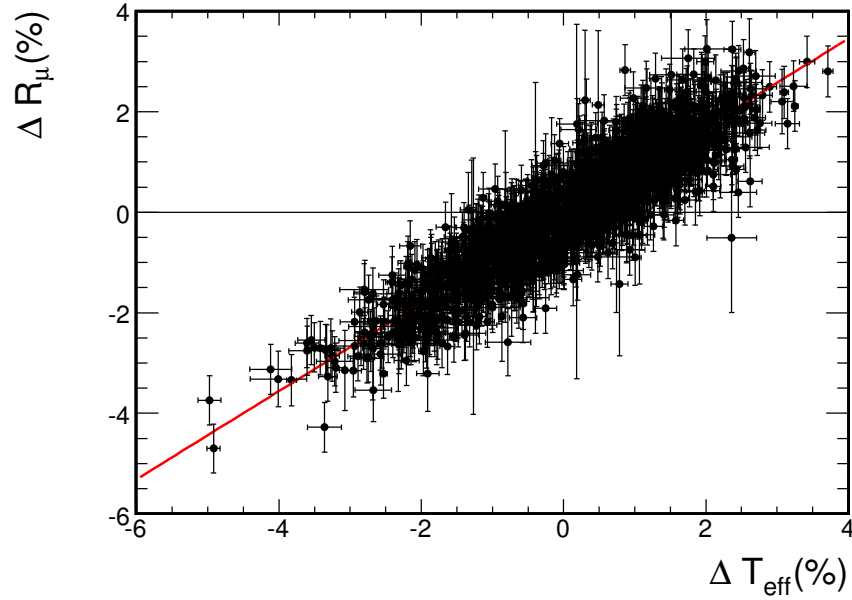
Figure 5.5: A plot of $\Delta R_\mu / \langle R_\mu \rangle$ vs. $\Delta T_{\text{eff}} / \langle T_{\text{eff}} \rangle$ for single muons. The fit has a $\chi^2/ndf = 1460/1441$, and the slope is $\alpha_T = 0.877 \pm 0.010$.

As a cross check, the daily deviations of R_μ were put in a histogram of temperature deviations, binned by $0.4\,\%$. The bin size was determined by the peak of the error distribution for T_{eff}, $\pm 0.2\,\%$, and this is comparable to having a graph of points with individual error bars of $\pm 0.2\,\%$. This is referred to as the "temperature series calculation". This method is particularly well suited for a low statistics sample such as the charge separated analysis (Sec. 5.1.6 on page 97), where the errors in the daily rate fluctuation are *larger* than the rate variation over a season. In a low statistics

situation, the systematic error in the temperature series method is smaller than the statistical error in the time series. The temperature series R(T) plot for the total muon sample can be seen in Fig. 5.6. A linear regression was performed on this temperature series, resulting in
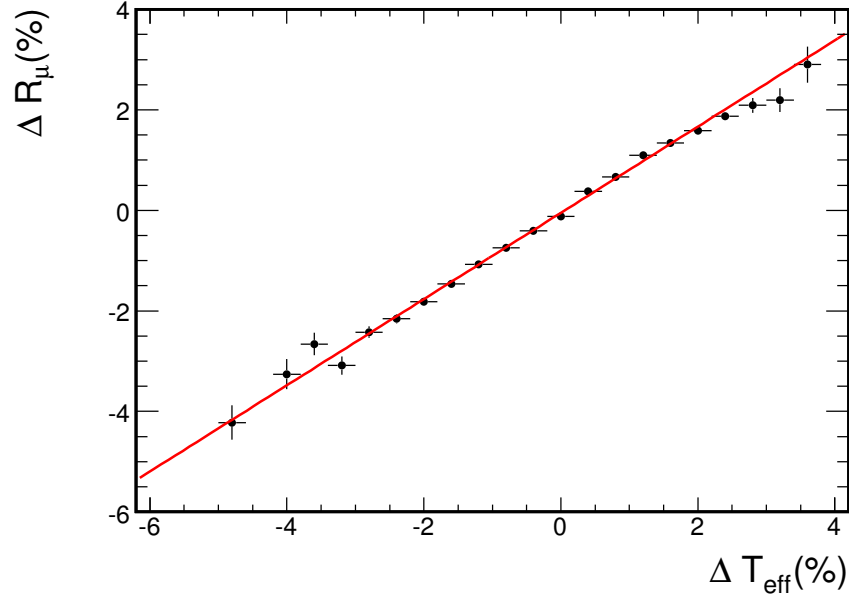
Figure 5.6: A histogram of the temperature series analysis, $\Delta R_\mu / \langle R_\mu \rangle$ vs. $\Delta T_{\text{eff}} / \langle T_{\text{eff}} \rangle / 0.4\,\%$ for single muons. The fit has a $\chi^2/ndf = 35/19$, and the slope is $\alpha_T = 0.858 \pm 0.010$.

$\alpha_T = 0.858 \pm 0.010$. This result is consistent with the time series calculation.

To compare this result with the MACRO result, α_T was calculated using the MACRO T_{eff}, Eq. 5 [133] and integrated to $25\,\text{g/cm}^2$ to provide the most direct comparison. This calculation resulted in $\alpha_T = 0.835 \pm 0.011$, consistent with the AMANDA [134] and MACRO [133] results, which are lower than the MACRO pion-only prediction [133]. A further calculation of α_T was performed using the IGRA temperature data. The result was $\alpha_T = 0.817 \pm 0.011$, which is lower than the result described above using ECMWF temperature data. This value is consistent with the reported value within the lower statistics and systematic error introduced by the fact that the temperature data is taken $150\,\text{km}$ away from the detector (see Sec. 5.1.5 on the following page).

5.1.4 Sudden Stratospheric Warmings

While the temperature of the stratosphere is constant over daily timescales and changes slowly with the seasons, there are well known events which disrupt this behavior. The breaking of the polar cyclone has been observed during winter many times in the northern hemisphere, and less often in the southern hemisphere.

Planetary waves in the atmosphere can have horizontal wavelengths of several thousand kilometers. In winter, these waves can propagate up to the stratosphere and can cause upper atmosphere vortex structure. Just like waves in water, these waves can *break* and cause temperatures in the polar stratosphere to rise by over $50\,\mathrm{K}$ in a few days. These events are known as Sudden Stratospheric Warmings (SSW) and appear as a displacement or splitting of a large persistent low pressure system which resides over the pole, known as the wintertime stratospheric polar vortex. The distribution of the major land-masses provides a means of generating these waves, as air is pushed up as it moves over steep terrain. Thus, most observations of SSW have been near the north pole. Such a temperature anomaly was observed in the winter of 2005 and can be seen in Fig. 5.1.4 on the next page   The muon data over the winter of 2004-2005 can be seen in Fig. 5.8 on page 95. The spike at the beginning of February can be explained by the SSW described in 5.1.4 on the next page.   A study of SSW detection with muons detected by MINOS has been submitted to Nature Physics [141]. This is the first time a SSW has been observed with a muon signal, and may give rise to new means of investigation in atmospheric physics.

5.1.5 Systematic Errors

To estimate the error caused by using the International Falls IGRA data, which was measured some distance away from the muon data, the relationship between the effective temperature and muon rate was found for other locations. The IGRA network includes many sites throughout the world, so an additional seven sites were chosen for their location relative to the detector. These sites surrounded the detector in all directions. It was found that there was no measurable correlation between separation in longitude and effect on α_T. There is a dependence of α_T on latitude, which was estimated by plotting $\alpha_T(\Delta\mathrm{Lat})$ and fitting a line. The slope of that line, multiplied by $\Delta\mathrm{Lat}$ of the detector from International Falls gives an error of 0.036.

One source of error is in the value of $\langle E_{th}\cos\theta\rangle$, which is used in the calculation of T_{eff} (Eq. 5.13 on page 83). This value was chosen as the minimum energy required for a muon to
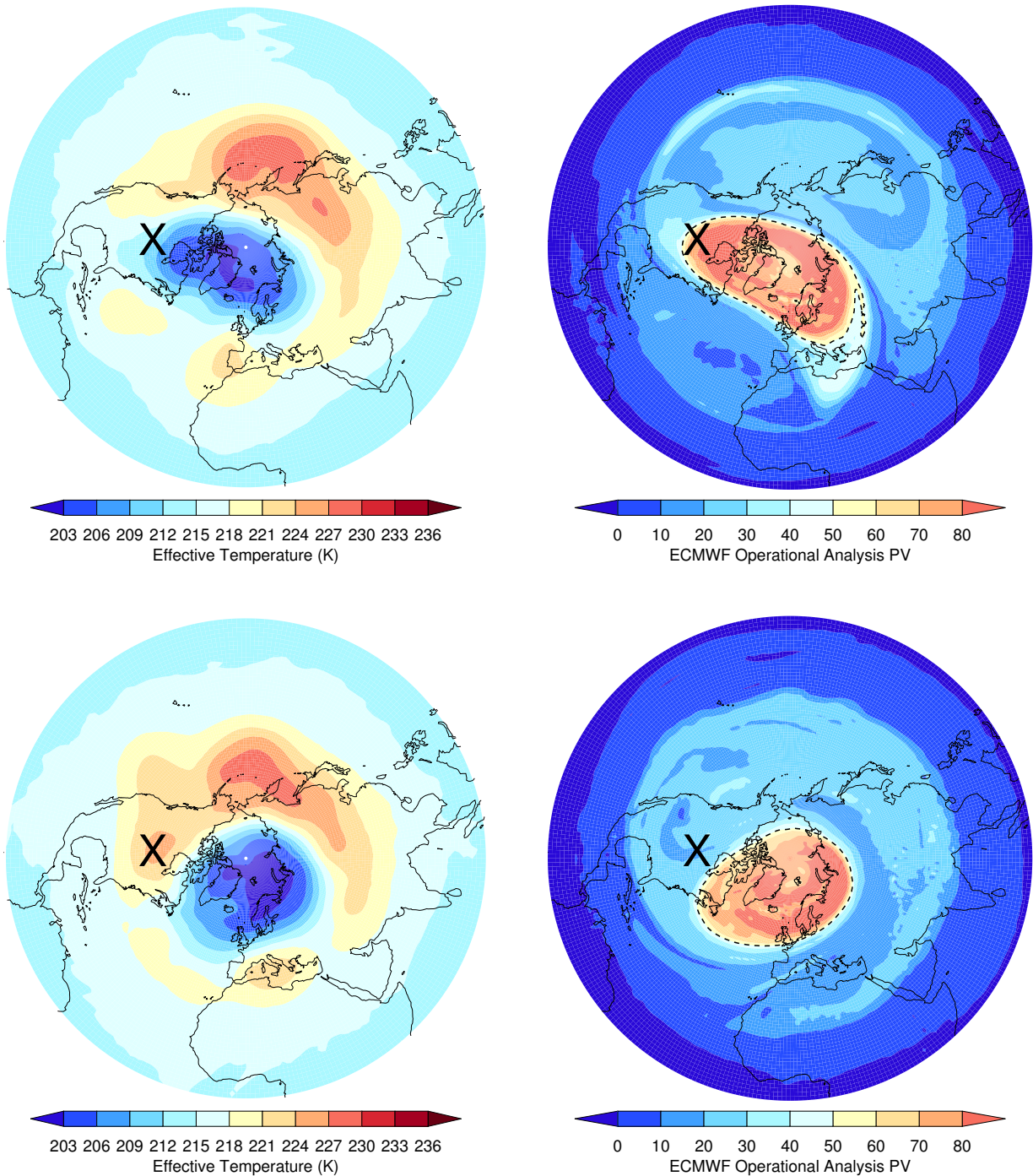
Figure 5.7: Effective temperature (left) and potential vorticity at 850K (right) for 6 and 16 February 2005 (top and bottom respectively) derived from ECMWF. Units are K and $10^{-4}\,\mathrm{K\,m^2\,kg^{-1}\,s^{-1}}$, respectively. The location of Soudan is marked by an X. Figure from [141].
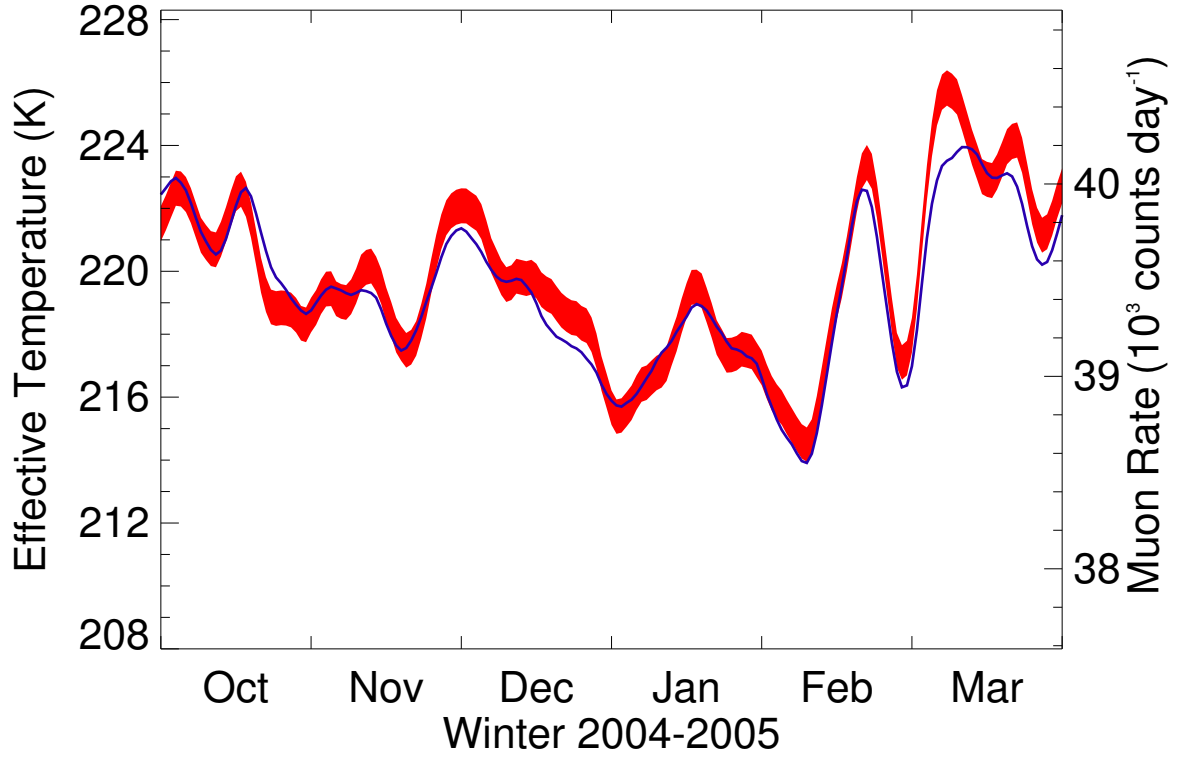
Figure 5.8: Timeseries of effective temperature for winter 2004–2005 (blue) from ECMWF and daily muon rate ± 1 standard deviation registered at MINOS Far Detector (red). A five day smoothing has been twice applied to both data. The ticks on the horizontal axis correspond to the start of the labeled month. Figure from [141].

traverse the depth of the Far Detector, which has its own uncertainties. Rather than quantifying these uncertainties individually, the value of $\langle E_{th} \cos\theta \rangle$ was varied $(0.7 \pm 0.1 \, \mathrm{TeV})$, which was then used to calculate α_T. The effect of this variation was a deviation of less than ± 0.01.

Another source of error could come from the use of the ECMWF temperature data, as opposed to *in situ* measurements in the atmosphere above the detector. This error was estimated using Integrated Global Radiosonde Archive (IGRA) balloon temperature measurements [142] and ECMWF data at International Falls, MN for measurements at noon and midnight. The two distributions had a correlation of 0.986. The distribution of the differences between these values was well described by a Gaussian distribution with $\sigma = 0.46 \, \mathrm{K}$, which was assumed to be a systematic error associated with each temperature measurement. The ECMWF data is preferable to the IGRA data for a number of reasons:

1. the data set is more complete: 262 days of IGRA data did not pass data quality cuts and were excluded from the data set. Most important is the fact that the balloons had varying maximum altitudes, and many times, the balloons could not reach their maximum height in the winter, which could introduce a bias if more summer than winter data is included.

2. The IGRA balloon flights were performed at International Falls, MN, USA, about $150\,km$ northwest of the Far Detector, which introduced a systematic error in α_T estimated to be ± 0.036.

The systematic error was estimated by choosing at random a modification out of the $T_E - T_I$ distribution, including it in the daily average value of T_{eff}, and recalculating α_T. The $T_E - T_I$ distribution was reduced by the factor $\sqrt{2}$ to account for the fact that the T_I distribution is not free from instrumental error, and the deviation of T_E from T_I is an overestimate of the actual error in the model. This resulted in a change in $\alpha_T \pm 0.014$.

Since the seasonal effect is cyclic and the peak-to-peak fluctuations of both muon rate and T_{eff} vary less than the statistical error on each data point, it is presumed that the average of α_T for the four years is the same as the mean of the four individual values α_T. This may not be the case, however, so a study of α_T for individual years was performed. The data was broken into four samples, with each sample containing data from an entire year over the period August 1 to July 31. The first subsample contained data from 366 days, since that was a leap year, and each of the next three subsamples contained data from 365 days. Both the time series and temperature series α_T were calculated for each subsample, and the results are summarized in Table 5.1. For the

Table 5.1: Fit statistics of α_T for one year subsamples.

Time Period	α_T	R	χ^2/ndf
Aug 1, 2003 - July 31, 2004	0.893 ± 0.023	0.870	419.4/360
Aug 1, 2004 - July 31, 2005	0.875 ± 0.018	0.935	349.9/361
Aug 1, 2005 - July 31, 2006	0.869 ± 0.021	0.908	337/353
Aug 1, 2006 - July 31, 2007	0.889 ± 0.024	0.891	335.6/362

time series, $\langle\alpha_T\rangle_{year} = 0.881 \pm 0.022$, which is consistent with $\langle\alpha_T\rangle$ from Sec. 5.1.3 on page 87.

The systematic errors described in this section have been summarized in Table 5.2. These systematic errors were added in quadrature and are included with the error from the linear fit to

Table 5.2: Input α_T parameter values and associated errors.

Parameter	Value	Units
$E_{th}\cos\theta$	700 ± 100	GeV
B_π^1	1.460 ± 0.007	-
B_K^1	1.740 ± 0.028	-
$\langle T_{\text{eff}}\rangle$	221.435 ± 0.46	K
Ex. Total	**0.017**	%

obtain the experimental value of $\alpha_T = 0.877 \pm 0.010$ (stat.) ± 0.017 (syst.).

5.1.6 Charge Separated

For the charge separated sample, further cuts were required to exclude events with low confidence charge sign determination. The curvature of the track is used to determine the momentum and charge of the particle, so cuts on number of planes, track length and confidence of charge sign measurement were determined to maximize the purity of the sample. The additional cuts are:
Analysis Cuts

1. "Single Track", only one track found by the reconstruction algorithm.

2. "Fit Quality", a track with $\chi^2_{fit}/ndf < 1.$. A track that was poorly reconstructed might not have reliable pointing.

3. "Fiducial", a muon vertex must begin within 50 cm of the detector in x, y, and its endpoint must be less than 50 cm outside of the detector

4. "Track Length at least 2.0 m", any event with a track shorter than 2.0 m may not be reliably reconstructed.

5. "Number of Planes at least 20", a track that passes fewer planes may not give reliable strip information to the track fitter.

Charge Confidence Cuts

1. "Track Quality Cut" charge over momentum divided by the error in the determination of charge over momentum ($\frac{q/p}{\sigma_{q/p}} > 2.2$),

2. Minimum Information Cut (MIC),'' a track was required to have at least 60 planes where the hit information was within 3.5 m of the detector center'' [60].

The cuts and associated values were determined from previous investigations of the muon charge ratio [60].

A different reconstruction algorithm was used for the results published in PRD (R1.14), so crosschecks were performed to ensure the same level of data quality was maintained by the cut values placed as they were. The data selected was the same sample used in the MINOS Charge Ratio Paper [60], that which was accumulated from August 1, 2003 to February 28, 2006. A summary of the effect of these cuts on this sample is shown in Table 5.3.   To make a

Table 5.3: Fraction of events that survive charge-separation cuts for the Charge Ratio paper data set (8.1.03 - 2.28.06) for the current reconstruction. This selection was made to provide a scaled comparison of reconstruction version.

	Forward	Reverse
Seasonal Cuts (Sec. 5.1.3 on page 87)	25.457×10^6	7.505×10^6
	Fraction Remaining	
Analysis Cuts		
1. Single Track	0.964	0.964
2. Planes	0.675	0.675
3. Length	0.671	0.671
4. χ^2_{fit}/ndf	0.664	0.664
5. Fiducial Volume	0.631	0.632
Charge Confidence Cuts		
1. Track Quality Cut	0.232	0.231
2. MIC	0.057	0.057

fair comparison, the cut statistics from the published paper were scaled to begin with a track that passes the Seasonal Effect cuts, for a proper comparison, as seen in Table 5.4 on the next page.

A few differences arose between the two datasets. The definition of the track fit quality, χ^2, changed between reconstruction versions, so the accompanying distributions changed as well. The spirit of this cut remains with the new maximum value of 1, as shown in Fig. 5.9 on page 100(L), while Fig. 5.9 on page 100(R) shows χ^2/ndf for R1.14.   Other distributions that were compared include charge ratio as a function of "Track Quality Cut" (current reconstruction in

Table 5.4: Fraction of events that survive charge-separation cuts for the Charge Ratio paper data set for the R1.14, used in the MINOS Charge Ratio PRD [60].

	Forward	Reverse
Seasonal Cuts (Sec. 5.1.3 on page 87)	22.91×10^6	7.405×10^6
	Fraction Remaining	
Analysis Cuts		
1. Single Track	0.924	0.928
2. Planes	0.701	0.703
3. Length	0.697	0.693
4. χ^2_{fit}/ndf	0.676	0.679
5. Fiducial Volume	0.541	0.543
Charge Confidence Cuts		
1. Track Quality Cut	0.178	0.177
2. MIC	0.061	0.060

Fig. 5.10 on page 101 (L), R1.14 in Fig. 5.10 on page 101 (R)) and charge ratio as a function of fit momentum in the detector (current reconstruction in Fig. 5.11 on page 101 (L), R1.14 in Fig. 5.11 on page 101 (R)).

While there are very slight differences in the distributions as well as the fit values, the overall agreement is striking considering the fact that Cedar uses completely different track fitting and finding algorithms as well as different magnetic field maps.

As described in [60], the proper way to combine the forward and reverse magnetic field charge ratios such that systematic differences between them cancel is by the geometric mean. For the current reconstruction, the total charge ratio as a function of track quality cut can be seen in Fig. 5.12 on page 106 (L), and the total charge as a function of fit momentum can be seen in Fig. 5.12 on page 106 (R). The systematic effects that cause structure in the distribution in one field direction appear as a reflection in the opposite field configuration, and thus cancel.

The charge ratia for both these distributions are well within the systematic errors of the published charge ratio,

$$r = 1.374^{+0.012}_{-0.010} \text{ (sys.)}. \tag{5.24}$$

Thus, it can be concluded that the systematic differences between reconstruction versions have been examined and the charge selection cuts that were applied to the previous reconstruction are still valid for the current reconstruction.
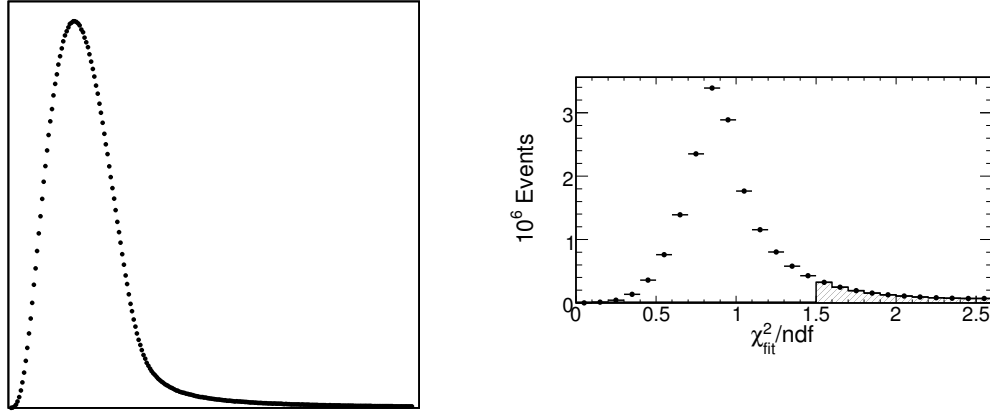
Figure 5.9: The χ^2/ndf distributions; for the current reconstruction (L) and for reconstruction R1.14 (R), used for the published muon data [60]

.

After these additional cuts, the charge ratio for forward and reverse fields are combined such that geometric acceptances to cancel (geometric mean). This gives 1.376, which is well within the systematic errors of the published MINOS charge ratio [60].

Fig. 5.13 on page 107 shows the deviation in rate for both positive (top) and negative (bottom) muons, binned by day.

In all, 5.7% of the data set survived these cuts for both the forward and reverse field detector configurations. A temperature series analysis (described in Sec. 5.1.3 on page 87 for the all muon sample) was performed to find α_T for μ^+, μ^-, and the charge ratio. The temperature series analysis was used because the extra charge separation cuts reduce the statistics significantly, and the temperature series analysis is less sensitive to low statistics. The temperature series R(T) plot for the μ^+ and μ^- samples can be seen in Fig. 5.14 on page 108. For the charge separated samples, $(\alpha_T)_{\mu^+} = 0.782 \pm 0.056$, $(\alpha_T)_{\mu^-} = 0.788 \pm 0.066$. These numbers are consistent with each other, so there is no measurable difference between the temperature effect on μ^+ and μ^-. The hard cuts that were required for a high purity charge ID resulted in an implicit high energy cut. Since α_T increases with muon energy (Eq. 5.20 on page 84), the fact that the α_T values are
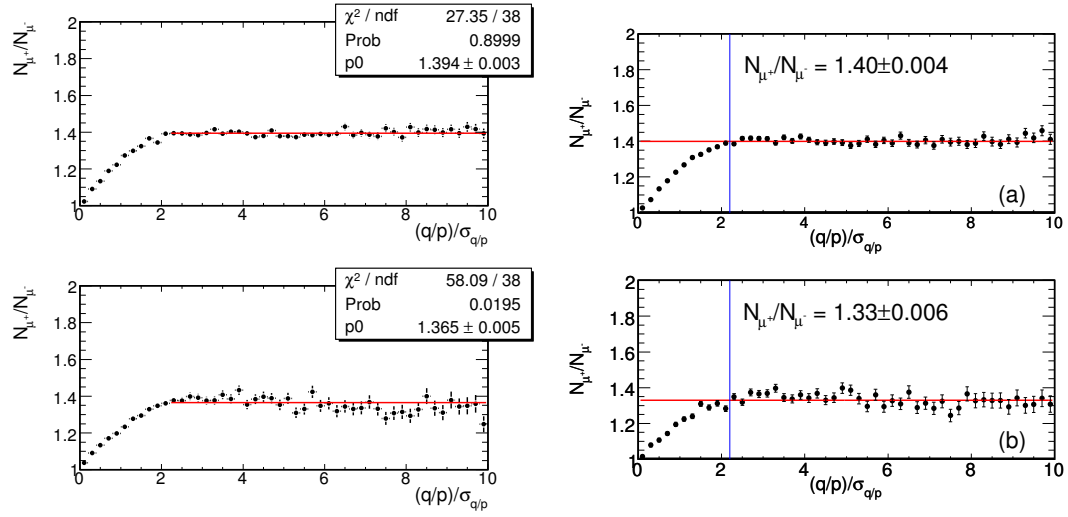
Figure 5.10: The charge ratio as a function of track quality cut parameter qp/σ_{qp} for the current reconstruction (L) and the reconstruction R1.14 (R), used for the published muon data [60] . The top plot is the forward field distribution, the bottom plot is the reverse field distribution.
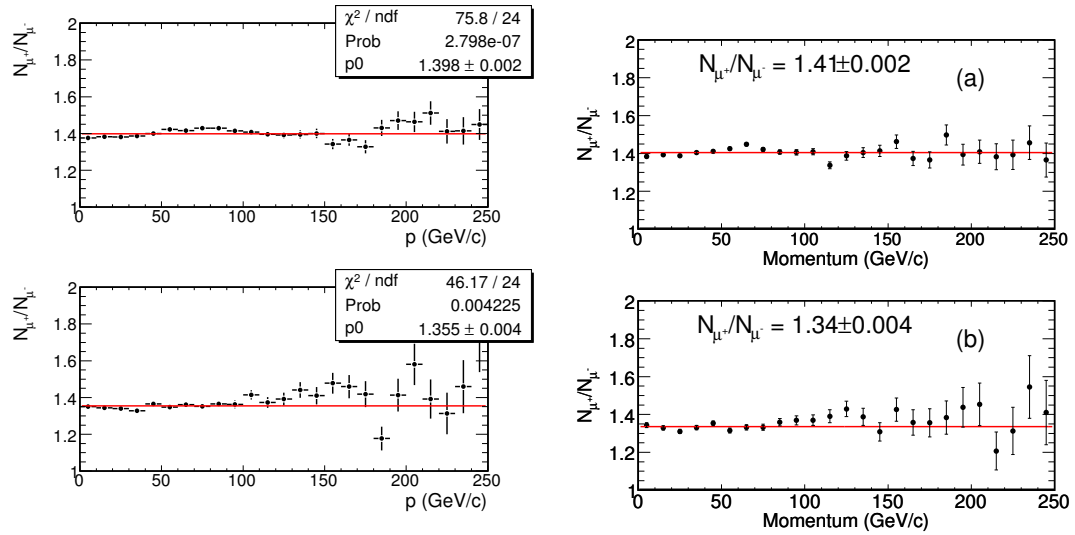
Figure 5.11: The charge ratio as a function of fit momentum for the current reconstruction (L), used for the muon data in this analysis, and for reconstruction R1.14 (R), used for the published muon data [60] . The top plot is the forward field distribution, the bottom plot is the reverse field distribution.

102

Table 5.5: Fraction of events that survive charge-separation cuts for the entire Seasonal Effect dataset (8.1.03 - 7.31.07).

	Forward	Reverse
Seasonal Cuts (Sec. 5.1.3 on page 87)	45.378×10^6	7.748×10^6
	Fraction Remaining	
Analysis Cuts		
1. Single Track	0.964	0.964
2. Planes	0.675	0.675
3. Length	0.671	0.671
4. χ^2_{fit}/ndf	0.664	0.664
5. Fiducial Volume	0.631	0.632
Charge Confidence Cuts		
1. Track Quality Cut	0.232	0.231
2. MIC	0.057	0.057

lower for the charge separated sample is consistent with the expectation.

Since α_T is measured experimentally as the change in number of muons collected over a period of time with respect to the change in temperature, this phenomenology can be applied to changes in the charge ratio. The charge ratio is given by $r = N_{\mu^+}/N_{\mu^-}$, and an effective temperature charge ratio coefficient r_T can be written:

$$\frac{\Delta r}{\langle r \rangle} = r_T \frac{\Delta T_{\text{eff}}}{\langle T_{\text{eff}} \rangle} \tag{5.25}$$

where $\Delta r \equiv N_{\mu^+,day}/N_{\mu^-,day} - \langle r \rangle$. A temperature series analysis was performed on the daily deviation of the charge ratio, and the $\Delta r(T)$ plot can be seen in Fig. 5.15 on page 109. For the charge ratio sample, $(r_T) = 0.05 \pm 0.13$. The reported α_T values include both fit errors as well as systematic errors added in quadrature. The values of α_T are consistent with each other and with the result from the all muon sample. As expected, there was no observed temperature dependence on the charge ratio.

5.2 Comparison of α_T to Expectation

The theoretical prediction of α_T for properly weighted atmospheric temperature distribution can be written as:

$$\alpha_T = \frac{T}{I_\mu^0}\frac{\partial I_\mu}{\partial T}. \tag{5.26}$$

Barrett [59] shows that the theoretical α_T can be written in the more useful form:

$$\alpha_T = -\frac{E_{th}}{I_\mu^0}\frac{\partial I_\mu}{\partial E_{th}} - \gamma \tag{5.27}$$

The prediction for α_T can be calculated using the differential muon intensity [43] and a little algebra (see Sec. 5.1.2 on page 79:

$$\alpha_T = \frac{1}{D_\pi}\frac{1/\epsilon_K + A_K^1(D_\pi/D_K)^2/\epsilon_\pi}{1/\epsilon_K + A_K^1(D_\pi/D_K)/\epsilon_\pi} \tag{5.28}$$

where

$$D_\pi = \frac{\gamma}{\gamma+1}\frac{\epsilon_\pi}{1.1E_{th}\cos\theta} + 1,$$
$$D_K = \frac{\gamma}{\gamma+1}\frac{\epsilon_K}{1.1E_{th}\cos\theta} + 1$$

Note that this can be reduced to MACRO's previously published expression $\langle\alpha_T\rangle_\pi$ [133], which was only valid for pion induced muons, by setting $A_K = 0$ (no kaon contribution).

To compare the experimental α_T to the theoretical expectation, a simple *Monte Carlo* calculation was performed to find the expected average value given by Eq. 5.20 on page 84.A muon energy and $\cos\theta$ were chosen out of the differential muon intensity [43], A random azimuthal angle, ϕ, was chosen and combined with $\cos\theta$ and the Soudan rock overburden map [60] to find the slant depth D (kmwe). The threshold surface energy required for a muon to survive this column depth is found from the expression for threshold energy [60]. If the chosen E_μ was greater than E_{th}, it was used in the calculation of the theoretical $\langle\alpha_T\rangle$. This was repeated for 10,000 successful E_μ to find $\langle\alpha_T\rangle = 0.865 \pm 0.015$ for MINOS, which is very near to the experimental value, 0.877 ± 0.010 (stat.) ± 0.017 (syst.). The uncertainty on the expected value of α_T was found by estimating the relative contribution to the error from each value used in the calculation. These uncertainties are summarized in Table 5.6 on the next page.

To compare the MINOS result with other underground experiments, this process was repeated for standard rock, flat overburden, and $D = H/\cos\theta$, where H is the detector depth in mwe, using

**Table 5.6:** Input α_T parameter values and associated errors.

Parameter	Value	Units
γ	1.7 ± 0.1	-
m_π	139.57018 ± 0.00035	MeV/c^2
τ_π	2.6033 ± 0.005	10^{-8} s
m_K	493.677 ± 0.013	MeV/c^2
τ_K	1.2385 ± 0.0025	10^{-8} s
m_μ	$105.6583693 \pm 0.000000003$	MeV/c^2
H(T)	6.4 ± 0.1	km
ϵ_π	114 ± 3	GeV
ϵ_K	851 ± 14	GeV
Rock Map	± 10	%
Th. Total	**0.015**	%

10,000 successful muons at depths from 0 to 4,000 mwe. The result of this calculation, along with data from other experiments, can be seen in Fig. 5.16 on page 110 as the solid line. This curve includes the "negative temperature effect" (muon decay correction) term,

$\delta' = (1/E\cos\theta)(m_\mu c^2 H/c\tau_\mu)(\gamma/\gamma + 1)\ln(1030/\lambda_p \cos\theta)$ [59], which goes to zero for $E_\mu > 50$ GeV. Two results included in the MACRO survey [133] have been excluded because their calculation of α_T cannot correctly be compared to the other results. Poatina [138] did not calculate an effective temperature coefficient, rather they calculated the correlation between underground muon rate and the temperature of the 100 hPa temperature level, which is not the same as the effective temperature coefficient measured here. Utah [147] did not publish error bars and touted the fact that their result was consistent with the Poatina result. The Sherman [144] result was recalculated using the methods described above. Note that the other results used a T_{eff} expression that did not include kaons.

The kaon component of air showers that can be observed at 1400 mwe is about 10%, but the energy is too low for kaon-induced muon production to be affected by changes in temperature. The result is the large gap between the pion only curve and the Kπ curve. As the depth increases, the energy of sampled muons also increases, which results in a greater contribution by kaon in- duced muons to α_T. The asymptotic behavior of the theoretical α_T approaching one as primary energy increases is expected from Eq. 5.18 on page 84. At very high primary energies, the in- tensity is proportional to the critical meson energy, which depends on temperature . Thus, for

an isothermal atmosphere, intensity will be directly proportional to the temperature (the constant of proportionality, α_T, will be one). The MINOS result matches the expectation and has tighter error bars than both recent results, AMANDA (± 0.05) [134] and MACRO (± 0.07) [143]. The dashed line is the result of the same calculation using the MACRO calculation of $\langle \alpha_T \rangle_\pi$ [143]. The new kaon-inclusive $\langle \alpha_T \rangle$ distribution fits the data with a $\chi^2/ndf = 8.0/9$, an improvement of $\Delta\chi^2 = 3.9$ compared to the pion-only distribution.
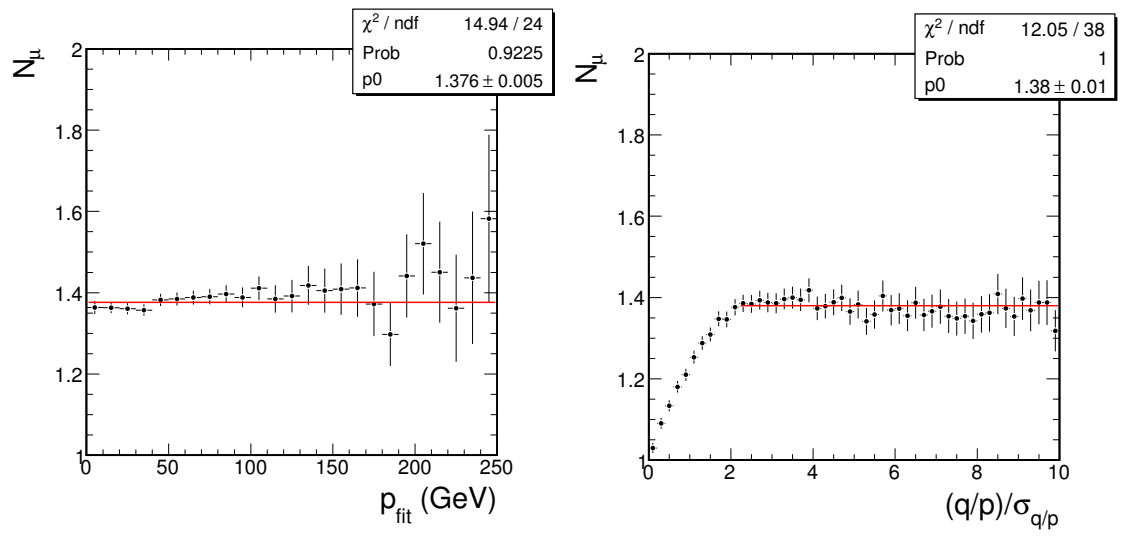
Figure 5.12: The charge ratio as a function of fit momentum (L) and track quality cut (R) for the current reconstruction, used for the muons data in this analysis. This plot is for combined forward and reverse muon data.
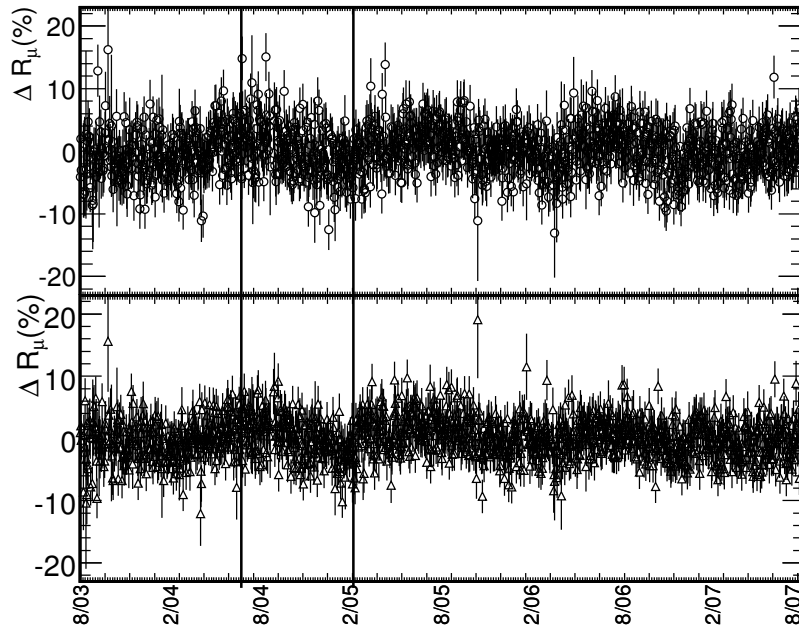
Figure 5.13: (top) ΔR_μ for μ^+ (open triangles) and μ^- (open circles) muons, binned by day. (bottom) ΔT_{eff}, binned by day. Both distributions show the expected seasonal fluctuations seen in the combined muon sample. The vertical bars indicate when the detector ran in nominal reverse field mode.
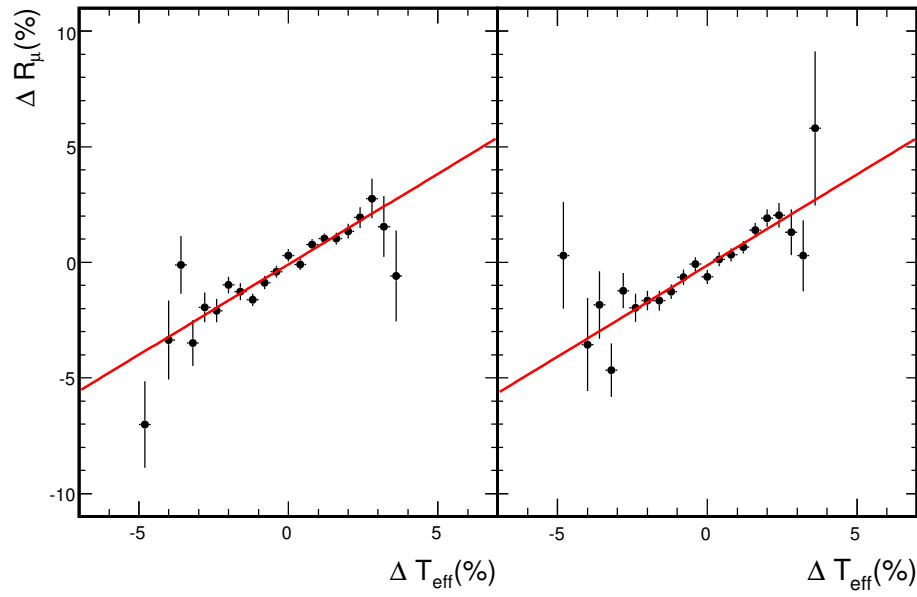
Figure 5.14: A histogram of $\Delta R_\mu / \langle R_\mu \rangle$ vs. $\Delta T_{\text{eff}} / \langle T_{\text{eff}} \rangle /0.4\,\%$ for μ^+(L) and μ^-(R). The fit results are $\alpha_T = 0.782 \pm 0.056$, $\chi^2/ndf = 27.6/19$ for μ^+, $\alpha_T = 0.788 \pm 0.066$, $\chi^2/ndf = 20.9/19$ for μ^-.
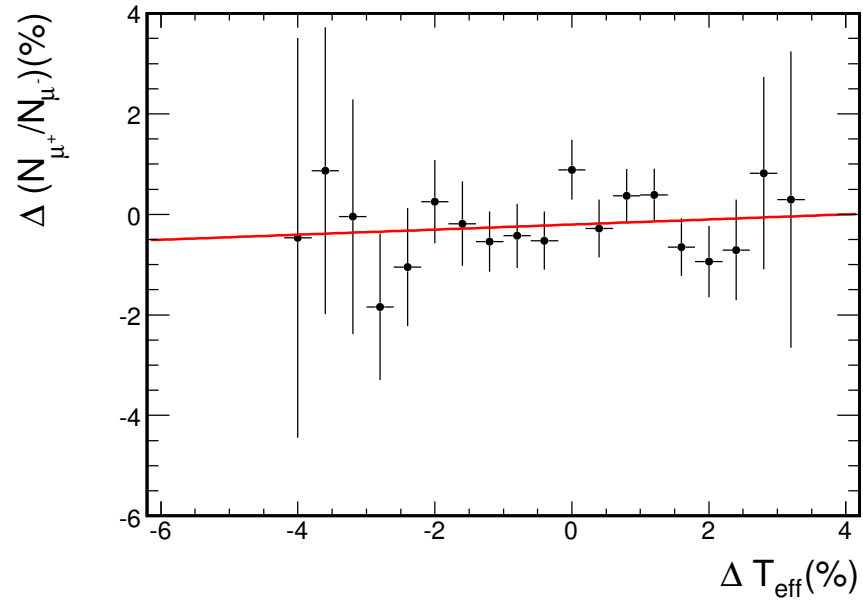
Figure 5.15: A histogram of $\Delta r_\mu / \langle r_\mu \rangle$ vs. $\Delta T_{\text{eff}} / \langle T_{\text{eff}} \rangle$ /0.4 % for r_μ. The fit results are $r_T = 0.05 \pm 0.13$ with $\chi^2/ndf = 17.64/19$.
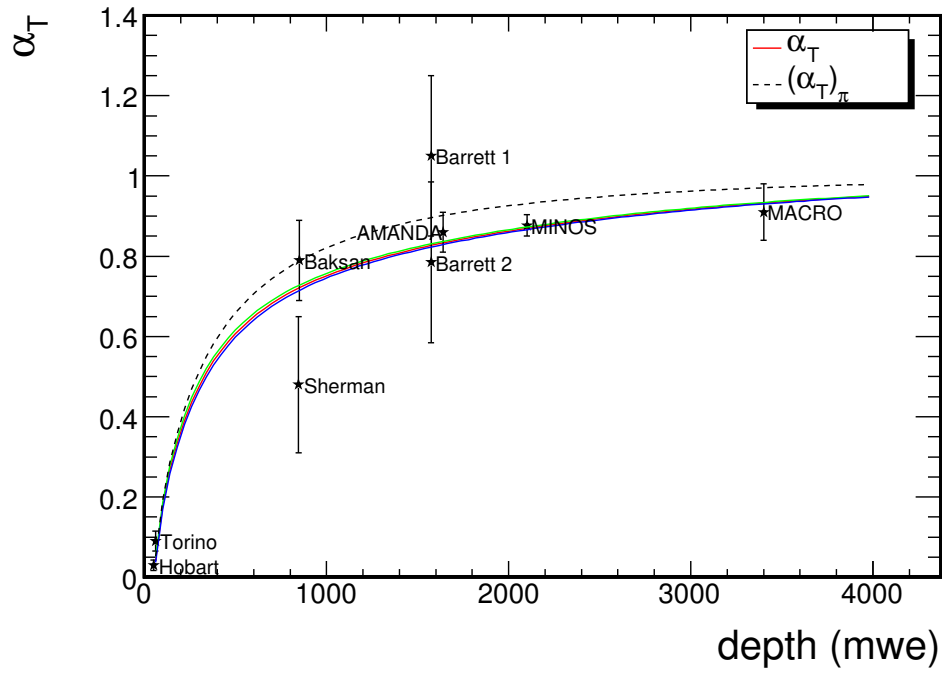
Figure 5.16: The new theoretical $\langle \alpha_T(X) \rangle$ (solid curve) and the MACRO $\langle \alpha_T(X) \rangle_\pi$ (dashed curve) for slant depths up to 4000 mwe. The MINOS point is from this analysis, Barrett 1, 2 [59], AMANDA [134], MACRO [143]; other points are Torino [137], Sherman [144], Hobart [145] and Baksan [146]. The green line is the upper error bound, and the blue line is the lower error bound.

Chapter 6

Atmospheric K/π Measurement

The physics behind the seasonal effect has been studied indirectly by a number of groups over the years, mostly with the aim of applying the knowledge to airshower studies. The most complete treatment of the seasonal variation in underground muon intensity was reported in Ch. 5, and some extensions to that study are reported here.

6.1 Seasonal Effect *Monte Carlo*

A full cosmic ray airshower simulation was developed for the study of processes that affect the production of muons that are observed underground. This *Monte Carlo* was described in Sec. 4.3.2. Each day's environmental conditions were obtained from the ECMWF was found using their global atmospheric model [136]. Temperature and geopotential height (gravitational potential energy per unit mass at that level) were determined on a regular pressure grid four times daily, at 0000 h, 0600 h, 1200 h and 1800 h. The standard input for CORSIKA is an atmospheric data file, which contains pressure and density information on a regular height grid from 0 to 120 km. To find the height of a pressure level, the Hyposometric equation is integrated from the lower pressure level boundary, P_l, to the higher pressure level boundary, P_h [148]:

$$\Delta H = -\frac{R}{g} \int_{P_l}^{P_h} \langle T \rangle \, d\ln P, \tag{6.1}$$

where $R = 8.31432\,\mathrm{J/mol \cdot K}$ is the ideal gas constant, $g = 9.807\,\mathrm{m/s^2}$ is the acceleration of gravity, and

$$\langle T \rangle \equiv \frac{\int_{P_l}^{P_h} \langle T \rangle \, d\ln P}{\int_{P_l}^{P_h} d\ln P} \tag{6.2}$$

This integration is done for each pressure level, and the resulting ΔH values are summed. The integration constant, or initial height of the first pressure level, is given by the ECMWF global atmospheric model [136]. The density can be found by $\rho = \mu P / RT$, where $\mu = 28.9644\,\mathrm{g/mol}$ (the average molecular weight of the atmosphere) assuming that the atmosphere consists of an ideal gas. The pressure on a regular height grid is found with a cubic spline implementation from the Gnu Scientific Library [149].
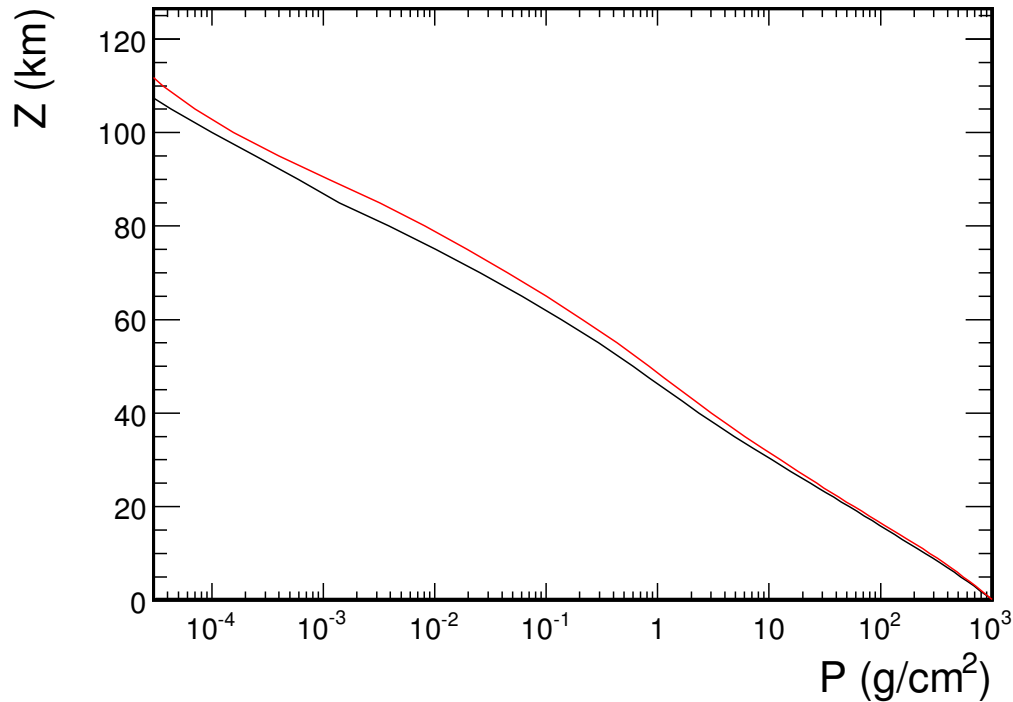
Figure 6.1: The atmospheric scale height as a function of pressure level averaged for summer months (red line) and winter months (black line). The pressure levels are at a greater scale height in the summer than winter, which contributes to greater muon production.

The environmental data obtained from ECMWF includes temperatures up to a pressure of $1\,\mathrm{g/cm^2}$, which corresponds to about $50\,\mathrm{km}$. This is the part of the atmosphere where muons are
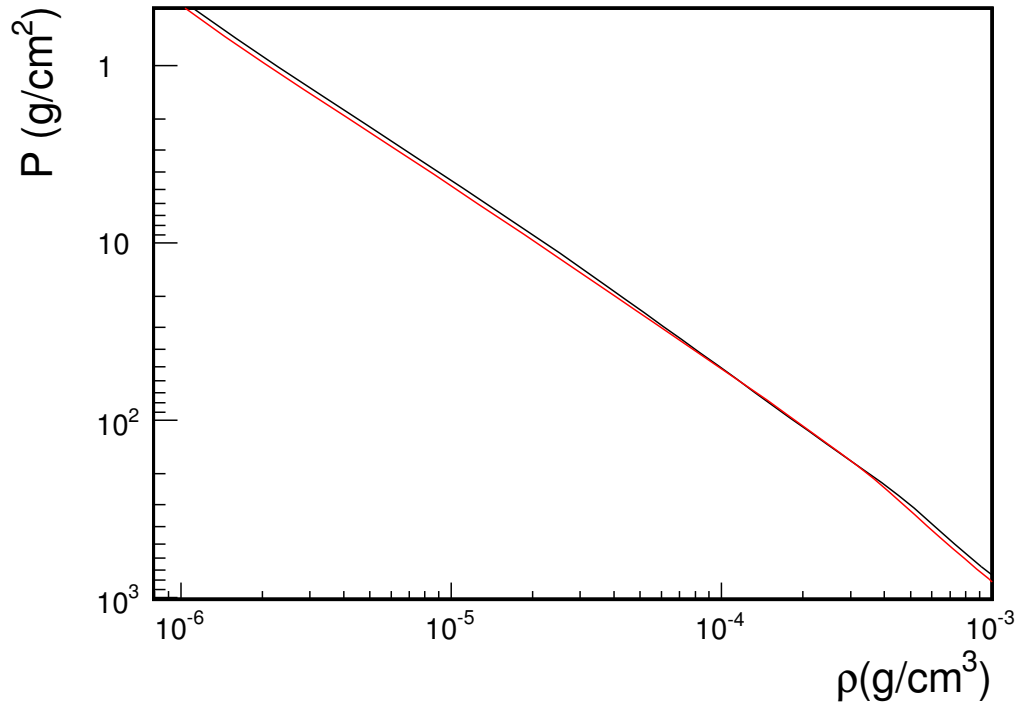
Figure 6.2: The atmospheric pressure level as a function of density averaged for summer months (red line) and winter months (black line). The pressure levels are less dense in the summer than winter, which contributes to greater muon production.

produced (see Sec. 4.1). Above this level, there is not sufficient material for an incident cosmic ray to have a high probability of interaction, so the rate of underground muons is insensitive to changes in this part of the atmosphere. Some reasonable values were necessary for input into CORSIKA, but the seasonal effect simulation is not dependent upon the accuracy of these values. For the levels immediately above the ECMWF data to 86 km, the 1976 US Standard Atmosphere [150], a parameterization of the stratopause, mesosphere and mesopause, was used. The remainder of the atmosphere, up to 120 km as required for the simulation input, used the COSPAR International Reference Atmosphere (CIRA) [151], an empirical atmosphere model. CIRA compiled monthly mean temperatures at geopotential heights from 0 to 120 km on a 10° latitude grid. The temperature as a function of pressure at the latitude of the Soudan site and the pressure on the regular height grid was interpolated from CIRA. An example table is shown in Table 6.1 and Table 6.2.

This procedure was repeated to simulate the atmosphere for all 1461 days in the data set.

Table 6.1: An example atmosphere input file, 0 - 25 km.

Atmospheric Model 2003-11-11 06:00:00		
Col. #1	#2	#3
Alt [km]	rho [g/cm^3]	thick [g/cm^2]
0.000	1.25071e-03	1.02332e+03
1.000	1.12427e-03	9.04592e+02
2.000	1.00394e-03	7.98416e+02
3.000	8.99860e-04	7.03148e+02
4.000	8.10952e-04	6.17516e+02
5.000	7.31993e-04	5.40464e+02
6.000	6.59421e-04	4.70995e+02
7.000	5.92402e-04	4.08485e+02
8.000	5.29315e-04	3.52645e+02
9.000	4.64255e-04	3.03272e+02
10.000	3.99369e-04	2.60186e+02
11.000	3.43047e-04	2.23111e+02
12.000	2.95384e-04	1.91245e+02
13.000	2.54804e-04	1.63765e+02
14.000	2.20125e-04	1.40079e+02
15.000	1.89515e-04	1.19704e+02
16.000	1.61884e-04	1.02241e+02
17.000	1.37514e-04	8.73005e+01
18.000	1.17482e-04	7.45253e+01
19.000	1.01307e-04	6.35772e+01
20.000	8.72189e-05	5.41979e+01
21.000	7.43340e-05	4.61756e+01
22.000	6.29749e-05	3.93329e+01
23.000	5.33730e-05	3.35176e+01
24.000	4.53639e-05	2.85784e+01
25.000	3.86584e-05	2.43804e+01

Table 6.2: An example atmosphere input file, 27.5 - 120 km.

| Atmospheric Model 2003-11-11 06:00:00		
Col. #1	#2	#3
Alt [km]	rho [g/cm^3]	thick [g/cm^2]
27.500	2.60008e-05	1.64010e+01
30.000	1.73950e-05	1.10595e+01
32.500	1.16140e-05	7.48571e+00
35.000	7.82649e-06	5.08647e+00
37.500	5.28124e-06	3.46844e+00
40.000	3.53219e-06	2.37824e+00
42.500	2.37083e-06	1.65662e+00
45.000	1.60132e-06	1.15786e+00
47.500	1.13324e-06	8.19402e-01
50.000	8.01979e-07	5.79882e-01
55.000	4.08454e-07	2.78600e-01
60.000	1.99225e-07	1.27724e-01
65.000	9.25112e-08	5.55182e-02
70.000	4.06027e-08	2.27028e-02
75.000	1.66762e-08	8.83628e-03
80.000	6.50137e-09	3.25460e-03
85.000	2.39035e-09	1.12664e-03
90.000	8.25379e-10	4.53465e-04
95.000	3.33027e-10	1.77037e-04
100.000	1.29747e-10	7.09783e-05
105.000	5.14015e-11	3.08776e-05
110.000	2.15041e-11	1.52705e-05
115.000	9.74607e-12	8.74905e-06
120.000	5.01924e-12	0.00000e+00

The interpolated atmospheric data on the height grid is shown in Fig. 6.1 & 6.2. Fig. 6.1 shows the atmospheric scale height as a function of pressure level. The red line is the summer average, the black line is the winter average. Fig. 6.1 shows the atmospheric pressure level as a function of density. The red line is the summer average, the black line is the winter average. Because the variation between summer and winter density is so small, the x-axis was truncated to show the behavior in the region of interest, from $1030 \, \mathrm{g/cm^2}$ to $1 \, \mathrm{g/cm^2}$.

After the atmosphere was simulated for each six hour period in the data set, the seasonal effect was simulated by producing a constant number of cosmic ray airshowers and propagating them through the particular atmosphere. MINOS records about 10,000 muons underground per six hour period, which requires the simulation of 2.5 million airshowers with energies above 2.2 TeV. Since the number of airshowers is constant and the rock does not vary, the variation of the atmosphere using the input data files simulates the seasonal effect. Since the simulation of muons through rock is very CPU intensive, only one year was simulated for each high energy hadronic model. The simulated change in muon rate can be seen in Fig. 6.3, with the red points representing QGSJet and the black points representing Sibyll. The corresponding temperature distribution can be seen in Fig. 6.4.

The deviation in rate is nearly identical for each hadronic model, and there is a clear correlation between the change in temperature and the change in rate for the simulated muons. A time series analysis, described in Sec. 4.1 and shown in Fig. 6.5, was performed on the simulated data to find $\alpha_T(sim)0.736 = \pm 0.021$ which is not consistent with the measured value (see Sec. 5.1.3) or with the predicted value (see Sec. 5.2).

Since this is a full cosmic ray simulation, information about the meson that generated a particle observed in the detector is known. Thus, it is possible to investigate the seasonal effect separately for pion induced muons and kaon induced muons. Plots of the time series $\Delta R(\Delta T)$ can be seen for pion induced muons in Fig. 6.6 and kaon induced muons in Fig. 6.7.

It encouraging to see that the atmospheric input produced the expected daily fluctuations, and that the seasonal effect was observed in the *Monte Carlo*. However, it is worrisome that $\alpha_T = 0.735 \pm 0.02$ from the simulation is significantly lower than $\alpha_T = 0.876 \pm 0.01(\mathrm{stat.}) \pm 0.017(\mathrm{syst.})$ from the data. Since the temperature data was convoluted on to a height grid and used as input, one would expect higher correlation between changes in muon rate and changes in atmospheric temperature, as well as better agreement with the measured seasonal effect. The
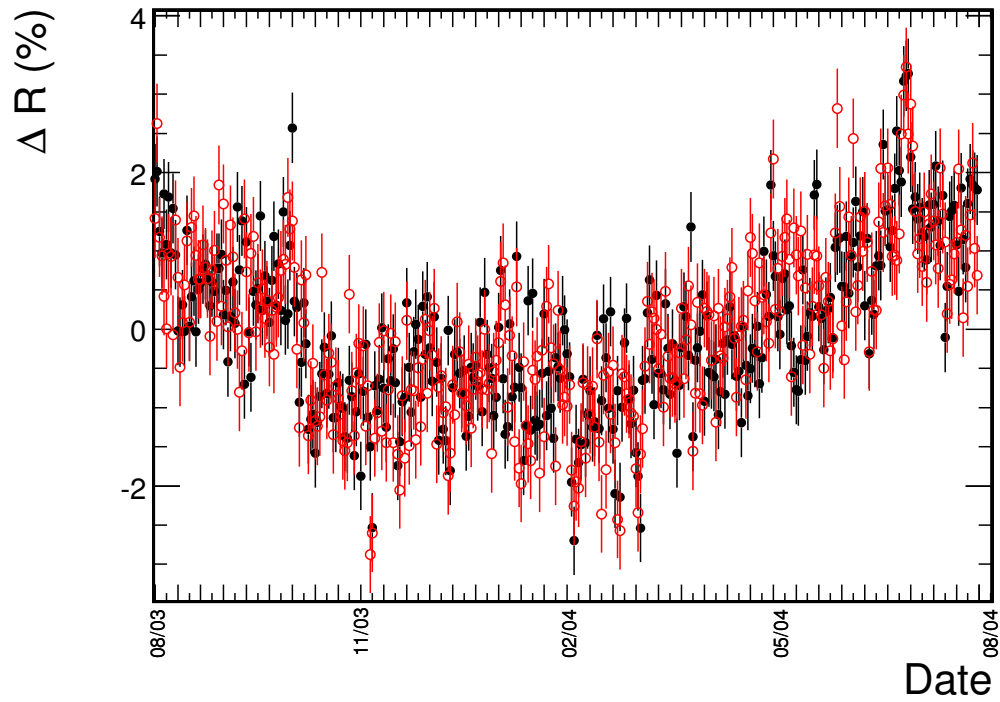
Figure 6.3: The change in mean rate for simulated muons during the first year of MINOS running, 08/03-08/04. The black triangles were simulated with Sibyll, while the red circles were simulated with QGSJet.
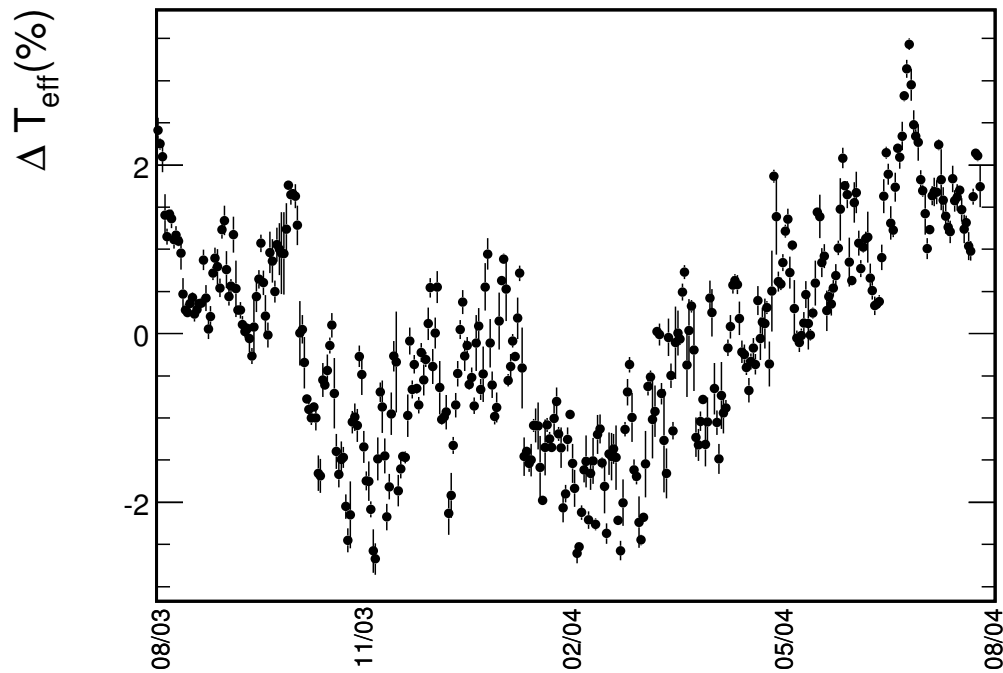
Figure 6.4: The daily deviation from $\langle T_{\text{eff}} \rangle$ over a period of one year, beginning when the Far Detector was complete, 08/03-08/04.
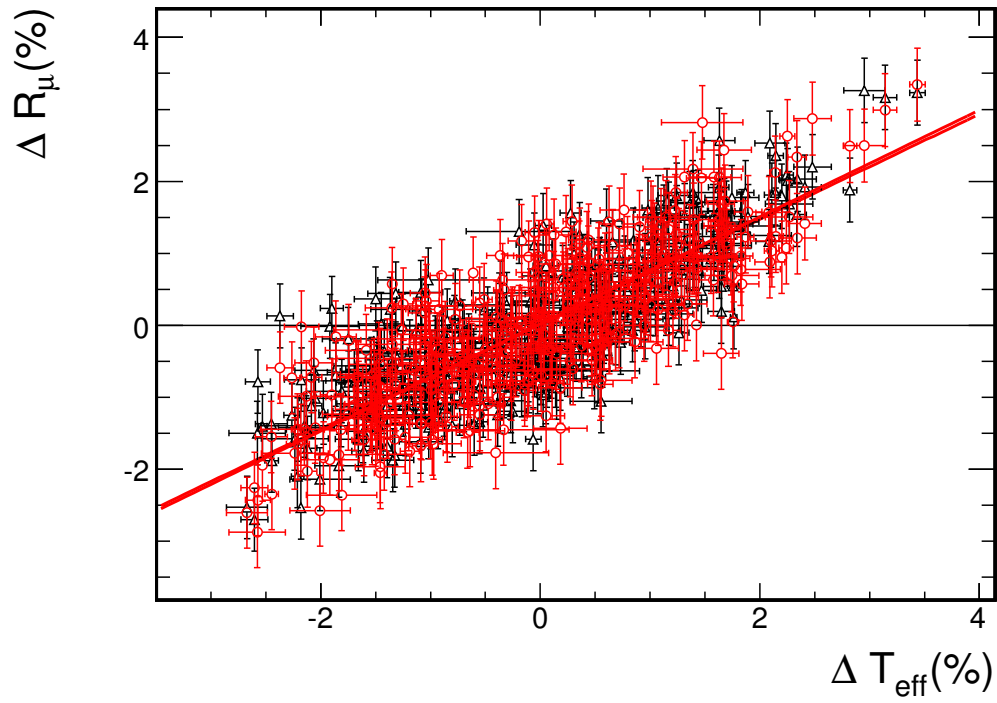
Figure 6.5: A plot of $\Delta R_\mu / \langle R_\mu \rangle$ vs. $\Delta T_{\rm eff} / \langle T_{\rm eff} \rangle$ for simulated single muons. The black triangles were simulated with Sibyll, while the red circles were simulated with QGSJet. The fit has a $\chi^2/ndf = 552.5/359$, and the slope is 0.729 ± 0.01999 for Sibyll, and $\chi^2/ndf = 508.4/359$, and the slope is 0.7435 ± 0.02214 for QGSJet.
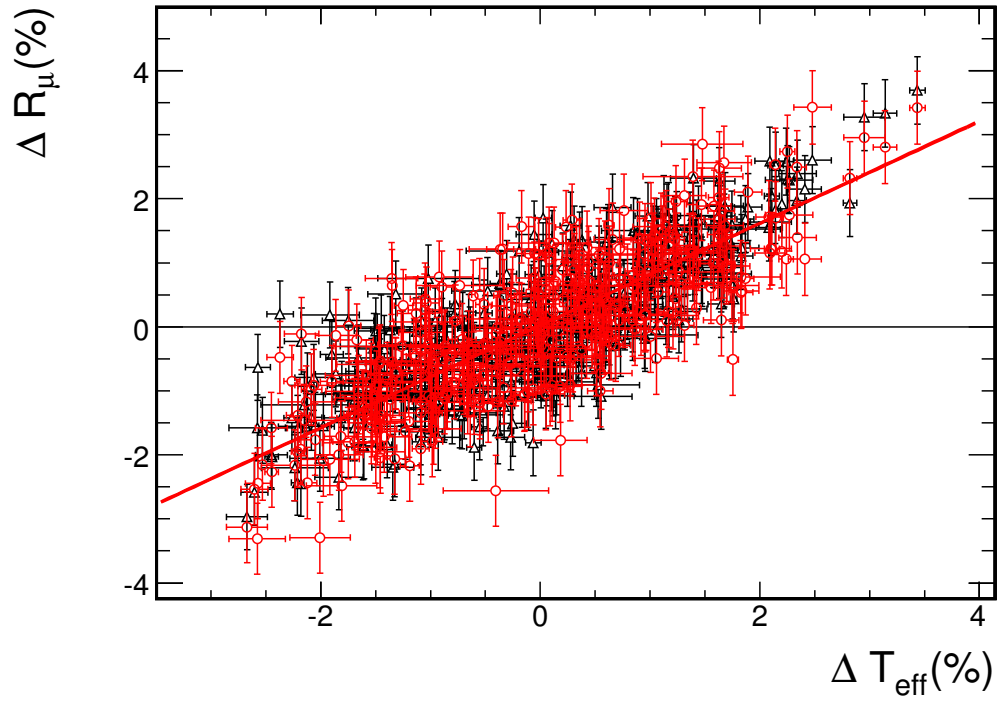
Figure 6.6: A plot of $\Delta R_\mu / \langle R_\mu \rangle$ vs. $\Delta T_{\text{eff}} / \langle T_{\text{eff}} \rangle$ for simulated pion induced muons. The black triangles were simulated with Sibyll, while the red circles were simulated with QGSJet. The fit has a $\chi^2/ndf = 524/359$, and the slope is 0.7958 ± 0.0233 for Sibyll, and $\chi^2/ndf = 513.5/359$, and the slope is 0.7996 ± 0.02483 for QGSJet.

Figure 6.7: A plot of $\Delta R_\mu / \langle R_\mu \rangle$ vs. $\Delta T_{\text{eff}} / \langle T_{\text{eff}} \rangle$ for simulated kaon induced muons. The black triangles were simulated with Sibyll, while the red circles were simulated with QGSJet. The fit has a $\chi^2/ndf = 449.4/359$,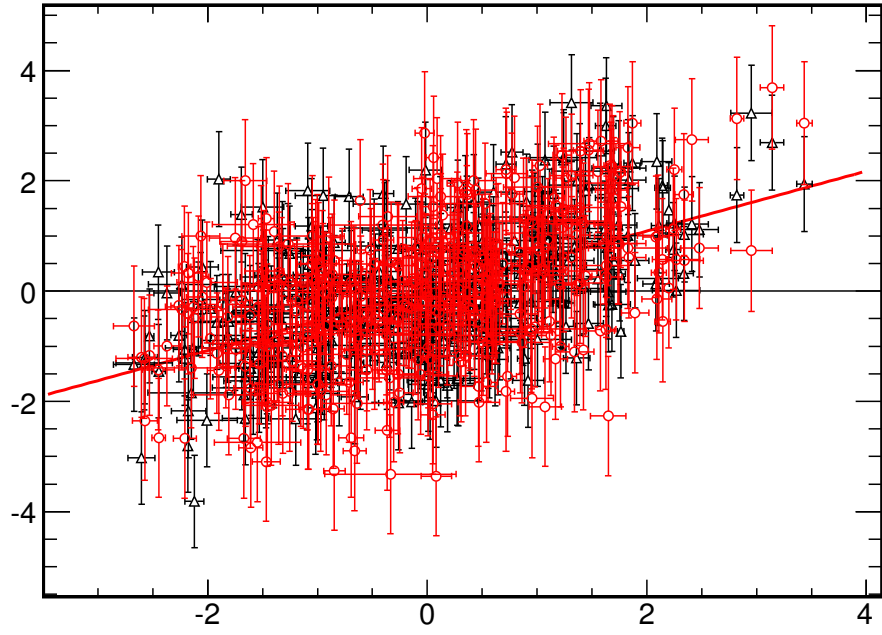 and the slope is 0.5422 ± 0.03707 for Sibyll, and $\chi^2/ndf = 378.1/359$, and the slope is 0.5316 ± 0.04742 for QGSJet.

theoretical prediction for the total α_T is 0.865 ± 0.015, which is in good agreement with the observation. Recall that in the pion scaling limit, only pions are assumed to contribute to the seasonal effect. Such an effect can be written:

$$(\alpha_T)_\pi \equiv 1 / \left[\frac{\gamma}{\gamma+1} \frac{\epsilon_\pi}{1.1 E_{th} \cos\theta} + 1 \right], \qquad (6.3)$$

Similarly, if only kaon induced muons are considered to contribute to the seasonal effect, an expression can be written to find this component:

$$(\alpha_T)_K \equiv 1 / \left[\frac{\gamma}{\gamma+1} \frac{\epsilon_K}{1.1 E_{th} \cos\theta} + 1 \right], \qquad (6.4)$$

This way, a prediction can be made of $\alpha_T(\pi) = 0.928 \pm 0.008$ and $\alpha_T(K) = 0.635 \pm 0.029$. The theoretical value for $\alpha_T(\pi)$ is greater than the *Monte Carlo* value by 0.13, and the theoretical value for $\alpha_T(K)$ is greater than the *Monte Carlo* value by 0.098, which are on the same order of magnitude as the difference between the total α_T from the data and *Monte Carlo* (0.14). Such large disagreement between the data and *Monte Carlo* suggests the following possibilities:

1. **The seasonal effect is not well understood** This is doubtful because there is a significant correlation (0.91) between the changes in rate and changes in temperature in the data.

2. **There are large errors in the atmospheric input** This is a likely cause of at least some of the disagreement. Surely the temperature changes are more complicated than the simplifications that were made so that the calculation was possible.

3. **The Monte Carlo does not accurately account for this atmospheric physics** The *Monte Carlo* simulations employed for cosmic ray physics are very good at predicting gross features, but the detailed level of this investigation might be beyond current capabilities.

Changes in atmospheric temperature cause changes in the primary interaction height, which is important to shower development and therefore airshower experiments. This is a matter that warrants further investigation.

6.2 α_T as a Function of $E \cos\theta$

It has been shown that the relevant parameter regarding underground muon intensity is surface energy times the cosine of the zenith angle (Sec. 2.1.5 and Ref. [60]). It has also been shown that

the theoretical expression for α_T depends on $E\cos\theta$ (Sec. 5.2). This distribution can also give insight into discrimination between the MACRO model and the new Kπ model.

Since the $E\cos\theta$ distribution falls off rapidly for higher energies (Sec. 4.6) and the seasonal effect is statistically limited, the data were divided into four bins, with the last bin containing all the data that was greater than 2 TeV. The temperature series method was used because of statistical considerations (Sec. 5.1.3). The muon data were integrated from the minimum value to infinity to account for the fact that the theoretical expression for α_T is dependent upon the threshold energy. The distribution of $\alpha_T(E\cos\theta)$ can be seen in Fig. 6.8, along with the MACRO model and the new Kπ model.
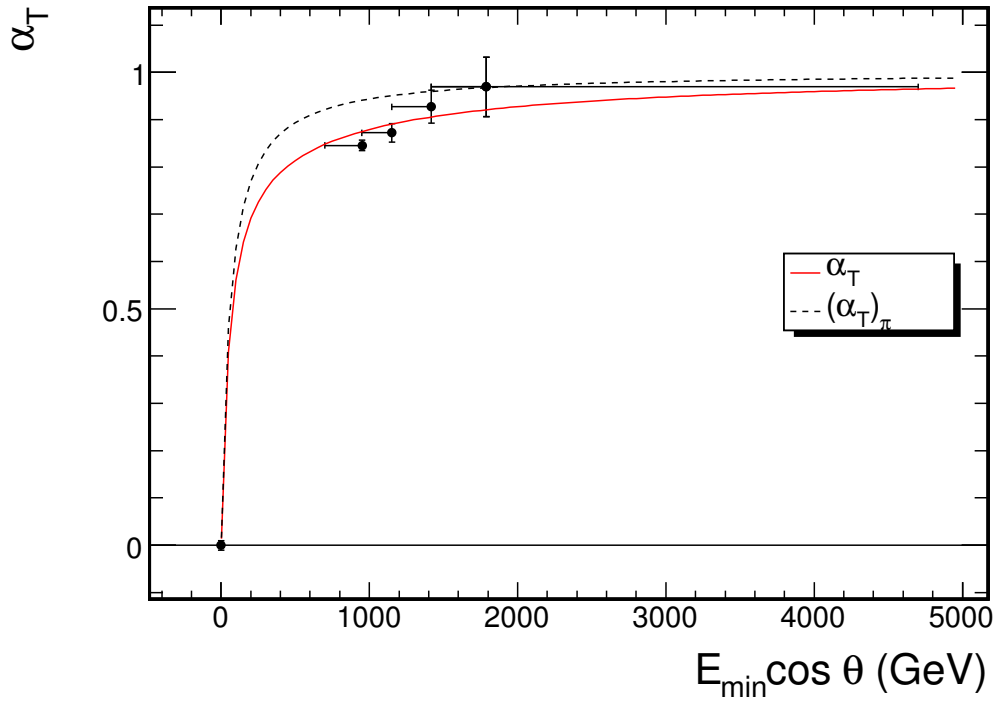
Figure 6.8: The plot of $\alpha_T(E\cos\theta)$ data, along with the theoretical expectation from Eq. 6.9. The lower horizontal error bar denotes the low limit of the bin, the point denotes the average value of the bin,

The lower two data points show good agreement with the new Kπ model, while the higher two data points fall somewhere in between the models. This analysis is extremely statistically limited, and further data collection by MINOS will not improve the statistics because the daily rate is the

important quantity. It is possible that further investigation or a larger detector could make a more definite statement.

6.3 Method for K/π Ratio Measurement

The difference between the pion-only and kaon inclusive model for the seasonal effect suggests that it is possible to measure the K/π ratio for $E_M >1$ TeV. Previous measurements have been made at accelerators for P+P collisions [152], Au+Au collisions [153], Pb+Pb collisions [154, 155]. Many other older measurements for various reactions are summarized in [156] and references therein. This measurement has never been made for $P + A_{atm}$, where A_{atm} is an atmospheric nucleus, most often nitrogen.

The intensity for muons can be written as (Eq. 2.22 on page 23):

$$I_\mu = \int_{E_{th}}^\infty \frac{A \times E^{-(\gamma+1)}}{cm^2 sr GeV} \left(\frac{1}{1 + 1.1 E_\mu \cos\theta/\epsilon_\pi} + \frac{\eta}{1 + 1.1 E_\mu \cos\theta/\epsilon_K} \right) \tag{6.5}$$

$$\simeq B \times E_{th}^{-\gamma} \left(\frac{1}{\gamma + (\gamma+1)1.1 E_{th} \cos\theta/\epsilon_\pi} + \frac{\eta}{\gamma + (\gamma+1)1.1 E_\mu \cos\theta/\epsilon_K} \right). \tag{6.6}$$

The theoretical prediction of α_T for properly weighted atmospheric temperature distribution can be written as:

$$\alpha_T = \frac{T}{I_\mu^0} \frac{\partial I_\mu}{\partial T}. \tag{6.7}$$

Barrett [59] shows that the theoretical α_T can be written in the more useful form:

$$\alpha_T = -\frac{E_{th}}{I_\mu^0} \frac{\partial I_\mu}{\partial E_{th}} - \gamma \tag{6.8}$$

This can be calculated using the intensity found in Eq. 6.5 and a little algebra:

$$\alpha_T = \frac{1}{D_\pi} \frac{1/\epsilon_K + A_K(D_\pi/D_K)^2/\epsilon_\pi}{1/\epsilon_K + A_K(D_\pi/D_K)/\epsilon_\pi} \tag{6.9}$$

where

$$D_\pi \equiv \frac{\gamma}{\gamma+1} \frac{\epsilon_\pi}{1.1 E_{th} \cos\theta} + 1,$$

$$D_K \equiv \frac{\gamma}{\gamma+1} \frac{\epsilon_K}{1.1 E_{th} \cos\theta} + 1$$

This is the kaon inclusive model. In the pion scaling limit, the theoretical α_T has the simpler form:

$$(\alpha_T)_\pi \equiv 1 / \left[\frac{\gamma}{\gamma + 1} \frac{\epsilon_\pi}{1.1 E_{th} \cos\theta} + 1 \right], \tag{6.10}$$

The theoretical α_T asymptotically approaches one as energy increases. This means that for very large energies, the muon intensity is proportional to ϵ, which depends linearly on temperature.

The expression for the experimental α_T is written as

$$\frac{\Delta R_\mu}{\langle R_\mu \rangle} = \alpha_T \frac{\Delta T_{\text{eff}}}{\langle T_{\text{eff}} \rangle}, \tag{6.11}$$

where $R \equiv N/t$. The fluctuations in rate will be proportional to the fluctuations in temperature. Since $E_{th} \gg \epsilon_\pi$, we expect α_T to be nearly one for pions. This will not be the case for kaons, since $E_{th} \sim \epsilon_K$. Thus, we expect the kaon influence to cause an overall decrease in total α_T. We can then break the left hand side of Eq. 6.11 into meson components:

$$\frac{\Delta R_\mu^\pi + \Delta R_\mu^K}{\langle R_\mu^\pi \rangle + \langle R_\mu^K \rangle} = \alpha_T \frac{\Delta T_{\text{eff}}}{\langle T_{\text{eff}} \rangle} \tag{6.12}$$

Rearranging gives:

$$\frac{\langle T_{\text{eff}} \rangle}{\alpha_T \Delta T_{\text{eff}}} \left(\frac{\Delta R_\mu^\pi}{\langle R_\mu^\pi \rangle} + \frac{\Delta R_\mu^K}{\langle R_\mu^\pi \rangle} \right) - 1 = \frac{R_\mu^K}{R_\mu^\pi} = \frac{N_K}{N_\pi} \tag{6.13}$$

Recall that in the pion scaling limit, only pions are assumed to contribute to the seasonal effect. Such an effect can be written:

$$\frac{\Delta R_\mu^\pi}{\langle R_\mu^\pi \rangle} = (\alpha_T)_\pi \frac{\Delta T_{\text{eff}}}{\langle T_{\text{eff}} \rangle}, \tag{6.14}$$

Since this is a linear effect that is found by counting rates, it is possible to apply the same separation to the kaon component. The kaon component can then be written:

$$\frac{\Delta R_\mu^K}{\langle R_\mu^K \rangle} = (\alpha_T)_K \frac{\Delta T_{\text{eff}}}{\langle T_{\text{eff}} \rangle}, \tag{6.15}$$

The ratio of the muon counting rates R_μ^K / R_μ^π is equivalent to the ratio of muons from kaons to muons from pions N_μ^K / N_μ^π, which will be written $r_\mu(K/\pi)$. Rearranging and inserting Eq. 6.14 and Eq. 6.15 into Eq. 6.12 gives:

$$r^\mu(K/\pi) = \frac{1}{\alpha_T} \left((\alpha_T)_\pi + (\alpha_T)_K \frac{\langle R_\mu^K \rangle}{\langle R_\mu^\pi \rangle} \right) - 1 \tag{6.16}$$

A little more algebra gives the compact result:

$$r_\mu(K/\pi) = \frac{(\alpha_T)_\pi/\alpha_T - 1}{1 - (\alpha_T)_K/\alpha_T} \tag{6.17}$$

The value for $r_\mu(K/\pi)$ can be predicted by integrating Eq. 6.5 on page 123:

$$r_\mu(K/\pi) = \frac{I_\mu^K}{I_\mu^\pi} = 4.82 \times \eta \tag{6.18}$$

where

$$I_\mu^K = \int_{E_{th}\cos\theta}^{\infty} \frac{\eta A E_\mu^{-\gamma}}{1 + 1.1 E_\mu \cos\theta/\epsilon_K} dE_\mu \cos\theta \tag{6.19}$$

$$I_\mu^\pi = \int_{E_{th}\cos\theta}^{\infty} \frac{A E_\mu^{-\gamma}}{1 + 1.1 E_\mu \cos\theta/\epsilon_\pi} dE_\mu \cos\theta \tag{6.20}$$

and $E_{th}\cos\theta \sim 700\,\mathrm{GeV}$, determined empirically from MINOS data. The parameter η is defined as

$$\eta = 0.635 \times r(K/\pi) \frac{(1 - r_\pi)}{(1 - r_K)} \frac{1 - (r_K)^{\gamma+1}}{1 - (r_\pi)^{\gamma+1}} = 0.365 \times r(K/\pi) \tag{6.21}$$

where $r(K/\pi) = \frac{Z_{NK}}{Z_{N\pi}}$ [61] is the ratio of kaons to pions produced in the primary cosmic ray interactions. Inserting Eq. 6.21 into Eq. 6.18 and rearranging gives an expression for $r(K/\pi)$ in terms of $r_\mu(K/\pi)$:

$$r(K/\pi) = 0.59 \times r_\mu(K/\pi) \tag{6.22}$$

The parameter $\alpha_T = 0.877 \pm 0.027$ (statistical plus systematic errors) is measured by MINOS. The parameter $(\alpha_T)_\pi = 0.928 \pm 0.008$ can be found using the pion-only model in Eq. 6.10. In order to finish the calculation, a measurement of the parameter $(\alpha_T)_K$ must be made. A similar expression to Eq. 6.10 can be written for kaons if we assume that only kaons produce the observed muons. An equation can be derived from Eq. 6.7, setting the pion component to zero. This gives:

$$(\alpha_T)_K \equiv 1 \Big/ \left[\frac{\gamma}{\gamma + 1} \frac{\epsilon_K}{1.1 E_{th} \cos\theta} + 1 \right], \tag{6.23}$$

The parameter $(\alpha_T)_K = 0.635 \pm 0.029$ is found from a calculation made with this model. The various input values needed to calculate $r_\mu(K/\pi)$ with Eq. 6.17 are summarized in Table 6.3 on the next page. Putting these numbers into Eq. 6.17 gives: $r_\mu(K/\pi) = 0.21 \pm 0.08$. Using

Table 6.3: Input values for $r_\mu(K/\pi)$ measurement with associated errors.

Parameter	Value
α_T	0.877 ± 0.027
$(\alpha_T)_K$	0.635 ± 0.029
$(\alpha_T)_\pi$	0.928 ± 0.008

$r_\mu(K/\pi)$ and Eq. 6.22 on the preceding page, a measurement of the ratio of kaon production to pion production for E_p 7 TeV, can be performed:

$$r(K/\pi) = 0.59 \times (0.21 \pm 0.08) = 0.12 \pm 0.05 \tag{6.24}$$

A comparison of this measurement to other measurements is shown in Fig. 6.9 on the following page. These measurements don't directly compare because they are for different reactions and only the MINOS result is for a reaction where the constituent particles do not have equivalent transverse momenta. Nevertheless, they are all presented on the same axes for a broad overview of measurements that have been made.
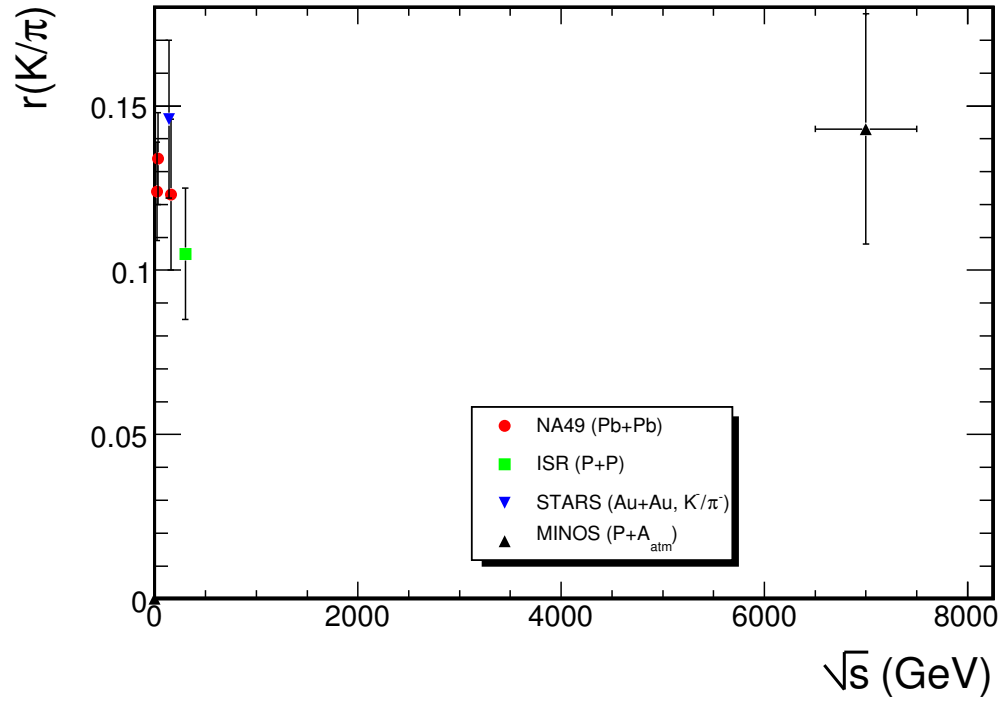
Figure 6.9: A compilation of selected measurements of K/π for interactions of various center of mass energies. The STARS value was from Au+Au collisions at RHIC [153], the NA49 measurement was from Pb+Pb collisions at SPS [154, 155], and the ISR measurement was from P+P collisions [152].

Chapter 7

Moon Shadow

Optical telescopes use a standard catalog of stars to establish the resolution and pointing reliability of a new instrument. This is not possible for a cosmic ray detector, as there are no cosmic ray sources available for calibration. There is a well observed phenomena in the otherwise isotropic cosmic ray sky, though it is a deficit, not a source. It is important for cosmic ray and neutrino point source searches to study the resolution and pointing of a cosmic ray detector, and the moon provides a means for this because it absorbs incident cosmic rays, causing deficits from its location. The physical extent and shape of the deficit gives information about the resolution of the detector, while the location of the deficit center gives information about the absolute pointing of the detector. The moon has a $0.5°$ diameter as viewed from Earth, and the cosmic ray deficit it causes has been measured by air shower arrays (CYGNUS [157], CASA [158] , Tibet [159]), as well as underground detectors (Soudan 2 [160], MACRO [161, 82], L3+C [162]).
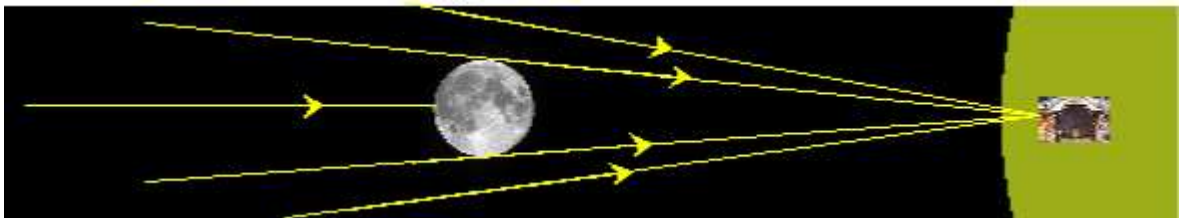
Figure 7.1: The creation of the muon shadow of the Moon. Though the Moon subtends a diameter of a mere $0.5°$, it blocks sufficient Cosmic Ray primaries to makes its presence known.

MINOS observes underground muons with a minimum energy of $0.7\,\mathrm{TeV}$, and the sharply

peaked energy spectrum has a mean value of about $1.0\,\mathrm{TeV}$. This mean energy corresponds to a mean primary energy of about $10\,\mathrm{TeV}$. The moon deficit is affected by phenomena associated with cosmic ray propagation and interaction resulting from geomagnetic fields, Interplanetary Magnetic Field (IMF), multiple Coulomb scattering, etc. Multiple Coulomb scattering occurs in the rock and causes a general spreading of the moon deficit disc. The geomagnetic field is nearly a dipole, and causes an eastward deflection of positive primaries, which results in relative east-west shift in the observed shadow of magnitude $\Delta\theta = 1.7° Z/E_p(TeV)$ [163, 164]. The IMF is caused by the sun, which has an ambient dipole field that is 100 times greater than the geomagnetic field at the same distance. This field is carried through the solar system by the solar wind, the stream of energetic charged particles that emanate from the atmosphere of the sun. Since the sun has a 27 day rotation period, the magnetic field that is carried by the solar wind has a spiral shape, called a Parker spiral [165]. The IMF causes deflection of primaries that strongly depends on the solar wind, and its complex shape makes it very hard to model. The IMF causes a deflection that smears the moon's shadow, though this effect is small since a primary travels a relatively short distance from the moon to Earth.

The sun also subtends a disk of diameter $0.5°$ as viewed from earth, and has sufficient size to provide an observable sink in the cosmic ray sky. The the sun shadow is more difficult to observe because is much farther away which gives the IMF more time to deflect the charged cosmic rays, and the sun's own magnetic field further smears the edges of the deficit it causes. Both the solar magnetic field and the IMF vary according to an 11 year solar activity cycle that peaks as the sun's magnetic field changes polarity. The amount of solar activity increases as the sun approaches solar maximum, when the sun's dipole field changes polarity. The most recent solar maximum occurred in February, 2001.

7.1 Data

7.1.1 Event Selection

This analysis encompassed events recorded over 1614 days, from 1 August 2003 - 31 December 2007, for a total of 1506.8 live-days. The data set includes 60.85 million cosmic ray induced muon tracks. Cosmic ray muons were triggered by recording hits on 4/5 planes or exceeding a pulse-height threshold and were written to a temporary disk at Soudan and later sent to Fermilab

for reconstruction. Several cuts were required to ensure that the detector was in a reliable state when the data was taken (Pre-Analysis cuts) and that only well reconstructed tracks were included in the sample (Analysis cuts).

Pre-Analysis Run Cuts, Event Cuts

1. "Demuxing Failures", where the demultiplexing algorithm was unable to cleanly distinguish a pixel hit from one strip over another.

2. "Bad Run", 612 runs were excluded from the analysis for failing the following criteria [60]:

   (a) require physics data, runs must be more than 5 minutes

   (b) Runs must contain "good physics data", which includes correct trigger bits, complete readout, and minimal dead chips

   (c) remove runs with anomalous rates: 0 Hz < cosmic ray rate < 1 Hz

   (d) remove runs that the Atmospheric Neutrino Analysis has flagged as having far too many contained events

3. "HV/COIL status error", a muon was excluded if the magnet coil was in an unknown or bad state.

4. "Spill Trigger" Since the MINOS experiment is designed to measure beam neutrino oscillations, there is a different trigger used when the neutrino beam pulses to maximize the detection of beam-produced neutrinos. This trigger is based on the timing of the beam pulse and it opens the detector to record all hits during a $100\,\mu$s window. The muon data that is recorded $\pm 50\,\mu$s of a beam pulse is excluded since it could be of terrestrial, not cosmic origin.

Analysis Cuts

1. "Upward Going", a track was excluded if it was reconstructed as upward going, $\cos\theta < 0.1$.

2. "Fit Quality", a track with $\chi^2_{fit} < 0$, ndf<1, or $\chi^2_{fit}/ndf > 1.5$. A track that was poorly reconstructed might not have reliable pointing.

3. "Fiducial", a muon vertex and end point in x and y must be inside of the detector

4. "Track Length < 1.55 m", any event with a track shorter than 1.55 m may not be reliably reconstructed.

5. "Number of Planes < 10", a track that passes fewer planes may not give reliable strip information to the track fitter.

6. "$\Delta(\sigma_{vtx}, \sigma_{end}) > 0.021$" If the endpoint position is well known but the vertex is not, then the muon has questionable reconstruction pointing.

The parameter values for three of the analysis cuts, Track Length, Number of Planes, and $\Delta(\sigma_{vtx}, \sigma_{end})$ were determined empirically using a *Monte Carlo* simulation of the cosmic ray muon data. 7.5 million simulated muons were created in the rock surrounding the detector, then propagated through the detector. These events were reconstructed using the same algorithms as were used to process the data. These muons were simulated without regard for extra-terrestrial objects (such as the moon), so to optimize the cut values, the moon was artificially inserted as follows. A simulated muon was assigned an arrival time by choosing a random time out of the Poisson distribution of mean value $\Delta T = 2.2$ [166]. The location of the moon at that time was found using Jet Propulsion Laboratory's DE405 Fortran Ephemeris [167], accessed with the c-version of Naval Observatory Vector Astronomy Subroutines (NOVAS-c) [168]. NOVAS-c also converted the DE405 rectangular coordinates to celestial coordinates relative to the location of the Far Detector in latitude, longitude, and elevation, as well as corrected for nutation, earthtilt and precession. The one dimensional space angle separation of the muon from the moon was found using the Haversine formula [169]. If the muon's true angular separation from the moon was found to be less than $0.26°$, that muon was cast out, just as it would have been had the parent cosmic ray actually encountered the moon.

The reconstructed muon angular separation from the moon, $\Delta\theta$, was binned in $S_{bin} = 0.10°$ increments. Since radial distance from the center of the moon is measured over a two dimensional projection, the solid angle of bin (i) increases when moving out from the center as $\Delta\Omega_i = (2i - 1) * S_{bin}\pi$. Weighting the number of events in each bin by the reciprocal of the area resulted in the distribution $N_i/\Delta\Omega_i$, the differential muon density. the distribution a function of the form [160]:

$$\frac{\Delta N_\mu}{\Delta\Omega} = \lambda(1 - (R_m^2/\sigma^2)e^{-\theta^2/2\sigma^2}) \tag{7.1}$$

where λ is the average differential muon flux, σ accounts for smearing from detector resolution, multiple Coulomb scattering and geomagnetic deflection, and $R_m = 0.26°$, the angular radius of the moon. The significance of the deficit can be found by fitting to Eq. 7.1 on the preceding page and finding the difference between this χ^2 value and the χ^2 value obtained by a linear fit to the same deficit. The deficit distribution was plotted for a cut on number of planes greater than five, then incremented by one plane on up to greater than forty. The significance of the deficit was maximized if muons with at least 10 planes were included. The same was done for track length from 1 m to 4 m, incremented by 0.1 m, and the significance was maximized if muons with length at least 1.55 m were included. This was repeated for $\Delta(\sigma_{vtx}, \sigma_{end})$, over the range $\Delta(\sigma_{vtx}, \sigma_{end}) = 0$ to 0.2, and the significance was maximized if muons with $\Delta(\sigma_{vtx}, \sigma_{end}) <$ 0.021 were included.

These cuts were applied to the muons in the data sample, and number that survived each cut can be seen in Table 7.1.1.

Table 7.1: Number of events that survive each pointing cut

Total Tracks	67.99×10^6
Cut	**Fraction Remaining**
Data Quality Cuts	
1. Reconstructed Tracks	0.8887
2. Good Run List	0.8754
3. Light Injection Removal	0.8713
4. Spill Removal	0.8712
Analysis Cuts	
1. Fit Quality	0.821
2. Fiducial	0.800
3. Number of Planes < 10	0.727
4. Length <1.55 m	0.714
5. $\Delta(\sigma_{vtx}, \sigma_{end}) >0.021$	0.613

The number of muons collected near the moon's and sun's location over the duration of the data set can be seen in Fig 7.2 on the next page. The number of muons collected in a $10° \times 10°$ half angle cone centered on the moon's location is represented by the black curve, the number collected $10° \times 10°$ half angle cone centered on the sun's location is represented by the red curve. The data are binned in 13.66 day $(T_{moon}/2, T_{moon} = 27.32$ days) increments. The number of muons

collected near the sun's location is highly correlated to season, which stands to reason given that the sun's position in the sky varies considerably throughout the year as a result of earth's orbit. The number of muons collected near the moon's location shows a short term oscillation that depends on the moon's orbital period.   There are 91,097 muons in the half angle cone centered on the
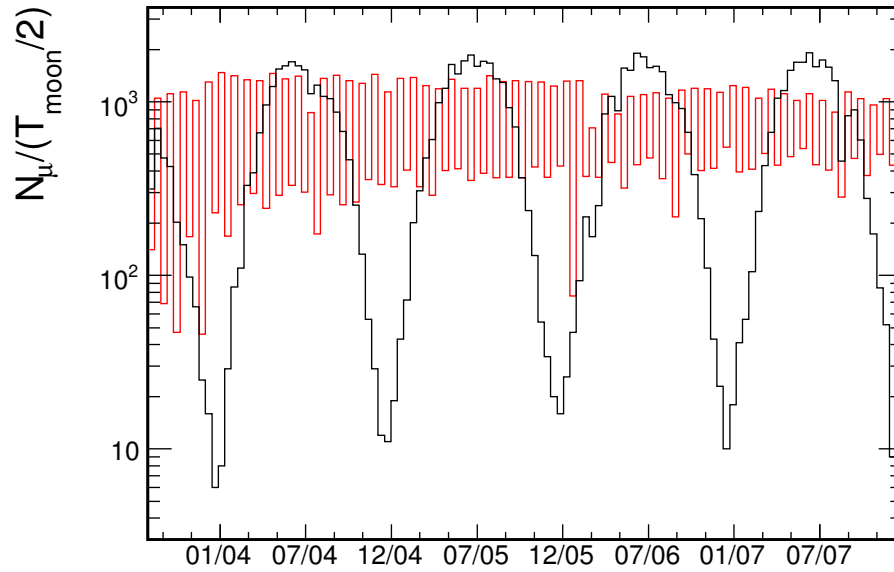
Figure 7.2: The number of muons collected in a $10° \times 10°$ half angle cone centered on the moon's location (red curve) and sun's location (black curve). The data are binned in 13.66 day increments, which it half of the moon's orbital period.

moon and 81,794 muons in the half angle cone centered on the sun. The reason for this difference is the detector is at a high latitude, thus the number of muons collected in winter near the sun's location will be fewer as compared to the number collected near the moon, as seen in Fig. 7.2. The data set includes four full yearly cycles plus an extra five months, and those extra months come after the summer solstice, so the amount of time the sun spends above the horizon (and the angle of the sun above the horizon) continues to decrease as the period progresses. This produces the observed difference in statistics.

7.1.2 Dimuons

The resolution of an underground detector is limited by multiple Coulomb scattering in the surrounding rock, the smearing effects of the geomagnetic and interplanetary magnetic fields, as well as the geometric limitation of the apparatus itself. The dominant effect 2070 mwe underground is multiple Coulomb scattering since magnetic field effects decrease with energy. In order to optimize the cuts for good pointing, what good pointing means to the Far Detector must first be determined. The resolution of the detector was found using 3.12 million dimuons collected from 8/03-12/07. Each pair was required to have exactly two tracks, such that reconstruction difficulties arising from demultiplexing three or more tracks were avoided and no *a priori* choice of which two tracks from an event should be used had to be made. Dimuons are created by the same parent cosmic ray, of sufficient energy to generate more than one meson. The transverse momentum of these pairs is negligible compared to their longitudinal momentum, and they have angular separation < 0.05 at production [161], thus their trajectories are essentially parallel. Thus, the amount of angular separation these pair have gives a measure of how much spreading took place between creation and detection, which is the effective resolution of the detector. Pairs were excluded by the same criteria used for single muons (see Sec. 7.1.1 on page 129). 1.77 million muons survived, and the distribution of their angular separation is shown in Fig. 7.3 on the next page Resolution is defined to be the angular separation where 68% of the distribution lies, and this can be seen in Fig. 7.3 on the following page. This value is 0.62 for MINOS.

7.1.3 Background Simulation

The background for this analysis was calculated using a simple *Monte Carlo* simulation that exploits two key features of the muons induced by cosmic ray primaries: the time between consecutive cosmic ray arrivals follows the well known gamma distribution (Poisson of order one) [166] and the cosmic ray sky is isotropic, Thus, a bootstrap method that independently chooses the arrival time and location in space efficiently simulates a cosmic ray muon. This simulation chose a muon out of the known distribution of events in the detector (in horizon coordinates), paired it with a random time chosen from the known time distribution, and found the muon's location in celestial coordinates. This was done for every muon to create one background sample, and the number of background samples is only limited by CPU availability.
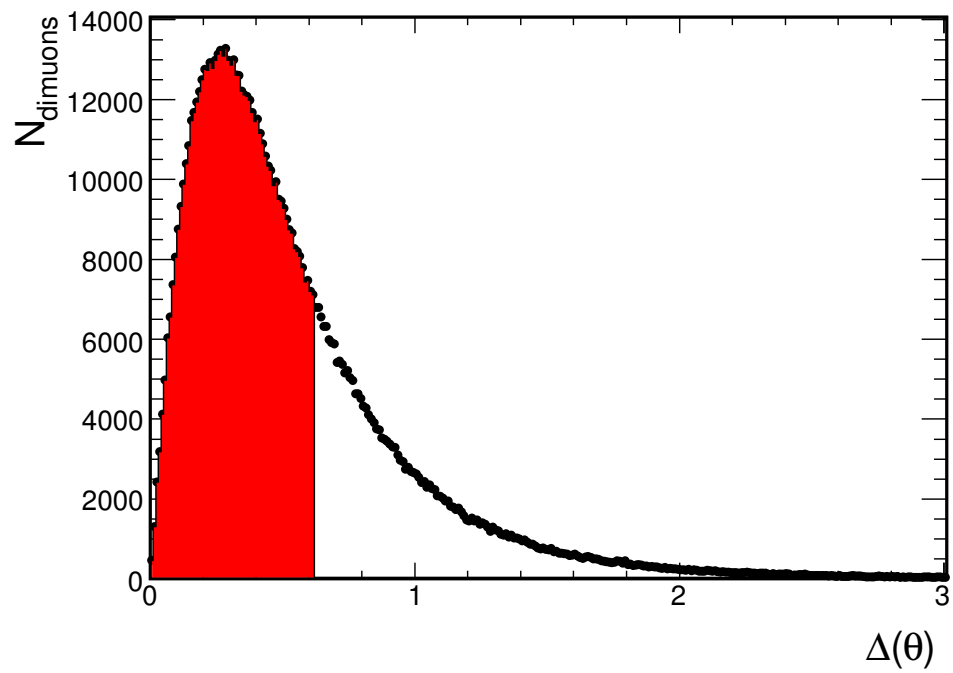
Figure 7.3: The angular separation in degrees of dimuon pairs. The shaded region represents 68% of the distribution, which is the resolution of the detector.

7.2 Moon Shadow

The location of the moon, and the separation of each muon from the moon ($\Delta\theta$), was found using the method described in Sec. 7.1.1 on page 129 The $\Delta\theta$ distribution is shown in Fig. 7.4 with statistical error bars. There is a deviation from a flat distribution as $\theta \rightarrow 0$, and that deviation is attributed to muons blocked by the moon.   A fit to Eq. 7.1 on page 131 yields $\chi_G^2/ndf =$
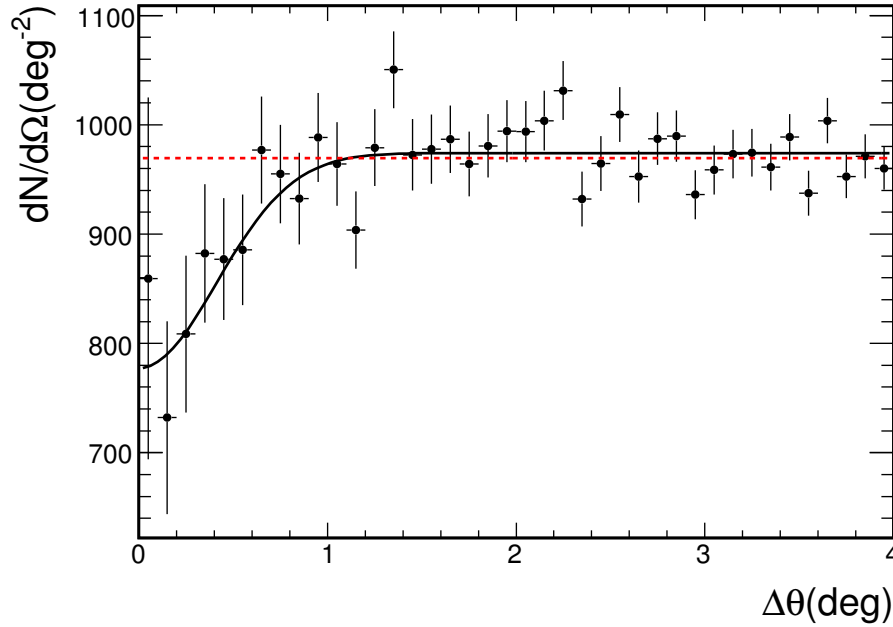
Figure 7.4: The differential muon flux with respect to displacement from the moon's location, binned in 0.1^o. The dashed curve is the result of a linear fit , while the solid curve is the best fit from Eq. 7.1 on page 131.

36.4/38, an improvement of 18.7 over the linear fit ($\chi_L^2/ndf = 55.1/39$), with parameters $\lambda = 974 \pm 4.4$ and $\sigma = 0.41 \pm 0.06°$. The change in χ^2 over 38 degrees of freedom corresponds to a 3×10^{-5} chance probability.

7.2.1 Two Dimensions

The one dimensional moonshadow is a good test of a detector's pointing reliability and resolution, but it assumes *a priori* that the moon is located at $\Delta\theta = 0$ and heavily weights the small $\Delta\theta$

bins to normalize to solid angle. Detector mis-alignment, multiple Coulomb scattering in the rock and the geomagnetic field can smear the trajectories of cosmic rays and make the moon appear to shift, which could obscure part of the deficit observed in the one dimensional moonshadow. A two dimensional maximum likelihood grid search assumes no particular location of the moon, and is thus a more powerful tool to assess absolute detector pointing.

The Far Detector Point Spread Function (FDPSF) is specific to the type, geometry and amount of rock overburden, which determines the energy at which muons are sampled, the geometry of the detector, and myriad other smearing effects. Dimuon events offer a means to determine the point spread function since they are created with nearly parallel trajectories. The resulting distribution of separation angles at the detector automatically accounts for these smearing effects (see Sec. 7.1.2 on page 134). To find the Far Detector point spread function, the distribution of dimuon separation angles in celestial coordinates ($\Delta RA \cdot \cos(Dec), \Delta Dec$) was found. Scaling ΔRA by $\cos(Dec)$ accounts for the differing solid angle subtended by an RA separation at a given Dec. This is the distribution of expected smearing of muon tracks in the Far Detector. A simple *Monte Carlo* was written to quantify the expected scattering about the moon by sending muons toward a $0.5°$ disk. If the muon fell in the region of the disk, it was excluded; if not, an angular separation was selected at random from the FDPSF. The resulting deficit the expected effect of the moon on Cosmic Ray primaries observable in the Far Detector, and can be seen in Fig. 7.5 on the next page.

One thousand background samples of the isotropic cosmic ray sky were generated using the method in Sec. 7.1.3 on page 134. These were averaged to create a smooth, isotropic background grid, sorted in equal solid angle bins $0.10°$ on a side. The data were sorted in to a similar grid. A grid search utilizing a log-likelihood method was employed to find the most probable position of a moon-like deficit. The moon template was placed at a fixed position (x,y) on the grid, and the likelihood that (x,y) is the position of the moon with shadowing strength I_s was found by:

$$\lambda(x, y, I_s) = 2 \sum_{i=1}^{n_{bin}} \left[N_i^{th} - N_i^{obs} + N_i^{obs} \ln \frac{N_i^{obs}}{N_i^{th}} \right],$$
(7.2)

where $N_i^{th} = N_i^{back} I_s(x, y)$, N_i^{back} is the number of muons from the smoothed background grid for (x,y). To determine the strength of this deficit, the parameter Λ was defined as:

$$\Lambda = \lambda(x, y, 0) - \lambda(x, y, I_s),$$
(7.3)

which is a measure of the deviation from the null (no-moon) hypothesis.
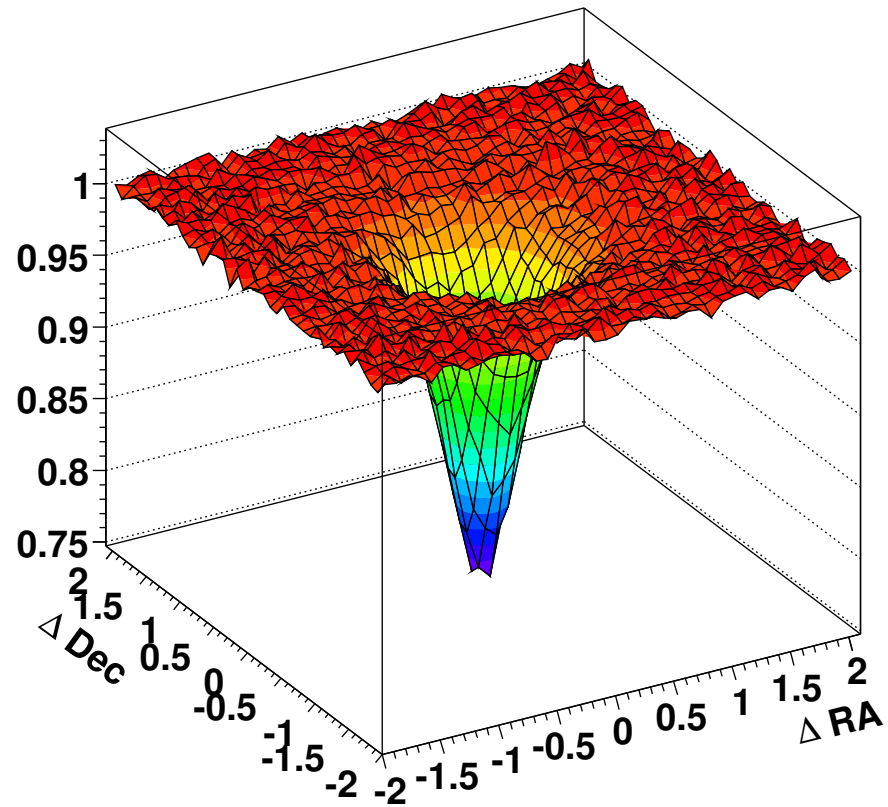
Figure 7.5: The expected Cosmic Ray shadow of the moon as seen in the Far Detector.

The two dimensional distribution of these deviations was drawn on a $2° \times 2°$ grid, binned in $0.10°$ on a side, and can be seen in Fig. 7.6 for celestial coordinates, The greatest deficit is $\Lambda = 23.5$, centered on $(-0.15°, -0.15°)$. The distribution of Λ is the same as for a χ^2 distribution with one degree of freedom, so $\Lambda = 23.5$ has a χ^2 probability of 6.5×10^{-7} (5σ).
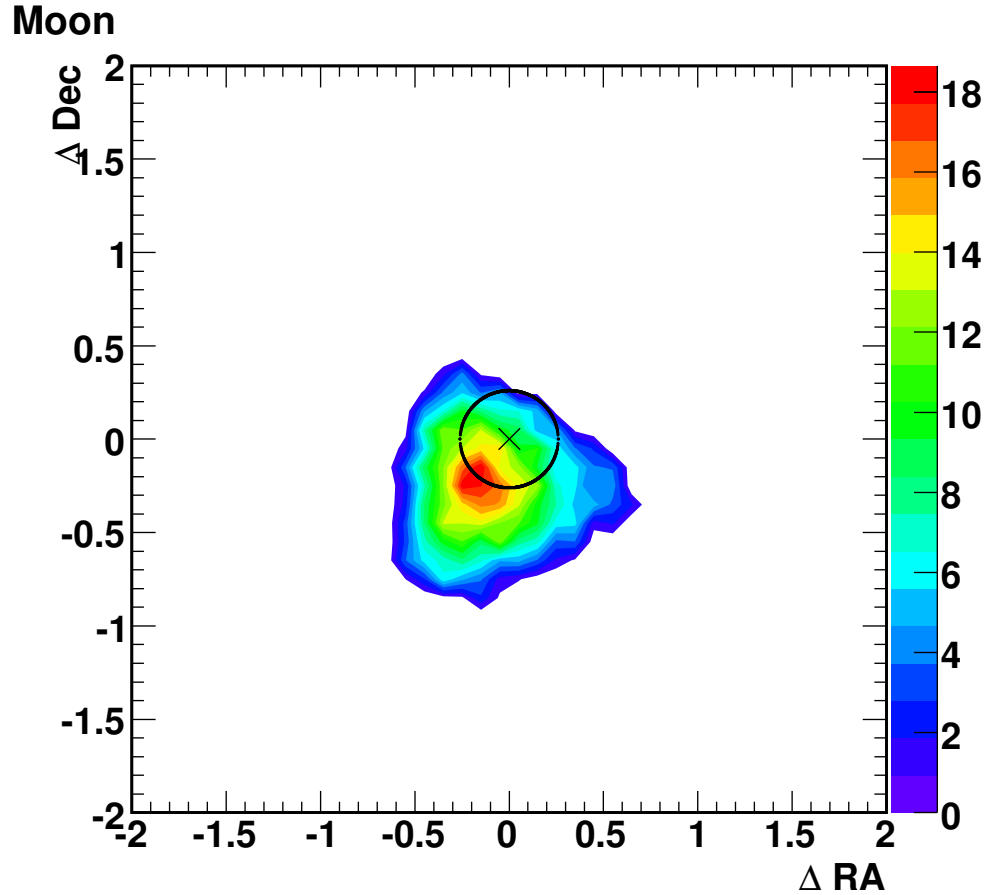
Figure 7.6: The two dimensional moon induced muon deficit in $0.01 \deg^2$ bins, in celestial coordinates. The greatest deficit is $\Lambda = 23.5$, centered on $(-0.15°, -0.15°)$

As a cross-check of the significance, a *Monte Carlo* method was used to create many thousands of simulated (fake) moon grids were created using the same background method in Sec. 7.1.3 on page 134. Searching through many fake moon grids gave the probability of randomly finding a moon-like deficit for a particular value of Λ. Each $2° \times 2°$ grid allowed 160 searches, for a total

of 95 million searches. There were 60 bins that had $\Lambda > 23.5$ in celestial coordinates, thus the chance probability of this deficit is $6.3 \times 10^{-7}(5\,\sigma)$. The probability distribution can be seen in Fig. 7.7.
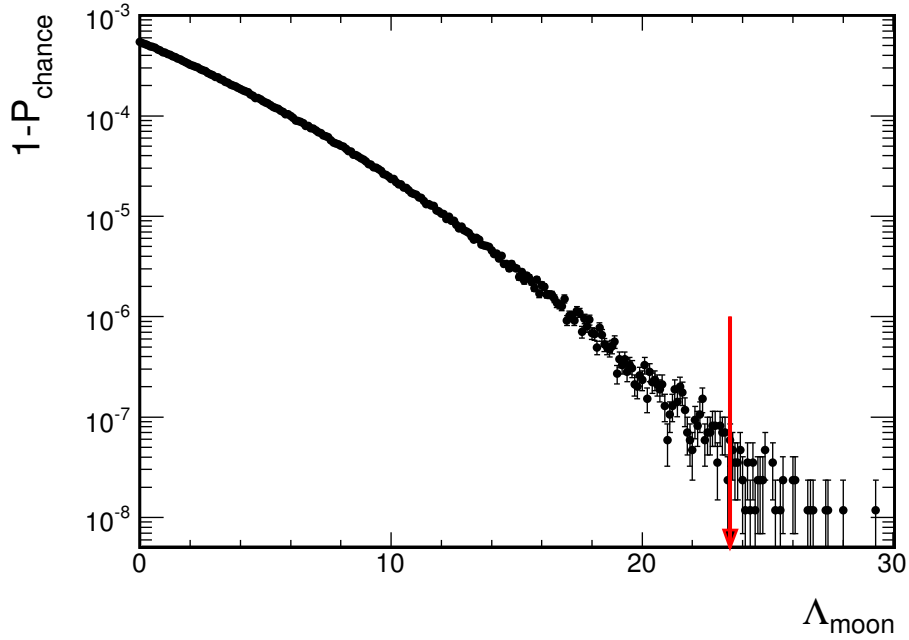
Figure 7.7: The distribution of Λ values in celestial coordinates. There were 60 searches with $\Lambda > 23.5$, which corresponds to a chance probability of $6.3 times 10^{-7}(5\,\sigma)$. The arrow denotes the position of Λ_{max}.

As mentioned in the introduction, the IMF could have some small effect on the moon shadow. This is easily observed by dividing the data into separate day/night samples. Daytime is defined here as when the sun's zenith angle was less than zero, to divide the statistics into two samples. The day-time sample contained 37,792 muons within a $10° \times 10°$ window drawn around the moon, while the night-time sample contained 53,305 muons within a $10° \times 10°$ window drawn around the moon. The reason for this difference is that the detector is only down for maintenance during the day (the mine crew works from 7:30 AM to 5:30 PM), coupled with the fact that more of the data were collected in the fall and winter than spring and summer (see Sec. 7.1.1 on page 129) . Integrating over four and a half years accounts for the 25% increase in muons collected near the moon at night. The moon shadow observed during the day can be seen in Fig. 7.8 on the next page,

while the moon shadow at night can be seen in Fig. 7.9 on the following page. The
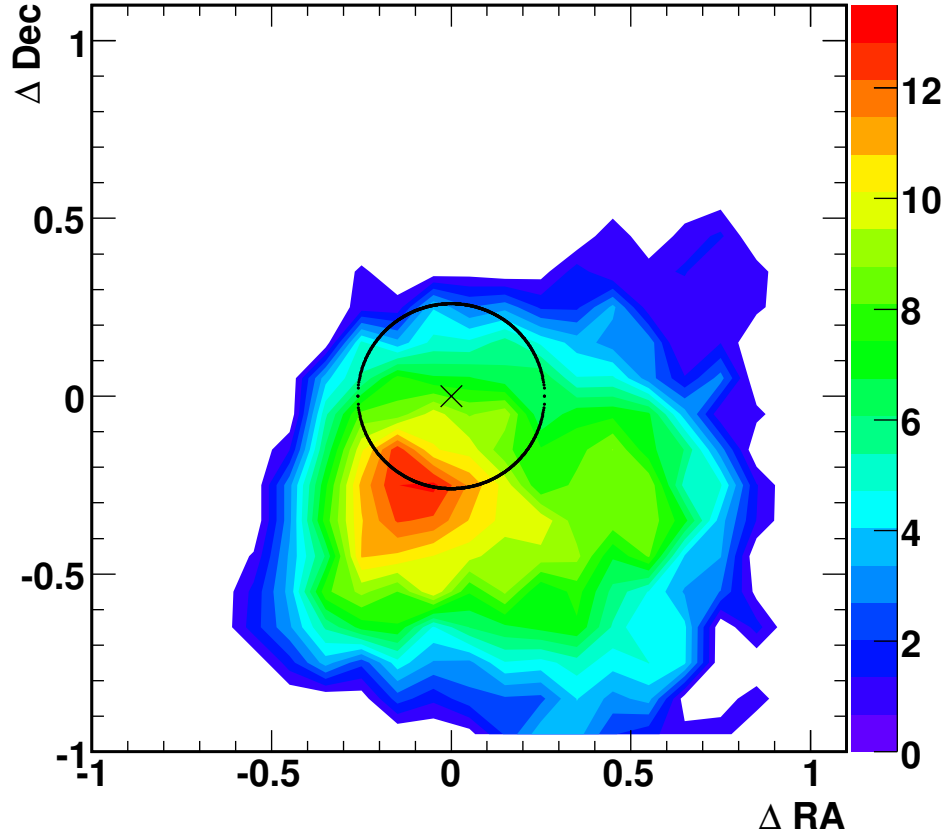
Figure 7.8: The distribution of Λ values in celestial coordinates when the moon was visible during the night. The center of the deficit is at $(-0.15°, -0.15°)$.

center of the deficit is at $(-0.1°, -0.25°)$ for the data taken at night, with $\Lambda_{max} = 13.0$, while for the data taken at night, the center of the deficit is at $(-0.15°, -0.15°)$, with $\Lambda_{max} = 10.9$. The center offsets in both plots are consistent with the center of the moonshadow for the all-muon sample, the 25% greater Λ_{max} for the night-time sample is consistent with the expectation from 25% greater statistics, and the sum of Λ_{max}^{day} and Λ_{max}^{night} is consistent with Λ_{max}^{total}. Thus the IMF has no measurable effect on the shadow of the moon as measured by MINOS.
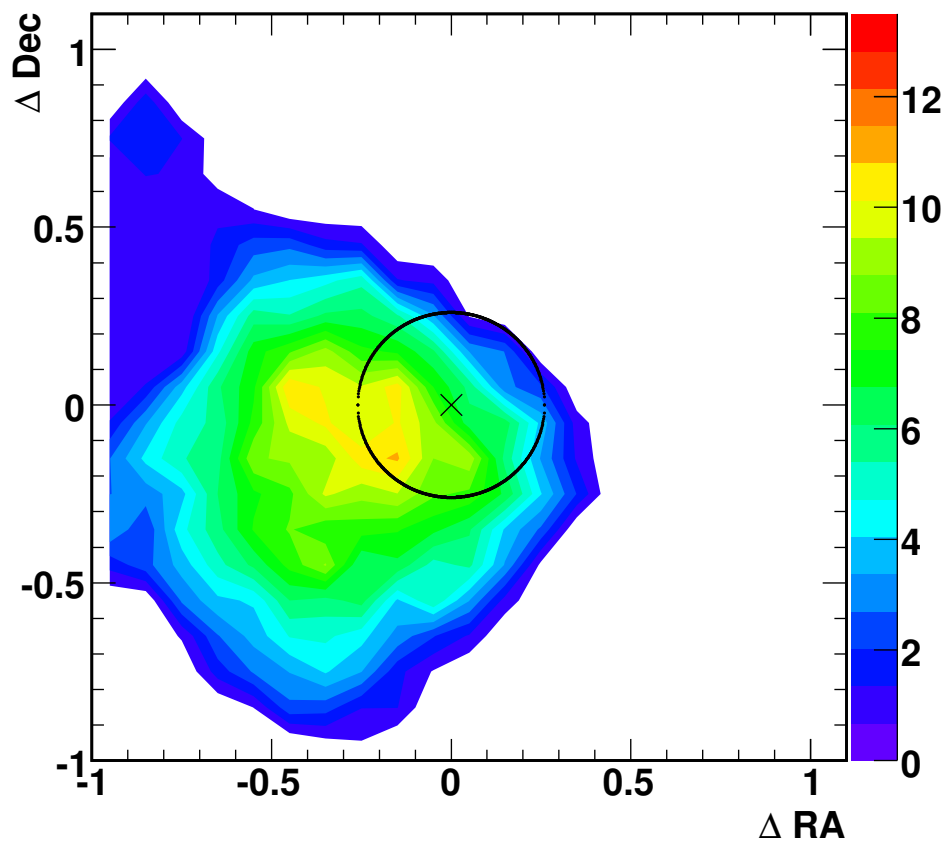
Figure 7.9: The distribution of Λ values in celestial coordinates when the moon was visible during the day. The center of the deficit is at $(-0.1°, -0.25°)$.

7.3 Sun Shadow

The one dimensional shadowing procedure from Sec. 7.2 on page 136 and the two dimensional log-likelihood analysis described in Sec. 7.2.1 on page 136 were performed for separation of cosmic muons from the location of the sun. As viewed from Earth, the sun obscures the same 0.5° diameter disk as the moon. Historically, this has been a more difficult [82] measurement to make for reasons already mentioned in the introduction.

The one dimensional sun shadow can be seen in Fig. 7.10. There is a significant
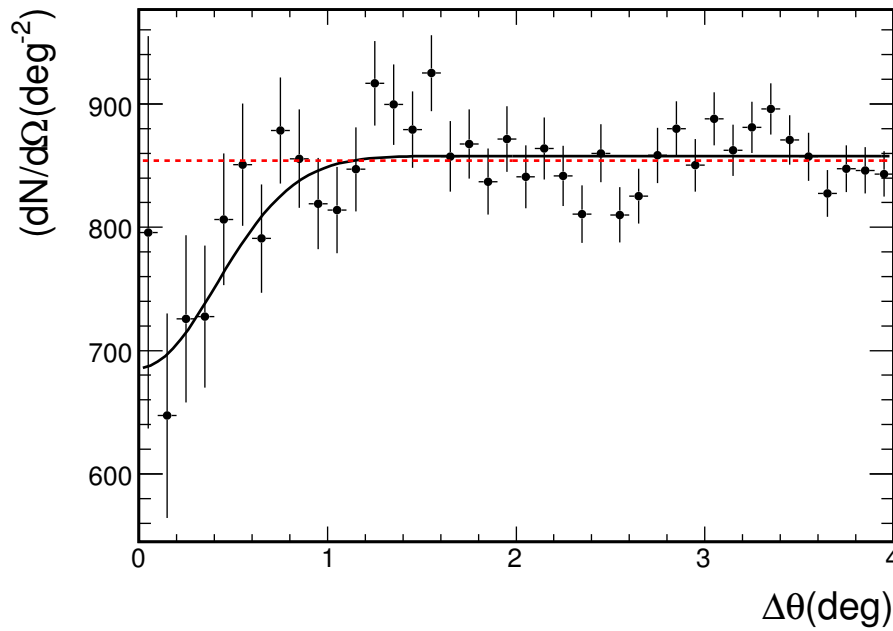
Figure 7.10: The differential muon flux with respect to displacement from the sun's location, binned in 0.10^o. The dashed curve is the calculated background, and a linear (no sun effect) fit gives $\chi_L^2/ndf = 55.5/39$. The solid curve is the best fit from Eq. 7.1 on page 131. The Gaussian (sun-induced deficit) fit gives $\chi_G^2/ndf = 41.6/38$, with parameters $\lambda = 857.9 \pm 4.1$ and $\sigma = 0.41 \pm 0.07^\circ$.

deficit in the location of the sun attributed to the sun's blocking of the primary cosmic rays. The improvement in χ^2 of 13.9 ($\chi_L^2/ndf = 55.5/39, \chi_G^2/ndf = 41.6/38$) corresponds to a 4×10^{-4} chance probability. The Gaussian fit parameter σ for the sun shadow is consistent with the value found by the fit to the moon shadow.

The two dimensional sun shadow can be seen in Fig. 7.11. The sun $\Lambda_{max} = 17.5$, which has a χ^2 probability of 1.6×10^{-5} (4.3σ). Fig. 7.12 on the next page shows the distribution
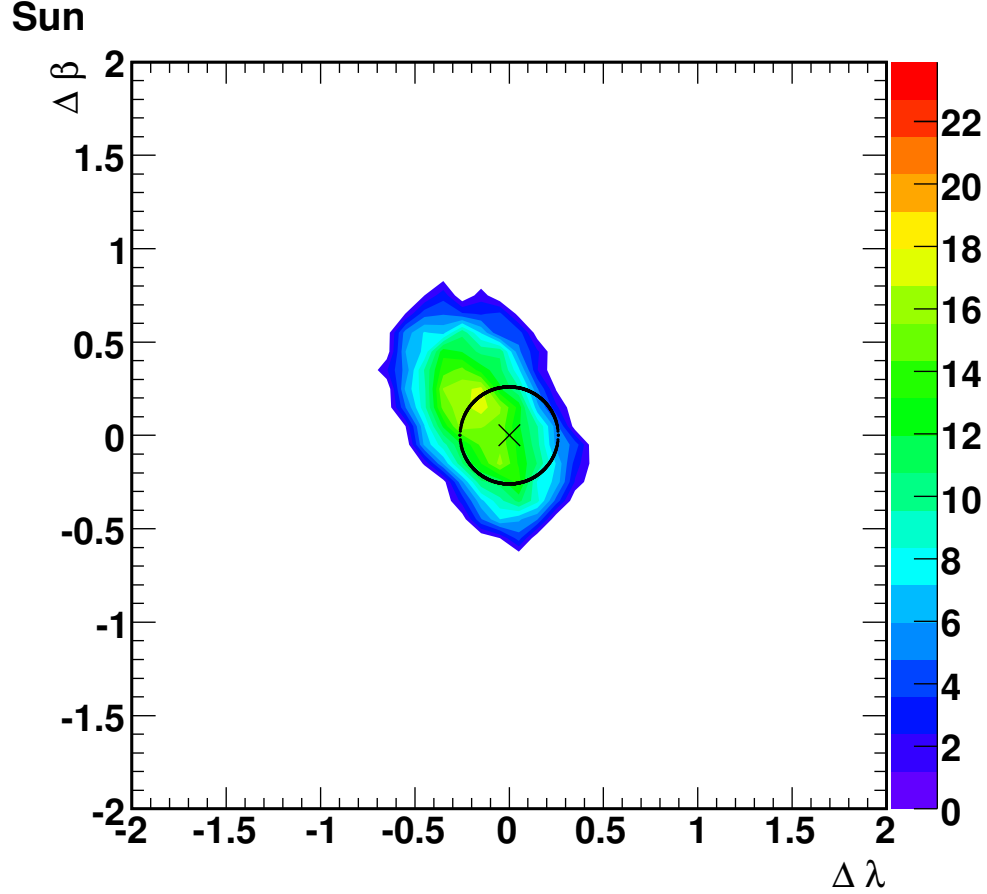
Figure 7.11: The two dimensional sun induced muon deficit in $0.01 \deg^2$ bins, in ecliptic coordinates. The greatest deficit is $\Lambda = 17.5$, centered on $(-0.20°, 0.20°)$.

of significances for fake sun searches. There were 240 searches out of 24.9 million that resulted in a lambda max greater than 17.5, which gives a $1.4 \times 10^{-5} (4.3\,\sigma)$ chance probability.

A greater IMF means a less prominent sun shadow, so the significance of the observable shadowing caused by the sun should decrease as the IMF decreases. Since the IMF is caused by solar activity, the significance of observable shadowing should increase as the number of sunspots, one measure of solar activity, decreases. The number of muons collected in a $10° \times 10°$ half angle
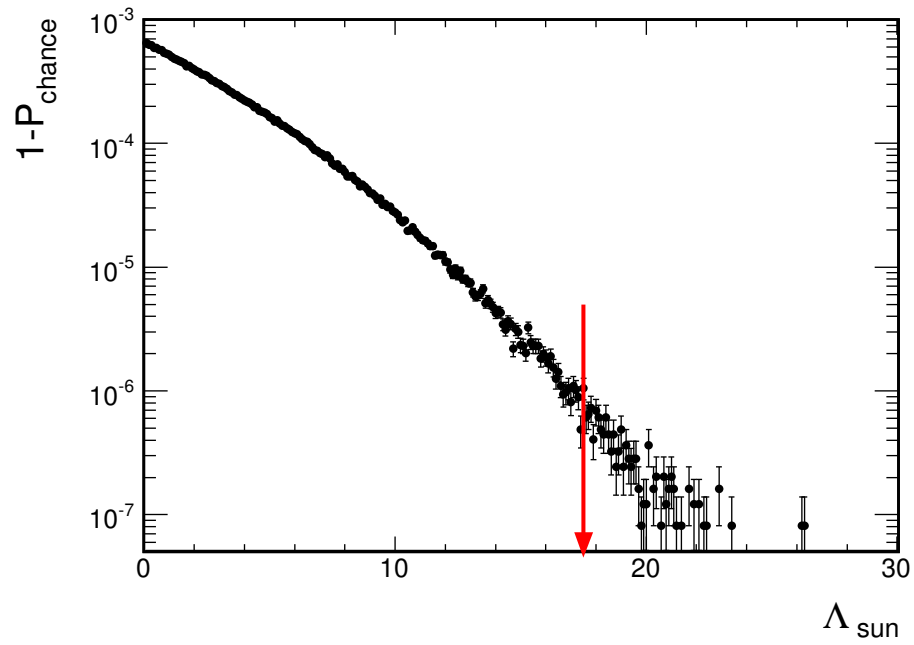
Figure 7.12: The distribution of Λ values in celestial coordinates for fake grids centered on the sun. There were searches with $\Lambda > 17.5$, which corresponds to a chance probability of $1.4 \times 10^{-5}(4.3\,\sigma)$. The arrow denotes the position of Λ_{max}.

cone centered on the sun's location can be seen in the black curve of Fig. 7.13, while the number of sunspots/day can be seen in the black curve. The muon data are binned in 13.66 day increments. The last maximum of the 11 year solar cycle occurred in 2001, and the next
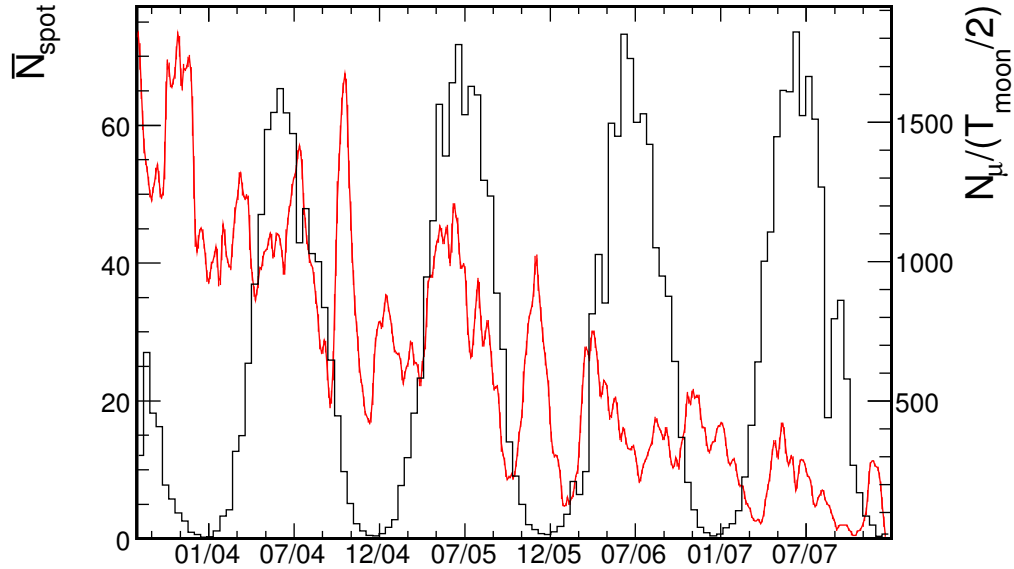
Figure 7.13: The number of muons collected in a $10° \times 10°$ half angle cone centered on the sun's location (black curve), along with the number of sunspots per day (red curve). The muon data are binned in 13.66 day increments.

minimum was predicted to occur in March, 2008 [170]. The first sunspot of the solar cycle 24 was observed on January 4, 2008 [171]. Fig. 7.13 shows the daily number of sunspots decreasing toward a minimum at the end of 2007. To search for a correlation between solar activity and strength of sun shadowing effects, the data were divided into four separate one dimensional grids of roughly equal statistics, and fit with both a linear curve and a Gaussian (shadowing) curve. The first period was Aug. 1, 2003 - Sep. 30, 2004, followed by Oct. 1, 2004 - Oct. 31, 2005, Nov. 1, 2005 - Nov. 30, 2006 and Dec. 1, 2006 - Dec. 31, 2007. These graphs can be see in Fig. 7.14 on the following page. There is an increase in significance of the sun shadow which is correlated to the decrease in solar activity as the sun approaches solar minimum. The results of these fits are summarized in Tab. 7.3 on page 148. The significance of the shadow
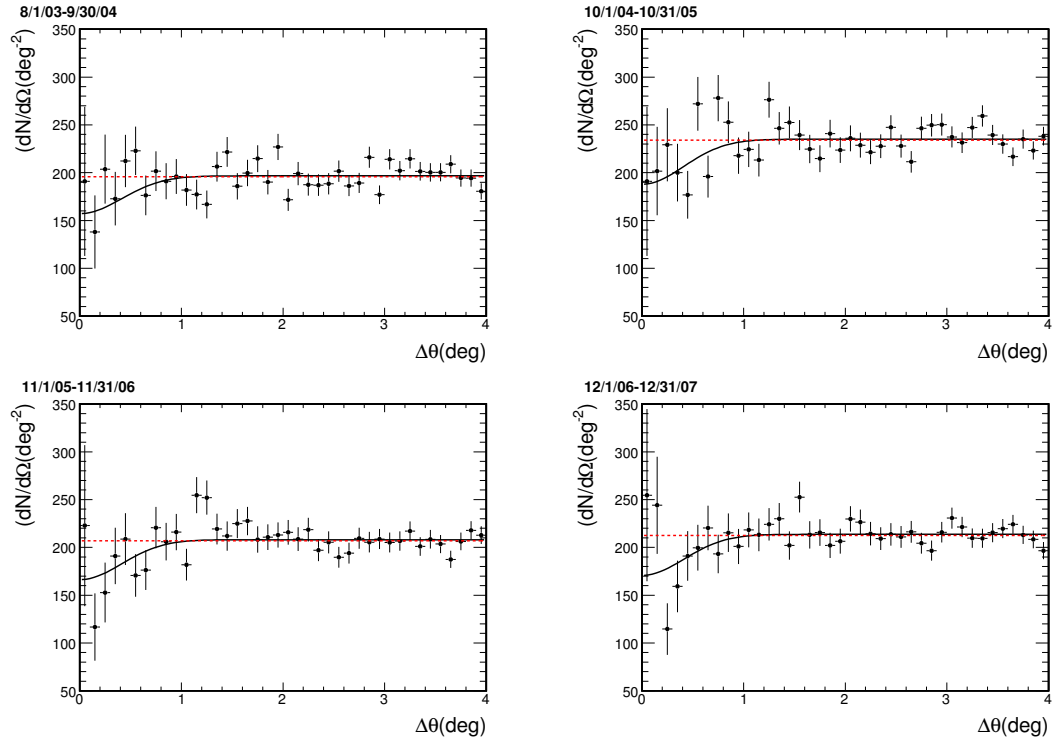
Figure 7.14: The differential muon flux with respect to displacement from the sun's location as a function of year, binned in 0.1^o. The dashed curve is the calculated background, while the solid curve is the best fit from eq. 7.1 on page 131.

Table 7.2: Significance of each year's sun shadow distribution; $\Delta\chi^2 \equiv \chi_L^2 - \chi_G^2$

Aug. 1, 2003 - Sep. 30, 2004	48.2318 - 46.0631	1.21×10^{-1}
Oct. 1, 2004 - Oct. 31, 2005	51.2708 - 48.6417	9.91×10^{-2}
Nov. 1, 2005 - Nov. 31, 2006	51.2831 - 41.1754	1.78×10^{-3}
Dec. 1, 2006 - Dec. 31, 2007	36.3565 - 28.2736	8.83×10^{-4}

seems to increase as the data is recorded further from solar maximum.

Chapter 8

Particle Astrophysics

Particle Astrophysics is a field still in its infancy. The many technical challenges (the elusive nature of the neutrino, the galactic magnetic field that deflects charged cosmic rays, the power law cosmic ray spectrum, the GZK effect) make it difficult indeed to hope for a catalog of particle sources in any near term time frame. The same could have been said about all cosmic objects at some point in history, and yet there are now fully developed fields of observation spanning the entire range of the electromagnetic spectrum, from 300 Hz, 1.24×10^{-12} eV radio to 300×10^{15} Hz, 1.24×10^{6} eV gamma ray. A number of papers have been written on searches for neutrino point sources [4, 88, 172, 173, 174, 88] diffuse astrophysical neutrino fluxes [175, 176] and cosmic ray point sources [177, 2], but no signal has yet been found (beyond SN 1987A, Ch. 1 on page 1). Thus, the field remains open.

In order that these searches were not biased and that trials factors were not increased unnecessarily, blind analyses were performed. Cuts were optimized with *Monte Carlo* and initial correlation investigations were performed with *Monte Carlo* in the case of the search for an astrophysical cosmic ray source and fake GRB trigger times and locations and muon data recorded before the beginning of the Swift catalog (August 2003 - November 2004) in the case of the GRB induced neutrino search.

8.1 Search for an Astrophysical Cosmic Ray Source

Before an individual source can be examined, an all-sky survey must be performed. Though signals have been reported in only a very few locations on the sky, the analysis must not be biased by an *a priori* assumption of a source.

8.1.1 Statistics

An excess of muons in the context of this discussion is defined as a signal above background greater than the expected random fluctuation of the actual cosmic ray background. The data set is sufficiently large such that Gaussian statistics apply. The significance of an observed number of muons over background is given in terms of a Gaussian deviation:

$$D_\sigma = \frac{N_{\text{obs}} - N_{\text{back}}}{\sqrt{N_{\text{back}}}},$$ (8.1)

where N_{obs} is the number of observed muons and N_{back} is the number of background muons. In Gaussian statistics, a confidence limit of three or five sigma from the expectation is a measure of how likely it is that a given signal could be caused by a random statistical background fluctuation. A 3σ deviation corresponds to a 0.27% likelihood that it is a background fluctuation mimicking a signal, while a 5σ deviation has a 0.000057% likelihood of background mimicking signal [178]. For a situation such as the one being investigated, simply finding a signal that deviates by 5σ does not ensure a source detection since there are multiple bins in which the search is taking place. A survey over multiple bins increases the trials factor for the search. For 32,000 bins, the actual probability that constitutes a $3\,\sigma$ likelihood is .000068%, and for a $5\,\sigma$ likelihood, 0.000000014%. D_σ is the deviation that one would expect if an unbinned search were performed, if one were only looking in one place for a signal. Therefore, to get a true 3σ detection, a deviation $D_\sigma{=}5.2\sigma$ must be found; for 5σ, $D_\sigma{=}6.7\sigma$ is required.

Especially important to the search for a sensitive signal is the signal-to-noise ratio. An unbinned search is the most sensitive to the detection of a source [179], but impractical for an all sky survey with an instrument of limited angular resolution. It has been shown that a binned survey is only 10% less sensitive if the bin size properly represents the angular resolution of the instrument [179]. To determine the proper bin size, a simple *Monte Carlo* was written to simulate a point source. The MINOS point spread function (Sec. 7.1.2 on page 134) was used to simulate the scattering that real muons would undergo while traversing the rock. A total of 1,000 simulated

sources with excesses of 300 muons over background were created, and the bin size was adjusted to maximize the signal to noise ratio using the Gaussian parameter D_σ. The background was taken to be 9 events per half angle cone $0.1\,°$ on a side, from the background near the moon described in Sec. 7.1.3 on page 134. The bin size was adjusted from $0.1\,°$ on a side in $0.1\,°$ increments to allow more signal events. A histogram of D_σ as a function of bin size can be seen in Fig. 8.1. The maximum signal to noise ratio was found with a bin radius of $0.45\,°$, which corresponds to a
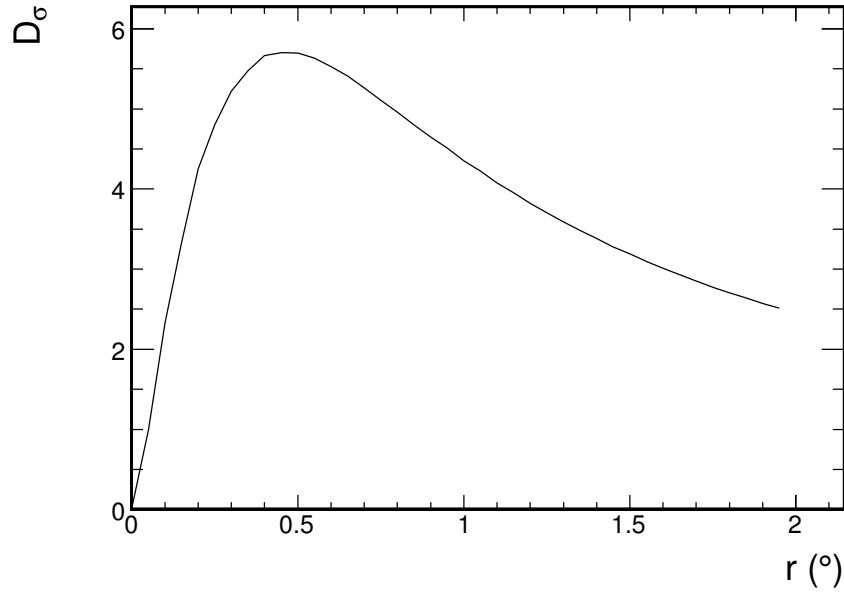
Figure 8.1: Simulated point source significance as a function of bin radius.

square bin $1\,°$ on a side.

8.1.2 The Data

The data for the cosmic ray point source search were accumulated from 1 August, 2003 until 31 December, 2007, numbering 67.9943×10^6 triggers. A number of data quality cuts were performed to ensure that instrumental noise and detector instabilities were removed from the data sample (Sec. 4.4 on page 61, and pointing cuts were performed to ensure that the muon track reliably pointed back to the sky (Sec. 7.1.1 on page 129). An additional cut required zenith angle to be less than $76°$ because that was the limit of the rock map. After all cuts were applied, 61.26%

of the data remained. The effect of these cuts can be seen in Table 8.1.2.

**Table 8.1:** Number of events that survive cuts for the cosmic ray source data set.

| Cut	Fraction Remaining
Total Triggers	67.99×10^6
1. Data Quality Cuts (Sec. 4.4 on page 61)	0.8712
2. Pointing Cuts (Sec. 7.1.1 on page 129)	0.6127
3. Zenith$< 76°$	0.6126

8.1.3   The Search

From the simulated data, a master background histogram in celestial coordinates of equal solid angle, α and $\sin(\delta)$, was created. A problem arises, however, when a source is divided into two bins. This occurs if the signal location falls along the line between adjacent cones. This would be comparable to having a bin size that is too small; the source would be divided up and potentially lost, given the subtlety of the excess that is sought. To overcome this difficulty, four interdependent analyses were performed, with each one shifting the binning of the data histogram slightly such that if a source were divided amongst bins in one grid, it would not be in the next. The first analysis, Survey 1, used the exact same binning as the background, while Survey 2, used bins shifted in α by half a bin width (0.5^o), keeping δ the same. Survey 3 used bins shifted δ by a half bin width with α the same, while Survey 4 shifted both a half of a bin width. The four surveys, as described, make sure that any source divided between bins in one survey will not be divide in another survey. The all-sky cosmic ray muon surveys can be seen in Figs. 8.2 on the next page, 8.3 on page 154, 8.4 on page 155, and 8.5 on page 156.   The relative isotropy is broken by pockets of excess. The question now becomes: "Are any of the excesses greater than the expectation of random background fluctuations?".

Averaging 1000 simulations of the data set allows for a very smooth background determination. In the absence of a source, the subtraction of the smooth, simulated background from the data will give a value of zero in most cases, with the expected random fluctuations surrounding the mean. The background subtracted data is shown for each of the four surveys in figure 8.6 on page 157, fit with a Gaussian distribution.   The four distributions have been normalized to
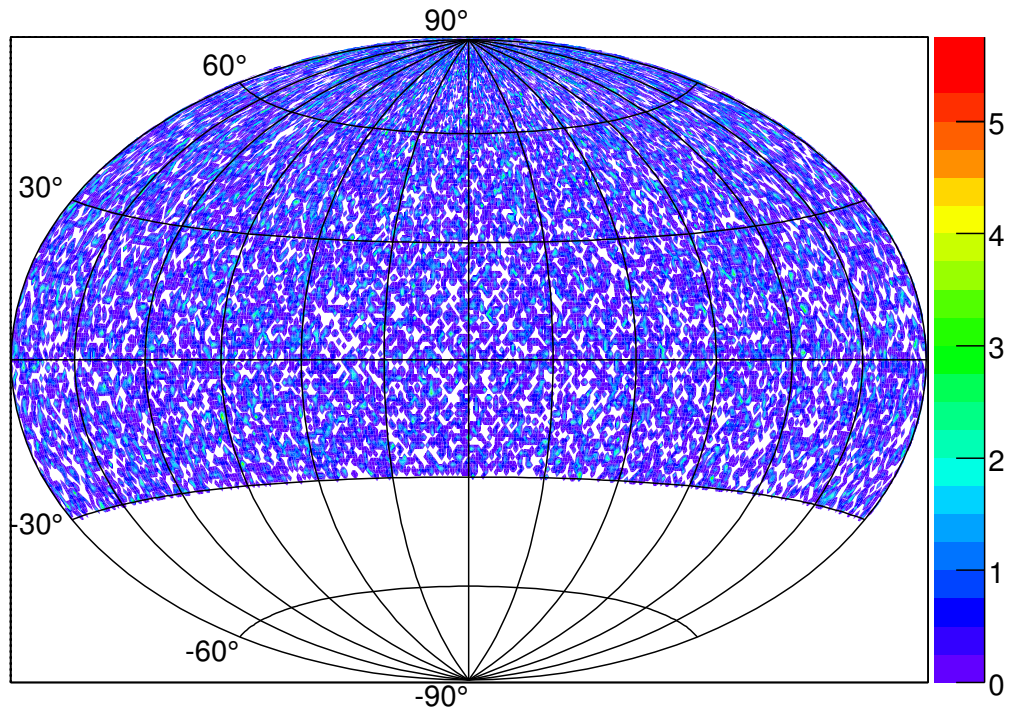
Figure 8.2: The signal above background (D_σ) for the sky visible to the Far Detector in celestial coordinates for Survey 1. The horizontal grid lines represent 2 h or $30°$, the vertical scale is in degrees, and the color scale is signal strength D_σ.
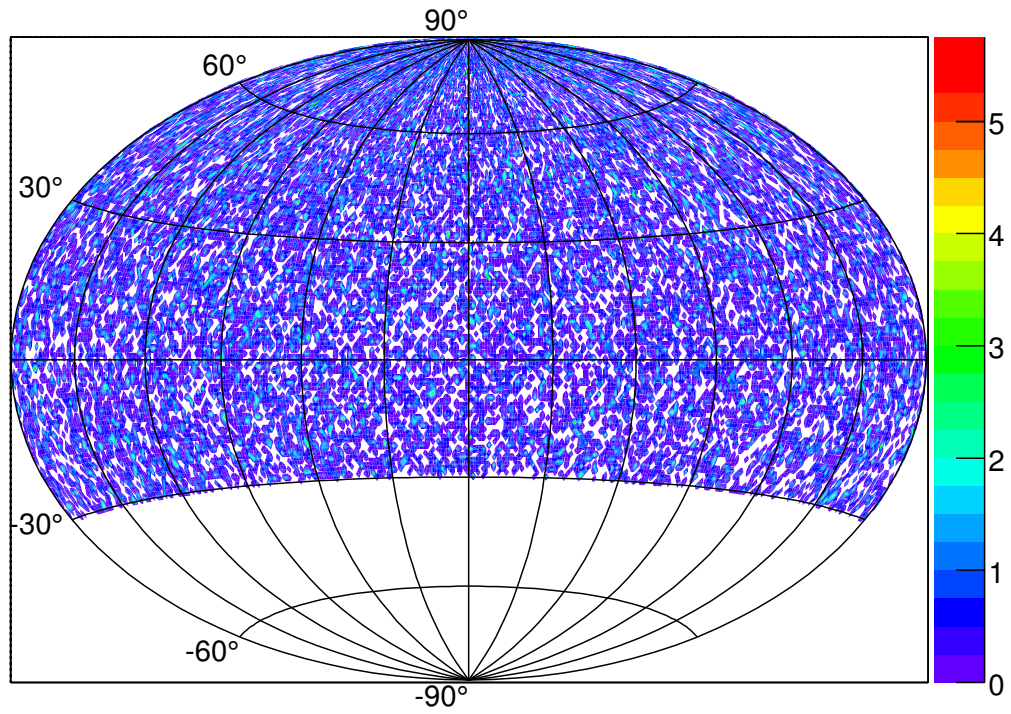
Figure 8.3: The signal above background (D_σ) for the sky visible to the Far Detector in celestial coordinates for Survey 2. The horizontal grid lines represent 2 h or 30 °, the vertical scale is in degrees, and the color scale is signal strength D_σ.
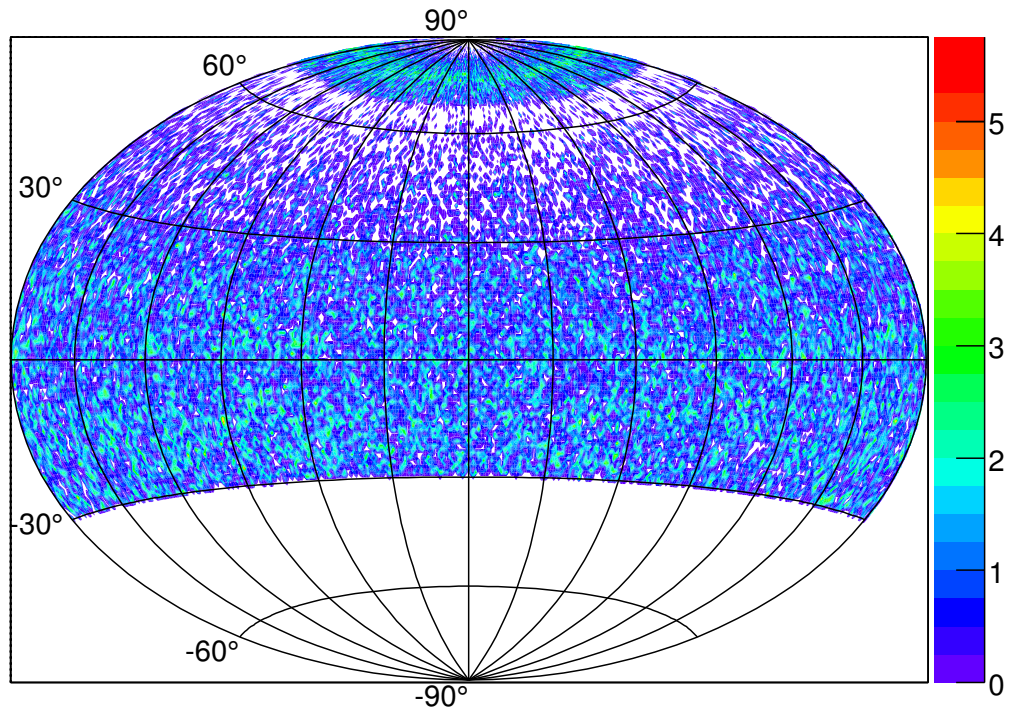
Figure 8.4: The signal above background (D_σ) for the sky visible to the Far Detector in celestial coordinates for Survey 3. The horizontal grid lines represent 2 h or 30 °, the vertical scale is in degrees, and the color scale is signal strength D_σ.
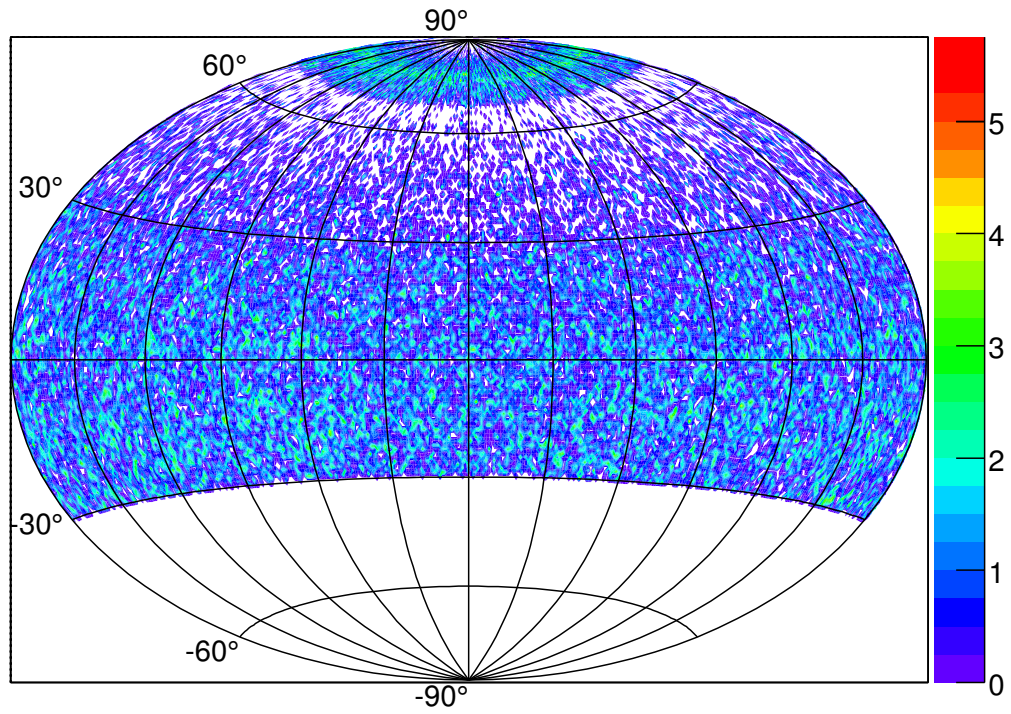
Figure 8.5: The signal above background (D_σ) for the sky visible to the Far Detector in celestial coordinates for Survey 4. The horizontal grid lines represent 2 h or 30 °, the vertical scale is in degrees, and the color scale is signal strength D_σ.
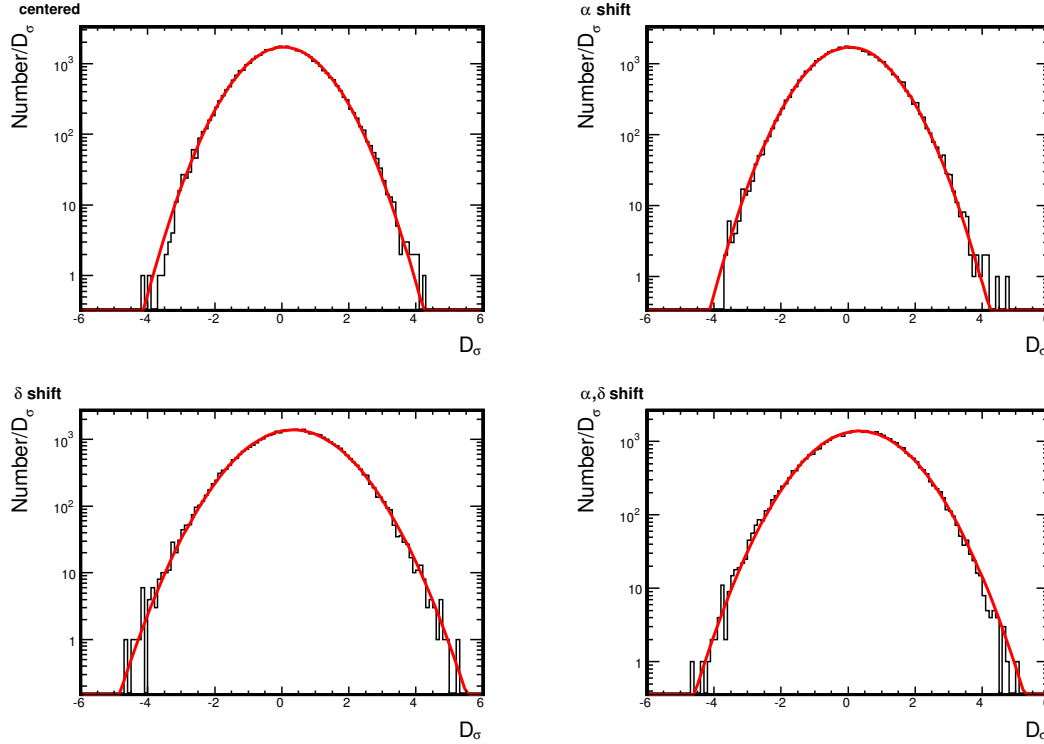
Figure 8.6: Histograms of the background reduced data for each of the four searches. The horizontal scale is measured in units of deviations from the mean. The upper left survey is with the data centered on the background grid, upper right is with the data shifted 0.5^o in α, lower left is with a data shift of 0.5^o in δ, and the lower right is with both coordinates shifted by 0.5^o.

D_σ and so are given in terms of deviations from the mean, which is zero. The width of the distribution is then one, as expected. No significant excesses are immediately obvious from these fits, however the overall statistical fluctuation for each distribution is easily seen. Any possible cosmic ray signal will exist in the tails of the normal distribution, where the deviations are significant, not random, so a more careful look at these regions is necessary. A table of fit parameters and histogram statistics is shown in table 8.2 on the following page for each of the four surveys. The mean is as expected, very nearly zero, while the width is one.   Tab. 8.3 on the next page shows the combined survey data, with each survey listed separately. The method of shifting the survey grid is verified by the lack of redundancy in excess (deficit) detections. None of the survey bins out of the five with D_σ greater than 4.5 were the same between different surveys. If this had been

Table 8.2: The statistics for the Gaussian fit to each search.

Survey	Mean	σ	χ^2/ndf
1 (centered)	0.048±0.0049	1.008±0.003	75/78
2 (α shifted)	0.046±0.0049	1.01±0.003	75/78
3 (δ shifted)	0.33±0.0059	1.2 ±0.004	99/93
4 (α,δ shift)	0.34±0.0060	1.2±0.004	113/89

the case, and if there really was a signal, the likelihood of the detection would be increased over a single survey. These four surveys are not independent, however, so the likelihood of a detection is not increased by four as a result of these surveys. The purpose of this method is not to extend the statistics of the survey, it is to catch a signal that is divided into two bins.   Any deviation that is

Table 8.3: The bins in the All Sky Survey with D_σ greater than 4.3; α is given in hours to be consistent with standard astronomical units.

Position ($\alpha(h), \delta(^o)$)	N_{obs}	N_{back}	Probability (%)	D_σ
4 (0.17, 83.96)	2657	2928.8	0.0220	-5.0
3 (0.75, 83.96)	2639	2931.6	0.0028	-5.4
4 (0.75, 83.96)	2633	2931.6	0.0015	-5.5
4 (2.00, 83.96)	2654	2928.9	0.0163	-5.0
3 (3.83, -21.17)	96	58.3	0.0354	4.9
3 (4.96, -24.98)	253	187.2	0.0664	4.8
4 (4.96, -24.98)	256	187.2	0.0216	5.0
2 (6.33, 72.85)	2410	2201.1	0.3680	4.4
3 (7.12, 67.25)	1445	1257.1	0.0050	5.3
4 (7.62, 83.96)	2656	2918.8	0.0497	-4.9
1 (9.29, 45.33)	1413	1260.4	0.7435	4.3
4 (10.45, 83.96)	2622	2921.7	0.0012	-5.5
2 (10.92, 68.97)	1796	1607.2	0.1078	4.7
4 (11.08, 83.96)	2645	2928.0	0.0073	-5.2
4 (14.62, 83.96)	2659	2930.5	0.0229	-5.0

greater than "3σ" ($D_\sigma > 5.2$) from an isotropic sky is significant. With a 0.27% chance of random fluctuations mimicking a signal at this level, should a survey bin have such a large deviation from the mean, a true source detection in that bin is likely. A table of all the bins with $D_\sigma > 5.2$ (the "three sigma" level) can be seen in table 8.3. The probability given is the likelihood that such a value is a statistical fluctuation as opposed to a signal. There is only one bin that indeed pass the

"three sigma" figure of merit for reporting a rare occurrence, none of them are in the region of a known astrophysical object, such as an x-ray binary [180]. More important to the suggestion of a signal is the fact that there are many areas of equivalent negative deviation. In all, there are nine regions of excess beyond the three sigma level, while there are seven regions of deficit. Surely, the number of regions of deficit with this magnitude indicate statistical fluctuations. Though it is possible that a source lies in one of the regions of excess, the greater number of regions of equivalent deficit belie a statistical deviation, not a true signal. The symmetry of these deviations is consistent with the Gaussian distribution for random background fluctuation.

8.1.4 Cosmic Ray Flux Limits

In the absence of a statistically significant signal, limits on the the cosmic ray flux can be set for a source existing in an individual region of the sky. This is the upper limit to the cosmic-ray induced muon flux from a particular source that could be observed by the Far Detector. If there were a cosmic ray source, it must have a flux greater than this value to be observed. This answers the question "how sensitive was the search?" and allows comparison with other experiments.

The flux limit with 95% confidence can be found using the expression

$$J_\mu(95\%) \leq \frac{n_\mu(95\%)}{0.522\epsilon(\Omega)A_{\text{eff}}(\Omega)t(\Omega)}\text{cm}^{-2}\text{s}^{-1} \tag{8.2}$$

where Ω is the solid angle of a particular bin in celestial coordinates, $(\alpha, \sin\delta)$. For a Gaussian distribution of statistical fluctuations, $n_\mu(95\%)$ can be written [181]:

$$\frac{2}{\sqrt{\pi}}\int_{n_\mu(95\%)}^{\infty}\frac{e^{-(n_\mu-\bar{n}_\mu)^2/2\sigma^2}}{\sqrt{2}\sigma}dn_\mu = 0.05 \tag{8.3}$$

where $\bar{n}_\mu = n_{\text{obs}} - n_{\text{back}}$ and $\sigma^2 = n_{\text{obs}}$ The three terms in the denominator that depend on angle, $\epsilon(\Omega), A_{\text{eff}}(\Omega), t(\Omega)$, also depend implicitly on time since the calculation is being performed in celestial coordinates, and the location of the detector changes continuously with respect to celestial coordinates because it is at a fixed place on a rotating earth. These values can be found for bin i:

$$\epsilon(\Omega_i) = \int_0^{2\pi}\int_0^{76°}\int \epsilon(\phi,\theta,t)d\phi d\theta dt \tag{8.4}$$

$$A_{\text{eff}}(\Omega_i) = \int_0^{2\pi}\int_0^{76°}\int A_{\text{eff}}(\phi,\theta,t)d\phi d\theta dt \tag{8.5}$$

$$t(\Omega_i) = \int_0^{2\pi}\int_0^{76°}\int t(\phi,\theta,t)d\phi d\theta dt. \tag{8.6}$$

The 95% confidence flux limits can be seen in figure 8.7 on the next page.
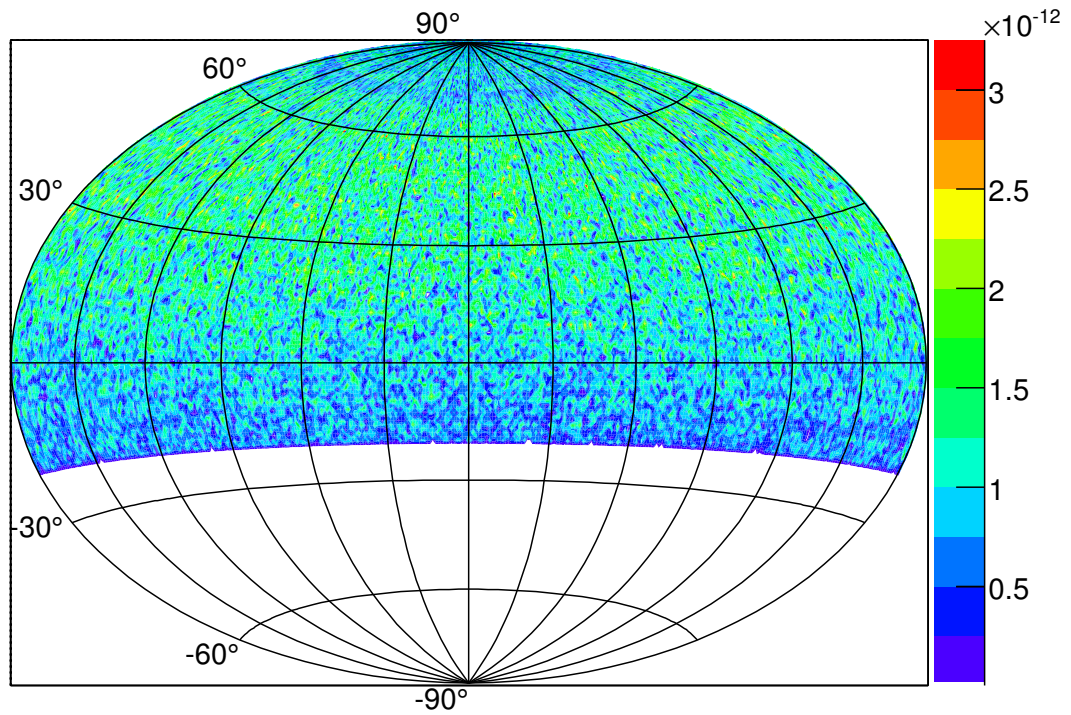
Figure 8.7: The 95% confidence flux limits for the Far Detector in celestial coordinates. The horizontal grid lines represent 2 h or $30°$, the vertical scale is in degrees, and the color scale is the flux limit in units $N_\mu \mathrm{cm}^{-2}\mathrm{s}^{-1}$.

8.2   Search for Gamma Ray Burst Particle Signature

A gamma ray burst is a catastrophic event that briefly floods the sky with highly energetic photons (See Ch. 2.2 on page 25). The gamma ray sky is relatively quiet, so GRBs outshine all other gamma ray sources combined, including the sun. The relativistic fireball that expands rapidly outward from the central engine of the GRB creates an enormous shock wave when it encounters the ISM, which accelerates protons to 10^{15} eV. This leads to pion production when these protons interact with the 10^6 eV photons carrying the bulk of the fireball energy [3], which decay to produce neutrinos. Neutrinos have become a golden channel to investigate GRBs because they are transparent to magnetic fields, the GRB shock wave and all other light matter. Many searches have been carried out, with no signal yet reported [4, 88, 5].

8.2.1   The Data

The Swift Gamma Ray observatory (Ch. 2.3.4 on page 33) has been observing GRBs and making rapid afterglow measurements since December 2004. The collaboration's first data catalog was published in July, 2007 and contained spectral data and positions for 237 GRB [182]. These GRB were distributed uniformly, consistent with extra-galactic origin, and this distribution can be seen in Fig. 8.8 on the following page.   GRBs are divided into two groups, long (T_{90}, the time to 90% fluence, greater than 2 s) and short, with distinctly different physical processes describing each group. This difference is indicated on the GRB skymap with the long GRBs represented by black circles, and the short GRBs represented by red circles.

The quality of timing information is very important to neutrino identification since the zenith angle distribution of detector events is asymmetric (see Sec. 4.6 on page 66). The beginning muon data set for this analysis are the 37.485 million events collected from 1 August, 2003 through 31 December 2007, after pointing cuts were applied (see Sec. 7.1.1 on page 129). Downward going (cosmic ray induced) events outnumber upward going (neutrino induced) events by a factor of 10^5, and a timing error could have the result that the vertex and end point of a track are swapped, so a cosmic ray muon could be reconstructed as a neutrino candidate event. Only a detector with good timing resolution can separate upward going from downward going events. The timing resolution of the Far Detector can be seen in Fig. 8.9 on page 164. The mean value of 2.6 ns is sufficient to separate downward from upward going tracks.   The direction of the track (upward or
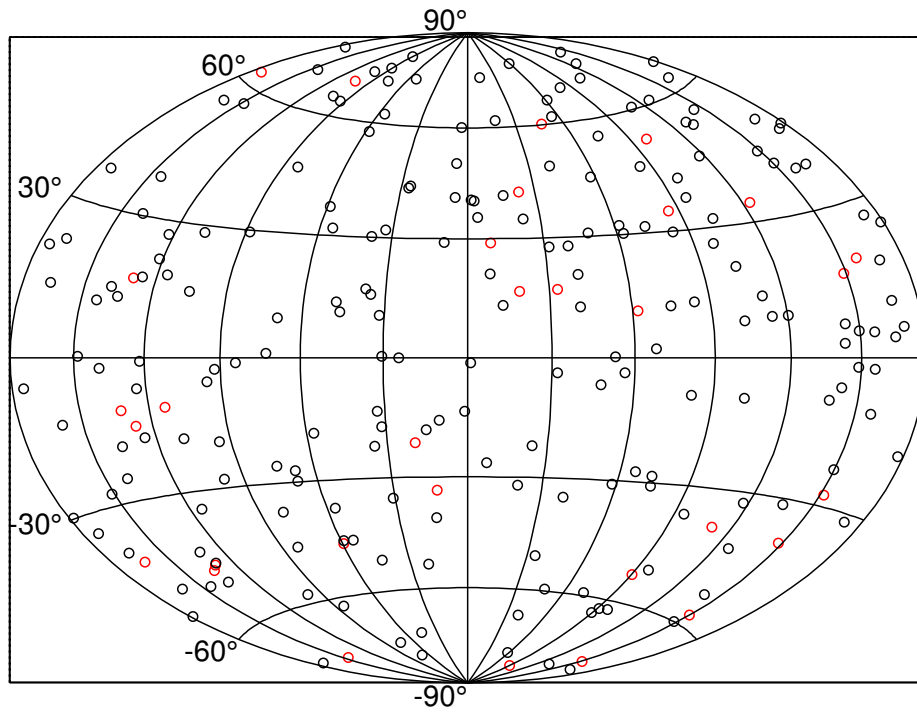
Figure 8.8: The distribution of GRB for the first Swift catalog in celestial coordinates. The horizontal grid lines represent 2 h or 30 ° and the vertical scale is in degrees. The black circles denote long GRBs, the red circles denote short GRBs.
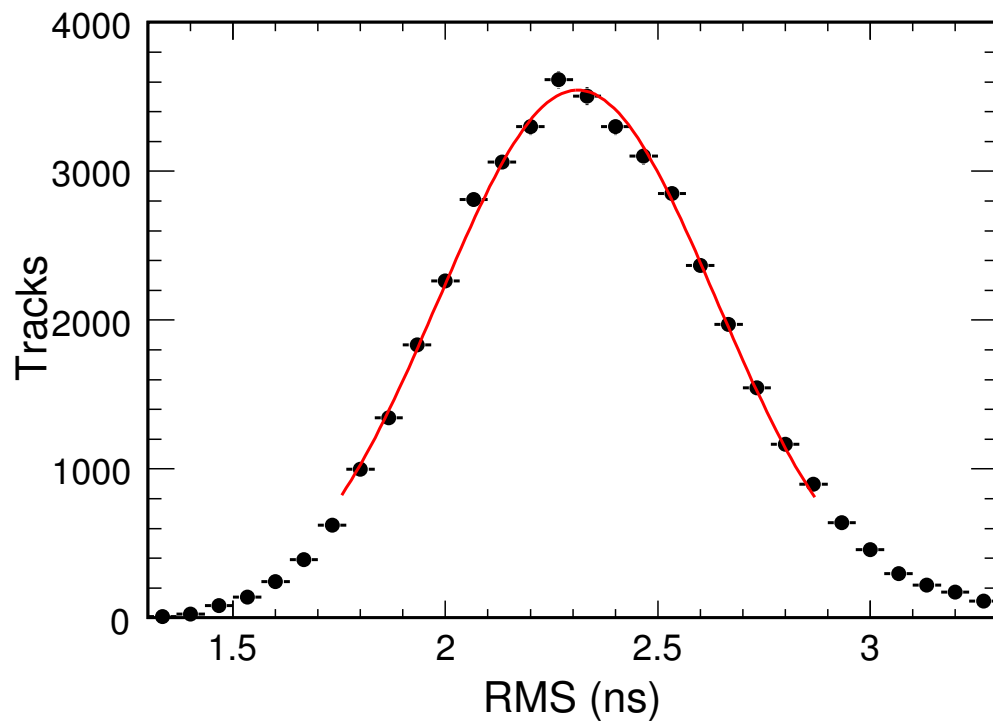
Figure 8.9: The timing resolution of the Far Detector.

downward) was determined by plotting the time difference ΔT (ns) of each hit along the track as a function of its distance ΔS (m) from the first hit. If the y positions of the hits increase along the length of the track, ΔS is positive; for y decreasing along the track, ΔS is negative. An example of this fitting procedure can be seen in Fig. 8.10, for a track with "good" timing information. Upward-going events have a positive slope for the straight line fit to the $\Delta T/\Delta S$ distribution.
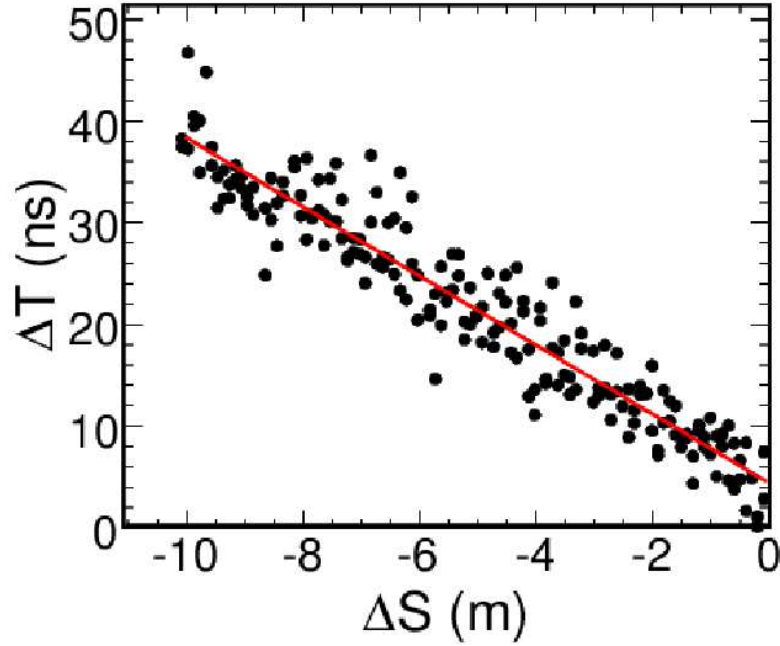
Figure 8.10: The track slope measurement for a track with high quality timing information.

To ensure that only events with good timing information are selected, three additional cuts are applied [118]:

1. "Double Ended Strip Cut", to ensure the presence of sufficient timing information in the events, tracks were excluded if the number of strips with with signals on both ends were fewer than half .

2. "$\chi^2_{1/\beta}/ndf < 3.0$ Cut", require $\chi^2_{1/\beta}/ndf < 3.0$ for an event.

3. "Directionality Cut", the slope of the line fit to the hits as a function of their y positions must agree with the reconstructed incoming direction of the track.

After these additional cuts 34.99 million events remained, about half of the total number of trig-gers. The effect of these cuts on the data set can be seen in Table 8.2.1. These data will be used to search for a correlation between a gamma ray burst and neutrino.   The zenith angle

Table 8.4: Number of events that survive each timing cut.

Cut	Fraction Remaining
Total Triggers	67.99×10^6
1. Data Quality Cuts (Sec. 4.4 on page 61)	0.8712
2. Pointing Cuts (Sec. 7.1.1 on page 129)	0.612657
3. Double Ended Strip Cut	0.528657
4. χ^2_{time} / ndf <3.0	0.514576
5. Directionality Cut	0.514571

distribution of muons after timing cuts can be seen in Fig. 8.11 on the following page. The fall off as $\cos\theta \to 0$ reflects the power law energy energy spectrum of cosmic ray muons and increasing rock depth. Matter is practically transparent to neutrinos and the flattening of the distribution for $\cos\theta < 0$ reflects the neutrino origin of these muons.

8.2.2   Search for GRB and Neutrino Coincidence

The reported Swift position error is less than 7.0' (1.75°), and most often 2.0' (0.5°) which is nearly an order of magnitude improvement over previous instruments. The pointing resolution for muons in the Far Detector is 0.6°, but the kinematics of the interaction between neutrinos and nucleons reduces the resolution of the measurement. The rms angle between a neutrino and the muon it produces is 3.7° [88]. From these considerations, a 5° half angle cone was chosen as the angular separation to be considered spatially coincident.

The most often compared theory of neutrinos produced by GRBs is that they are produced in the skywave of the expanding fireball at the same time as the gamma rays, and that the shock wave is transparent to both the gamma rays and neutrinos (see Sec. 2.2.1 on page 26). Thus, neutrinos and gamma rays should arrive at the same time (unlike supernovae, where a burst of neutrinos precedes the outburst of photons). The longest duration GRB in the Swift catalog, GRB060929, had T_{90} = 554 s, while the shortest, GRB050925, had T_{90} = 0.07 s. There were 15 GRB that did
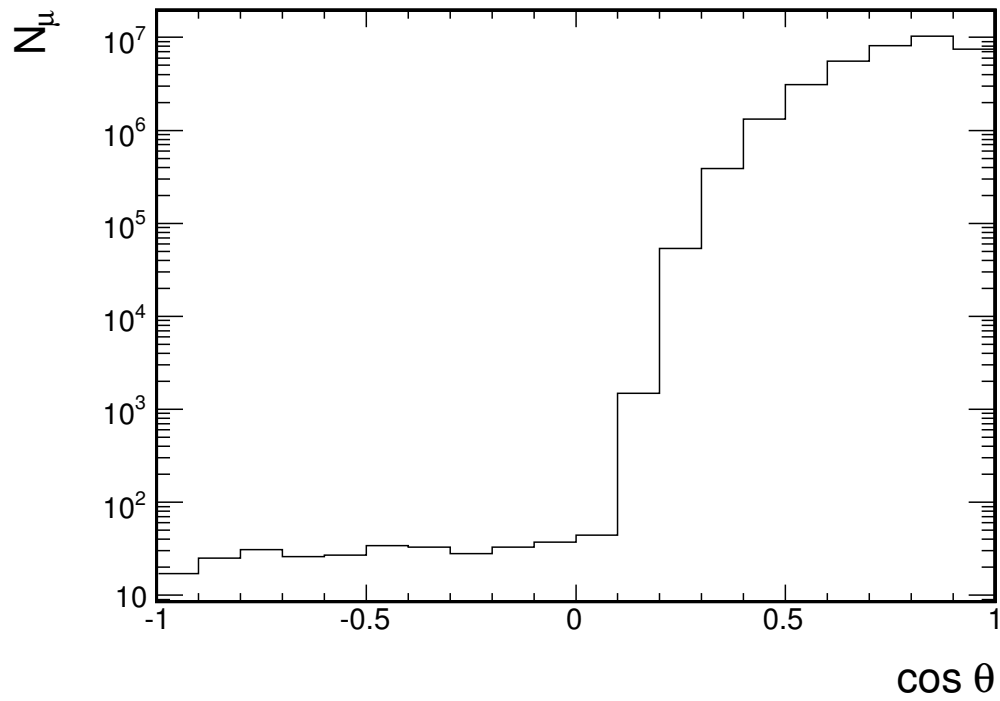
Figure 8.11: The zenith angle distribution of muons after timing cuts.

Upward going muons are distinguished from downward going muons using $1/\beta$, and the distribution of $1/\beta$ can be seen in Fig. 8.12 on the next page.
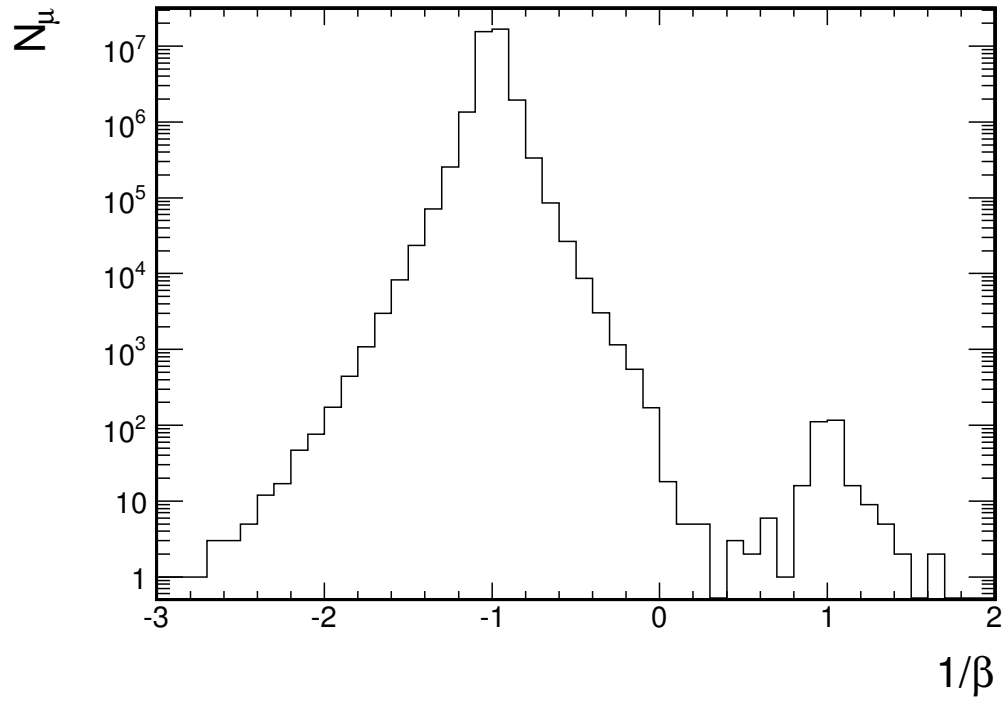
Figure 8.12: The $1/\beta$ distribution of muons after timing cuts. Muons with $1/\beta > 0$ were created by meson decay in the atmosphere and propagated down to the detector through the rock, while muons with $1/\beta < 0$ were created by neutrino interactions in the rock.

not have T_{90} information for various reasons including instrumental failures or incomplete data. Rather than excluding these events from the search, it was assumed that they were simply short GRBs and assigned $\langle T_{90} \rangle = 2\,\text{s}$. This is valid because the gamma ray sky is so quiet, so little is known about gamma ray progenitors, and if some of the information is lost, it is not possible to recover T_{90} since it is an integration.

Because the GRB and muon data are so well known in space and the window of time around each GRB is relatively small, the background on the search is minimal. The average muon rate after timing cuts were applied is $0.27\,\text{Hz}$. Considering that the average GRB T_{90} is $70\,\text{s}$, $10\,\text{s}$ before and after T_{90} are added to the time search window, and that a $5\,^\circ$ half angle cone search window is used, 0.037 events would be expected in each search window. Of course the background depends on bin solid angle, so a background map was constructed from the known contribution of atmospheric neutrinos and cosmic ray muons. The cosmic ray muon contribution to the background was calculated using the *Monte Carlo* described in Sec. 8.1.3 on page 152. The atmospheric neutrino contribution to the background was calculated using the *Monte Carlo* described in 4.3 on page 57. A contained vertex sample was generated equivalent to 4000 years of Far Detector, and an uncontained vertex sample was generated equivalent to 5000 years of Far Detector running. These samples were scaled to the 4.12 year total livetime. The same cuts described in Sec. 8.2.1 on page 162 were applied to these three *Monte Carlo* samples, and they were put in a histogram with square bins equivalent to the solid angle of a $5\,^\circ$ half angle cone, scaled by the $90\,\text{s}$ mean time window. This histogram can be seen in Fig. 8.13 on the following page   Neutrinos interact in the rock above the detector and generate muons just as often as they do below the detector. Ordinarily, the signal from these downward going neutrinos is obscured by the much higher cosmic ray induced muon flux, so neutrino analyses are restricted to upward going or contained vertex events. Using only upward going events restricts the searchable sky by half, and contained vertex events are lower energy, so their pointing is worse than $3.7\,^\circ$.

All 34.99 million muons that pass the cuts were used in the analysis, which is a departure from all previous analyses, which only used events positively identified as neutrino induced. This is not necessary because backgrounds are quantified and low, much less than one event for every search window. This allowed for the first search for a GRB neutrino coincidence in the energy range $10^2\,\text{GeV} < E_\nu < 10^5\,\text{GeV}$ in the northern sky. MACRO [4] used only upward going muons and so was insensitive to the northern sky, Super-K [88] used only partially contained events, which
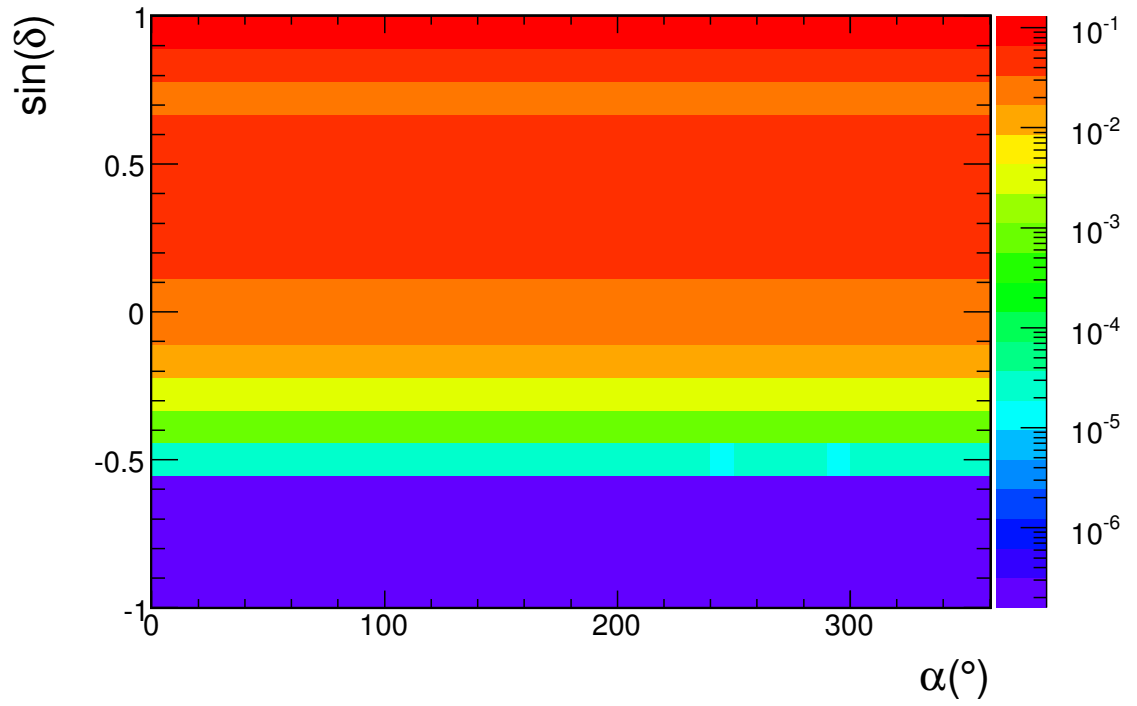
Figure 8.13: The background distribution of muons in the Far Detector in celestial coordinates. This distribution includes contributions from both cosmic ray and atmospheric neutrino induced muons.

have an average energy of $10\,\mathrm{GeV}$, and AMANDA/IceCube [5] has a threshold energy of $10^5\,\mathrm{GeV}$. It is in this small region of space that the MINOS explored for the first time.

To perform the search, a time window of $T_{90} \pm 10\,\mathrm{s}$ was drawn around the trigger time for each burst. For muons within this window, the angular separation from the GRB trigger location was calculated. If it was found to be within the $5\,^{\circ}$ half angle cone, it was considered coincident. A list of GRBs with coincident muons observations can be seen in Table 8.2.2. Also listed are the expected background and probability of such a coincidence occurring by chance.

Table 8.5: GRBs with a coincident neutrino signal.

GRB	T_{90}	N_{obs}	N_{bkg}	Prob (%)
041220 $(291.3°, 60.6°)$	5.6	2	0.0402	0.18
050421 $(307.3°, 73.6°)$	15	1	0.0651	14.46
050505 $(141.8°, 30.2°)$	58.9	1	0.0584	13.06
050607 $(300.2°, 9.1°)$	26.4	1	0.0585	13.09
050712 $(77.7°, 64.9°)$	51.6	1	0.1325	27.50
050713A $(320.6°, 77.0°)$	124.7	3	0.8086	9.30
050713B $(307.8°, 60.9°)$	54.2	1	0.0276	6.37
050716 $(338.6°, 38.6°)$	69.1	2	0.1087	1.26
060111B $(286.5°, 70.3°)$	58.8	1	0.1461	29.91
060204B $(211.8°, 27.6°)$	139.4	1	0.1193	25.10
060428B $(235.4°, 62.0°)$	57.9	2	0.1232	1.59
060502A $(240.9°, 66.6°)$	28.4	1	0.0900	19.50
060507 $(89.9°, 75.2°)$	183.3	3	1.6645	4.78
060515 $(127.3°, 73.5°)$	52	1	0.1330	27.60
060906 $(40.7°, 30.3°)$	43.5	1	0.0477	10.79
060929 $(263.1°, 29.8°)$	554	1	0.4366	66.87
061110B $(323.9°, 6.8°)$	134	1	0.0919	19.86
061126 $(86.6°, 64.2°)$	70.8	2	1.6645	4.78
070518 $(254.2°, 55.2°)$	5.5	1	0.0201	4.66
070521 $(242.7°, 30.2°)$	37.9	1	0.0438	9.93
070531 $(6.7°, 74.3°)$	44.5	1	0.1196	25.14
070616 $(32.1°, 56.9°)$	402.4	3	0.9975	14.46

8.2.3 Flux Limit on Neutrino Production in GRBs

In the absence of a statistically significant signal, a limit on the number of neutrinos emitted by a GRB can be placed. This is slightly more complicated than the limit discussed in Sec. 8.1.4 on page 159 because the signal is being observed indirectly, in muons created by neutrinos that may have been created by a GRB. The question of an upper limit on neutrino detection from zero muons observed involves the size of the detector, the amount and type of rock surrounding the detector, and the neutrino spectrum produced by a GRB. The flux of muons induced by a neutrino source of spectrum $\Phi_\nu(E_\nu) \propto E^{-\gamma}$ at declination δ can be written [4]:

$$\Phi_\mu(E_\mu^{th}, E_\nu, \delta) = N_A \int_{E_\mu^{th}}^{E_\mu^{max}} \frac{d\sigma_\nu}{dE_\mu'}(E_\mu', E_\nu) R_{\text{eff}}(E_\mu', E_\mu^{th}) A_{\text{eff}}(\delta) \epsilon(E_\mu', \delta) \Phi_\nu(E_\nu) dE_\mu', \quad (8.7)$$

where N_A is Avogadro's number, $\epsilon(E_\mu', \delta)$ is the efficiency as a function of muon energy, calculated using the detector *Monte Carlo*(Sec. 4.3 on page 57). The effective muon range, $R_{\text{eff}}(E_\mu', E_\mu^{th})$, is given by the probability that a muon of energy E_μ has energy above threshold E_{mu}^{th} after propagating distance X:

$$R_{\text{eff}}(E_\mu', E_\mu^{th}) = \int_0^\infty P_{\text{surv}}(E_\mu', E_\mu^{th}) dX \qquad (8.8)$$

The probability of muon survival was calculated with the PropMu muon propagation routine [183]. The cross section as a function of energy was found from [123] to 120 GeV for deep inelastic scattering (DIS). The DIS cross section for a neutrino scattering on a nucleon increases linearly above 120 GeV [184], so the cross section was extrapolated out to 10 TeV.

Now that the number of detected muons has been related to number of neutrinos observed, a 90% confidence flux limit can be calculated in a similar way as the 95% confidence flux limit in Sec. 8.1.4 on page 159:

$$J_\nu(90\%) \leq \frac{n_\nu(90\%)}{\epsilon(\Omega) A_{\text{eff}}(\Omega) t_{GRB}} \text{GeVcm}^{-2}\text{s}^{-1}, \qquad (8.9)$$

where t_{GRB} is the time window that was used for the particular GRB. The value for $n_\nu(90\%)$ can be found from a convolution of Eq. 8.7 and the 90% confidence limit for a small signal [185]:

$$\int_{\mu_\nu(90\%)}^\infty \frac{e^{-\mu} \mu^{n_{\text{bkg}}}}{n_{\text{bkg}}!} d\mu = 0.10 \qquad (8.10)$$

where the function $\text{LnGamma}(n_{\text{bkg}}) = n_{\text{bkg}}!$ for a decimal n_{bkg} value. Here, $n_\nu(90\%)$ is the 90% confidence upper limit of background fluctuations mimicking a signal. Assuming the Waxman-Bahcall spectral index $\gamma = 2$, $J_\nu(90\%)$ was calculated for each $5°$ half angle cone of the sky that

contained a GRB. These limits can be seen in Fig. 8.14.   The cumulative upper flux limit was
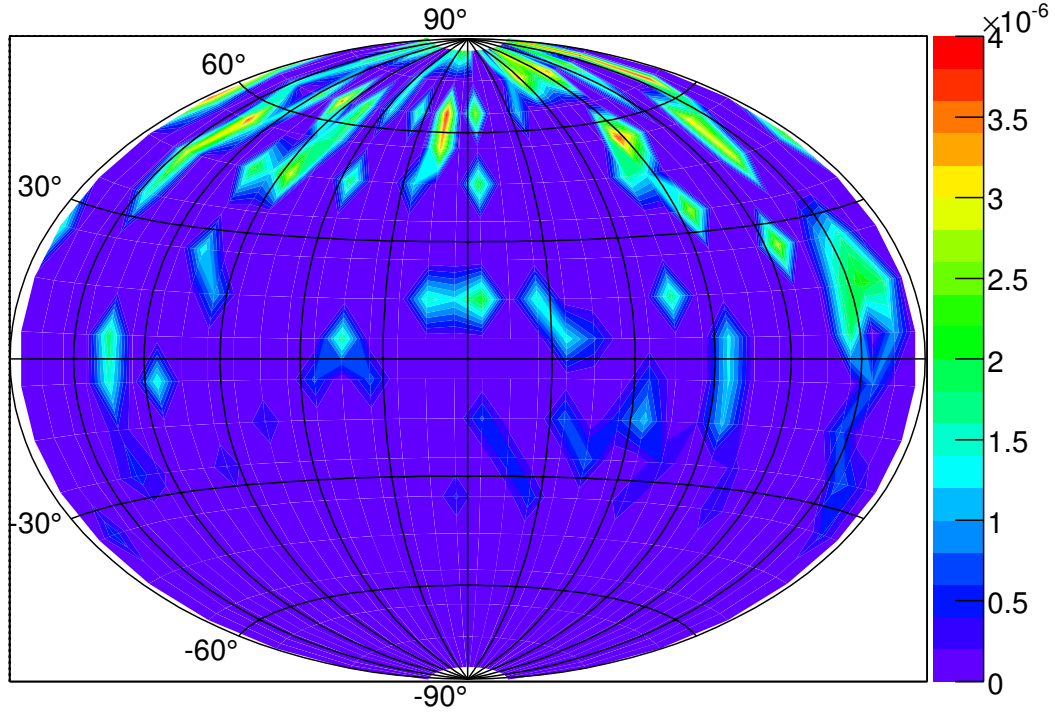
Figure 8.14: The neutrino flux limit assuming a Waxman-Bahcall spectral index. The horizontal grid
lines represent 2 h or 30 °, the vertical scale is in degrees, and the color scale is
$J_\nu(90\%)$ in units of $\mathrm{GeVcm^{-2}s^{-1}}$.

found by [4]:

$$\frac{N_{obs} - N_{bkg} + 1.28 \cdot RMS}{\sqrt{N_{GRB}} \cdot \langle A_{\mathrm{eff}} \rangle \sum t_{GRB}} \tag{8.11}$$

where RMS is the root mean squared of the distribution of $n_\nu(90\%)$. This gives $\Phi_{lim}(90\% =$
$1.7 \times 10^{-8}\,\mathrm{GeVcm^{-2}s^{-1}}$, assuming a Waxman-Bahcall spectrum. This value was compared to
the Waxman-Bahcall prediction as well as other experimental limits in Fig. 8.15 on the next page.
This new limit is slightly better than the MACRO [4] and AMANDA [5] limits as well as the
theoretical limit set by cosmic rays [6, 7], but does not constrain the model.
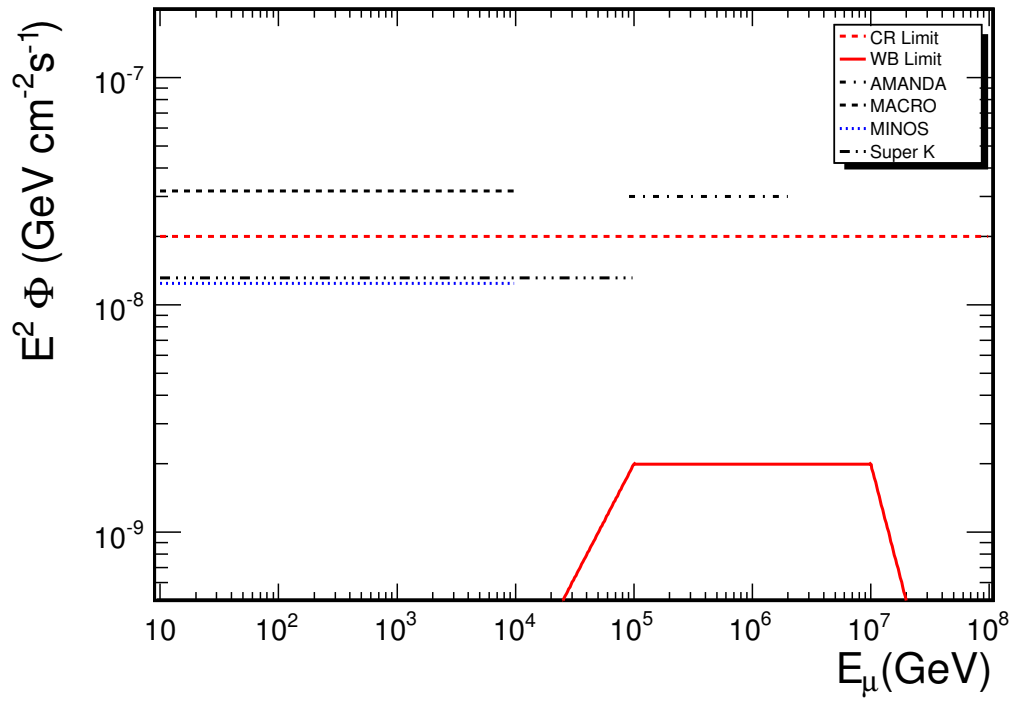
Figure 8.15: The Waxman-Bahcall GRB neutrino flux limit (solid red line), along with the Waxman-Bahcall limit from cosmic rays (dashed red line) [6,7]. Flux limits from MACRO [4], Super-K [88], AMANDA [5], and MINOS are shown in black lines, calculated assuming a Waxman-Bahcall spectrum.

Chapter 9

Conclusions

A four year sample of 53.12 million cosmic ray induced muons has been collected by the MINOS Far Detector and daily rate fluctuations have been compared to daily fluctuations in atmospheric temperature. These distributions were shown to be highly correlated, with a correlation coefficient of 0.906. The constant of proportionality relating the two distributions, α_T, was found to be $0.877 \pm 0.010(stat.) \pm 0.017(syst.)$. This value is in good agreement with the theoretical expectation of $\langle \alpha_T \rangle = 0.865 \pm 0.015$. A measurement of the temperature dependence on the rate of μ^+ separate from μ^- was performed for the first time. There was no statistically significant difference between $\alpha_T(\mu^+)$ and $\alpha_T(\mu^-)$. Additionally, r_T, the charge ratio temperature coefficient, was found to be consistent with zero. Thus, there is no observed temperature dependence on the muon charge ratio.

The experimental value of α_T for the combined muon sample has the lowest uncertainty of any such measurement. While other experiments have estimated the effect of atmospheric temperature on kaon induced muons [59, 133], this is the first result to quantify the kaon-inclusive effective temperature coefficient, which includes the effect of muons induced by kaons. There is a 2σ difference in the pion only model [133] and the new $K\pi$ model was applied to measure the $K/\pi = 0.21 \pm 0.08$ in airshowers for $E_{\mathrm{p}} > 7\,\mathrm{TeV}$.

Using 41.66 million muons accumulated over 1506.8 live-days, the MINOS Far Detector observed the cosmic ray shadow of the moon with a high significance. The one dimensional event deficit near the moon has a chance probability of 3×10^{-5}, and this was used to quantify the effective angular resolution of the detector, $0.41\pm0.06°$. The two dimensional moon shadow was found

with a significance of 6×10^{-7}, centered on $(-0.05°, -0.05°)$, which suggests that the absolute pointing of the detector is $0.05 \pm 0.10°$. No significant IMF effect on the moon shadowing signal was seen. The cosmic ray shadow of the sun over the same time period was measured, in one dimension with a chance probability of 4×10^{-4}, and in two dimensions with a chance probability of 2×10^{-5}, centered on $(-0.20°, 0.20°)$. The shadowing strength is consistent with the moon shadow, within the limit of fewer statistics, and the displacement is consistent with IMF effects. The shadow of the sun was observed separately over four one year periods, and the shadowing strength increased as the sun approached solar minimum.

Using 41.66 million muons accumulated over 1506.8 live-days and a smooth background, a search was performed for a cosmic ray point source. There were on average 400 events per $1 \deg^2$ bin, and there were as many bins with significant deficits of signal events as significant excesses of signal events. no bin had an excess greater than $3\,\sigma$, which suggests that no source was observed. In the absence of a source, 95% confidence flux limits were placed on muon sources. The lowest limit was $2.7 \times 10^{-16}\,\mathrm{cm}^{-2}\mathrm{s}^{-1}$, which is comparable to the previous best limit set by MACRO [1, 2].

A search for coincidence between neutrinos and gamma ray bursts in the Swift catalog was performed. The neutrino data set comprised 34.99 million muons, while the GRB catalog included 237 GRB recorded from December, 2004 until June 2007. A search for time and space coincidence between events in the Far Detector and GRB triggers was performed, and no significant signal was found. In the absence of a significant signal, 90% confidence flux limits were on the production of neutrinos in GRB. Assuming a Waxman-Bahcall neutrino spectrum, the average 90% flux limit was found to be $1.7 \times 10^{-8}\,\mathrm{GeVcm}^{-2}\mathrm{s}^{-1}$. This new limit is slightly better than the MACRO [4] and AMANDA [5] limits as well as the theoretical limit set by cosmic rays [6, 7], but does not constrain the model.

In the thirty years since their discovery, many mysteries about GRBs have been solved, but nearly as many have been uncovered. The prospect of observing GRBs in neutrinos is exciting both from the particle astrophysics perspective as well as the astronomical perspective. The IceCube neutrino detector was built to do just this, and when it is complete in 2010 it will have a square kilometer of detector area as well as a large catalog of potentially interesting objects from GLAST. IceCube's sensitivity to neutrinos falls off rapidly below $100\,\mathrm{TeV}$, and it is in this region that MINOS can make a contribution. This analysis represents the first attempt at finding a neutrino

signal from gamma ray bursts, and will hopefully pave the way for better, brighter analyses. As long as we are curious, there is no limit to discovery.

References

[1] Alec T. Habig. Muon astronomy and cosmic ray physics with the macro detector. *Ph.D. thesis, Indiana University (1996)*.

[2] H. Dekhissi. Search for cosmic ray point sources with the MACRO detector at gran sasso. *Astrophys. Space Sci.*, 273:295–304, 2000.

[3] Eli Waxman and John N. Bahcall. High energy neutrinos from cosmological gamma-ray burst fireballs. *Phys. Rev. Lett.*, 78:2292–2295, 1997.

[4] M. Ambrosio et al. Neutrino astronomy with the MACRO detector. *Astrophys. J.*, 546:1038–1054, 2001.

[5] A. Achterberg and K. Hurley. The search for muon neutrinos from northern hemisphere gamma-ray bursts with AMANDA. 2007.

[6] Eli Waxman and John N. Bahcall. High energy neutrinos from astrophysical sources: An upper bound. *Phys. Rev.*, D59:023002, 1999.

[7] John N. Bahcall and Eli Waxman. High energy astrophysical neutrinos: The upper bound is robust. *Phys. Rev.*, D64:023002, 2001.

[8] C. S. Lewis. Mere christianity. The Macmillian Company, New York, 1949.

[9] M. W. Friedlander. *Cosmic Rays*. Harvard University Press, Cambridge, MA, USA, 1989.

[10] T. Stanev. High energy cosmic rays. Berlin, Germany: Springer (2003) 319 p.

[11] Frederick Reines and Clyde L. Cowan. The neutrino. *Nature*, 178:446–449, 1956.

[12] Raymond Davis Jr., Don S. Harmer, and Kenneth C. Hoffman. Search for neutrinos from the sun. *Phys. Rev. Lett.*, 20:1205–1209, 1968.

[13] John N. Bahcall. Neutrinos from the sun. *Scientific American*, 220(1):28–37, July 1969.

[14] Ray W. Klebesadel, Ian B. Strong, and Roy A. Olson. Observations of Gamma-Ray Bursts of Cosmic Origin. *Astrophys. J.*, 182:L85, 1973.

[15] John N. Bahcall and Peter Meszaros. 5-GeV to 10-GeV neutrinos from gamma-ray burst fireballs. *Phys. Rev. Lett.*, 85:1362–1365, 2000.

[16] Julia K. Becker, Michael Stamatikos, Francis Halzen, and Wolfgang Rhode. Coincident GRB neutrino flux predictions: Implications for experimental UHE neutrino physics. *Astropart. Phys.*, 25:118–128, 2006.

[17] P. Meszaros and M. J. Rees. Multi-GeV neutrinos from internal dissipation in GRB fireballs. *Astrophys. J.*, 541:L5–L8, 2000.

[18] Dafne Guetta, D. Hooper, J. Alvarez-Muniz, F. Halzen, and E. Reuveni. Neutrinos from individual gamma-ray bursts in the BATSE catalog. *Astropart. Phys.*, 20:429–455, 2004.

[19] Sarira Sahu. Multi-GeV neutrinos due to n anti-n oscillation in gamma- ray burst fireballs. 2007.

[20] Eli Waxman. High energy cosmic-rays from gamma-ray burst sources: A stronger case. *Astrophys. J.*, 606:988–993, 2004.

[21] S. T. Scully and F. W. Stecker. On the spectrum of ultrahigh energy cosmic rays and the gamma ray burst origin hypothesis. *Astropart. Phys.*, 16:271–276, 2002.

[22] Peter L. Biermann, Gustavo A. Medina-Tanco, Ralph Engel, and Giovanna Pugliese. The last gamma ray burst in our galaxy? On the observed cosmic ray excess at particle energy 10**18-eV. *Astrophys. J.*, 604:L29–L32, 2004.

[23] G. Battistoni et al. Observations of a time-modulated muon flux in the direction of Cyg X-3. *Phys. Lett. B*, 155:465, 1985.

[24] M.L. Marshak et al. Time distributions for underground muons from the direction of Cygnus X-3. *Phys Rev. Lett.*, 55:1965, 1985.

[25] M.L. Marshak et al. Evidence for muon production by particles from Cygnus X-3. *Phys. Rev. Lett.*, 54:2079, 1985.

[26] B. Dingus et al. Search for signals from Cygnus X-3 at energies above 50 TeV. *Phy. Rev. Lett.*, 60:1785, 1988.

[27] W. W. M. Allison et al. Cygnus X-3 revisited: 10 years of muon and radio observations. 1999.

[28] M. A. Thomson et al. The observation of underground muons from the direction of Cygnus X-3 during the January 1991 radio flare. *Phys. Lett.*, B269:220–226, 1991.

[29] R. Bionta et al. Underground search for muons correlated with Cygnus x-3. *Phys. Rev. D*, 36:30, 1987.

[30] Y. Oyama et al. Search for high energy muons from Cygnus X-3. *Phys. Rev. Lett.*, 56:991, 1986.

[31] C. Berger et al. Search for muons from the direction of Cygnus X-3. *Phys. Lett. B*, 174, 1986.

[32] Corbato. *The Search for Anisotropies in the Underground Cosmic Ray Flux*. PhD thesis.

[33] K. S. Hirata et al. Observation in the Kamiokande-II Detector of the Neutrino Burst from Supernova SN 1987a. *Phys. Rev.*, D38:448–458, 1988.

[34] R. M. Bionta et al. Observation of a Neutrino Burst in Coincidence with Supernova SN 1987a in the Large Magellanic Cloud. *Phys. Rev. Lett.*, 58:1494, 1987.

[35] Mark Srednicki, Keith A. Olive, and Joseph Silk. High-Energy Neutrinos from the Sun and Cold Dark Matter. *Nucl. Phys.*, B279:804, 1987.

[36] S. Ritz and D. Seckel. DETAILED NEUTRINO SPECTRA FROM COLD DARK MATTER ANNIHILATIONS IN THE SUN. *Nucl. Phys.*, B304:877, 1988.

[37] Kin-Wang Ng, Keith A. Olive, and Mark Srednicki. DARK MATTER INDUCED NEU-TRINOS FROM THE SUN: THEORY VERSUS EXPERIMENT. *Phys. Lett.*, B188:138, 1987.

[38] N. Sato et al. Mass limits for dark matter particles derived from high- energy neutrinos from the sun. *Phys. Rev.*, D44:2220–2240, 1991.

[39] Kenneth Greisen. End to the cosmic ray spectrum? *Phys. Rev. Lett.*, 16:748–750, 1966.

[40] G. T. Zatsepin and V. A. Kuzmin. Upper limit of the spectrum of cosmic rays. *JETP Lett.*, 4:78–80, 1966.

[41] Pietro Antonioli et al. SNEWS: The SuperNova Early Warning System. *New J. Phys.*, 6:114, 2004.

[42] National Research Council Committee on Cosmic-Ray Physics. Opportunities in cosmic-ray physics and astrophysics. 1995.

[43] T. K. Gaisser. Cosmic rays and particle physics. 1990. Cambridge, UK: Univ. Pr. 279 p.

[44] The pierre auger project design report. FERMILAB-PUB-96-024.

[45] J. Abraham et al. Correlation of the highest-energy cosmic rays with the positions of nearby active galactic nuclei. *Astropart. Phys.*, 29:188–204, 2008.

[46] J. Abraham et al. Correlation of the highest energy cosmic rays with nearby extragalactic objects. *Science*, 318:938–943, 2007.

[47] Ray J. Protheroe and R. W. Clay. Ultra high energy cosmic rays. *Publ. Astron. Soc. Pac.*, 21:1–22, 2004.

[48] Enrico Fermi. On the Origin of the Cosmic Radiation. *Phys. Rev.*, 75:1169–1174, 1949.

[49] Thomas G. Pannuti, Glenn E. Allen, John C. Houck, and Steven J. Sturner. RXTE, ROSAT and ASCA Observations of G347.3-0.5 (RX J1713.7-3946): Probing Cosmic Ray Acceleration by a Galactic Shell-Type Supernova Remnant. *Astrophys. J.*, 593:377–392, 2003.

[50] R. Enomoto et al. The Acceleration of cosmic ray protons in the supernova remnant RX J1713.7-3946. *Nature*, 416:823–826, 2002.

[51] J.D. Jackson. *Classical Electrodynamics*. John Wiley & Sons, New York, NY, USA, 1999.

[52] M. Zeilik and S.A. Gregory. *Introductory Astronomy & Astrophysics*. Saunders College Publishing, Fort Worth, TX, USA, 1998.

[53] M. Kachelriess and D. Semikoz. Ultra-high energy cosmic rays from a finite number of point sources. 2004.

[54] R. M. Baltrusaitis et al. THE FLY'S EYE DETECTOR: PRESENT AND FUTURE. *Nucl. Instrum. Meth.*, A264:87–92, 1988.

[55] Jerome W. Elbert and Paul Sommers. In search of a source for the 320 EeV Fly's Eye cosmic ray. *Astrophys. J.*, 441:151–161, 1995.

[56] Konrad Bernlohr. *http://www.mpi-hd.mpg.de/hfm/CosmicRay/Showers.html*, 1999.

[57] T. K. Gaisser. *Cosmic Rays and Particle Physics*. Cambridge University Press, Cambridge, UK, 1990.

[58] T. K. Gaisser. The cosmic-ray spectrum: From the knee to the ankle. *J. Phys. Conf. Ser.*, 47:15–20, 2006.

[59] P. Barrett et al. Interpretation of cosmic-ray measurements far underground. *Reviews of Modern Physics*, 24:133–175, 1952.

[60] P. Adamson et al. Measurement of the atmospheric muon charge ratio at tev energies with minos. *Phys. Rev.*, D76:052003, 2007.

[61] M. Goodman and P. Schreiner. The k/π ratio from the seasonal variations of muons in minos. docdb 4910.

[62] Y. Sekido et al. Point source of cosmic rays in Orion. *Physical Review*, 113:1108–1114, 1958.

[63] S. Standil R.P. Bukata. *Canadian J. of Phys.*, 43, 1965.

[64] M. Samorski and W. Stamm. Detection of 2×10^{15} to 2×10^{16} gev gamma-rays from Cyg X-3. *Ap.J. Lett.*, L 17:268, 1983.

[65] J. Lloyd-Evans, R.N. Coy, T. Lambert, J. Lapikens, N. Patel, R.J.O. Reid, and A.A. Watson. Observations of γ rays$> 10^{15}$ ev from Cygnus x-3. *Nature*, 305, 1983.

[66] Peter Meszaros. Gamma-Ray Bursts. *Rept. Prog. Phys.*, 69:2259–2322, 2006.

[67] S. Covino. A Closer Look at a Gamma-Ray Burst. *Science*, 315:1798–1799, 2007.

[68] B.W. Carroll and D.A. Ostlie. *An Introduction to Modern Astrophysics*. Addison-Wesley Publishing, Reading, MA, USA, 1996.

[69] NASA. Legacy archive for microwave background data analysis (lambda). *http://lambda.gsfc.nasa.gov/product/map/current/params/lcdm_sz_lens_wmap5.cfm*, 2008.

[70] Eli Waxman. Cosmological gamma-ray bursts and the highest energy cosmic rays. *Phys. Rev. Lett.*, 75:386–389, 1995.

[71] N. Chiba et al. Akeno giant air shower array (AGASA) covering 100-km**2 area. *Nucl. Instrum. Meth.*, A311:338–349, 1992.

[72] N. Hayashida et al. The anisotropy of cosmic ray arrival directions around 10**18-eV. *Astropart. Phys.*, 10:303–311, 1999.

[73] M. Takeda et al. Extension of the cosmic-ray energy spectrum beyond the predicted Greisen-Zatsepin-Kuzmin cutoff. *Phys. Rev. Lett.*, 81:1163–1166, 1998.

[74] S. C. Corbato et al. HiRes: A High resolution Fly's Eye detector. *Nucl. Phys. Proc. Suppl.*, 28B:36–39, 1992.

[75] R. U. Abbasi et al. Measurement of the flux of ultrahigh energy cosmic rays from monocular observations by the High Resolution Fly's Eye experiment. *Phys. Rev. Lett.*, 92:151101, 2004.

[76] R. U. Abbasi et al. A search for arrival direction clustering in the HiRes-I monocular data above 10**19.5-eV. *Astropart. Phys.*, 22:139–149, 2004.

[77] J.W. Cronin. High energy astrophysics. In M. Riordan, editor, *Lepton-Photon Symposium 1989*. World Scientific Publishing Co. Pte. Ltd., Singapore, 1989.

[78] J. Ahrens et al. IceCube: The next generation neutrino telescope at the South Pole. *Nucl. Phys. Proc. Suppl.*, 118:388–395, 2003.

[79] IceCube Collaboration. The icecube collaboration: contributions to the 30th international cosmic ray conference (icrc 2007). *arXiv:0711.0353 [astro-ph]*.

[80] C. De Marzo et al. MACRO: A LARGE AREA DETECTOR AT THE GRAN SASSO LABORATORY. *Nuovo Cim.*, C9:281–292, 1986.

[81] M. Ambrosio et al. Low energy atmospheric muon neutrinos in MACRO. *Phys. Lett.*, B478:5–13, 2000.

[82] M. Ambrosio et al. Moon and sun shadowing effect in the macro detector. *Astropart. Phys.*, 20:145–156, 2003.

[83] W. W. M. Allison et al. The Soudan-2 detector: The Operation and performance of the tracking calorimeter modules. *Nucl. Instrum. Meth.*, A381:385–397, 1996.

[84] Mayly C. Sanchez et al. Observation of atmospheric neutrino oscillations in Soudan 2. *Phys. Rev.*, D68:113004, 2003.

[85] N. P. Longley et al. Ultrahigh-energy cosmic ray composition from surface air shower and underground muon measurements at Soudan-2. *Phys. Rev.*, D52:2760–2765, 1995.

[86] Y. Fukuda et al. The Super-Kamiokande detector. *Nucl. Instrum. Meth.*, A501:418–462, 2003.

[87] Y. Fukuda et al. Evidence for oscillation of atmospheric neutrinos. *Phys. Rev. Lett.*, 81:1562–1567, 1998.

[88] S. Fukuda et al. Search for neutrinos from gamma-ray bursts using Super- Kamiokande. *Astrophys. J.*, 578:317–324, 2002.

[89] David Saltzberg et al. Observation of the Askaryan effect: Coherent microwave Cherenkov emission from charge asymmetry in high energy particle cascades. *Phys. Rev. Lett.*, 86:2802–2805, 2001.

[90] C. Allen et al. Status of the Radio Ice Cherenkov Experiment (RICE). *New Astron. Rev.*, 42:319–329, 1998.

[91] H. Landsman, L. Ruckman, and G. S. Varner. Radio detection of GZK neutrinos: AURA status and plans. Prepared for 30th International Cosmic Ray Conference (ICRC 2007), Merida, Yucatan, Mexico, 3-11 Jul 2007.

[92] Sebastian Boeser et al. SPATS: A south pole acoustic test setup. *Int. J. Mod. Phys.*, A21S1:221–226, 2006.

[93] Predrag Miocinovic et al. Tuning into UHE neutrinos in Antarctica: The ANITA experiment. 2005.

[94] S. W. Barwick et al. Constraints on cosmic neutrino fluxes from the ANITA experiment. *Phys. Rev. Lett.*, 96:171101, 2006.

[95] G. J. Fishman and C. A. Meegan. Gamma-ray bursts. *Ann. Rev. Astron. Astrophys.*, 33:415–458, 1995.

[96] E. Costa, F. Frontera, J. Heise, M. Feroci, J. in't Zand, F. Fiore, M. N. Cinti, D. Dal Fiume, L. Nicastro, M. Orlandini, E. Palazzi, M. Rapisarda#, G. Zavattini, R. Jager, A. Parmar, A. Owens, S. Molendi, G. Cusumano, M. C. Maccarone, S. Giarrusso, A. Coletta, L. A. Antonelli, P. Giommi, J. M. Muller, L. Piro, and R. C. Butler. Discovery of an X-ray afterglow associated with the γ-ray burst of 28 February 1997. *Nature*, 387:783–785, June 1997.

[97] MIT. `http://space.mit.edu/HETE/`.

[98] J. Hjorth, J. Sollerman, P. Møller, J. P. U. Fynbo, S. E. Woosley, C. Kouveliotou, N. R. Tanvir, J. Greiner, M. I. Andersen, A. J. Castro-Tirado, J. M. Castro Cerón, A. S. Fruchter, J. Gorosabel, P. Jakobsson, L. Kaper, S. Klose, N. Masetti, H. Pedersen, K. Pedersen, E. Pian, E. Palazzi, J. E. Rhoads, E. Rol, E. P. J. van den Heuvel, P. M. Vreeswijk, D. Watson, and R. A. M. J. Wijers. A very energetic supernova associated with the γ-ray burst of 29 March 2003. *Nature*, 423:847–850, June 2003.

[99] S. S. Holt, N. Gehrels, and J. A. Nousek. *Gamma-Ray Bursts in the Swift Era.* Gamma-Ray Bursts in the Swift Era, Edited by Stephen S. Holt, Neil Gehrels, and John A. Nousek. Berlin: Springer, 2006. ISBN 0-7354-0326-0., 2006.

[100] Cheryl P. Hurkett et al. GRB 050505: A high redshift burst discovered by Swift. *Mon. Not. Roy. Astron. Soc.*, 368:1101–1109, 2006.

[101] NASA. `http://glast.gsfc.nasa.gov/`.

[102] W. Hofmann. Status of the HESS project. Prepared for 28th International Cosmic Ray Conferences (ICRC 2003), Tsukuba, Japan, 31 Jul - 7 Aug 2003.

[103] T. C. Weekes et al. VERITAS: The very energetic radiation imaging telescope array system. *Astropart. Phys.*, 17:221–243, 2002.

[104] V. Fonseca. The MAGIC telescope project. *Acta Phys. Polon.*, B30:2331–2349, 1999.

[105] R. Enomoto et al. Design study of CANGAROO-III, stereoscopic imaging atmospheric Cherenkov telescopes for sub-TeV gamma-ray detection. *Astropart. Phys.*, 16:235–244, 2002.

[106] Brenda L. Dingus. HAWC (High Altitude Water Cherenkov) observatory for surveying the TeV sky. *AIP Conf. Proc.*, 921:438–439, 2007.

[107] Robert W. Atkins et al. Milagrito, a TeV air-shower array. *Nucl. Instrum. Meth.*, A449:478–499, 2000.

[108] P. Adamson et al. The MINOS scintillator calorimeter system. *IEEE Trans. Nucl. Sci.*, 49:861–863, 2002.

[109] : D. G. Michael. The magnetized steel and scintillator calorimeters of the MINOS experiment. 2008.

[110] The MINOS Collaboration. The MINOS technical design report. Technical report, Fermilab, oct 1998.

[111] D. Jason Koskinen. An Overview of the Main Injector Neutrino Oscillation Search, the Rack Protection System, and Methods to Degauss a Large Iron Calorimeter Particle Detector. Master's thesis, University of Minnesota, Duluth, 2004.

[112] K. Lang et al. A comprehensive characterization of Hamamatsu 16- and 64- anode PMTs. *Nucl. Instrum. Meth.*, A461:571–573, 2001.

[113] J. Oliver, N. Felt, G. Feldman, A. Lebedev, and R. Lee. Design and performance of the readout system of the minos far detector. *IEEE Trans. Nucl. Sci.*, 51:2193–2195, 2004.

[114] Philip Adamson. An led calibration system for the minos long baseline neutrino oscillation experiment. *Ph.D. Thesis, University of Sussex (2001), Fermilab-Thesis-2001-49*.

[115] The MINOS Collaboration. Proposal for a cosmic ray veto shield for the MINOS far detector. Numi Note 1037.

[116] Benjamin Phillip Speakman. Atmospheric electron neutrinos in the MINOS far detector. *Ph.D. thesis, Univeristy of Minnesota (2007) FERMILAB-THESIS-2007-26*.

[117] P. Adamson et al. First observations of separated atmospheric nu/mu and anti- nu/mu events in the minos detector. *Phys. Rev.*, D73:072002, 2006.

[118] P. Adamson et al. Charge-separated atmospheric neutrino-induced muons in the minos far detector. *Phys. Rev.*, D75:092003, 2007.

[119] Dir. Peter Jackson. Lord of the Rings: The Two Towers. *New Line Cinema*, 2002.

[120] G. D. Barr, T. K. Gaisser, P. Lipari, Simon Robbins, and T. Stanev. A three-dimensional calculation of atmospheric neutrinos. *Phys. Rev.*, D70:023006, 2004.

[121] S. Agostinelli et al. GEANT4: A simulation toolkit. *Nucl. Instrum. Meth.*, A506:250–303, 2003.

[122] Jim Hylen et al. `http://www.hep.utexas.edu/numi/beamMC/MC-code.html`.

[123] H. Gallagher. The neugen neutrino event generator. *Nucl. Phys. Proc. Suppl.*, 112:188–194, 2002.

[124] Susan Marie Kasahara. A study of cosmic ray composition in the knee region using multiple muon events in the Soudan-2 detector. *Ph.D. Thesis, University of Minnesota (1997), UMI-97-21625.*

[125] Jurgen Wentz et al. Simulation of atmospheric muon and neutrino fluxes with CORSIKA. *Phys. Rev.*, D67:073020, 2003.

[126] N. N. Kalmykov, S. S. Ostapchenko, and A. I. Pavlov. Quark-gluon string model and EAS simulation problems at ultra-high energies. *Nucl. Phys. Proc. Suppl.*, 52B:17–28, 1997.

[127] R. S. Fletcher, T. K. Gaisser, Paolo Lipari, and Todor Stanev. SIBYLL: An Event generator for simulation of high-energy cosmic ray cascades. *Phys. Rev.*, D50:5710–5731, 1994.

[128] R. Brun and F. Rademakers. Root: An object oriented data analysis framework. *Nucl. Instrum. Meth.*, A389:81–86, 1997.

[129] William H. Press et al. *Numerical Recipes in C++, The Art of Scientific Computing, 2nd ed.* Cambridge University Press, Cambridge, UK, 2002.

[130] Y. Becherini et al. Time correlations of high energy muons in an underground detector. *Arxiv E-Print*, astro-ph 0502251, 2005.

[131] S. P. Ahlen et al. Arrival time distributions of very high-energy cosmic ray muons in macro. *Nucl. Phys.*, B370:432–444, 1992.

[132] M. Crouch. Muon Charge Ratio and Ratio of Neutrinos to Antineutrinos in Atmospheric Cosmic Rays. In *International Cosmic Ray Conference*, volume 6 of *International Cosmic Ray Conference*, page 165, 1987.

[133] M. Ambrosio et al. Seasonal variations in the underground muon intensity as seen by MACRO. *Astropart. Phys.*, 7:109–124, 1997.

[134] A. Bouchta. Seasonal variation of the muon flux seen by AMANDA. 1999. Prepared for 26th International Cosmic Ray Conference (ICRC 99), Salt Lake City, UT, 17-25 Aug.

[135] Brian J. Rebel. *Neutrino-Induced Muons in the MINOS Far Detector*. PhD thesis.

[136] *European Centre for Medium-Range Weather Forecasts ECMWF Operational Analysis data, [Internet] British Atmospheric Data Centre*, 2006-2007, Available from http://badc.nerc.ac.uk/data/ecmwf-op/.

[137] G. Cini Castagnoli and M.A. Dodero. *II Nuovo Cim. B*, 51, 1967.

[138] J.E. Humble et al. *Proc. 16th ICRC (Kyoto)*, 4, 1979.

[139] P. Adamson et al. Measurement of neutrino oscillation parameters by minos. *To be published in Phys Rev D*, 2007.

[140] F. James and M. Roos. Minuit: A system for function minimization and analysis of the parameter errors and correlations. *Comput. Phys. Commun.*, 10:343–367, 1975.

[141] P. Adamson et al. Sudden stratospheric warmings seen in minos deep underground muon data. *To be published in ?*, 2008.

[142] I. Durre, R. S. Vose, and D.B. Wuertz. Overview of the integrated global radiosonde archive. *Journal of Climate*, 19:53–68, 2006.

[143] M. Ambrosio et al. The search for the sidereal and solar diurnal modulations in the total macro muon data set. *Phys. Rev.*, D67:042002, 2003.

[144] N. Sherman. *Phys. Rev.*, 93, 1954.

[145] A.G. Fenton, R.M. Jacklyn, and R.B. Taylor. *II Nuovo Cimento B*, 22, 1961.

[146] Yu.M. Andreyev et al. *Proc. 20th ICRC (Moscow)*, 7, 1990.

[147] D.J. Cutler et al. *Proc. 17th ICRC (Paris)*, 4, 1981.

[148] T. N. Carlson. Mid-latitude weather systems. 1994. New York, USA: Routledge 507 p.

[149] M. Galassi et al. Gnu scientific library reference manual (2nd ed.).

[150] National Oceanographic and Atmospheric Administration. 1976 u.s. standard atmosphere. 1976. Washington, D.C., USA: U.S. Government Printing Office.

[151] Committee on Space Research. The cospar international reference atmosphere (cira-86), [internet]. British Atmospheric Data Centre.

[152] A. M. Rossi et al. Experimental Study of the Energy Dependence in Proton Proton Inclusive Reactions. *Nucl. Phys.*, B84:269, 1975.

[153] C. Adler et al. Kaon production and kaon to pion ratio in Au + Au collisions at s(NN)**(1/2) = 130-GeV. *Phys. Lett.*, B595:143–150, 2004.

[154] S. V. Afanasiev et al. Energy dependence of pion and kaon production in central Pb + Pb collisions. *Phys. Rev.*, C66:054902, 2002.

[155] C. Alt et al. Inclusive production of charged pions in p p collisions at 158-GeV/c beam momentum. *Eur. Phys. J.*, C45:343–381, 2006.

[156] M. Gazdzicki and D. Roehrich. Pion multiplicity in nuclear collisions. *Z. Phys.*, C65:215–223, 1995.

[157] D. E. Alexandreas et al. Observation of shadowing of ultrahigh-energy cosmic rays by the moon and the sun. *Phys. Rev.*, D43:1735–1738, 1991.

[158] A. Borione et al. Observation of the shadows of the moon and sun using 100- tev cosmic rays. *Phys. Rev.*, D49:1171–1177, 1994.

[159] M. Amenomori et al. Cosmic ray deficit from the directions of the moon and the sun detected with the tibet air shower array. *Phys. Rev.*, D47:2675–2681, 1993.

[160] J. H. Cobb et al. The observation of a shadow of the moon in the underground muon flux in the soudan 2 detector. *Phys. Rev.*, D61:092002, 2000.

[161] M. Ambrosio et al. Observation of the shadowing of cosmic rays by the moon using a deep underground detector. *Phys. Rev.*, D59:012003, 1999.

[162] P. Achard et al. Measurement of the shadowing of high-energy cosmic rays by the moon: A search for tev-energy antiprotons. *Astropart. Phys.*, 23:411–434, 2005.

[163] M. Urban, P. Fleury, R. Lestienne, and F. Plouin. Can we detect antimatter from other galaxies by the use of the earth's magnetic field and the moon as an absorber? *Nucl. Phys. Proc. Suppl.*, 14B:223–236, 1990.

[164] J. Heintze et al. Measuring the chemical composition of cosmic rays by utilizing the solar and geomagnetic fields. 1990. In *Adelaide 1990, Proceedings, Cosmic ray, vol. 4* 456-459.

[165] E. N. Parker. Dynamics of interplanetary gas and magnetic fields. *Astrophys. J.*, 128:664, 1958.

[166] E.W. Grashorn. Observation of seasonal variations with the minos far detector. In *International Cosmic Ray Conference*, 2007.

[167] E.M. Standish. JPL planetary and lunar ephemerides. *JPL IOM*, 312.F-98-04B, 1998.

[168] G. Kaplan et al. Mean and apparent place computations in the new IAU system. III- apparent, topocentric, and astrometric places of planets and stars. *Astronomical Journal*, 115:361, 1989.

[169] R.W. Sinnott. Virtues of the haversine. *Sky and Telescope*, 68(2), 1984.

[170] National Oceanographic and Atmospheric Administration. 2008. http://www.swpc.noaa.gov/SolarCycle/.

[171] Solar Influences Data Center. 2008. http://sidc.oma.be/news/101/welcome.html.

[172] J. Ahrens et al. Search for extraterrestrial point sources of neutrinos with AMANDA-II. *Phys. Rev. Lett.*, 92:071102, 2004.

[173] D. DeMuth et al. Horizontal muons and a search for AGN neutrinos in Soudan 2. *Astropart. Phys.*, 20:533–547, 2004.

[174] M. Ikeda et al. Search for Supernova Neutrino Bursts at Super- Kamiokande. *Astrophys. J.*, 669:519–524, 2007.

[175] M. Ambrosio et al. Search for diffuse neutrino flux from astrophysical sources with MACRO. *Astropart. Phys.*, 19:1–13, 2003.

[176] Molly E. C. Swanson et al. Search for diffuse astrophysical neutrino flux using ultra-high energy upward-going muons in Super-Kamiokande I. *Astrophys. J.*, 652:206–215, 2006.

[177] S. P. Ahlen et al. Muon astronomy with the MACRO detector. *Astrophys. J.*, 412:301–311, 1993.

[178] P.R. Bevington and D.K. Robinson. *Data Reduction and Error Analysis for the Physical Sciences, 2nd ed.* McGraw-Hill Inc., New York, 1992.

[179] D. E. Alexandreas et al. Point source search techniques in ultrahigh-energy gamma- ray astronomy. *Nucl. Instrum. Meth.*, A328:570–577, 1993.

[180] Franz-Josef Zickgraf, D. Engels, H. J. Hagen, D. Reimers, and W. Voges. The Hamburg/RASS catalogue of optical identifications. northern high-galactic latitude ROSAT bright source catalogue x-ray sources. *Astron. Astrophys.*, 406:535–554, 2003.

[181] O. Helene. Upper Limit of Peak Area. *Nucl. Instr. Meth.*, 212:319, 1983.

[182] T. Sakamoto et al. The First Swift BAT Gamma-Ray Burst Catalog. 2007.

[183] P. Lipari and T. Stanev. Propagation of multi - TeV muons. *Phys. Rev.*, D44:3543–3554, 1991.

[184] R. Gran. Private communication, May 2008.

[185] Gary J. Feldman and Robert D. Cousins. A Unified approach to the classical statistical analysis of small signals. *Phys. Rev.*, D57:3873–3889, 1998.